



HAL
open science

Nonlinear and dispersive numerical modeling of nearshore waves

Cécile Raoult

► **To cite this version:**

Cécile Raoult. Nonlinear and dispersive numerical modeling of nearshore waves. Fluid mechanics [physics.class-ph]. Université Paris-Est, 2016. English. NNT : 2016PESC1150 . tel-01547187

HAL Id: tel-01547187

<https://pastel.hal.science/tel-01547187>

Submitted on 26 Jun 2017

HAL is a multi-disciplinary open access archive for the deposit and dissemination of scientific research documents, whether they are published or not. The documents may come from teaching and research institutions in France or abroad, or from public or private research centers.

L'archive ouverte pluridisciplinaire **HAL**, est destinée au dépôt et à la diffusion de documents scientifiques de niveau recherche, publiés ou non, émanant des établissements d'enseignement et de recherche français ou étrangers, des laboratoires publics ou privés.

École Doctorale SIE

Laboratoire d'Hydraulique Saint-Venant

Thèse

Présentée pour l'obtention du grade de DOCTEUR

DE L'UNIVERSITE PARIS-EST

par

Cécile Raoult

Modélisation numérique non-linéaire et dispersive des vagues en zone côtière.

Spécialité : Mécanique des fluides

Soutenue le 12 décembre 2016 devant un jury composé de :

Rapporteur	Pr. Harry Bingham	(Technical University of Denmark)
Rapporteur	Pr. Pierre Ferrant	(Ecole Centrale Nantes)
Examineur	Pr. Kostas Belibassakis	(National Technical University of Athens)
Examineur	Pr. Frédéric Dias	(University College Dublin)
Directeur de thèse	Pr. Michel Benoit	(IRPHE & Ecole Centrale Marseille)
Co-encadrante de thèse	Dr. Marissa Yates	(LHSV & Cerema)
Président du jury	Dr. Agnès Maurel	(Institut Langevin)



Thèse effectuée au sein du **Laboratoire d'Hydraulique Saint-Venant**

de l'Université Paris-Est

6, quai Watier

BP 49

78401 Chatou cedex

France

Financements: ANR (bourse CIFRE # 1024-2013) et EDF R&D

Résumé

Au cours de cette thèse, un modèle potentiel résolvant les équations d'Euler-Zakharov a été développé dans le but de simuler la propagation de vagues et d'états de mer irréguliers et multidirectionnels, du large jusqu'à la côte, sur des bathymétries variables. L'objectif est de représenter les effets non-linéaires et dispersifs le plus précisément possible pour des domaines côtiers bidimensionnels (dans le plan horizontal) de l'ordre de quelques kilomètres.

La version 1DH initiale du modèle, résolvant le problème aux limites de Laplace à l'aide de schémas aux différences finies d'ordre élevé dans la direction horizontale combinés à une approche spectrale sur la verticale, a été améliorée et validée. L'implémentation de conditions aux limites de type Dirichlet et Neumann pour générer des vagues dans le domaine a été étudiée en détail. Dans la pratique, une zone de relaxation a été utilisée en complément de ces conditions pour améliorer la stabilité du modèle.

L'expression analytique de la relation de dispersion a été établie dans le cas d'un fond plat. Son analyse a montré que la représentation des effets dispersifs s'améliorait significativement avec l'augmentation de la résolution sur la direction verticale (i.e. avec le degré maximal de la base de polynômes de Tchebyshev utilisée pour projeter le potentiel des vitesses sur la verticale). Une étude de convergence menée pour des ondes solitaires modérément à fortement non-linéaires a confirmé la convergence exponentielle avec la résolution verticale grâce à l'approche spectrale, ainsi que les convergences algébriques en temps et en espace sur l'horizontale avec des ordres d'environ 4 (ou plus) en accord avec les schémas numériques utilisés.

La comparaison des résultats du modèle à plusieurs jeux de données expérimentales a démontré les capacités du modèle à représenter les effets non-linéaires induits par les variations de bathymétrie, notamment les transferts d'énergie entre les composantes harmoniques, ainsi que la représentation précise des propriétés dispersives. Une formulation visco-potentielle a également été implémentée afin de prendre en compte les effets visqueux induits par la dissipation interne et le frottement sur le fond. Cette formulation a été validée dans le cas d'une faible viscosité avec un fond plat ou présentant une faible pente.

Dans le but de représenter des champs de vagues 2DH, le modèle a été étendu en utilisant une discrétisation non-structurée (par nuage de points) du plan horizontal. Les dérivées horizontales ont été estimées à l'aide de la méthode RBF-FD (Radial Basis Function-Finite Difference), en conservant l'approche spectrale sur la verticale. Une étude numérique de sensibilité a été menée afin d'évaluer la robustesse de la méthode RBF-FD, en comparant différents types de RBFs, avec ou sans paramètre de forme et l'ajout éventuel d'un polynôme. La version 2DH du modèle a été utilisée pour simuler deux expériences en bassin, validant ainsi l'approche choisie et démon-

trant son applicabilité pour simuler la propagation 3D des vagues faisant intervenir des effets non-linéaires. Dans le but de réduire le temps de calcul et de pouvoir appliquer le code à des simulations sur de grands domaines, le code a été modifié pour utiliser le solveur linéaire direct en mode parallèle.

Mots-clé:

vagues, vagues côtières, propagation des vagues, modélisation numérique, fond variable, écoulement potentiel, Fonction de Base Radiales, vagues non-linéaires, modèle visco-potentiel

Nonlinear and dispersive numerical modeling of nearshore waves

Abstract

In this work, a potential flow model based on the Euler-Zakharov equations was developed with the objective of simulating the propagation of irregular and multidirectional sea states from deep water conditions to the coast over variable bathymetry. A highly accurate representation of nonlinear and dispersive effects for bidimensional (2DH) nearshore and coastal domains on the order of kilometers is targeted.

The preexisting 1DH version of the model, resolving the Laplace Boundary Value problem using a combination of high-order finite difference schemes in the horizontal direction and a spectral approach in the vertical direction, was improved and validated. The generation of incident waves through the implementation of specific Dirichlet and Neumann boundary conditions was studied in detail. In practice, these conditions were used in combination with a relaxation zone to improve the stability of the model.

The linear dispersion relation of the model was derived analytically for the flat bottom case. Its analysis showed that the accuracy of the representation of dispersive effects improves significantly by increasing the vertical resolution (i.e. the maximum degree of the Chebyshev polynomial basis used to project the potential in the vertical). A convergence study conducted for moderate to highly nonlinear solitary waves confirmed the exponential convergence in the vertical dimension owing to the spectral approach, and the algebraic convergence in time and in space (horizontal dimension) with orders of about 4 (or higher) in agreement with the numerical schemes used.

The capability of the model to represent nonlinear effects induced by variable bathymetry, such as the transfer of energy between harmonic components, as well as the accurate representation of dispersive properties, were demonstrated with comparisons to several experimental data sets. A visco-potential flow formulation was also implemented to take into account viscous effects induced by bulk viscosity and bottom friction. This formulation was validated in the limit of small viscosity for mild slope bathymetries.

To represent 2DH wave fields in complex nearshore domains, the model was extended using an unstructured discretization (scattered nodes) in the horizontal plane. The horizontal derivatives were estimated using the RBF-FD (Radial Basis Function - Finite Difference) method, while the spectral approach in the vertical remained unchanged. A series of sensitivity tests were conducted to evaluate numerically the robustness of the RBF-FD method, including a comparison of a variety of RBFs with or without shape factors and augmented polynomials. The 2DH version of the model was used to simulate two wave basin experiments, validating the approach and demonstrating the applicability of this method for 3D wave propagation, including nonlinear

effects. As an initial attempt to improve the computational efficiency of the model for running simulations of large spatial domains, the code was adapted to use a parallelized direct linear solver.

Keywords:

waves, coastal waves, wave propagation, numerical modeling, variable bottom, potential flow, Radial Basis Functions, nonlinear waves, visco-potential

Remerciements

Tout d'abord, je tiens à remercier mon directeur de thèse Michel Benoit et mon encadrante Marissa Yates pour toute l'aide qu'ils m'ont apportée pendant ces trois années. L'intérêt qu'ils ont porté à ce sujet m'a beaucoup motivée. Merci pour la patience, l'écoute et la disponibilité pour toutes les discussions aussi bien sur les aspects numériques que physiques de la propagation des vagues. Merci à Michel d'être resté disponible après son départ pour le soleil de Marseille et à Marissa d'avoir assuré la relève.

Je souhaite également remercier les membres du jury qui ont accepté de participer à ma soutenance, de l'intérêt qu'ils ont porté à mes travaux lors de la discussion. Merci aux Pr. Harry Bingham et Pierre Ferrant pour leurs commentaires et le temps qu'ils ont consacré à la lecture de mon manuscrit. Merci également à Dr. Agnès Maurel d'avoir présidé mon jury de thèse.

Je remercie EDF R&D et l'ANRT pour le financement de ce projet de thèse dans le cadre de la convention Cifre # 1024-2013 réalisé au laboratoire Saint-Venant. Un grand merci général à toutes les personnes du laboratoire Saint-Venant et du groupe P74 avec qui j'ai pu interagir. Merci à Jeff pour l'aide numérique et à Christophe pour l'aide logistique. Merci à Sébastien pour les discussions sur la viscosité. Merci à Jérémie pour les longues discussions parfois sans solution. Merci à Marine pour le soutien, le partage des galères et des bons moments corses. Et enfin merci à Steve le meilleur co-bureau de l'univers grâce à qui j'ai perfectionné mon Anglais, ma créativité artistique et mes aptitudes pour les combats de stickers. Merci à Eduardo pour m'avoir fait découvrir le monde expérimental, et merci à Agnès, Vincent et Philippe pour cette collaboration et toutes les discussions très enrichissantes qui en ont découlé.

Enfin, je tiens à remercier infiniment ma famille, mes parents et mes frères qui m'ont toujours soutenue et cru en moi (... souvent plus que moi). Merci à mes amis pour les moments de détente et de décompression parfois nécessaires. Et par dessus tout, je remercie Jonathan d'avoir été si patient, toujours attentif et attentionné, prêt à m'écouter pendant des heures parler de mes simulations qui me donnaient du fil à retordre.

Contents

Introduction	1
1 Derivation and analysis of the Euler-Zakharov mathematical model	7
1.1 From the Navier-Stokes equations to the Zakharov equations	8
1.1.1 The Euler equations and boundary conditions	8
1.1.2 Potential flow equations: the water wave problem	10
1.1.3 Expression as a function of surface quantities	11
1.1.4 Discussion of the assumptions	12
1.1.5 The Zakharov equations	13
1.2 Resolution of the Laplace BVP using a spectral method in the vertical	14
1.2.1 Change of the vertical coordinate	15
1.2.2 Expansion of the potential on the basis of Chebyshev polynomials	15
1.2.3 Application of the Chebyshev-Tau approach to obtain the linear system	19
1.3 Computation of flow properties	21
1.3.1 Horizontal and vertical velocities in the fluid domain	21
1.3.2 Pressure in the fluid domain	22
1.3.3 Depth averaged horizontal velocity	23
1.4 Linear properties of the model	24
1.4.1 Linearization of the equations for a flat bottom	24
1.4.2 The first order Stokes solution	24
1.4.3 Derivation of the linear dispersion relation of the proposed model	25
1.4.4 Accuracy of the dispersion relation of Misthyc	29
2 Numerical implementation of the 1DH model	35
2.1 Numerical methods	36

2.1.1	Integration in time	36
2.1.2	Derivatives in space	36
2.1.3	Resolution of the linear system	38
2.2	Boundary conditions for wave generation and absorption	38
2.2.1	Wave absorption	38
2.2.2	Wave generation	47
3	Validation of the 1DH version of the model	63
3.1	Reflection of linear waves propagating over Roseau-type bathymetric profile . .	65
3.2	Solitary wave propagation over a flat bottom	71
3.2.1	Objectives	71
3.2.2	Description	71
3.2.3	Simulations and evaluation criteria	72
3.2.4	Results	74
3.2.5	Conclusions	90
3.3	Nonlinear wave dynamics in constant water depth	92
3.4	Waves generated by an impulsive bottom motion	95
3.4.1	The linear solution	96
3.4.2	Comparison with the experimental data	96
3.5	Regular waves over a submerged bar	100
3.6	Random waves over a barred beach	104
4	Modeling viscous dissipation: the visco-potential approach	111
4.1	Introduction	112
4.1.1	Review of sources of wave energy dissipation	112
4.1.2	Review of wave attenuation due to viscous effects	113
4.1.3	On the inclusion of viscous dissipation in potential modeling approaches	114
4.2	Mathematical modeling of visco-potential flows	117
4.2.1	Linearized Navier-Stokes system	117
4.2.2	Dissipation due to bulk viscosity	118
4.2.3	Dissipation due to bottom friction	122
4.3	Numerical implementation of the viscous terms	126

4.3.1	Numerical implementation of the terms in the free surface boundary condition	126
4.3.2	Numerical implementation of the bottom friction term	127
4.4	Validation test cases	129
4.4.1	Bulk viscosity terms in the linear regime	129
4.4.2	Viscous standing wave in the linear regime	134
4.4.3	Attenuation of a solitary wave in a wave flume	141
4.4.4	Dissipation of waves propagating over a step	145
4.5	Conclusions	153
5	Development and implementation of the 2DH version of the model using Radial Basis Functions (RBF)	155
5.1	Presentation of the RBF method	156
5.1.1	General context	156
5.1.2	Condition number of the interpolation matrix	158
5.1.3	Accuracy of the estimates and choice of the RBF	160
5.1.4	Runge phenomenon and boundary errors	163
5.1.5	Stability for the resolution of time-dependent PDEs	163
5.2	Implementation of the RBF-FD method	164
5.2.1	Theory	164
5.2.2	Numerical implementation	167
5.3	Tests on the estimation of derivatives with the RBF-FD method.	169
5.3.1	Presentation of the test functions	169
5.3.2	Presentation of the tests	171
5.3.3	General results	172
5.3.4	RBFs depending on a shape parameter C	174
5.3.5	RBF not depending on a shape parameter	181
5.3.6	Conclusions and recommendations	184
6	Validation of the 2DH version of the model using RBFs in the horizontal plane	187
6.1	Regular waves propagating over a flat bottom	188
6.2	Regular waves propagating over a semi-circular step	193
6.3	Regular waves propagating over an elliptical shoal	200

6.4	Computational cost and optimization	207
6.4.1	Computational requirements of the code	207
6.4.2	Matrix reordering	207
6.4.3	Parallelization of the linear solver	208
6.4.4	Summary	210
	Conclusions and perspectives	211
	Appendix A : Dispersion relation for Misthyc	217
	Bibliography	221

List of Figures

1	Derivation and analysis of the Euler-Zakharov mathematical model	7
1.1	Diagram for the definition of the notations.	8
1.2	Eight first Chebyshev polynomials of the first kind $T_n(s)$ ($n = 0$ to 7).	16
1.3	Phase velocity ratio in comparison with first-order Stokes theory, for Misthyc with several values of N_T (solid lines), for the (2,2) Padé approximant (dashed green), the (4,4) Padé approximant (dashed light blue), Chazel et al. (2009) (dashed red) and Madsen et al. (2006) (dashed dark blue).	32
1.4	Phase velocity relative error in comparison with first-order Stokes theory, for Misthyc with several values of N_T (solid lines), the (2,2) Padé approximant (dashed green), the (4,4) Padé approximant (dashed light blue), Chazel et al. (2009) (dashed red) and Madsen et al. (2006) (dashed dark blue).	32
1.5	Phase velocity ratio in comparison with first-order Stokes theory, for Misthyc with several values of N_T (solid lines), Chazel et al. (2009) (dashed red) and Madsen et al. (2006) (dashed dark blue). The extent of the horizontal axis is from $kh = \pi$ (deep water threshold) to $kh = 100$	33
1.6	Relative phase velocity in comparison with first-order Stokes theory, for Misthyc with several values of N_T (solid lines), Chazel et al. (2009) (dashed red) and Madsen et al. (2006) (dashed dark blue). The extent of the horizontal axis is from $kh = \pi$ (deep water threshold) to $kh = 100$	34
2	Numerical implementation of the 1DH model	35
2.1	Shapes of the six $1 - C_r(x)$ coefficients considered in the first set of simulations for the absorption relaxation zone.	41
2.2	Comparison of the normalized wave height for $x \in [18, 24]$ m for different shapes of the relaxation coefficient. H_0 is the incident wave height, $H_0 = 2a = 0.12$ m.	42

2.3	Shape of the coefficient $1 - C_r(x)$ for several values of the α parameter considered in the second set of simulations for the absorption relaxation zone.	43
2.4	Comparison of the normalized wave height for $x \in [18, 24]$ m for several values of the parameter α . H_0 is the incident wave height, $H_0 = 2a = 0.12$ m.	44
2.5	Reflection coefficient as a function of the parameter α for three different lengths of the relaxation zone ($L_{relax} = 1L$ (blue), $1.5L$ (green) and $2L$ (red)).	45
2.6	Comparison of the normalized wave height for $x \in [18, 24]$ m for several values of the parameter μ_0 . H_0 is the incident wave height, $H_0 = 2a = 0.12$ m.	46
2.7	Reflection coefficient as a function of the parameter μ_0 for a damping zone of one wavelength.	46
2.8	Free surface elevation profile after 1500 time steps ($15T$). Comparison of the three methods to introduce the boundary condition in time, for the four implementation options (A, B, C, D), for Dirichlet boundary condition (left) and Neumann boundary conditions (right).	58
2.9	Comparison of the a_n coefficients computed at $t \approx 15T$, at $x = x_b$, for Dirichlet boundary conditions (red triangles) and Neumann boundary conditions (blue triangles). The coefficients corresponding to the linear potential expanded on the Chebyshev polynomial basis are presented for reference (black dots).	59
2.10	Comparison of the horizontal u and vertical w velocity profiles together with the velocity potential profile computed at $t \approx 15T$, at $x = x_b$, for Dirichlet boundary conditions (red) and Neumann boundary conditions (blue). The linear solution is presented for reference (black dashed line).	59
2.11	Comparison of the a_n coefficients computed at $t \approx 15T$, at $x = x_b$, for Dirichlet boundary conditions for options B, C and D . The coefficients corresponding to the linear potential expanded on the Chebyshev polynomial basis are presented for reference (black dots).	60
2.12	Comparison of the horizontal u and vertical w velocity profiles together with the velocity potential profile computed at $t \approx 15T$, at $x = x_b$, for Dirichlet boundary conditions for options B, C and D . The linear solution is presented for reference (black dashed line).	60
2.13	Comparison of the a_n coefficients computed at $t \approx 15T$, at $x = x_b$, for Neumann boundary conditions for options A and B . The coefficients corresponding to the linear potential expanded on the Chebyshev polynomial basis are presented for reference (black dots).	61

2.14	Comparison of the horizontal u and vertical w velocity profiles together with the velocity potential profile computed at $t \approx 15T$, at $x = x_b$, for Neumann boundary conditions for options A and B . The linear solution is presented for reference (black dashed line).	61
3	Validation of the 1DH version of the model	63
3.1	Bottom profiles and snapshots of free surface elevation (at an arbitrary time) for the two sets of (ϵ, β) considered: (a) $\epsilon = 1/3$ and $\beta = 0.25$, and (b) $\epsilon = 0.1$ and $\beta = 0.5$	66
3.2	Normalized wave height profiles for cases 1 and 2, for the first bathymetric profile ($\epsilon = 1/3, \beta = 0.25$). Comparison between Misthyc (blue) linear version with $N_T = 7$ and the coupled-mode model of Athanassoulis and Belibassakis (1999) (red).	68
3.3	Normalized wave height profiles for cases 3 and 4, for the second bathymetric profile ($\epsilon = 0.1, \beta = 0.5$). Comparison between Misthyc (blue) linear version with $N_T = 7$ and the coupled-mode model of Athanassoulis and Belibassakis (1999) (red).	69
3.4	Convergence with N_T of the reflection coefficient (R) and the transmission coefficient (T) obtained with Misthyc for case 3.	70
3.5	Convergence with N_T of the reflection coefficient (R) and the transmission coefficient (T) obtained with Misthyc for case 4.	70
3.6	Bathymetry and free surface profile at $\tilde{t} = 0$ for a solitary wave with nondimensional height $\delta = 0.5$ (the intermediate nonlinear case).	72
3.7	Free surface profiles at $\tilde{T} = 500$ for a range of Δt values ($M_x = 10$ and $N_T = 7$) for (a) $\delta = 0.3$, (b) $\delta = 0.5$ and (c) $\delta = 0.7$	77
3.8	Relative volume (left) and relative energy (right) time series for a range of Δt values ($M_x = 10$ and $N_T = 7$) for (a) $\delta = 0.3$, (b) $\delta = 0.5$ and (c) $\delta = 0.7$. Note that the axis scales change for each value of δ	78
3.9	Convergence as a function of the time step Δt and wave nonlinearity δ for $N_T = 7$ and $M_x = 10$	79
3.10	Free surface profiles at $\tilde{T} = 500$ for a range of Δx (CFL = 1.25 and $N_T = 7$) for (a) $\delta = 0.3$, (b) $\delta = 0.5$ and (c) $\delta = 0.7$	82
3.11	Relative volume (left) and relative energy (right) time series for a range of Δx values (CFL = 1.25 and $N_T = 7$) for (a) $\delta = 0.3$, (b) $\delta = 0.5$ and (c) $\delta = 0.7$. Note that the axis scales change for each value of δ	83

3.12	Convergence as a function of the horizontal resolution Δx and wave nonlinearity δ for $N_T = 7$ and CFL = 1.25.	84
3.13	Free surface profiles at $\tilde{T} = 500$ for several values of N_T (CFL = 1.25, with $M_x = 10$ and $M_t = 8$) for (a) $\delta = 0.3$, (b) $\delta = 0.5$ and (c) $\delta = 0.7$	87
3.14	Relative volume (left) and relative energy (right) time series for a range of N_T values (CFL = 1.25, with $M_x = 10$ and $M_t = 8$) for (a) $\delta = 0.3$, (b) $\delta = 0.5$ and (c) $\delta = 0.7$. Note that the vertical axis scales change for each value of δ	88
3.15	Convergence as a function of the Chebyshev polynomial order N_T (vertical space convergence) and wave nonlinearity δ with CFL = 1.25 ($M_x = 10$ and $M_t = 8$).	89
3.16	Simulation time as a function of (a) the time resolution Δt , (b) the spatial resolution Δx , and (c) the maximum order of the Chebyshev polynomial N_T (for $\delta = 0.3$ in red, $\delta = 0.5$ in blue, and $\delta = 0.7$ in green)	91
3.17	a) Spatial evolution of the first four harmonic amplitudes for test case A of Chapalain et al. (1992): experimental (circles) and Misthyc simulation (solid line) results. b) Spatial evolution of the phase difference between the first and second harmonic: experimental (circles) and Misthyc simulation (solid line) results.	93
3.18	Misthyc simulated free surface elevation η at four different positions in the wave channel for the test case A of Chapalain et al. (1992).	94
3.19	(left) Bathymetry at time t ($\zeta(t)$) and final bathymetry (ζ_0), and (right) temporal evolution of the bottom deformation.	95
3.20	Free surface time series at four locations: $(x - b)/h_0 =$ (a) 0, (b) 20, (c) 180, and (d) 400. Comparison between the linear solution (red dashed line) and results of the linear version of the model for $N_T = 3, 4, 7$ and 10.	97
3.21	Averaged absolute error Eq.(3.9) as a function of N_T for the four probes located at $(x - b)/h_0 = 0, 20, 180,$ and 400, and shown in Figure 3.20.	98
3.22	Free surface time series at four nondimensional positions in the domain: $(x - b)/h_0 =$ (a) 0, (b) 20, (c) 180, and (d) 400. Comparison between the present model simulations (black line) and Hammack (1973) measurements (red line). The associated linear solution (blue dotted line) is also shown.	99
3.23	Free surface profiles at $t\sqrt{g/h_0} = 2375$. Comparison between F&M09 final results (corresponding to their figure 3) with a resolution $\Delta x = 0.25$ m (dashed black line), a more recent simulation using the same model but with a resolution $\Delta x = 0.2$ m (solid black line), and Misthyc simulation results for several values of N_T ($N_T = 3$ light blue, $N_T = 5$, dashed blue and $N_T = 7$, red).	99
3.24	Bathymetry and position of wave probes in the Beji and Battjes (1993) experiments.	100

3.25	Comparison of measured and simulated (with $N_T = 7$) free surface elevation time series at probes 4 to 11 for case A of Dingemans (1994) (probe locations shown in Figure 3.24).	101
3.26	Spatial evolution of the first six harmonic amplitudes (at frequencies $f, 2f, \dots, 6f$) of the free surface elevation for case A of Dingemans (1994): observations (circles) and Misthyc simulation results (solid lines).	102
3.27	Comparison of measured and simulated free surface elevation time series at probes 6, 8, 10 and 11 for case A of Dingemans (1994). Results of simulations with 5 values of N_T (3, 4, 5, 7, 10) are compared (all other numerical parameters are constant).	103
3.28	Bathymetry and wave probe positions for the Becq-Girard et al. (1999) experiments.	104
3.29	Comparison of the measured and simulated variance spectra of the free surface position at probes 2, 5, 7, 9, 11, 13, 15 and 16 for the Becq-Girard et al. (1999) experiments (probe positions, Figure 3.28). The frequency scale is normalized by the peak frequency (f_p) to identify clearly the harmonic peaks (e.g. $2f_p, 3f_p, \dots$).	106
3.30	(a) Spatial evolution of the first five harmonic amplitudes for the Becq-Girard et al. (1999) experiments: observations (circles) and simulation results (Misthyc, solid lines). (b) Bathymetry.	107
3.31	Comparison of simulated and measured sea state parameters along the bathymetric profile for the Becq-Girard et al. (1999) experiments: (a) significant wave height (H_{m0}), (b) mean wave period ($T_{m-1,0}$), and (c) mean wave period ($T_{m0,2}$).	108
3.32	Comparison of simulated and measured sea state parameters along the bathymetric profile for the Becq-Girard et al. (1999) experiments: (a) skewness (or horizontal asymmetry), (b) vertical asymmetry, and (c) kurtosis.	109
4	Modeling viscous dissipation through the visco-potential approach	111
4.1	Set-up of the simulations of regular waves of amplitude $A = 0.05$ m, propagating in a periodic domain equal to one wavelength ($L = 2.5$ m), in constant water depth $h = 0.5$ m. The blue line is the initial free surface position and the red arrow indicates the direction of propagation of the wave.	130
4.2	Amplitude decay at the first node of the domain as a function of time with viscosity $\nu = 10^{-6} \text{ m}^2/\text{s}$, for cases 1-3.	131
4.3	Amplitude decay at the first node of the domain as a function of time with viscosity $\nu = 10^{-3} \text{ m}^2/\text{s}$, for cases 1-3.	132

4.4	Amplitude decay at the first node of the domain as a function of time with viscosity $\nu = 0.2263 \text{ m}^2/\text{s}$, for cases 1-3. (Note that the time interval in this figure is shorter than the simulated duration, contrary to Figures 4.2 and 4.3).	133
4.5	Set-up of the simulations of standing waves of amplitude a , oscillating in a periodic domain equal to one wavelength (L), in constant water depth h . Blue solid and dashed lines indicate the extreme positions of the free surface.	134
4.6	Evolution of the normalized kinetic energy of the system as a function of nondimensional time for $kh = \pi/3$ and $Re = 500$ ($\nu = 0.06264 \text{ m}^2/\text{s}$), for different values of Δx , Δt and N_T (see legend).	136
4.7	Evolution of the normalized kinetic energy of the system as a function of nondimensional time for $kh = \pi$ and $Re = 50$ ($\nu = 0.06264 \text{ m}^2/\text{s}$).	137
4.8	Evolution of the normalized kinetic energy of the system as a function of nondimensional time for $kh = \pi$ and $Re = 500$ ($\nu = 0.006264 \text{ m}^2/\text{s}$).	138
4.9	Evolution of the normalized kinetic energy of the system as a function of nondimensional time for $kh = \pi$ and $Re = 2500$ ($\nu = 0.001253 \text{ m}^2/\text{s}$).	139
4.10	Evolution of the normalized kinetic energy of the system as a function of nondimensional time for $kh = \pi/3$ and $Re = 500$ ($\nu = 0.06264 \text{ m}^2/\text{s}$).	139
4.11	Evolution of the normalized kinetic energy of the system as a function of nondimensional time for $kh = \pi/12$ and $Re = 500$ ($\nu = 0.06264 \text{ m}^2/\text{s}$).	140
4.12	Bathymetry, initial free surface elevation, and positions of wave gauges (black triangles) in the Liu et al. (2006) experiments.	141
4.13	Decrease of the amplitude of the soliton along the wave flume, for a) $\epsilon = 0.091$ and b) $\epsilon = 0.409$, comparing the experimental data (red dots), and numerical results without viscosity (light blue), with $\nu = 10^{-6} \text{ m}^2/\text{s}$ bottom pure slip condition (green), with $\nu = 10^{-6} \text{ m}^2/\text{s}$ no-slip bottom condition (blue), and with $\nu = 7.10^{-6} \text{ m}^2/\text{s}$ no-slip bottom condition (black)	143
4.14	Evolution of the amplitude of the soliton in the shoaling zone, for a) $\epsilon = 0.091$ and b) $\epsilon = 0.409$, comparing the experimental data (red dots), and the numerical results with $\nu = 7.10^{-6} \text{ m}^2/\text{s}$ (black).	143
4.15	Experimental set-up. ESPCI credit.	146
4.16	Bathymetry used in the numerical simulations, showing a zoom of the hyperbolic tangent form of the step transition in the bottom elevation.	146
4.17	Simulated space-time profile of the free surface elevation (in mm) for $f_1 = 1.9837$ Hz. The position of the step is indicated by the vertical white dashed line. The slope of the crest and trough lines show the wave celerity.	147

- 4.18 Simulated (solid line) and measured (dashed line) spatial evolution of the first five harmonic amplitudes for $f_1 = 1.9837$ Hz without including viscosity or surface tension in the simulations. The dashed line is the transversal mean of the measurements and the shaded zone is the standard deviation. 148
- 4.19 Simulated (solid line) and measured (dashed line) spatial evolution of the first five harmonic amplitudes for $f_1 = 1.9837$ Hz with bulk viscosity $\nu = 4.10^{-5} \text{ m}^2/\text{s}$, but without the effects of surface tension. For comparison, the results from the simulation without the effects of viscosity or surface tension are shown by the gray lines. 149
- 4.20 Simulated (solid line) and measured (dashed line) spatial evolution of the first five harmonic amplitudes for $f_1 = 1.9837$ Hz without the effects of viscosity but with surface tension $\sigma = 0.071 \text{ N/m}$. For comparison, the results from the simulation without the effects of viscosity or surface tension are shown by the gray lines. 150
- 4.21 Simulated (solid line) and measured (dashed line) spatial evolution of the first five harmonic amplitudes for $f_1 = 1.9837$ Hz with viscosity $\nu = 4.10^{-5} \text{ m}^2/\text{s}$ and surface tension $\sigma = 0.071 \text{ N/m}$ 151
- 4.22 Simulated space-time profile of the free surface elevation (in mm) for $f_1 = 1.9837$ Hz, with viscosity $\nu = 4.10^{-5} \text{ m}^2/\text{s}$ and surface tension $\sigma = 0.071 \text{ N/m}$. The position of the step is indicated by the vertical white dashed line. 152
- 4.23 Experimental space-time profile of the free surface elevation (in mm) for $f_1 = 1.9837$ Hz. The position of the step is indicated by the vertical white dashed line. 153
- 4.24 Simulated (solid line) and measured (dashed line) spatial evolution of the first five harmonic amplitudes for $f_1 = 3.8$ Hz with viscosity $\nu = 4.10^{-5} \text{ m}^2/\text{s}$ and surface tension $\sigma = 0.071 \text{ N/m}$. The dashed line is the transversal mean of the measurements and the shaded zone is the standard deviation. 154

5 Development and implementation of the 2DH version of the model using Radial Basis Functions (RBF) 155

- 5.1 Definition of a stencil with $N_{sten} = 9$ nodes. The node in red (x_1) is the center of the stencil and the blue dots are its supporting nodes. Black dots are non-supporting nodes. 165
- 5.2 Test function $f(x, y) = A \cos\left(\frac{2\pi}{L}(x \cos \theta + y \sin \theta)\right)$ with $L = 0.5 \text{ m}$, $A/L = 0.05$, and $\theta = 20^\circ$ 169
- 5.3 Analytical first and second-order derivatives of the test function $f(x, y)$ 170

5.4	Node sets for the size of stencil considered in the tests for infinitely smooth RBF $N_{sten} = 5, 13$ and 21 for interior nodes with centered stencils (left), and node set for a one-sided stencil for a node at the upper boundary of the domain with $N_{sten} = 21$ (right).	171
5.5	Examples of the local errors for the first and second-order derivatives (Figure 5.3) estimated with the MQ RBF, a stencil of 21 nodes, a shape parameter $C = 0.1$ and an added polynomial of degree 0 .	173
5.6	Averaged error for f_x as a function of the shape parameter C with the MQ RBF (added polynomial of degree 0 and $N_{sten} = 21$), for the four node sets defined in the text.	173
5.7	The four infinitely smooth RBFs that are studied MQ , GA , IMQ and IQ as a function of the radius $r = \ \underline{x} - \underline{x}_i\ $ with \underline{x}_i the center of the RBF, for three values of the shape parameter ($C = 0.5, 1$ and 2).	174
5.8	Global error for the estimate of f_x , for the four RBFs (see legend) as a function of the shape parameter C (with $N_{sten} = 21$ and added polynomial of degree 0).	175
5.9	Global error for the estimate of the first and second-order derivatives in x and y , for the IMQ RBF as a function of the shape parameter C (with $N_{sten} = 21$ and an added polynomial of degree 1).	176
5.10	Error for the estimate of f_x with the MQ as a function of the shape parameter C (with $N_{sten} = 13$ and added polynomial of degree 0) for the three different sets of nodes defined in Section 5.3.3.	176
5.11	Error for the estimate of f_x , for the IMQ RBF as a function of the shape parameter C (with added polynomial of degree 0) for different stencil sizes: $N_{sten} = 5, 13$ and 21 .	177
5.12	Error for the estimate of f_x , for the IMQ as a function of the shape parameter C (with added polynomial of order 1 and $N_{sten} = 21$) for several different node-spacings.	178
5.13	Error for the estimate of f_x , for the MQ as a function of the shape parameter C (with added polynomial of degree 0 and $N_{sten} = 21$). Comparison between solving the system with a LU decomposition and using a SVD filtering method for three values of the threshold μ .	179
5.14	Error for the estimate of f_x , for the IMQ as a function of the shape parameter C (with $N_{sten} = 21$) for added polynomials of degree 0 to 2 : (left panel) all nodes, (central panel) boundary nodes (boundary nodes 1 and boundary nodes 2), (right panel) interior nodes.	180

5.15	Effect of the normalization of the stencil on the error for the estimate of f_x , for the MQ as a function of the shape parameter C (with added polynomial of degree 0 and $N_{sten} = 21$): for the three sets of nodes defined in Section 5.3.3.	181
5.16	The three piecewise smooth RBFs studied, as a function of the radius $r = \ \underline{x} - \underline{x}_i\ $ with \underline{x}_i the center of the RBF.	182
5.17	Error for the estimate of f_x, f_y, f_{xx} and f_{yy} , for the three piecewise smooth RBFs considered in comparison with the error estimate of the IMQ as a function of the shape parameter C (with an added polynomial of degree 0).	183
5.18	Convergence of the error for the estimate of f_x as a function of the spatial resolution Δx . Comparison of the IMQ with $C = 0.4$ and the three piecewise smooth functions (for $N_{sten} = 21$).	184
5.19	Error for the estimate of f_x, f_y, f_{xx} and f_{yy} , for r^5 and r^7 PHS as a function of the stencil size N_{sten} and the degree of the added polynomial (shown in the legend).	185
6	Validation of the 2DH version of the model using RBFs in the horizontal plane	187
6.1	Three dimensional view of the free surface elevation at the end of the simulation obtained with $PHS r^7 + p3$ and $N_{sten} = 21$	189
6.2	Averaged error computed for the free surface elevation at the end of the simulation ($t = 12T$) for all simulations with MQ and GA RBFs (as a function of the shape parameter C for several values of N_{sten}), and for $PHS r^5 + p2$ and $r^7 + p3$ (independent of C) RBFs.	190
6.3	(a) Averaged error of the free surface position (Eq.(6.1)) at the end of each simulation, and (b) averaged condition number of the collocation matrix for the MQ RBF in (N_{sten}, C) -space. The crosses indicate simulations that were not stable for the entire $12T$	191
6.4	(a) (a) Averaged error of the free surface position (Eq.(6.1)) at the end of each simulation, and (b) averaged condition number of the collocation matrix for the GA RBF in (N_{sten}, C) -space. The crosses indicate simulations that were not stable for the entire $12T$	191
6.5	CPU time as a function of the stencil size N_{sten} , for simulations using the MQ RBF with $C = 1$ (duration of the simulation $12T$ with $\Delta t = T/100$, using 9090 nodes in the (x, y) -plane and $N_T = 7$).	192
6.6	Analytical bathymetry (Eq.(6.2)) of the experiments of Whalin (1971).	193
6.7	Three-dimensional view of the free surface elevation at the end of the simulation ($t = 18T$), obtained with $PHS r^7 + p3$ and $N_{sten} = 21$	194

6.8	Free surface elevation profile along the centerline of the tank at the end of the simulation (black line) and maximum and minimum free surface elevation (wave envelope) during the simulation (gray lines). The light gray shaded areas ($x < 0$ m and $x > 25$ m) indicate relaxation zones for wave generation and absorption.	195
6.9	Observed (circles) and simulated (solid lines) spatial evolution of the amplitude of first three harmonics (at frequencies f , $2f$ and $3f$) of the free surface elevation for $T = 2$ s, $A = 0.0075$ m of the experiments of Whalin (1971) obtained with <i>PHS</i> RBF $r^7 + p3$ with $N_{sten} = 21$.	196
6.10	Observed (triangles) and simulated (solid lines) spatial evolution of the amplitudes of first three harmonics (at frequencies f , $2f$ and $3f$, as shown in Figure 6.9) of the free surface elevation for the case $T = 2$ s, $A = 0.0075$ m of Whalin (1971): sensitivity of the results to the type of node sets and the choice of RBF.	197
6.11	Observed (triangles) and simulated (solid lines) spatial evolution of the amplitudes of first three harmonics (at frequencies f , $2f$ and $3f$, as shown in Figure 6.9) of the free surface elevation for the case $T = 2$ s, $A = 0.0075$ m of Whalin (1971): sensitivity of the results to the node spacing, for three resolutions.	198
6.12	Observed (triangles) and simulated (solid lines) spatial evolution of the amplitudes of first three harmonics (at frequencies f , $2f$ and $3f$, as shown in Figure 6.9) of the free surface elevation for the case $T = 2$ s, $A = 0.0106$ m of Whalin (1971).	199
6.13	Numerical domain and bathymetry of the experiments of Vincent and Briggs (1989). Horizontal and vertical white lines indicate the transects where the comparisons between the simulation results and the experimental measurements are completed. Hatched zones indicate the wave generation (left side) and absorption (right side) zones.	201
6.14	Contour plot of the free surface elevation at the end of the simulation ($t \approx 78T$) for case <i>M1</i> of Vincent and Briggs (1989). The dotted line indicates the limit of the elliptical shoal.	202
6.15	Average wave height along transect 4, for case <i>M1</i> of Vincent and Briggs (1989). The blue shaded zone around the simulation results shows the standard deviation due to reflections.	203
6.16	Average wave height along transects 7 and 9, for case <i>M1</i> of Vincent and Briggs (1989). The blue shaded zone around the simulation results accounts for the standard deviation due to reflections.	204
6.17	Spatial evolution of the first three harmonic amplitudes for the <i>M1</i> Vincent and Briggs (1989) experiments along transects 7 and 9 ($y = 13.72$ m).	204

6.18	Average wave height along transect 4 (top) and transects 7 and 9 (bottom), for case M1 of Vincent and Briggs (1989). Comparison of 3 combinations of PHS RBFs and N_{sten} (see legend).	205
6.19	Average wave height along transect 4 (top) and along transect 7-9 (bottom), case M1 Vincent and Briggs (1989). Comparison of 2 spatial resolutions.	206
6.20	Left, sparsity of the matrix associated with the Laplace BVP using a stencil of $N_{sten} = 5$ for a regular node set of (5x5) nodes. Right sparsity of the matrix associated with the Laplace BVP after using an adapted reverse Cuthill-McKee algorithm. The black dots are the nonzero elements.	208
6.21	Speed-up ratio (Eq.(6.5)) as a function of the number of MPI processes (N_{proc}), for the test case presented in Section 6.2 with 485,728 unknowns.	210
Appendix A		217

List of Tables

1	Derivation and analysis of the Euler-Zakharov mathematical model	7
1.1	Dispersion relation coefficients for $N_T = 7$	29
2	Numerical implementation of the 1DH model	35
2.1	Reflection coefficients for the different shapes of the relaxation coefficients considered in the first set of simulations (Figure 2.1).	42
2.2	Description of the four options considered to implement the lateral boundary condition for wave generation. The set of equations accounting for the node on the lateral boundary for the Laplace resolution is detailed.	54
3	Validation of the 1DH version of the model	63
3.1	Physical parameters for the four simulations of regular waves propagating over a Roseau-type bottom profile.	67
3.2	Analytical and simulated (with Misthyc and with the coupled-mode model of Athanassoulis and Belibassakis (1999)) reflection and transmission coefficients for the four cases of regular wave propagating over Roseau bathymetry profile. The reflection coefficient for case 2 was too small to be determined accurately from the wave height profile obtained with Misthyc.	70
3.3	Selected time steps Δt and associated quantities for convergence runs as a function of Δt ($M_x = 10$ and $N_T = 7$)	75
3.4	Selected spatial steps Δx and associated quantities for convergence runs as a function of Δx ($CFL = 1.25$ and $N_T = 7$)	80
4	Modeling viscous dissipation through the visco-potential approach	111
4.1	Nondimensional and physical parameters for the five simulations.	135

4.2	Maximum time steps for the simulations with and without a low-pass filter on the 10 first modes of $\partial^2\Phi/\partial z^2(z = -h)$ at each time step. X means that the simulation diverged even for the smallest time step tested $\Delta t = T/10000$	137
4.3	Simulation parameters for the two solitary waves.	142
4.4	Wave number and wavelength of the first and second harmonics with the associated beat length for the water depth $h^{(II)} = 2.0$ cm, and for surface tension $\sigma = 0$ N/m and $\sigma = 0.071$ N/m.	149
5	Development and implementation of the 2DH version of the model using Radial Basis Functions (RBF)	155
5.1	Commonly used RBFs including the form of the function, the necessary constraints on the free parameter, and the regularity of the function.	157
6	Validation of the 2DH version of the model using RBFs in the horizontal plane	187
6.1	Numerical parameters for the nine simulations compared for the case with $T = 2$ s, $A = 0.0075$ m of Whalin (1971). The parameters of the simulations presented in the first part of this section are in bold.	197
	Appendix A	217
2	Dispersion relation coefficients for N_T ranging from 2 to 9	218
3	Dispersion relation coefficients for N_T ranging from 10 to 12	219
4	Dispersion relation coefficients for $N_T =$ ranging from 13 to 15	220

Introduction

La modélisation de la transformation des vagues au cours de leur propagation depuis leur zone de génération jusqu'à la côte est d'intérêt majeur pour un grand nombre d'applications d'ingénierie marine et côtière. Selon la zone d'intérêt, les processus physiques à l'origine de ces transformations sont divers avec des échelles caractéristiques de temps et d'espace variées, qui requièrent des approches de modélisation différentes. Les modèles dits "spectraux" représentent des quantités moyennes caractéristiques de l'état de mer et sont généralement utilisés pour de grands domaines et par grande profondeur. Au contraire, les modèles dits "à résolution de phase" donnent l'évolution de l'élévation de surface libre au cours du temps et nécessitent une discrétisation plus fine. De ce fait, leur utilisation est limitée à de plus petits domaines. Ce travail porte sur cette deuxième catégorie de modèles, avec pour objectif de développer un modèle déterministe capable de simuler la propagation de champs de vagues irréguliers et multidirectionnels sur des bathymétries variables, du large jusqu'à la côte, avec une représentation précise des effets non-linéaires et dispersifs. Pour cela, le choix d'un modèle potentiel basé sur les équations d'Euler irrotationnelles a été retenu comme compromis entre des modèles ne prenant en compte que partiellement ces effets (équations de Saint-Venant, Berkhoff, Boussinesq) et les modèles très coûteux en temps (fondés sur les équations de Navier-Stokes). De plus, une approche spectrale sur la verticale est adoptée pour sa précision et sa flexibilité. Le chapitre 1 décrit le modèle mathématique utilisé alors que le chapitre 2 présente la mise en œuvre numérique de la version 1DH en insistant particulièrement sur les conditions de génération et d'absorption des vagues. Les capacités non-linéaires et dispersives de la version 1DH du modèle sont démontrées à travers l'application à six cas tests dans le chapitre 3. Le chapitre 4 traite de la prise en compte des effets visqueux de dissipation interne et de frottement sur le fond par une formulation visco-potentielle. Les chapitres 5 et 6 sont dédiés à l'extension du modèle en 2DH avec une étude de la méthode RBF-FD et la validation par comparaison à des données expérimentales en bassin à vagues.

Context and objectives of the PhD thesis

Waves generated by the wind at the surface of seas and oceans can propagate over several thousand kilometers from their generation zone to the coast. To be able to simulate wave propagation and transformation is of major interest for a wide variety of applications in marine and coastal environments. For example, coastal and marine engineers seek accurate descriptions of wave conditions for the construction of offshore facilities, the study of sediment transport to evaluate coastal erosion risks, the design of protective coastal structures to prevent overtopping and to reduce flooding risks, the study of wave agitation in harbors, or the estimation of the potential for marine renewable energy devices.

All of these applications require accurately modeling nearshore waves. Depending on the domain of interest, from the offshore, deep water wave conditions to the surf zone, a variety of different physical processes control wave transformation. In the deep ocean, interactions with the atmosphere are predominant, including wave generation from wind and wave energy dissipation by white-capping. Quadruplet wave interactions (between four wave components) are an important cause of deep-water wave spectrum transformation, usually leading to a frequency downshift in the wave spectrum and an increase in the wave period.

When approaching the shore, bottom interactions become non-negligible causing shoaling, refraction, and energy dissipation from bottom friction and depth-induced wave breaking. As waves propagate over variable bathymetric profiles, triplet wave interactions (between three wave components) become important in intermediate and shallow water, causing a decrease in the mean wave period. Currents may also interact with waves causing refraction or even wave blocking for specific conditions. In the vicinity of the coastline or marine structures, such as offshore platforms, dykes or breakwaters, run-up, swash, overtopping, diffraction and reflection from obstacles must also be considered.

These physical processes have different characteristic temporal and spatial scales, requiring different modeling approaches, which can be divided into two categories: phase-averaged (or spectral) models and phase-resolved (or deterministic) models.

1. **Phase-averaged (or spectral) models** are based on a spectro-angular representation of the sea state and its evolution following the conservation of wave action. These models simulate the evolution of the wave action or energy spectrum, from which several averaged quantities characterizing the wave field can be obtained (i.e. significant wave height, peak period, propagation direction of the dominant wave). Models of this category (e.g. WAM, Tomawac, SWAN and WaveWatch) are used for large-scale applications because of their computational efficiency, but they are unable to take into account the phase difference between different wave components. This is due to the fact that these models consider

only mean (phase-averaged) wave properties and do not resolve the dynamics of each wave profile. For example, a spectral wave model can predict the wave height in front of a coastal structure but is unable to predict the spatially varying modulation of the wave amplitude caused by wave reflection from the structure.

- 2. Phase-resolved (or deterministic) models** simulate the evolution of the free surface elevation and the associated kinematics in a deterministic manner. These models simulate the evolution of the free surface as a function of time and space, requiring finer spatial and temporal resolutions (on the order of 10-100 points per wavelength and 10-100 time steps per wave period) and thus longer computational times. In comparison to large-scale spectral models, their use is limited to more local scales of the order of kilometers. Moreover, until recently, to meet the efficiency requirements of operational engineering studies, many simplifying assumptions were often made for the derivation of these models: linear theory (i.e. Berkhoff equations) or long wave assumption (shallow water equations), which leads only to a partial representation of the nonlinear and dispersive effects. With a growing need for a more accurate representation of these effects that are non-negligible in the nearshore area, more complex wave models were developed to take into account the nonlinear and dispersive properties of waves (i.e. Boussinesq, Green-Naghdi, Euler equations) as discussed in the next section.

This PhD thesis falls within the scope of the latter type of models with the objective of developing a deterministic model capable of simulating the propagation of irregular and directional wave fields over variable bathymetries from the offshore to the coast with a highly accurate representation of the nonlinear and dispersive effects for bidimensional models on the order of kilometers. To achieve this goal, several approaches are possible, and a brief review of existing phase-resolving models is presented in the following section.

Brief review of phase-resolved numerical wave models

Most fluid flow problems can be described by the Navier-Stokes equations since they account for nonlinearities, vorticity and viscosity. Models based on these equations can be very accurate when studying wave interactions with structures in the surf zone (e.g. [Lara et al. \(2006\)](#); [Shao \(2006\)](#)). These equations can be solved with two very different approaches. Either with an Eulerian approach tracking the free surface position with a volume of fluid method, as for example, in the widely used code OpenFOAM® ([Higuera et al., 2013a,b](#)), solving the RANS (Reynolds Averaged Navier-Stokes) equations for two incompressible phases. Another option is to use a Lagrangian approach where the fluid is represented as particles and the trajectories of each particles is computed considering their interactions, as for instance with the SPH (Smoothed Particle Hydrodynamics) method (e.g. [Dalrymple and Rogers \(2006\)](#)). These models are highly accurate

when studying local-scale processes, but the domain size and resolution are limited due to the computational time, even with the use of GPU parallelized codes (Dalrymple et al., 2011). Moreover, these models usually suffer from a significant level of numerical diffusion, which prevents them from being used for propagating waves over long distances. For both of these reasons, to model large spatial domains, these codes are usually coupled with more computationally efficient models, such as potential flow models, to simulate the far-field processes (Narayanaswamy et al., 2010).

Some assumptions can be made to simplify the problem and thus reduce the computational time. For example, the nonlinear shallow water equations (NLSWE) are derived by depth integrating the Navier-Stokes equations to model waves with a wavelength significantly longer than the water depth (e.g. tidal waves, storm surges), but this set of equations does not take into account wave dispersion, and therefore they cannot be applied to model accurately short waves. However, by including non-hydrostatic pressure in the NLSWE and dividing the water depth into a sufficient number of layers, the frequency dispersion of waves can be greatly improved (Stelling and Zijlema, 2003; Zijlema and Stelling, 2005, 2008; Zijlema et al., 2011). For example, with only two layers, the accuracy of the deep water dispersion relation is similar to that of extended Boussinesq-type models. The dispersion of such non-hydrostatic models can be further improved by optimizing the location of the levels (Zhu et al., 2014).

When viscous and turbulent effects are negligible, the flow can be represented well by potential flow theory, which consists of solving the Laplace problem in the fluid domain, supplemented by nonlinear free surface boundary conditions. One way of solving this problem is to use the Boundary Integral Equations Method (BIEM), which projects the problem on the boundary surface of the fluid domain using Green's formula (Grilli et al., 1989; Wang et al., 1995). These models enable an accurate description of nonlinear and even overturning waves and are well adapted to simulate wave-structure interactions (e.g. Dombre et al. (2015)). This method is mainly used for calculating local-scale interactions owing to the long computational times. However, with the use Fast Fourier Transform (FFT) (Fructus and Grue, 2007; Newman and Lee, 2002) or Fast Multipole Algorithm methods (Fochesato et al., 2007), the computational time can be reduced considerably.

Another way of solving the problem is to make additional assumptions about the nonlinear and dispersive properties of waves. By doing a Taylor expansion of the vertical velocity about a specified level and truncating it to a finite number of terms, Boussinesq-type models assume a polynomial variation of the vertical velocity, thus reducing the problem by one dimension. Boussinesq-type models are derived with the assumption that nonlinearity and frequency dispersion are weak or moderate (Kirby, 2003; Madsen and Schäffer, 1998). Using only a quadratic polynomial approximation of the vertical flow distribution gives poor results for wave propaga-

tion in intermediate depths. A lot of work has been done to improve the frequency dispersion following various approaches such as: using higher degree polynomials for the vertical approximation with the Green-Naghdi equations (Zhao et al., 2014), using Padé approximants (Agnon et al., 1999) combined with an expansion of the Laplace solution from an arbitrary level (Madsen et al., 2002), and resolving in two arbitrary layers to maintain low-order spatial derivatives (Chazel et al., 2009; Lynett and Liu, 2004). Additional modeling approaches include those of Kennedy et al. (2001), Fuhrman and Bingham (2004), and Engsig-Karup et al. (2006).

The system of potential flow equations can also be reformulated as a function of free surface quantities, also known as the Zakharov equations (Zakharov, 1968). The temporal evolution of the free surface elevation η and the free surface velocity potential $\tilde{\Phi}$ are given as a function of these two variables and the vertical velocity at the free surface \tilde{w} . The primary challenge is to express the vertical velocity \tilde{w} as a function of η and $\tilde{\Phi}$, a problem commonly called ‘Dirichlet-to-Neumann’ or DtN. One possibility is to solve directly the Laplace equation using finite element (Ma et al., 2001; Wu et al., 1998) or finite difference (Engsig-Karup et al., 2009; Li and Fleming, 1997) methods. When using finite difference methods, Kreiss and Oliger (1972) and Bingham and Zhang (2007) recommend using fourth-order schemes with a stretched vertical grid (clustering points near the free surface) instead of using second-order schemes with a regular grid. When considering rectangular domains with a flat bottom, a high-order spectral approach (HOS) is optimal (Dommermuth and Yue, 1987; Ducrozet et al., 2012a; West et al., 1987). This method is faster than finite difference methods but less flexible with regard to the domain geometry and bathymetry, even if progress has been made in taking into account variable and moving bottoms (Gouin et al., 2016; Guyenne and Nicholls, 2007; Smith, 1998). However, one limitation of this approach is the need to work with periodic domains in the horizontal plane, which can restricts some applications to coastal and harbor domains.

An additional approach is to use a spectral method only in the vertical dimension either by expanding the velocity potential with a local mode series (Belibassakis and Athanassoulis, 2011) or by projecting it on a polynomial basis (Kennedy and Fenton, 1997; Tian and Sato, 2008). By using high-order finite difference schemes in the horizontal, these models maintain a flexible approach for variable domain geometries and bathymetry. A comparison between a vertical spectral approach and a finite difference approach in the vertical dimension shows the improved accuracy and efficiency of the spectral method in 1DH (Yates and Benoit, 2015) and 2DH (Christiansen et al., 2013). Others approaches can be used, such as the extension of the DtN operator as a sum of global convolution terms and local integrals with kernels decaying quickly in space (Clamond and Grue, 2001; Fructus et al., 2005). A more complete review and discussion of nonlinear potential flow models for wave simulation can be found in Gouin (2016).

Based on this analysis, the nonlinear potential flow approach is attractive, as it is in principle more accurate than Boussinesq or Serre-Green-Naghdi models in representing nonlinear and

dispersive wave effects in large water depths, while it does not suffer from the shortcomings of CFD Navier-Stokes codes for large-scale applications. Furthermore, under the assumption of non-overtopping waves, a spectral approach in the vertical can be adopted, which results in both an accurate and flexible model, as mentioned above.

Content and organization of the PhD dissertation

In this work, a potential flow theory numerical model, based on the Zakharov equations, is validated and extended. The existing model, called *Misthyc*, solves the Laplace boundary problem (based on previous work (Yates and Benoit, 2015)) with a combination of high-order finite difference schemes for the horizontal dimension (1DH version) and a spectral approach using Chebyshev polynomials in the vertical dimension (Tian and Sato, 2008). In this work, this approach was extended to two horizontal dimensions, using a Radial Basis Function-Finite Difference (RBF-FD) approach to estimate the horizontal derivatives to enable using an unstructured discretization of the domain by a set of scattered nodes.

A variety of numerical and physical aspects of wave modeling were addressed during this PhD and are presented in the following chapters. In Chapter 1, the mathematical model is derived with emphasis on the underlying assumptions. The resolution of the Laplace boundary value problem using a spectral approach in the vertical is presented, and the accuracy of the linear dispersion relation resulting from this approximation is studied. In Chapter 2, the numerical methods used for the 1DH version of the model are described in detail with a focus on the implementation of the boundary conditions for wave generation and wave absorption. The application of the 1DH version of the model to a series of challenging test cases demonstrates, in Chapter 3, the nonlinear and dispersive capabilities of the code. In Chapter 4, a visco-potential formulation is considered to take into account the dissipative effects induced by bulk viscosity and bottom friction. This formulation of the model is validated in comparison to analytical solutions and then applied to simulate wave tank experiments. Chapter 5 presents the extension of the model to two horizontal dimensions using the RBF-FD method to estimate horizontal derivatives for a set of scattered nodes. Then, a series of sensitivity tests of the accuracy and stability of the model as a function of the parameters related to the RBF method are conducted to evaluate the robustness of this approach for estimating derivatives. In Chapter 6, the 2DH version of the model is validated first by a comparison to results from the 1DH version for a case that is uniform in the y direction, and then by comparisons to two sets of experiments conducted in wave basins. Finally, the last Chapter concluded with a summary of the main contributions of the PhD thesis and with a discussion of possibilities for future improvements to the model.

Chapter 1

Derivation and analysis of the Euler-Zakharov mathematical model

Dans ce chapitre, le modèle mathématique sur lequel repose le modèle numérique développé est présenté. Les équations surfaciques de Zakharov décrivant l'évolution temporelle de la position de la surface libre η et du potentiel des vitesses à la surface libre $\tilde{\Phi}$ sont établies à partir des équations de Navier-Stokes, en insistant sur les hypothèses. La vitesse verticale à la surface libre, nécessaire à l'intégration en temps des équations de Zakharov, est obtenue en résolvant le problème aux limites de Laplace à l'aide d'une méthode spectrale pour la direction verticale. Cette approche nécessite un changement de coordonnées sur la verticale, la projection du profil vertical du potentiel des vitesses Φ sur la base des polynômes de Tchebyshev de première espèce (tronquée à un degré maximal N_T) et l'application de la méthode Tchebyshev-Tau, aboutissant au système linéaire à résoudre pour obtenir le potentiel Φ dans tout le domaine. À partir de la connaissance de Φ , les champs de vitesse verticale et horizontale et de pression peuvent être calculés. La version linéaire du modèle est finalement dérivée pour un fond plat dans le but d'établir la relation de dispersion linéaire. La précision de celle-ci est étudiée en fonction de la résolution verticale (N_T) et comparée à celles issues d'autres modèles de type Boussinesq d'ordre élevé. Les propriétés dispersives de la version linéaire du modèle s'améliorent avec l'augmentation de la valeur de N_T et pour $N_T \geq 9$, l'erreur relative sur la célérité de phase par rapport à la théorie de Stokes reste inférieure à 2.5% pour $kh \leq 100$.

1.1 From the Navier-Stokes equations to the Zakharov equations

In this section we consider a domain Ω , with a fluid of density ρ , submitted to the atmospheric pressure $p_{atm}(x, y, t)$ and the acceleration of gravity \underline{g} , moving with a velocity $\underline{v}(x, y, z, t) = (u, v, w)^T$. The domain is delimited in the vertical by the free surface at elevation $z = \eta(x, y, t)$ and the bottom (which can also vary in time) at elevation $z = -h(x, y, t)$.

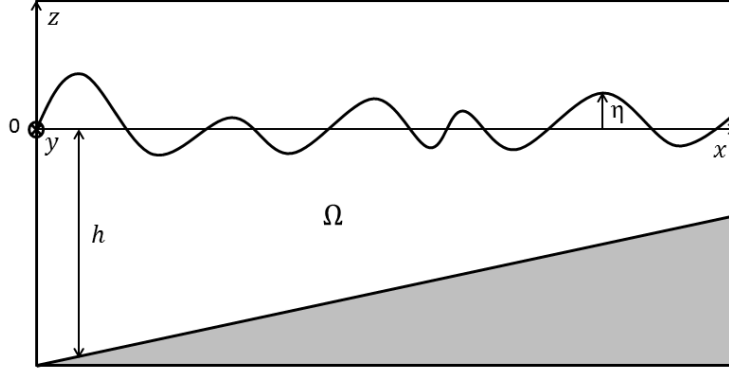


Figure 1.1: Diagram for the definition of the notations.

1.1.1 The Euler equations and boundary conditions

The starting point is the classical Navier-Stokes system of equations for a Newtonian fluid:

$$\begin{cases} \frac{\partial \rho}{\partial t} + \nabla \cdot (\rho \underline{v}) = 0 & \text{in } \Omega & (1.1a) \\ \frac{\partial \rho \underline{v}}{\partial t} + \nabla \cdot (\rho \underline{v} \otimes \underline{v}) = -\nabla p + \nabla \cdot \underline{\tau} + \rho \underline{g} & \text{in } \Omega & (1.1b) \end{cases}$$

where p is the pressure, and $\underline{\tau}$ is the viscous stress tensor. It is first assumed that the flow is **incompressible**, meaning that the fluid density is considered constant and homogeneous. In this case, system (1.1) can be simplified to:

$$\begin{cases} \nabla \cdot \underline{v} = 0 & \text{in } \Omega & (1.2a) \\ \frac{\partial \underline{v}}{\partial t} + (\underline{v} \cdot \nabla) \underline{v} = -\frac{1}{\rho} \nabla p + \nu \Delta \underline{v} + \underline{g} & \text{in } \Omega & (1.2b) \end{cases}$$

where $\nabla \equiv (\frac{\partial}{\partial x}, \frac{\partial}{\partial y}, \frac{\partial}{\partial z})^T$ denotes the gradient operator.

Making the additional assumption of an **inviscid fluid**, the momentum equations (Eq.(1.2b)) reduce to the Euler equations:

$$\frac{\partial \underline{v}}{\partial t} + \underline{v} \cdot \nabla \underline{v} = -\frac{1}{\rho} \nabla p + \underline{g} \quad \text{in } \Omega \quad (1.3)$$

To resolve the fluid dynamics, in addition to Eq.(1.2a)-(1.3) in the fluid domain Ω , boundary conditions must be specified. The kinematic free surface boundary condition (KFSBC) expresses the impermeability of the free surface (a particle of fluid cannot go through the free surface). Mathematically, the free surface is defined as $F(x, y, z, t) \equiv z - \eta(x, y, t) = 0$, and the impermeable condition is then expressed by the zero Lagrangian (or material) derivative of F :

$$\frac{DF}{Dt} = 0 \Leftrightarrow \frac{\partial F}{\partial t} + \underline{v} \cdot \nabla F = 0. \quad (1.4)$$

$$\Leftrightarrow -\frac{\partial \eta}{\partial t} - u \frac{\partial \eta}{\partial x} - v \frac{\partial \eta}{\partial y} + w = 0 \quad \text{at } z = \eta(x, y, t). \quad (1.5)$$

Introducing the outward unit normal vector at the free surface \underline{n} :

$$\underline{n} = \frac{1}{\sqrt{1 + |\nabla_H \eta|^2}} \left(-\frac{\partial \eta}{\partial x}, -\frac{\partial \eta}{\partial y}, 1 \right)^T \quad (1.6)$$

where ∇_H is the horizontal gradient operator, Eq.(1.5) can be rewritten as:

$$-\frac{\partial \eta}{\partial t} + \underline{v} \cdot \underline{n} \sqrt{1 + |\nabla_H \eta|^2} = 0 \quad \text{at } z = \eta(x, y, t). \quad (1.7)$$

Usually, the dynamic boundary condition at the free surface (DFSBC) is derived from the continuity of the normal stress at the interface meaning that if the free surface is only subjected to atmospheric pressure, the pressure at the free surface position equal the atmospheric pressure. Nevertheless, a discontinuity of the normal stress can appear due to a normal force generated by surface tension. This force is proportional to the mean curvature of the interface and acts in the direction towards the center of curvature of the surface. Taking into account the effects of surface tension, the DFSBC can be written as (Dingemans, 1997b):

$$p(x, y, \eta(x, y, t), t) = p_{atm}(x, y, t) - \sigma \nabla_H \cdot \left(\frac{\nabla_H \eta}{\sqrt{1 + |\nabla_H \eta|^2}} \right). \quad (1.8)$$

where σ is the coefficient of surface tension expressed as a force per unit length (N/m). For a water-air interface at 20 °C, $\sigma = 0.074$ N/m.

At the bottom $z = -h(x, y, t)$, an impermeability condition is applied. Following the treatment of the KFSBC, the function $G(x, y, z, t) \equiv z + h(x, y, t)$ is introduced, and the impermeability condition is expressed by setting the Lagrangian derivative of G to zero.

$$\frac{DG}{Dt} = 0 \Leftrightarrow \frac{\partial G}{\partial t} + \underline{v} \cdot \nabla G = 0. \quad (1.9)$$

$$\Leftrightarrow \frac{\partial h}{\partial t} + u \frac{\partial h}{\partial x} + v \frac{\partial h}{\partial y} + w = 0 \quad \text{at } z = -h(x, y, t). \quad (1.10)$$

The flow is then described by the following set of equations:

$$\left\{ \begin{array}{ll} \nabla \cdot \underline{\mathbf{v}} = 0 & \text{in } \Omega \quad (1.11a) \\ \frac{\partial \underline{\mathbf{v}}}{\partial t} + (\underline{\mathbf{v}} \cdot \nabla) \underline{\mathbf{v}} = -\frac{1}{\rho} \nabla p + \underline{\mathbf{g}} & \text{in } \Omega \quad (1.11b) \\ -\frac{\partial \eta}{\partial t} - \underline{\mathbf{v}}_{\text{H}} \cdot \nabla_{\text{H}} \eta + w = 0 & \text{at } z = \eta(x, y, t) \quad (1.11c) \\ p(x, y, \eta(x, y, t), t) = p_{\text{atm}}(x, y, t) - \sigma \nabla_{\text{H}} \cdot \left(\frac{\nabla_{\text{H}} \eta}{\sqrt{1 + |\nabla_{\text{H}} \eta|^2}} \right) & \text{at } z = \eta(x, y, t) \quad (1.11d) \\ \frac{\partial h}{\partial t} + \underline{\mathbf{v}}_{\text{H}} \cdot \nabla_{\text{H}} h + w = 0 & \text{at } z = -h(x, y, t) \quad (1.11e) \end{array} \right.$$

where $\underline{\mathbf{v}}_{\text{H}} = (u, v)^T$ is the horizontal part of the fluid velocity.

At the lateral boundaries (denoted as $\partial\Omega_{\text{lat}}$), periodic, Dirichlet or Neumann boundary conditions must be imposed to close the system.

1.1.2 Potential flow equations: the water wave problem

By assuming **irrotational flow**, potential flow theory can be used. The velocity potential $\Phi(x, y, z, t)$ is introduced such that $\underline{\mathbf{v}} = \nabla \Phi$. The preceding set of equations (1.11) can be rewritten in terms of the new variable Φ .

The continuity equation (Eq.(1.11a)) becomes the Laplace equation:

$$\nabla \cdot \underline{\mathbf{v}} = 0 \quad \Rightarrow \quad \nabla \cdot \nabla \Phi = 0 \quad \Rightarrow \quad \Delta \Phi = 0 \quad \text{in } \Omega. \quad (1.12)$$

where Δ is the Laplacian operator.

From the Euler equations (Eq.(1.11b)), the Bernoulli equation can be obtained:

$$\frac{\partial \underline{\mathbf{v}}}{\partial t} + (\underline{\mathbf{v}} \cdot \nabla) \underline{\mathbf{v}} = -\frac{1}{\rho} \nabla p + \underline{\mathbf{g}} \quad \text{in } \Omega \quad (1.13)$$

$$\Leftrightarrow \frac{\partial \nabla \Phi}{\partial t} + \nabla \Phi \cdot \nabla (\nabla \Phi) = -\frac{1}{\rho} \nabla p - \nabla(gz) \quad \text{in } \Omega \quad (1.14)$$

$$\Leftrightarrow \nabla \left(\frac{\partial \Phi}{\partial t} + \frac{1}{2} (\nabla \Phi)^2 + \frac{p}{\rho} + gz \right) = 0 \quad \text{in } \Omega \quad (1.15)$$

The zero gradient in Eq.(1.15) means that the scalar argument in parenthesis is independent of the variables x , y and z and therefore is an arbitrary function of time only, here chosen to be zero.

Thus it is noted that Φ is defined up to a constant, which will be discussed further in Section 2.2.2.3. Eq.(1.15) then becomes:

$$p(x, y, z, t) = -\rho \left(gz + \frac{\partial \Phi}{\partial t} + \frac{1}{2}(\nabla \Phi)^2 \right) \quad (1.16)$$

At the free surface, the KFSBC (Eq.(1.11c)) becomes:

$$\frac{\partial \eta}{\partial t} + \nabla_{\text{H}} \Phi \cdot \nabla_{\text{H}} \eta - \frac{\partial \Phi}{\partial z} = 0, \quad \text{at } z = \eta(x, y, t) \quad (1.17)$$

and the DFSBC (Eq.(1.11d)), is reformulated using the Bernoulli equation (Eq.(1.16)) at the free surface:

$$\frac{\partial \Phi}{\partial t} + \frac{1}{2}(\nabla \Phi)^2 + g\eta = -\frac{p_{\text{atm}}(x, y, t)}{\rho} + \frac{\sigma}{\rho} \nabla_{\text{H}} \cdot \left(\frac{\nabla_{\text{H}} \eta}{\sqrt{1 + |\nabla_{\text{H}} \eta|^2}} \right) \quad \text{at } z = \eta(x, y, t) \quad (1.18)$$

The bottom impermeability boundary condition (Eq.(1.11e)) becomes:

$$\frac{\partial h}{\partial t} + \nabla_{\text{H}} \Phi \cdot \nabla_{\text{H}} h + \frac{\partial \Phi}{\partial z} = 0 \quad \text{at } z = -h(x, y, t) \quad (1.19)$$

The nonlinear potential flow problem is thus:

$$\left\{ \begin{array}{ll} \Delta \Phi = 0 & \text{in } \Omega \quad (1.20a) \\ \frac{\partial \eta}{\partial t} + \nabla_{\text{H}} \Phi \cdot \nabla_{\text{H}} \eta - \frac{\partial \Phi}{\partial z} = 0 & \text{at } z = \eta(x, y, t) \quad (1.20b) \\ \frac{\partial \Phi}{\partial t} + \frac{1}{2}(\nabla \Phi)^2 + g\eta = -\frac{p_{\text{atm}}(x, y, t)}{\rho} + \frac{\sigma}{\rho} \nabla_{\text{H}} \cdot \left(\frac{\nabla_{\text{H}} \eta}{\sqrt{1 + |\nabla_{\text{H}} \eta|^2}} \right) & \text{at } z = \eta(x, y, t) \quad (1.20c) \\ \frac{\partial h}{\partial t} + \nabla_{\text{H}} \Phi \cdot \nabla_{\text{H}} h + \frac{\partial \Phi}{\partial z} = 0 & \text{at } z = -h(x, y, t) \quad (1.20d) \end{array} \right.$$

This is usually called the “water wave problem”. Note that the pressure does not appear explicitly in this problem, but can be computed from Eq.(1.16) once Φ is known. One of the main difficulties encountered during the resolution of this set of equations is related to the fact that it is a free boundary problem: the fluid domain is bounded by the free surface η , which is also an unknown of the problem.

1.1.3 Expression as a function of surface quantities

By making the assumption that the **water column is continuous from the bottom to the free surface** ($\eta(x, y, t)$ is single-valued), the velocity potential at the free surface can be defined as $\tilde{\Phi}(x, y, t) \equiv \Phi(x, y, \eta(x, y, t), t)$.

Using the chain rule, the following equations express the link between the derivatives of the free

surface velocity potential $\tilde{\Phi}$ and the derivatives of the global velocity potential Φ :

$$\frac{\partial \tilde{\Phi}}{\partial \alpha} = \frac{\partial \Phi}{\partial \alpha} + \frac{\partial \eta}{\partial \alpha} \frac{\partial \Phi}{\partial z}, \quad (1.21)$$

where $\alpha = x, y$ or t .

Expressing the KFSBC (Eq.(1.20b)) and the DFSBC (Eq.(1.20c)) as a function of the free surface potential $\tilde{\Phi}(x, y, t)$ using the above expressions, the following set of equations is obtained:

$$\left\{ \begin{array}{l} \frac{\partial \eta}{\partial t} = -\nabla_{\text{H}} \tilde{\Phi} \cdot \nabla_{\text{H}} \eta + \tilde{w}(1 + (\nabla_{\text{H}} \eta)^2) \\ \frac{\partial \tilde{\Phi}}{\partial t} = -g\eta - \frac{1}{2}(\nabla_{\text{H}} \tilde{\Phi})^2 + \frac{1}{2}\tilde{w}^2(1 + (\nabla_{\text{H}} \eta)^2) - \frac{p_{\text{atm}}(x, y, t)}{\rho} + \frac{\sigma}{\rho} \nabla_{\text{H}} \cdot \left(\frac{\nabla_{\text{H}} \eta}{\sqrt{1 + |\nabla_{\text{H}} \eta|^2}} \right) \end{array} \right. \quad (1.22)$$

$$\left\{ \begin{array}{l} \frac{\partial \eta}{\partial t} = -\nabla_{\text{H}} \tilde{\Phi} \cdot \nabla_{\text{H}} \eta + \tilde{w}(1 + (\nabla_{\text{H}} \eta)^2) \\ \frac{\partial \tilde{\Phi}}{\partial t} = -g\eta - \frac{1}{2}(\nabla_{\text{H}} \tilde{\Phi})^2 + \frac{1}{2}\tilde{w}^2(1 + (\nabla_{\text{H}} \eta)^2) - \frac{p_{\text{atm}}(x, y, t)}{\rho} + \frac{\sigma}{\rho} \nabla_{\text{H}} \cdot \left(\frac{\nabla_{\text{H}} \eta}{\sqrt{1 + |\nabla_{\text{H}} \eta|^2}} \right) \end{array} \right. \quad (1.23)$$

with \tilde{w} the vertical velocity at the free surface:

$$\tilde{w}(x, y, t) \equiv \frac{\partial \tilde{\Phi}}{\partial z}(x, y, \eta(x, y, t), t) \quad (1.24)$$

These two coupled equations Eq.(1.22) and (1.23) involve only free surface quantities: the first one describing the temporal evolution of the free surface elevation η and the second one expressing the evolution of the free surface potential $\tilde{\Phi}$. In order to integrate these equations in time, it is necessary to determine $\tilde{w}(x, y, t)$ at each time step from $\eta(x, y, t)$ and $\tilde{\Phi}(x, y, t)$, which is called a Dirichlet-to-Neumann (DtN) problem. Different approaches have been proposed to solve this problem, for example using a high-order spectral approach (HOS) (Dommermuth and Yue, 1987; West et al., 1987), which is efficient for rectangular domains with a flat bottom. Other approaches can be used, such as the extension of the DtN operator as a sum of global convolution terms and a local integral with kernels decaying quickly in space (Clamond and Grue, 2001; Fructus et al., 2005), or the expansion of the Laplace solution from an arbitrary level combined with the use of Padé approximant, based on a Boussinesq approximation (Madsen et al., 2002). See also the recent review and discussion by Wilkening and Vasan (2015). Here, as presented in the next section, the DtN problem will be resolved by solving a Laplace boundary value problem (BVP) for the potential Φ in the entire domain Ω using a spectral approach in the vertical direction (Tian and Sato, 2008; Yates and Benoit, 2015).

1.1.4 Discussion of the assumptions

To build the mathematical model Eq.(1.22)-(1.23), four assumptions were made. The consequences of these assumptions and their validity are discussed.

- **assumption 1: incompressible flow**

This assumption means that the density of the fluid is homogeneous in space and constant in time. In the ocean, the water density varies with temperature and salinity with typical scales of variation on the order of tens of kilometers in the horizontal. These scales of variability are

much larger than the domain over which the evolution of the free surface elevation is aimed to be modeled. Vertical variations of the density do not have a significant impact on free surface gravity waves, except in estuarine environments where vertical density gradients, due to the overflow of freshwater in saltwater, can be important. This assumption seems reasonable.

- assumption 2: **inviscid fluid**

Internal forces due to the fluid viscosity are generally negligible for the considered wavelengths. A viscous fluid tends to generate friction on the bottom or other solid walls with the development of a boundary layer where energy is dissipated. In deep water, the boundary layer thickness is very small in comparison with the water depth, so the effects of bottom friction are negligible. With decreases in the water depth approaching the coast, this assumption becomes less valid since the boundary layer may impact wave propagation. Therefore, viscous effects may become non-negligible in shallow water. The introduction of some dissipative effects will be discussed in Chapter 5.

- assumption 3: **irrotational flow**

This assumption implies that the particles of fluid do not have a rotational movement. It is a reasonable assumption in case of low viscosity and/or when the bottom friction, which creates turbulence and induces vorticity, can be neglected. This assumption is no longer true in the breaking and swash zones.

- assumption 4: **continuity of the water column from the bottom to the surface**

Since the free surface is single-valued, it is not possible to simulate directly wave overturning. This assumption is justified as long as waves are not overturning, so wave breaking cannot be resolved with this approach. Some dissipative terms could be added to Eq.(1.22) and Eq.(1.23) in order to parameterize wave breaking dissipation in the model.

1.1.5 The Zakharov equations

Finally, here, two additional weak assumptions are made:

- The atmospheric pressure is chosen to be homogeneous and constant.

This assumption limits the model to study waves subjected only to gravitational effects. The effect of wind on waves (due to gradients in atmospheric pressure) are not considered here. The pressure variations at the free surface are assumed negligible for the spatial scales of the domains of interest, so the atmospheric pressure is held constant. As the pressure is defined within a constant, it is chosen equal to zero for convenience, without limiting the generality of the problem.

- Surface tension is neglected.

Surface tension effects become noticeable for short waves with wavelengths on the order of centimeters. For real applications, the wavelengths considered will be on the order of meters and thus the effects of surface tension can be neglected. For the simulation of small-scales experiments, the effects of surface tension may become important, as will be shown in Chapter 5.

Thus, taking into account these two hypotheses, the set of equations resolved by the model (unless otherwise specified) is:

$$\left\{ \begin{array}{l} \frac{\partial \eta}{\partial t} = -\nabla_{\mathbb{H}} \tilde{\Phi} \cdot \nabla_{\mathbb{H}} \eta + \tilde{w}(1 + (\nabla_{\mathbb{H}} \eta)^2) \\ \frac{\partial \tilde{\Phi}}{\partial t} = -g\eta - \frac{1}{2}(\nabla_{\mathbb{H}} \tilde{\Phi})^2 + \frac{1}{2}\tilde{w}^2(1 + (\nabla_{\mathbb{H}} \eta)^2) \end{array} \right. \quad (1.25)$$

$$\left\{ \begin{array}{l} \frac{\partial \tilde{\Phi}}{\partial t} = -g\eta - \frac{1}{2}(\nabla_{\mathbb{H}} \tilde{\Phi})^2 + \frac{1}{2}\tilde{w}^2(1 + (\nabla_{\mathbb{H}} \eta)^2) \end{array} \right. \quad (1.26)$$

1.2 Resolution of the Laplace BVP using a spectral method in the vertical

To integrate the Zakharov equations in time, the estimation of the vertical velocity at the free surface \tilde{w} is necessary. This is achieved by resolving the following Laplace BVP for the potential Φ in the entire fluid domain Ω :

$$\left\{ \begin{array}{ll} \Delta_{\mathbb{H}} \Phi + \Phi_{zz} = 0 & \text{in } \Omega \quad (1.27a) \\ \Phi = \tilde{\Phi} & \text{at } z = \eta(x, y, t) \quad (1.27b) \\ \nabla_{\mathbb{H}} \Phi \cdot \nabla_{\mathbb{H}} h + \Phi_z = 0 & \text{at } z = -h(x, y, t) \quad (1.27c) \\ \nabla \Phi \cdot \underline{n}_{lat} = 0 & \text{on } \partial\Omega_{lat} \quad (1.27d) \end{array} \right.$$

Here, a Neumann condition is applied at the vertical lateral boundaries (denoted as $\partial\Omega_{lat}$), to consider the particular case of impermeable lateral boundaries. \underline{n}_{lat} denotes the unit normal vector at the lateral wall. In the following, spatial derivatives will be denoted by subscripts (i.e. $f_x \equiv \partial f / \partial x$).

With a time invariant lateral boundary condition, the problem is dependent on time through the shape of the domain. Lateral boundary conditions can vary in time, for example in the case of wave generation, but this case is not considered in this section. Therefore, at each step of the time integration scheme, the Laplace BVP has to be solved at least once taking into account the new shape of the domain. For instance, using the classical fourth order Runge-Kutta scheme, four resolutions are required. However, no derivatives in time appear in the BVP.

The numerical approach chosen to solve the Laplace BVP is the application of a spectral method in the vertical direction. [Yates and Benoit \(2015\)](#) showed that using a spectral method is more accurate and efficient than using finite difference schemes. Following the work of [Tian and Sato \(2008\)](#), the method is divided into three main steps:

1. a change of variables for the vertical coordinate,
2. an expansion of the velocity potential Φ using the basis of orthogonal Chebyshev polyno-

mials of the first kind T_n ($n = 0, 1, \dots$), truncated at a given order N_T ,

3. and an application of the Chebyshev-Tau method in the vertical.

An outline of the method is given in [Yates and Benoit \(2015\)](#) for the case of a single horizontal dimension (i.e. $\underline{x} = x$). Here the method is presented for the case of two horizontal dimensions (i.e. $\underline{x} = (x, y)$).

1.2.1 Change of the vertical coordinate

First, a change of the vertical coordinate from $z \in [-h(\underline{x}, t), \eta(\underline{x}, t)]$ to $s \in [-1, 1]$ is made to reduce the uneven time varying domain to a constant rectangular domain extending from the bottom at $s = -1$ to the free surface at $s = +1$.

$$s(\underline{x}, z, t) = \frac{2z + h^-(\underline{x}, t)}{h^+(\underline{x}, t)} \quad (1.28)$$

where $h^+(\underline{x}, t) = h(\underline{x}, t) + \eta(\underline{x}, t)$ and $h^-(\underline{x}, t) = h(\underline{x}, t) - \eta(\underline{x}, t)$.

With this change of variables:

$$\Phi(\underline{x}, z, t) \equiv \varphi(\underline{x}, s(\underline{x}, z, t), t)$$

Using the chain rule, the system of equations (1.27) is rewritten in terms of $\varphi(\underline{x}, s, t)$:

$$\left\{ \begin{array}{ll} \varphi_{xx} + \varphi_{yy} + 2(s_x \varphi_{xs} + s_y \varphi_{ys}) + \\ (s_x^2 + s_y^2 + s_z^2) \varphi_{ss} + (s_{xx} + s_{yy}) \varphi_s = 0 & \text{in } \Omega \quad (1.29a) \\ \varphi(x, y, 1) = \tilde{\Phi}(x, y) & \text{at } s = +1 \quad (1.29b) \\ h^+(h_x \varphi_x + h_y \varphi_y) + 2(1 + h_x^2 + h_y^2) \varphi_s = 0 & \text{at } s = -1 \quad (1.29c) \\ (\varphi_x + s_x \varphi_s) n_{latx} + (\varphi_y + s_y \varphi_s) n_{laty} = 0 & \text{on } \partial\Omega_{lat} \quad (1.29d) \end{array} \right.$$

where n_{latx} and n_{laty} are the components in the (x, y) -plane of the unit vector \underline{n}_{lat} normal to lateral boundaries.

1.2.2 Expansion of the potential on the basis of Chebyshev polynomials

The second step is based on the assumption that the velocity potential can be approximated by its projection on a subset of the function space of finite dimension. Following the work of [Tian and Sato \(2008\)](#), the chosen set of base functions are Chebyshev polynomials of the first kind (denoted T_n , with n the degree of the polynomial). Chebyshev polynomials are easy to compute, are orthogonal for a weighted dot product, and converge rapidly over a large domain.

By selecting a subset of the $N_T + 1$ first polynomials, the following approximation is made:

$$\varphi(\underline{x}, s, t) \approx \varphi_{N_T}(\underline{x}, s, t) = \sum_{n=0}^{N_T} a_n(\underline{x}, t) T_n(s) \quad (1.30)$$

where the $a_n(\underline{x}, t)$ coefficients are a set of unknown coefficients to be determined for each \underline{x} , at each time step. However, since there are no time derivatives in the Laplace BVP, in the following, the a_n will be written only as a function of \underline{x} to lighten the equations. This step allows separating the horizontal variations $a_n(\underline{x})$ of the velocity potential from the vertical variations $T_n(s)$.

Chebyshev polynomials of the first kind are a set of orthogonal polynomials defined on the interval $[-1, 1]$. They can be defined in two different ways (e.g. [Boyd, 2001](#)):

- by a recurrence relation: $T_0(s) = 1$, $T_1(s) = s$, and $T_n(s) = 2s T_{n-1}(s) - T_{n-2}(s)$
- or with a trigonometric approach: $T_n(\cos\theta) = \cos(n\theta)$, $\theta \in]-\infty, +\infty[$

The eight first Chebyshev polynomials are plotted in Figure 1.2. A Chebyshev polynomial of degree p has p different simple roots, and $|T_p(s)| \leq 1$ for $s \in [-1, 1]$.

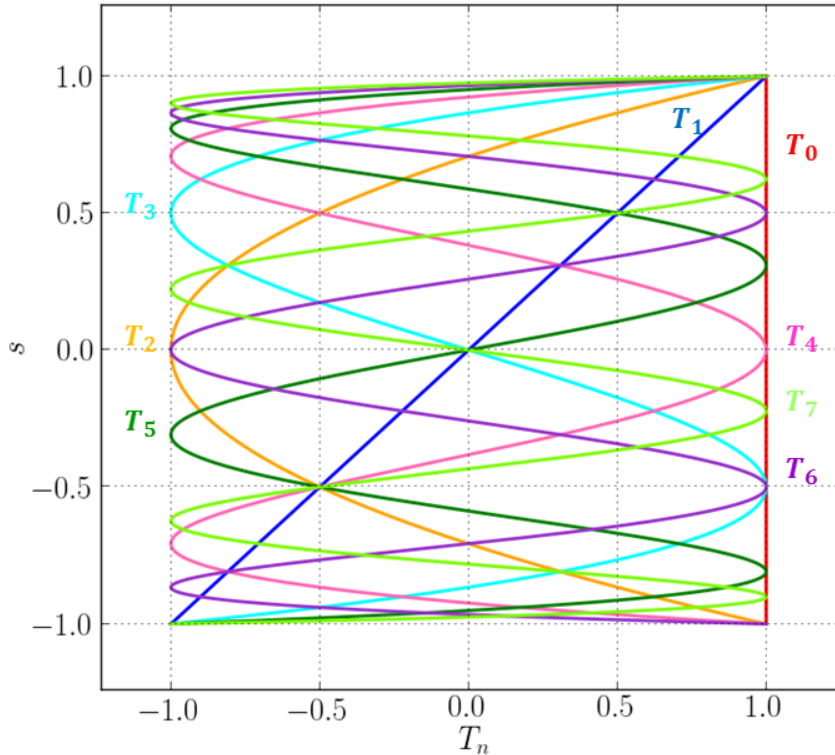


Figure 1.2: Eight first Chebyshev polynomials of the first kind $T_n(s)$ ($n = 0$ to 7).

These polynomials form an orthogonal basis on the interval $[-1,1]$ with respect to the weight $1/\sqrt{1-s^2}$. The inner product is then defined as:

$$(f, g) \equiv \int_{-1}^1 fg \frac{ds}{\sqrt{1-s^2}}. \quad (1.31)$$

Thus, for two Chebyshev polynomials T_n and T_p of orders n and p , respectively:

$$(T_n, T_p) = \begin{cases} 0 & \text{if } p \neq n \\ \frac{\pi}{2} & \text{if } p = n \text{ and } n \geq 1 \\ \pi & \text{if } p = n = 0 \end{cases} \quad (1.32)$$

Finally, the inner product of any function f defined on the interval $[-1,1]$ with a Chebyshev polynomial T_p of order p is :

$$\langle f \rangle_p \equiv \frac{2}{\pi c_p} (f, T_p) \quad \text{with} \quad \begin{cases} c_0 = 2 \\ c_p = 1 \text{ if } p \geq 1 \end{cases} \quad (1.33)$$

The coefficient $\frac{2}{\pi c_p}$ is introduced so that the basis of Chebyshev polynomials is orthonormal (i.e. $\langle T_n \rangle_p = \delta_{np}$, where δ_{np} is the Kronecker symbol).

By substituting the approximation of φ (Eq.(1.30)) into the set of equations (1.29), a new set of equations is obtained, that depends only on the a_n coefficients, the T_n functions, and their respective spatial derivatives.

The Laplace equation (Eq.(1.29a)) in the fluid domain becomes:

$$\begin{aligned} \sum_{n=0}^{N_T} a_{n,xx} T_n + \sum_{n=0}^{N_T} a_{n,yy} T_n + 2 s_x \sum_{n=0}^{N_T} a_{n,x} T_{n,s} + 2 s_y \sum_{n=0}^{N_T} a_{n,y} T_{n,s} + \\ (s_x^2 + s_y^2 + s_z^2) \sum_{n=0}^{N_T} a_n T_{n,ss} + (s_{xx} + s_{yy}) \sum_{n=0}^{N_T} a_n T_{n,s} = 0 \end{aligned} \quad (1.34)$$

The Dirichlet condition (Eq.(1.29b)) at the free surface ($s = +1$) is:

$$\sum_{n=0}^{N_T} a_n = \tilde{\Phi}(\underline{x}) \quad (1.35)$$

The impermeable boundary condition (Eq.(1.29c)) at the bottom ($s = -1$) is:

$$h^+ h_x \sum_{n=0}^{N_T} (-1)^n a_{n,x} + h^+ h_y \sum_{n=0}^{N_T} (-1)^n a_{n,y} + 2(1 + h_x^2 + h_y^2) \sum_{n=0}^{N_T} (-1)^{n-1} n^2 a_n = 0 \quad (1.36)$$

The impermeable lateral boundary condition (Eq.(1.29d)) becomes:

$$\left(\sum_{n=0}^{N_T} a_{n,x} T_n + s_x \sum_{n=0}^{N_T} a_n T_{n,s} \right) n_{latx} + \left(\sum_{n=0}^{N_T} a_{n,y} T_n + s_y \sum_{n=0}^{N_T} a_n T_{n,s} \right) n_{laty} = 0 \quad (1.37)$$

The terms s_x, s_y, s_z, s_{xx} and s_{yy} can be expressed as polynomial functions of s :

$$s_i = \frac{h_i^- h^+ - s h_i^+ h^+}{h^{+2}} \quad (i=x \text{ or } y),$$

$$s_{ii} = \frac{h_{ii}^- h^+ - 2h_i^+ h_i^- + (2h_i^{+2} - h_{ii}^+ h^+) s}{h^{+2}} \quad (i=x \text{ or } y),$$

$$s_z = \frac{2}{h^+}.$$

Replacing the derivatives of s by their expressions, and after some rearrangement, the Laplace equation Eq.(1.34) becomes:

$$\sum_{n=0}^{N_T} \alpha a_{n,xx} + \sum_{n=0}^{N_T} \beta a_{n,yy} + \sum_{n=0}^{N_T} \gamma a_{n,x} + \sum_{n=0}^{N_T} \delta a_{n,y} + \sum_{n=0}^{N_T} \zeta a_n = 0 \quad (1.38)$$

with :

$$\alpha = \beta = T_n$$

$$\gamma = \frac{m_{0101} T_{n,s} + m_{1101} s T_{n,s}}{m_{0220}}$$

$$\delta = \frac{m_{0011} T_{n,s} + m_{1011} s T_{n,s}}{m_{0220}}$$

$$\zeta = \frac{m_{0002} T_{n,ss} - m_{1002} s T_{n,ss} + m_{2002} s^2 T_{n,ss} + m_{0001} T_{n,s} + m_{1001} s T_{n,s}}{m_{0220}}$$

where the m_{ijkl} terms only depend on h^+ and h^- and their spatial derivatives:

$$m_{0220} = h^{+2}$$

$$m_{0101} = 2h^+ h_x^-$$

$$m_{1101} = -2h^+ h_x^+$$

$$m_{0011} = 2h^+ h_y^-$$

$$m_{1011} = -2h^+ h_y^+$$

$$\begin{aligned}
 m_{0002} &= 4 + h_x^{-2} + h_y^{-2} \\
 m_{1002} &= 2 (h_x^- h_x^+ + h_y^- h_y^+) \\
 m_{2002} &= h_x^{+2} + h_y^{+2} \\
 m_{0001} &= -2h_x^- h_x^+ - 2h_y^- h_y^+ + h^+ h_{xx}^- + h^+ h_{yy}^- \\
 m_{1001} &= 2h_x^{+2} + 2h_y^{+2} - h^+ h_{xx}^+ - h^+ h_{yy}^+
 \end{aligned}$$

The impermeability condition at the lateral boundaries (Eq.(1.37)) becomes:

$$\sum_{n=0}^{N_T} 2\alpha n_{latx} a_{n,x} + \sum_{n=0}^{N_T} 2\beta n_{laty} a_{n,y} + \sum_{n=0}^{N_T} (\gamma n_{latx} + \delta n_{laty}) a_n = 0 \quad (1.39)$$

1.2.3 Application of the Chebyshev-Tau approach to obtain the linear system

The aim of this last step is to obtain a linear system for the a_n coefficients, but Eq.(1.38) and (1.39) still depend on \underline{x} and s . In order to eliminate the dependence on s , both equations can be projected on polynomials T_p by applying the inner product $\langle \cdot \rangle_p$ previously defined (Eq.(1.33)). Then, the resulting equations only depend on the $a_n(\underline{x})$. In the case of simple boundary conditions at $s = -1$ and $s = +1$ that can be satisfied by the Chebyshev polynomials (the chosen test functions), the projection is done for p from 0 to N_T . This is called the Galerkin method. Nevertheless, when the boundary conditions are complicated or for particular problems, it is not always possible to find a test function verifying them, so a solution is to apply only the projection for p from 0 to $N_T - 2$ supplemented by the two equations to account for the surface and bottom boundary conditions Eq.(1.35) and Eq.(1.36). This method, called the Chebyshev-Tau method (Canuto et al., 1988), will be used here.

Looking at the expressions for $\alpha(s)$, $\beta(s)$, $\delta(s)$, $\gamma(s)$ and $\zeta(s)$, the following terms have to be estimated: $\langle T_n \rangle_p$, $\langle T_{n,s} \rangle_p$, $\langle T_{n,ss} \rangle_p$, $\langle s T_{n,s} \rangle_p$, $\langle s T_{n,ss} \rangle_p$ and $\langle s^2 T_{n,ss} \rangle_p$. The notation B_{pikn} is introduced:

$$B_{pikn} \equiv \langle s^i \frac{d^k T_n}{ds^k} \rangle_p = \frac{2}{\pi c_p} \left(s^i \frac{dT_n}{ds^k}, T_p \right) \quad (1.40)$$

The B_{pikn} can be determined analytically as a function of n and p using the recurrence relation of the Chebyshev polynomials or from linear combinations of previously defined B_{pikn} .

$$\langle T_n \rangle_p = B_{p00n} = \delta_{pn}$$

$$\langle T_{n,s} \rangle_p = B_{p01n} = \frac{2}{c_p} \begin{cases} n & \text{if } p = n - 1, n - 3, n - 5, \dots \\ 0 & \text{otherwise} \end{cases}$$

$$\langle T_{n,ss} \rangle_p = B_{p02n} = \frac{1}{c_p} \begin{cases} n(n^2 - p^2) & \text{if } p = n - 2, n - 4, n - 6, \dots \\ 0 & \text{otherwise} \end{cases}$$

$$\langle s T_{n,s} \rangle_p = B_{p11n} = \sum_{r=0}^{n-1} B_{r01n} \begin{cases} \frac{1}{2}(B_{p00(r-1)} + B_{p00(r+1)}) & \text{if } r \geq 1 \\ B_{p001} & \text{if } r = 0 \end{cases}$$

$$\langle s T_{n,ss} \rangle_p = B_{p12n} = \sum_{r=0}^{n-2} B_{r02n} \begin{cases} \frac{1}{2}(B_{p00(r-1)} + B_{p00(r+1)}) & \text{if } r \geq 1 \\ B_{p001} & \text{if } r = 0 \end{cases}$$

$$\langle s^2 T_{n,ss} \rangle_p = B_{p22n} = \sum_{r=0}^{n-2} B_{r02n} \begin{cases} \frac{1}{4}(B_{p00(r-2)} + 2B_{p00r} + B_{p00(r+2)}) & \text{if } r \geq 2 \\ \frac{1}{4}(3B_{p001} + B_{p003}) & \text{if } r = 1 \\ \frac{1}{2}(B_{p000} + B_{p002}) & \text{if } r = 0 \end{cases}$$

The B_{pikn} terms are constant, depending only on the Chebyshev polynomials T_n , and can be computed once at the beginning of each simulation, after the maximal order of the Chebyshev polynomials N_T is chosen.

The final set of equations to be solved is for the coefficients $a_n(\underline{x})$, which depend only on $\underline{x} = (x, y)$ and time (and not on the vertical coordinate s).

$$\left\{ \begin{array}{l} a_{p,xx} + a_{p,yy} + \sum_{n=0}^{N_T} C_{pn}^x a_{n,x} + \sum_{n=0}^{N_T} C_{pn}^y a_{n,y} + \sum_{n=0}^{N_T} D_{pn} a_n = 0 \quad \text{in } \Omega \quad (1.41a) \\ \sum_{n=0}^{N_T} a_n = \tilde{\Phi}(\underline{x}, t) \quad \text{at } s = +1 \quad (1.41b) \\ h^+ h_x \sum_{n=0}^{N_T} (-1)^n a_{n,x} + h^+ h_y \sum_{n=0}^{N_T} (-1)^n a_{n,y} + \\ 2(1 + h_x^2 + h_y^2) \sum_{n=0}^{N_T} (-1)^{n-1} n^2 a_n = 0 \quad \text{at } s = -1 \quad (1.41c) \\ 2 n_{latx} a_{p,x} + 2 n_{laty} a_{p,y} + \sum_{n=0}^{N_T} (n_{latx} C_{pn}^x + n_{laty} C_{pn}^y) a_n = 0 \quad \text{on } \partial\Omega_{lat} \quad (1.41d) \end{array} \right.$$

where $C_{pn}^x = (m_{0101} B_{p01n} + m_{1101} B_{p11n})/m_{0220}$ is the coefficient for $a_{n,x}$,

$C_{pn}^y = (m_{0011} B_{p01n} + m_{1011} B_{p11n})/m_{0220}$ is the coefficient for $a_{n,y}$,

and $D_{pn} = (m_{0002} B_{p02n} - m_{1002} B_{p12n} + m_{2002} B_{p22n} + m_{0001} B_{p01n} + m_{1001} B_{p11n})/m_{0220}$.

For each node \underline{x} , $N_T + 1$ unknown coefficients a_n must be determined. When applying the operator $\langle \cdot \rangle_p$ for p from 0 to $N_T - 2$ to Eq.(1.38) for nodes inside the domain or to Eq.(1.39) for nodes on the lateral boundaries, $N_T - 1$ equations are obtained. To have a well-posed problem, two additional equations are needed to complete the set of equations at each node. The Dirichlet boundary condition at the surface (Eq.(1.41b)) and the impermeable condition at the bottom (Eq.(1.41c)) are used for this purpose. The horizontal spatial derivatives of the a_n coefficients are defined as linear combinations of the values in the vicinity of the node considered, leading to a set of coupled equations.

Once the $a_n(\underline{x})$ coefficients are determined, the vertical velocity at the free surface $\tilde{w}(\underline{x})$ is readily obtained from:

$$\tilde{w}(\underline{x}) = \Phi_z(\underline{x}, z = \eta) = s_z \varphi_s(s = +1) \approx \frac{2}{h^+(\underline{x})} \sum_{n=0}^{N_T} a_n(\underline{x}) n^2 \quad (1.42)$$

The vertical velocity can then be used to evaluate the right hand side of Eq.(1.25) and Eq.(1.26), required by the numerical scheme to integrate in time.

1.3 Computation of flow properties

The main results obtained with the model are surface quantities: the free surface elevation η and the free surface velocity potential $\tilde{\Phi}$. Nevertheless, it also can be of interest to calculate other properties inside the fluid domain. Since the Laplace BVP is resolved for the velocity potential $\Phi(\underline{x}, z, t)$ in the entire domain, it is possible to compute some properties of the flow at a given time t , such as the velocity profile or the pressure field, or the depth-averaged velocity. For convenience, the derivation of these expressions is done hereafter for the 1DH case ($\underline{x} = x$). Extension to the 2DH case is straightforward.

1.3.1 Horizontal and vertical velocities in the fluid domain

To visualize the flow inside the fluid domain $\underline{v} = (u, w)$, one must compute the gradient of the velocity potential $\Phi(x, z, t)$ at a number of points discretizing the domain:

$$\left\{ \begin{array}{l} u = \frac{\partial \Phi}{\partial x} = \frac{\partial \varphi}{\partial x} + \frac{\partial \varphi}{\partial s} \frac{\partial s}{\partial x} \\ w = \frac{\partial \Phi}{\partial z} = \frac{\partial \varphi}{\partial s} \frac{\partial s}{\partial z} \end{array} \right. \quad (1.43a)$$

$$\quad (1.43b)$$

From the spectral approach used in the vertical in the model, the velocity potential in 1DH is

given by Eq.(1.30) repeated here for convenience:

$$\Phi(x, z, t) \approx \varphi_{N_T}(x, s, t) = \sum_{n=0}^{N_T} a_n(x, t) T_n(s) \quad (1.44)$$

Expressions for the horizontal and vertical velocities are then deduced:

$$\left\{ \begin{array}{l} u = \sum_{n=0}^{N_T} a_{n,x} T_n + \frac{h_x^- - s h_x^+}{h^+} \sum_{n=1}^{N_T} a_n T_{n,s} \\ w = \frac{2}{h^+} \sum_{n=1}^{N_T} a_n T_{n,s} \end{array} \right. \quad (1.45a)$$

$$\left. \begin{array}{l} \\ \\ \end{array} \right\} w = \frac{2}{h^+} \sum_{n=1}^{N_T} a_n T_{n,s} \quad (1.45b)$$

To compute the velocity components at a given point (x, z) , one must first compute the coordinates of the point in the (x, s) -plane, with the change of variables from Eq.(1.28), knowing the value of $\eta(x)$. Values of $T_n(s)$ and $T_{n,s}(s)$ are also required and can be obtained analytically, whereas the first order spatial derivative of the a_n coefficients is obtained numerically with a fourth order finite difference scheme in the 1DH case, using the RBF-FD method in the 2DH case, as explained in the following.

1.3.2 Pressure in the fluid domain

The pressure at any point (x, z) of the domain is given by the Bernoulli equation (Eq.(1.16)):

$$p(x, z, t) = -\rho \left(\frac{\partial \Phi}{\partial t} + \frac{1}{2} \left(\frac{\partial \Phi}{\partial x} \right)^2 + \frac{1}{2} \left(\frac{\partial \Phi}{\partial z} \right)^2 + gz \right)$$

The most difficult term to estimate is $\frac{\partial \Phi}{\partial t}$ at the point x , the Eulerian derivative of the velocity potential Φ , more particularly when the point is such that it is outside the fluid domain (i.e. above the free surface) at $t - \Delta t$ and inside the fluid domain at t (or conversely). Because of the time varying limits of the fluid domain, it is difficult to estimate directly the time derivative of Φ with a finite difference scheme. Thus, this derivative will be estimated in the (x, s) -space. Using the spectral approximation of the potential:

$$\frac{\partial \Phi}{\partial t}(x, z, t) \approx \sum_{n=0}^{N_T} [a_{n,t} T_n + a_n T_{n,s} s_t], \quad (1.46)$$

with $s_t = \frac{1}{h^+} (h_t (1 - s) - \eta_t (1 + s))$. The derivative $a_{n,t}(x, t)$ is computed with a backward finite difference scheme of first or second order:

- first order scheme: $a_{n,t}(x, t) = \frac{a_n(x, t) - a_n(x, t - \Delta t)}{\Delta t}$
- second order scheme: $a_{n,t}(x, t) = \frac{3a_n(x, t) - 4a_n(x, t - \Delta t) + a_n(x, t - 2\Delta t)}{2\Delta t}$

The accuracy of the results is highly dependent on the approximation of the time derivative and the time step. Other required terms are obtained easily: h_t is zero in case of fixed bottom or known if the evolution of the bottom elevation is prescribed, and η_t is already estimated as the left hand-side of the first of the two Zakharov equations (Eq.(1.25)). Thus the pressure can be estimated at any point inside the fluid domain at any given time t .

1.3.3 Depth averaged horizontal velocity

The depth averaged horizontal velocity $\bar{u}(x)$ at a location x , is obtained by integrating the vertical profile of the horizontal velocity from the bottom to the top of the water column:

$$\bar{u}(x) = \frac{1}{h(x) + \eta(x)} \int_{-h(x)}^{\eta(x)} u(x, z) dz = \frac{1}{2} \int_{-1}^1 u(x, s) ds \quad (1.47)$$

Using the expression of the horizontal velocity in the (x, s) -space, obtained from the spectral approximation of the potential (Eq.(1.43a)), this expression becomes:

$$\bar{u}(x) = \frac{1}{2} \left[\sum_{n=0}^{N_T} a_{n,x} \int_{-1}^1 T_n ds + \sum_{n=1}^{N_T} a_n \left(\frac{h_x^-}{h^+} \int_{-1}^1 T_{n,s} ds - \frac{h_x^+}{h^+} \int_{-1}^1 s T_{n,s} ds \right) \right] \quad (1.48)$$

By defining $S_j^i(n) = \int_{-1}^1 s^j T_{n,s^i} ds$, Eq.(1.48) can be rewritten as:

$$\bar{u}(x) = \frac{1}{2} \left[\sum_{n=0}^{N_T} a_{n,x} S_0^0(n) + \sum_{n=1}^{N_T} a_n \left(\frac{h_x^-}{h^+} S_0^1(n) - \frac{h_x^+}{h^+} S_1^1(n) \right) \right] \quad (1.49)$$

For any value of n the expressions of $S_0^0(n)$, $S_0^1(n)$ and $S_1^1(n)$ are the following:

$$\begin{aligned} S_0^1(n) &= \int_{-1}^1 T_{n,s} ds = [T_n]_{-1}^1 \\ &= 1 - (-1)^n = \begin{cases} 0 & \text{if } n \text{ is even} \\ 2 & \text{if } n \text{ is odd} \end{cases} \end{aligned}$$

$$\begin{aligned} S_0^0(n) &= \int_{-1}^1 T_n ds = \begin{cases} [T_1]_{-1}^1 = 2 & \text{if } n = 0 \\ \frac{1}{2} \left[\frac{T_{n+1}}{n+1} - \frac{T_{n-1}}{n-1} \right]_{-1}^1 & \text{for } n > 0 \end{cases} \\ &= \begin{cases} 0 & \text{if } n = 2p + 1, p \geq 0 \\ \frac{-2}{n^2 - 1} & \text{if } n = 2p, p \geq 0 \end{cases} \end{aligned}$$

$$\begin{aligned}
S_1^1(n) &= \int_{-1}^1 s T_{n,s} ds = [s T_n]_{-1}^1 - \int_{-1}^1 T_n ds \\
&= T_n(1) + T_n(-1) - S_0^1 \\
&= \begin{cases} 0 & \text{if } n \text{ is odd} \\ \frac{2n^2}{n^2-1} & \text{if } n \text{ is even} \end{cases}
\end{aligned}$$

Finally, Eq.(1.49) becomes:

$$\bar{u}(x) = \frac{1}{2} \left[\sum_{p=0}^{N_T/2} a_{2p,x} \frac{2}{1-(2p)^2} + 2 \frac{h_x^-}{h^+} \sum_{p=1}^{(N_T+1)/2} a_{2p-1} - \frac{h_x^+}{h^+} \sum_{p=1}^{N_T/2} a_{2p} \frac{2(2p)^2}{(2p)^2-1} \right] \quad (1.50)$$

1.4 Linear properties of the model

1.4.1 Linearization of the equations for a flat bottom

In this section, the linear version of the model is considered for only one horizontal dimension ($\underline{x} = x$). It is derived by assuming that the amplitude of free surface deformation is small. It is obtained: (i) by neglecting the non-linear terms in the Zakharov equations (Eq.(1.22) and Eq.(1.23)), and (ii) by taking the upper limit of the fluid domain to be the elevation $z = 0$ (free surface elevation at rest) instead of $z = \eta(x, t)$. The water depth is held constant (i.e. the bottom is fixed and flat). By introducing $\tilde{\Phi}_0 \equiv \Phi(x, z = 0, t)$ and $\tilde{w}_0 \equiv \frac{\partial \Phi}{\partial z}(x, z = 0, t)$, the velocity potential and the vertical velocity at $z = 0$, respectively, the linear version of the model can be written as:

$$\left\{ \begin{array}{ll} \frac{\partial \eta}{\partial t} = \tilde{w}_0 & \text{at } z = 0 \quad (1.51a) \\ \frac{\partial \tilde{\Phi}_0}{\partial t} = -g\eta & \text{at } z = 0 \quad (1.51b) \\ \Delta \Phi = 0 & \text{in } \Omega, \text{ for } -h < z < 0 \quad (1.51c) \\ \frac{\partial \Phi}{\partial z} = 0 & \text{at } z = -h \quad (1.51d) \end{array} \right.$$

1.4.2 The first order Stokes solution

When considering regular progressive waves with period T (or angular frequency $\omega = \frac{2\pi}{T}$), wavelength L (or wave number $k = \frac{2\pi}{L}$) and amplitude A , the exact solution of the set of linear equations Eq.(1.51a)-Eq.(1.51d) is given by first-order Stokes theory (Dean and Dalrymple, 1991):

$$\Phi(x, z, t) = \frac{gA}{\omega} \frac{\cosh(k(h+z))}{\cosh(kh)} \sin(kx - \omega t), \quad (1.52)$$

which is used as the analytical reference to study the accuracy of the results obtained with the model. The proposed model solves the same set of equations, but because of the numerical approach and the discretization of the problem, the model solution may differ from the exact analytical solution. Particular attention is paid to the dispersion relation:

$$\omega_{Stokes}^2 = gk \tanh(kh) \quad \text{or} \quad \hat{\omega}_{Stokes}^2 = \mu \tanh(\mu) \quad (1.53)$$

with $\mu \equiv kh$, the relative water depth, and $\hat{\omega} \equiv \omega \sqrt{\frac{h}{g}}$, the non-dimensional angular frequency. The phase celerity of the wave can be deduced from Eq.(1.53):

$$\left(\frac{C}{\sqrt{gh}} \right)_{Stokes}^2 = \left(\frac{\hat{\omega}_{Stokes}}{\mu} \right)^2 = \frac{\tanh \mu}{\mu} \quad (1.54)$$

The relative water depth μ is also known as a parameter measuring frequency dispersion. From the expression of the phase celerity, one can notice that: (i) in shallow water (“small” μ i.e. $\frac{h}{L} < \frac{1}{20} \Leftrightarrow \mu < \frac{\pi}{10}$) the celerity of the wave tends towards \sqrt{gh} corresponding to non-dispersive waves (i.e. waves propagate at the same celerity regardless of their period), and (ii) in deep water (“large” μ i.e. $\frac{h}{L} > \frac{1}{2} \Leftrightarrow \mu > \pi$) $\frac{C}{\sqrt{gh}} \approx \frac{1}{\sqrt{\mu}}$ or $C \approx \sqrt{\frac{g}{k}} = \frac{g}{\omega}$. Thus, frequency dispersion becomes important for large values of μ (deep water or short waves). Even if the relative water depth of the wave is not very large, the relative water depth corresponding to its higher harmonics may become large. Therefore, it is important to have high accuracy for large values of μ .

1.4.3 Derivation of the linear dispersion relation of the proposed model

1.4.3.1 Analytical expression of the dispersion relation

To derive the dispersion relation of the linearized model, a progressive wave solution of a sinusoidal form is sought:

$$\Phi(x, z, t) = \frac{gA}{\omega} f(z) \sin(kx - \omega t), \quad (1.55)$$

where $f(z)$ represents the vertical variation of the velocity potential (in the case of first-order Stokes wave theory, $f(z) = \frac{\cosh(k(h+z))}{\cosh(kh)}$ from Eq.(1.52)). The accuracy of the model is verified in comparison to the vertical variation of the Stokes theory velocity potential. In particular, according to Stokes theory, $f(z = 0) = 1$ must be satisfied.

From the expression of the velocity potential (Eq.(1.55)), $\tilde{\Phi}_0$ and its time derivative are obtained:

$$\tilde{\Phi}_0 = \frac{gA}{\omega} f(0) \sin(kx - \omega t) \quad (1.56)$$

and

$$\frac{\partial \tilde{\Phi}_0}{\partial t} = -gAf(0) \cos(kx - \omega t). \quad (1.57)$$

By introducing Eq.(1.57) into Eq.(1.51b), the following expression for η is deduced :

$$\eta = -\frac{1}{g} \frac{\partial \tilde{\Phi}_0}{\partial t} = Af(0) \cos(kx - \omega t) \quad (1.58)$$

If the condition $f(0) = 1$ is true, this expression of the free surface elevation corresponds to a sinusoidal wave of amplitude A propagating in the x -direction.

Then, \tilde{w}_0 can be expressed as:

$$\tilde{w}_0 = \frac{\partial \Phi}{\partial z}(x, z = 0, t) = \frac{gA}{\omega} f'(0) \sin(kx - \omega t) \quad (1.59)$$

where $f'(0) \equiv \frac{df}{dz}(z = 0)$.

Finally, replacing $\frac{\partial \eta}{\partial t}$ and \tilde{w}_0 by Eq.(1.58) and Eq.(1.59) their expressions in Eq.(1.51a), the dispersion relation of the linear version of the model is obtained:

$$\frac{\omega^2}{g} f(0) = f'(0), \quad (1.60)$$

which in the non dimensional space, corresponds to:

$$\hat{\omega}^2 = \frac{f'(0)}{f(0)} h. \quad (1.61)$$

1.4.3.2 Expression of the dispersion relation as a function of the a_n

The dispersion relation is determined from the vertical variation of the velocity potential. The accuracy of estimation of this vertical variation is related to the spectral resolution of the numerical method. Thus, the decomposition of $f(z)$ on the basis of the Chebyshev polynomials is studied. First, a change of variables of the vertical coordinate from z to s is completed (Eq.(1.28 for a flat bottom $h = cst$ and $\eta = 0$) following the steps previously shown in Section 1.2.1. Derivatives of s with respect to x are zero because of the flat bottom assumption.

$$s_x = s_{xx} = s_{zz} = s_{zx} = 0 \quad \text{and} \quad s_z = \frac{2}{h}.$$

Following the change of variables, $f(z)$ becomes $\bar{f}(s)$. Using the chain rule ($\frac{df}{dz} = \frac{d\bar{f}}{ds} s_z$), Eq.(1.61)

can be rewritten in terms of \bar{f} :

$$\hat{\omega}^2 = 2 \frac{\bar{f}'(1)}{\bar{f}(1)}. \quad (1.62)$$

The function \bar{f} can then be expanded on the basis of the $N_T + 1$ first Chebyshev polynomials:

$$\bar{f}(s) \approx \sum_{n=0}^{N_T} a_n T_n(s). \quad (1.63)$$

Contrary to the expansion of the velocity potential in the non-linear version of the model, the coefficients a_n are now constant. The dependence on x does not appear in the function \bar{f} , that only depends on s , but in the argument ($k \cdot x - \omega t$) of the sine functions.

Furthermore, the properties of the Chebyshev polynomials give the following expressions for $\bar{f}(1)$ and $\bar{f}'(1)$:

$$\bar{f}(1) = \sum_{n=0}^{N_T} a_n \quad \text{and} \quad \bar{f}'(1) = \sum_{n=0}^{N_T} a_n n^2.$$

Thus the approximation of $\hat{\omega}^2$ for a polynomial of maximum order N_T ($\hat{\omega}_{N_T}^2$) can be expressed as a function of the a_n coefficients:

$$\hat{\omega}_{N_T}^2 = \frac{2 \sum_{n=0}^{N_T} a_n n^2}{\sum_{n=0}^{N_T} a_n}. \quad (1.64)$$

1.4.3.3 Resolution of the Laplace BVP

To get the a_n coefficients, the Laplace BVP is solved in the fluid domain. In the coordinate system (x, s) , where $\varphi(x, s) \equiv \Phi(x, z)$, the Laplace equation (Eq.(1.51c)) is written as:

$$\varphi_{xx} + 2s_x \varphi_{xs} + (s_x^2 + s_z^2) \varphi_{ss} + s_{xx} \varphi_s = 0. \quad (1.65)$$

In the case of a flat bottom, Eq.(1.65) can be simplified to:

$$\varphi_{xx} + \frac{4}{h^2} \varphi_{ss} = 0. \quad (1.66)$$

By substituting for φ , this simplifies to:

$$\mu^2 \bar{f}(s) - 4 \bar{f}''(s) = 0. \quad (1.67)$$

in which the square of the dispersion parameter μ appears.

When $\bar{f}(s)$ is replaced by its approximation (Eq.(1.63)), Eq.(1.67) becomes:

$$\sum_{n=0}^{N_T} a_n (\mu^2 T_n - 4 T_{n,ss}) = 0. \quad (1.68)$$

Finally, in order to eliminate the s coordinate, the Chebyshev-Tau operator (Eq.(1.33)) can be applied to Eq.(1.68) for $0 \leq p \leq N_T$:

$$\sum_{n=0}^{N_T} a_n (\mu^2 \langle T_n \rangle_p - 4 \langle T_{n,ss} \rangle_p) = 0 \Rightarrow \sum_{n=0}^{N_T} a_n (\mu^2 B_{p00n} - 4B_{p02n}) = 0 \quad (1.69)$$

where $B_{p00n} = \delta_{pn}$ and $B_{p02n} = \frac{1}{c_p} \begin{cases} n(n^2 - p^2) & \text{if } p = n - 2, n - 4, n - 6, \dots, 0 \\ 0 & \text{otherwise.} \end{cases}$

with c_p defined in Eq.(1.33).

A linear system of $N_T + 1$ equations is then formed for the unknown coefficients a_n . This system is made of:

- an equation imposing the free surface boundary condition (following Stokes theory):

$$f(0) = 1 \Leftrightarrow \bar{f}(1) = 1 \Rightarrow \sum_{n=0}^{N_T} a_n = 1, \quad (1.70)$$

- an equation imposing the impermeability of the bottom:

$$\left. \frac{\partial \Phi}{\partial z} \right|_{z=-h} = 0 \Rightarrow \bar{f}'(-1) = 0 \Rightarrow \sum_{n=0}^{N_T} (-1)^{n-1} a_n n^2 = 0, \quad \text{and} \quad (1.71)$$

- the $N_T - 1$ equations corresponding to the inner product of the Laplace equation with T_p for p from 0 to $N_T - 2$:

$$\sum_{n=0}^{N_T} a_n (\mu^2 B_{p00n} - 4B_{p02n}) = 0 \quad \text{for } p = 0, \dots, N_T - 2. \quad (1.72)$$

An example of the linear system, in matrix format, for $N_T=4$ is:

$$\begin{pmatrix} 1 & 1 & 1 & 1 & 1 \\ 0 & 1 & -4 & 9 & -16 \\ \mu^2 & 0 & -16 & 0 & -128 \\ 0 & \mu^2 & 0 & -96 & 0 \\ 0 & 0 & \mu^2 & 0 & -192 \end{pmatrix} \cdot \begin{pmatrix} a_0 \\ a_1 \\ a_2 \\ a_3 \\ a_4 \end{pmatrix} = \begin{pmatrix} 1 \\ 0 \\ 0 \\ 0 \\ 0 \end{pmatrix}$$

The solution of the system gives the expression of the a_n coefficients as a function of μ^2 , from which the non-dimensional dispersion relation can be deduced:

$$\hat{\omega}_{N_T}^2 = 2 \sum_{n=1}^{N_T} a_n n^2. \quad (1.73)$$

1.4.3.4 Analytical resolution of the linear system

The linear system of the a_n coefficients can be solved “by hand” for small values of N_T (2 to 4), but for larger values of N_T the calculations become cumbersome. Therefore, a computer algebra program wxMaxima (<http://andrevj.github.io/wxmaxima/>) is used to find the analytical expression of the non-dimensional angular frequency corresponding to the linearized model with a flat bottom as a function of the dispersion parameter μ for several values of N_T . The results can be expressed as a rational function of μ :

$$\frac{\hat{\omega}_{N_T}^2}{\mu^2} = \left(\frac{C}{\sqrt{gh}} \right)_{N_T}^2 = \frac{1 + \sum_{p=1}^{N_T-2} \alpha_p \mu^{2p}}{1 + \sum_{p=1}^{N_T-1} \beta_p \mu^{2p}}. \quad (1.74)$$

The values of the coefficients α_p and β_p for $N_T = 7$ are given as an example (Table 1.1). The coefficients for N_T from 2 to 15 are shown in Appendix A and will be compared to the theoretical expression in the next section. For values of N_T greater than 15, there was not sufficient computer memory (within a desktop linux machine) to obtain the analytical expressions.

α_p for $p = 1$ to $N_T - 2$	β_p for $p = 1$ to $N_T - 1$
$\alpha_1 = \frac{23}{160}$	$\beta_1 = \frac{229}{480}$
$\alpha_2 = \frac{443}{92160}$	$\beta_2 = \frac{937}{30720}$
$\alpha_3 = \frac{197}{3686400}$	$\beta_3 = \frac{4259}{7372800}$
$\alpha_4 = \frac{287}{1415577600}$	$\beta_4 = \frac{37507}{9909043200}$
$\alpha_5 = \frac{7}{30198988800}$	$\beta_5 = \frac{697}{90596966400}$
	$\beta_6 = \frac{17}{6088116142080}$

Table 1.1: Dispersion relation coefficients for $N_T = 7$

1.4.4 Accuracy of the dispersion relation of Misthyc

To study the accuracy of the dispersive properties of the model, the dispersion relation of Misthyc is compared with Stokes’ analytical expression. Dispersion relations obtained with Boussinesq-models are also compared to these results. Boussinesq models are often used to simulate water wave propagation. They do not resolve exactly the same set of equations, and their dispersion relation is different from Stokes analytical solution. Some Boussinesq models have a dispersion relation corresponding to a rational approximation of Padé type, which means that

$\tanh\mu/\mu$ is approximated as a rational function of μ . Rational functions with the same order in the numerator and denominator are known to give more accurate results. Relations for the order (2,2) and (4,4) Padé approximants are considered in this comparison:

- the dispersion relation using a (2,2) Padé approximant is:

$$\left(\frac{C}{\sqrt{gh}}\right)^2 = \frac{\tanh \mu}{\mu} \approx \frac{1 + \frac{1}{15}\mu^2}{1 + \frac{2}{5}\mu^2}, \quad (1.75)$$

- the dispersion relation using a (4,4) Padé approximant is:

$$\left(\frac{C}{\sqrt{gh}}\right)^2 = \frac{\tanh \mu}{\mu} \approx \frac{1 + \frac{1}{9}\mu^2 + \frac{1}{945}\mu^4}{1 + \frac{4}{9}\mu^2 + \frac{1}{63}\mu^4}. \quad (1.76)$$

The Padé approximants may not be accurate enough to simulate well waves propagating in deep water conditions ($kh > \pi$). Higher-order models have been proposed by several authors. Here, two models are considered for further comparison. Their derived linear dispersion relations are:

- from the linearized two-layer Boussinesq model of [Chazel et al. \(2009\)](#):

$$\left(\frac{C}{\sqrt{gh}}\right)^2 = \frac{1 + a_2\mu^2 + a_4\mu^4 + a_6\mu^6}{1 + b_2\mu^2 + b_4\mu^4 + b_6\mu^6 + b_8\mu^8}, \quad (1.77)$$

One can notice that this corresponds to the analytical expression for the dispersion relation of Misthyc (Eq.(1.74)) for $N_T = 5$ but with different coefficients:

$$a_2 = 2S + \frac{1}{12}, \quad a_4 = S(2S + \frac{1}{12}), \quad a_6 = S^3$$

$$b_2 = 2S + \frac{5}{12}, \quad b_4 = 3S^2 + \frac{2}{3}S + \frac{1}{144}, \quad b_6 = S^2(2S + \frac{5}{12}), \quad b_8 = S^4$$

and with $S = \sigma(1 - \sigma)/12$ where $\sigma = 0.314$ is the recommended value.

- from the linearized extended Boussinesq model of [Madsen et al. \(2006\)](#):

$$\left(\frac{C}{\sqrt{gh}}\right)^2 = \frac{1 + a_2\mu^2 + a_4\mu^4 + a_6\mu^6 + a_8\mu^8}{1 + b_2\mu^2 + b_4\mu^4 + b_6\mu^6 + b_8\mu^8 + b_{10}\mu^{10}}, \quad (1.78)$$

One can notice that this corresponds to the analytical expression for the dispersion relation of Misthyc (Eq.(1.74)) for $N_T = 6$ but with different coefficients:

$$a_2 = \frac{1}{6} - \frac{\sigma^2}{9}, \quad a_4 = \frac{1}{120} - \frac{\sigma^2}{54} + \frac{4\sigma^4}{567}$$

$$a_6 = \frac{\sigma^2}{270} - \frac{\sigma^3}{72} + \frac{29\sigma^4}{1701} - \frac{\sigma^5}{135} + \frac{2\sigma^6}{2835}$$

$$a_8 = \frac{\sigma^4}{7560} - \frac{\sigma^5}{1620} + \frac{17\sigma^6}{17010} - \frac{11\sigma^7}{17010} + \frac{8\sigma^8}{59535}$$

$$b_2 = \frac{1}{2} - \frac{\sigma^2}{9} \quad , \quad b_4 = \frac{1}{24} - \frac{\sigma^2}{18} + \frac{4\sigma^4}{567}$$

$$b_6 = \frac{\sigma}{120} - \frac{5\sigma^2}{216} + \frac{\sigma^3}{54} - \frac{5\sigma^4}{1134} + \frac{\sigma^5}{945} - \frac{\sigma^6}{2835}$$

$$b_8 = \frac{\sigma^3}{1080} - \frac{\sigma^4}{252} + \frac{7\sigma^5}{1215} - \frac{\sigma^6}{315} + \frac{4\sigma^7}{8505} + \frac{\sigma^8}{59535}$$

$$b_{10} = \frac{\sigma^5}{113400} - \frac{\sigma^6}{22680} + \frac{2\sigma^7}{25515} - \frac{\sigma^8}{17010} + \frac{\sigma^9}{59535} - \frac{\sigma^{10}}{893025}$$

where $\sigma = 0.5$ is the recommended optimal value.

The dispersion relations are compared by plotting the ratio between the phase velocity obtained by each model and the phase velocity of first-order Stokes theory (Figure 1.3) for kh in the range $[10^{-2}, 10^2]$ (where $kh = 10^2$ is approximately 30 times the value usually taken as the infinite depth limit). All of the models eventually diverge from $C/C_{Stokes} = 1$ for different large values of kh , with different trends. Both Padé approximants diverge with larger values of the phase velocity whereas the two “improved” Boussinesq models of Chazel et al. (2009) and Madsen et al. (2006) diverge with lower values of the phase velocity. The phase velocities obtained with Misthyc do not diverge monotonically. For shallow and intermediate water conditions, the models are nearly equivalent, and differences become visible only for deep water conditions. The phase velocity obtained with Misthyc using $N_T = 3$ diverges for $kh \approx 0.4$ and the (2,2) Padé approximants diverge for $kh \approx 2$. Then, the curves corresponding to Misthyc with $N_T = 5$ and $N_T = 7$ begin to diverge for smaller kh than the Boussinesq models of Chazel et al. (2009) and Madsen et al. (2006). With $N_T = 20$, $C/C_{Stokes} \approx 1$ for the range of kh values considered here ($0.01 \leq kh \leq 100$).

The relative error is also evaluated in comparison to the phase velocity given by first-order Stokes theory (Figure 1.4). By setting a threshold of 2.5% error with respect to the Stokes phase velocity, this error level is exceeded for increasing values of kh , when N_T increases: $kh \approx 6.9$ for $N_T = 3$, and $kh \approx 56$ for $N_T = 7$, and the threshold is not exceeded for $N_T > 15$ (for $kh \leq 100$). The

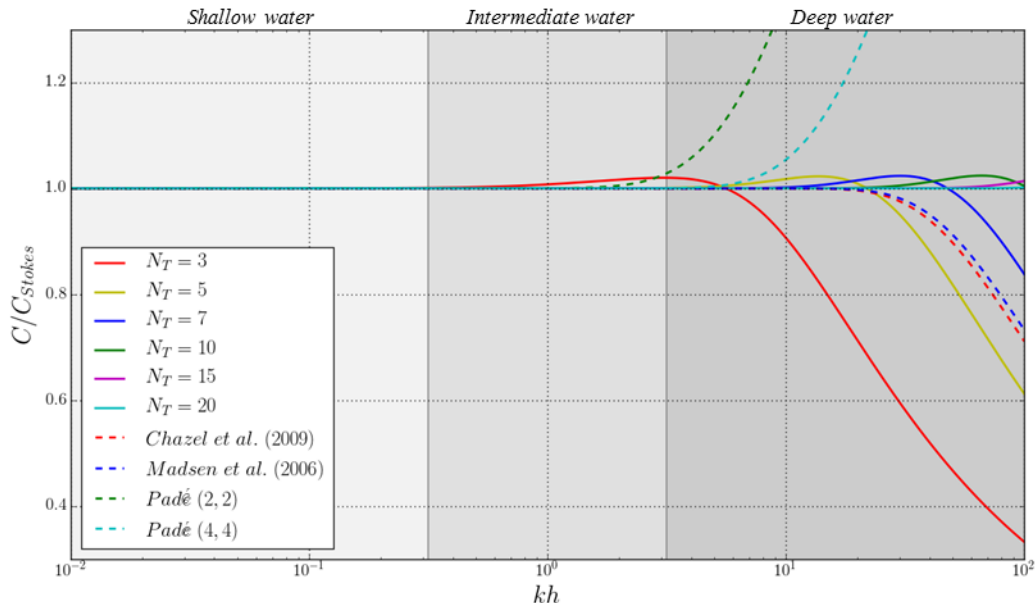


Figure 1.3: Phase velocity ratio in comparison with first-order Stokes theory, for Misthyc with several values of N_T (solid lines), for the (2,2) Padé approximant (dashed green), the (4,4) Padé approximant (dashed light blue), Chazel et al. (2009) (dashed red) and Madsen et al. (2006) (dashed dark blue).

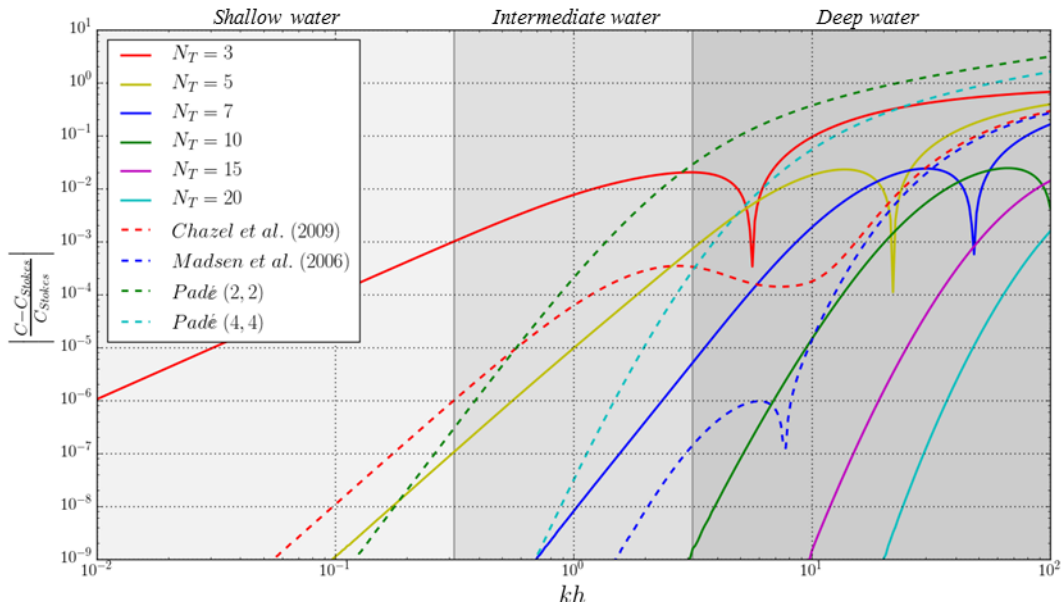


Figure 1.4: Phase velocity relative error in comparison with first-order Stokes theory, for Misthyc with several values of N_T (solid lines), the (2,2) Padé approximant (dashed green), the (4,4) Padé approximant (dashed light blue), Chazel et al. (2009) (dashed red) and Madsen et al. (2006) (dashed dark blue).

accuracy of the dispersion relation is thus improved with larger N_T . Moreover, the relative error of Chazel et al. (2009) is larger than the error obtained with the (2,2) and (4,4) Padé approximants in shallow and intermediate water, but the trend reverses for a narrow range of kh for deep water conditions.

Misthyc is then compared with the two “improved” Boussinesq models considered here in deep water conditions ($\pi \leq kh \leq 100$). The phase velocity ratios are plotted for $N_T = 7 - 12$ in Figure 1.5. Considering the value of kh where C/C_{Stokes} diverges from 1, Misthyc obtains results similar to those of the two Boussinesq models for values of N_T of about 8-9. Looking at the phase velocity ratio relative error (Figure 1.6) for $kh < 6$ the relative error of the Boussinesq model of Chazel et al. (2009) is larger than for Misthyc with $N_T = 7$ but becomes smaller for a narrow range of kh in deep water conditions. For $kh < 30$, the relative error of the Boussinesq model of Madsen et al. (2006) is smaller than the errors for Misthyc with $N_T = 7$. For $kh > 30$ both considered Boussinesq models have a larger relative error than Misthyc with $N_T > 10$. For both Boussinesq models, the 2.5% error limit is exceeded at $kh \approx 30 - 33$ and at $kh \approx 55$ for Misthyc with $N_T > 7$.

Thus, the dispersive properties of the linear version of Misthyc improve with an increasing value of N_T . This flexibility is an advantage when using the model in shallow or intermediate water because a smaller value of N_T can be used to reduce the computational time significantly. For $N_T > 10$ the relative error remains under the 2.5% threshold for $kh \in [0.01, 100]$.

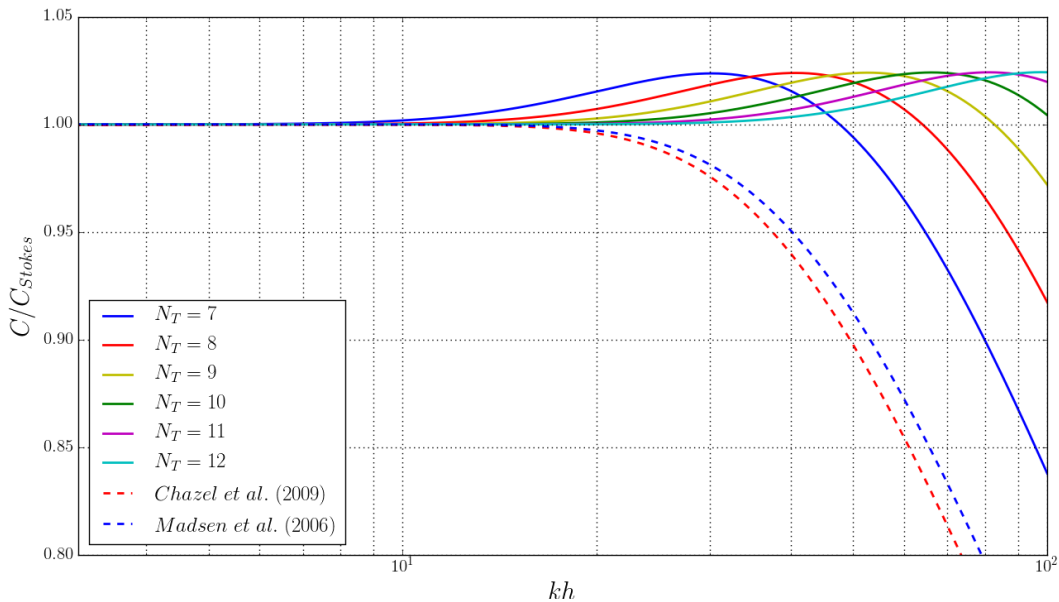


Figure 1.5: Phase velocity ratio in comparison with first-order Stokes theory, for Misthyc with several values of N_T (solid lines), Chazel et al. (2009) (dashed red) and Madsen et al. (2006) (dashed dark blue). The extent of the horizontal axis is from $kh = \pi$ (deep water threshold) to $kh = 100$.

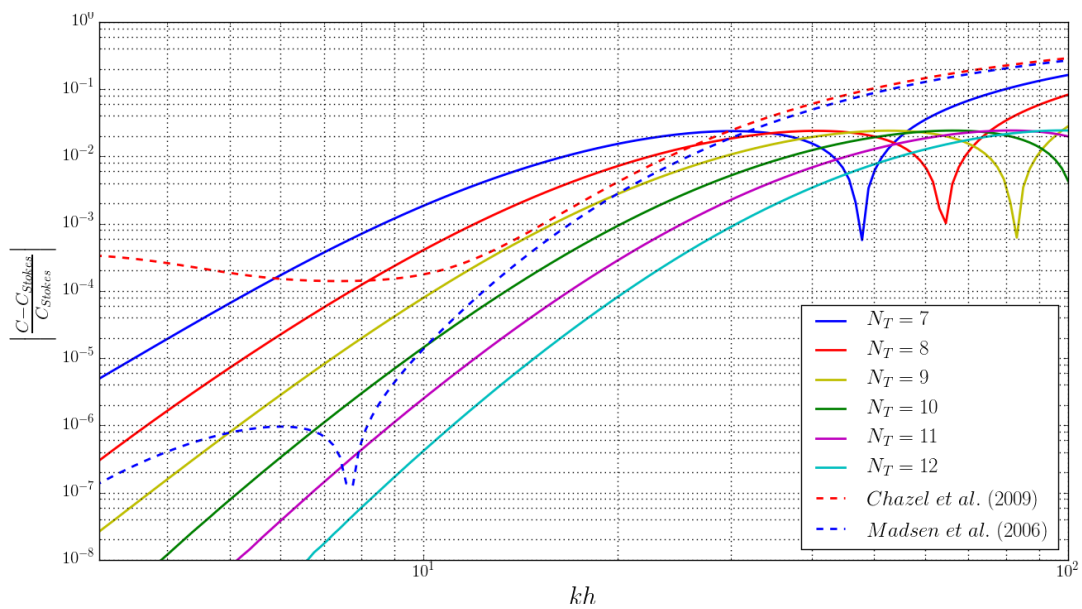


Figure 1.6: Relative phase velocity in comparison with first-order Stokes theory, for Misthyc with several values of N_T (solid lines), [Chazel et al. \(2009\)](#) (dashed red) and [Madsen et al. \(2006\)](#) (dashed dark blue). The extent of the horizontal axis is from $kh = \pi$ (deep water threshold) to $kh = 100$.

Chapter 2

Numerical implementation of the 1DH model

Dans ce Chapitre, dans un premier temps, les méthodes numériques utilisées pour l'implémentation de la version 1DH du modèle sont présentées brièvement. Un schéma explicite de Runge-Kutta à l'ordre 4 avec un pas de temps constant est utilisé pour l'intégration en temps et un schéma aux différences finies avec un pas d'espace variable est utilisé pour estimer les dérivées horizontales. La résolution numérique du système linéaire est réalisée à l'aide du solveur direct MUMPS. Dans un second temps, les conditions aux limites pour l'absorption et la génération de vagues sont étudiées. Deux méthodes d'absorption sont comparées : l'utilisation d'une zone de relaxation dans laquelle η et $\tilde{\Phi}$ sont forcés à tendre progressivement vers 0 et l'ajout de termes dissipatifs dans les conditions aux limites à la surface libre. Suite aux tests de sensibilité effectués, le choix se porte sur l'utilisation d'une zone de relaxation d'au moins deux longueurs d'onde de long pour plus de généralité. La condition à la limite appliquée à la frontière où se situe le générateur de vague est étudiée vis à vis de la précision du champ de vague généré pour des conditions de hauteur de vague incidente, période et direction fixées. Les vagues sont générées selon la théorie linéaire. Quatre types d'implémentation, différenciant par le jeu d'équations appliqué au point situé sur la frontière lors de la résolution du problème de Laplace, sont testés et comparés dans le cas de conditions à la limite de type Dirichlet ou Neumann. Suite à cette étude, il est décidé d'ajouter une zone de relaxation qui stabilise la génération et donne des résultats similaires quel que soit le choix d'implémentation de la condition à la limite.

2.1 Numerical methods

2.1.1 Integration in time

To integrate the Zakharov equations in time, the classical fourth order Runge Kutta (RK4) scheme, with a constant time step, is chosen. This explicit method estimates the value of $f(t + \Delta t)$ from the value of $f(t)$ and an approximation of the derivative through a weighted average of the derivative at t , $t + \Delta t/2$ and $t + \Delta t$. At each time step the error is of the order $O(\Delta t^5)$ and the cumulative error is of the order $O(\Delta t^4)$. This common method is used for a wide range of applications, because of its stability and efficiency.

For an equation of the type $\frac{\partial y}{\partial t} = f(t, x, y)$ (here, $y = \eta$ or $y = \tilde{\Phi}$), the RK4 scheme gives the following expression for $y_{t+\Delta t}$:

$$y_{t+\Delta t} = y_t + \frac{\Delta t}{6}(k_1 + 2k_2 + 2k_3 + k_4) \quad (2.1)$$

$$\text{with } \begin{cases} k_1 = f(t, x, y(x, t)) \\ k_2 = f(t + \frac{\Delta t}{2}, x, y(x, t) + k_1 \frac{\Delta t}{2}) \\ k_3 = f(t + \frac{\Delta t}{2}, x, y(x, t) + k_2 \frac{\Delta t}{2}) \\ k_4 = f(t + \Delta t, x, y(x, t) + k_3 \Delta t) \end{cases}$$

A RK4 scheme with a constant time step is currently used because the given accuracy is sufficient for the current applications. Nevertheless, a scheme with an adaptive time step (see e.g. [Clamond et al., 2007](#)) or another iterative scheme may improve the accuracy and/or computational time. Symplectic schemes could also be considered as the Zakharov system is Hamiltonian (e.g. [Xu and Guyenne, 2009](#)). [Clamond et al. \(2007\)](#) have shown however that a strategy using a high-order explicit scheme with adaptive an time-step seems more appropriate for practical integration of such systems. This topic deserves additional study and tests, but in this work, the well-known and robust RK4 scheme is retained.

2.1.2 Derivatives in space

To calculate the spatial derivatives in the system of equations, so-called collocation methods are used. The derivatives at computational nodes are replaced by algebraic approximations involving a set of neighboring nodes. The m^{th} order derivative of a function f at a node $x = x_i$ is expressed as a linear combination of the values of the function f at the node x_i and at its n closest neighbors. n is related to the targeted approximation order in the Taylor series expansion:

$$\left. \frac{d^m f}{dx^m} \right|_{x=x_i} = \sum_{k=0}^n \alpha_k^m f(x_k) \quad (2.2)$$

where $i \in [0, n]$, and the α_k^m coefficients are the optimal weights, for the m^{th} order derivative, depending on the number of nodes ($n + 1$) used to obtain the derivative estimate at node $x = x_i$. In the following, the optimal weights for a stencil of size $n + 1$ are denoted $\alpha_{k,n}^m$.

[Fornberg \(1988\)](#) developed a recursive algorithm to compute the optimal weights using the Lagrange interpolator polynomials. The n^{th} order Lagrange polynomial is defined from the $n + 1$ values of $f(x_k)$ ($k = 0$ to n):

$$p_n(x) = \sum_{k=0}^n L_{k,n}(x) f(x_k) \quad (2.3)$$

$$\text{with } L_{k,n}(x) = \frac{(x - x_0) \dots (x - x_{k-1})(x - x_{k+1}) \dots (x - x_n)}{(x_k - x_0) \dots (x_k - x_{k-1})(x_k - x_{k+1}) \dots (x_k - x_n)} \quad (2.4)$$

The following approximation is obtained:

$$\left. \frac{d^m f(x)}{dx^m} \right|_{x=x_i} \approx \left. \frac{d^m p_n}{dx^m} \right|_{x=x_i} = \sum_{k=0}^n \left. \frac{d^m L_{k,n}(x)}{dx^m} \right|_{x=x_i} f(x_k) = \sum_{k=0}^n \alpha_{k,n}^m f(x_k) \quad (2.5)$$

From the definition of $L_{k,n}(x)$ (Eq.(2.4)), recurrence relations can be derived. The first one is the relation between $L_{k,n}$ and $L_{k,n-1}$ when $k \neq n$:

$$L_{k,n}(x) = \frac{(x - x_n)}{(x_k - x_n)} L_{k,n-1}(x) \quad (2.6)$$

The second relation is obtained for $k = n$, making the link between $L_{n,n}$ and $L_{n-1,n-1}$:

$$L_{n,n}(x) = \left(\frac{\prod_{l=0}^{n-2} (x_{n-1} - x_l)}{\prod_{l=0}^{n-1} (x_n - x_l)} \right) (x - x_{n-1}) L_{n-1,n-1}(x) \quad (2.7)$$

Now, the n^{th} order Taylor series expansion of $L_{k,n}(x)$ at $x = x_i$ is considered:

$$L_{k,n}(x) \approx \sum_{m=0}^n \left. \frac{d^m L_{k,n}(x)}{dx^m} \right|_{x=x_i} \frac{(x - x_i)^m}{m!} = \sum_{m=0}^n \alpha_{k,n}^m \frac{(x - z)^m}{m!} \quad (2.8)$$

When introduced into Eq.(2.6) and Eq.(2.7), two recurrence relations for the $\alpha_{k,n}^m$ coefficients ($m > 0$) are obtained by equating the terms $(x - z)^m$ with the same order m :

$$\begin{cases} \alpha_{k,n}^m = \frac{1}{(x_k - x_n)} [k \alpha_{k,n-1}^{m-1} - (x_n - x_i) \alpha_{k,n-1}^m] & \text{for } k \neq n \\ \alpha_{n,n}^m = \left(\frac{\prod_{l=0}^{n-2} (x_{n-1} - x_l)}{\prod_{l=0}^{n-1} (x_n - x_l)} \right) [m \alpha_{n-1,n-1}^{m-1} - (x_{n-1} - x_i) \alpha_{n-1,n-1}^m] & \text{for } k = n \end{cases} \quad (2.9)$$

In the model, the fortran code provided by [Fornberg \(1988\)](#) is used. It computes recursively

the optimal weights to estimate the first and second derivatives at a given node x_i , given the abscissa coordinates of the $n + 1$ nodes forming the stencil ($x_k, k = 0, n$) and the maximal order of the targeted derivative. Misthyc is coded to allow the flexibility to choose the order of spatial derivatives. However, to obtain high accuracy, $n = 4$ is used in all of the following applications of the 1DH version of the model. The first and second order derivatives are then approximated with an error of order $O(\Delta x^5)$ in the case of a centered stencil, i.e. with two points on both side of the node where the derivatives are estimated. When the stencil is not centered (for nodes on or close to the boundaries of the domain), first order derivatives are estimated with an accuracy of order $O(\Delta x^4)$ but second order derivatives are only $O(\Delta x^3)$ accurate. To recover the $O(\Delta x^4)$ accuracy for nodes on the boundaries, one must take $n = 5$.

2.1.3 Resolution of the linear system

At each sub-step of the RK4 scheme, the discretization of the Laplace BVP in (x, s) , with NPX nodes in x and N_T the maximum order of the Chebyshev polynomials, results in a system of $NPX(N_T + 1)$ linear equations for the coefficients $a_n(x_i)$, for $n = 0, \dots, N_T$ and $i = 1, \dots, NPX$. The corresponding matrix is sparse, and the system is currently solved in Misthyc using the direct solver MUMPS (“MULTifrontal Massively Parallel Solver”, v4.10.0) (Amestoy et al., 2001, 2006), using the default settings. Iterative solvers could be also used, and will be tested in the future.

2.2 Boundary conditions for wave generation and absorption

2.2.1 Wave absorption

2.2.1.1 Brief review of wave absorption in numerical models

Wave absorption is necessary in numerical models to prevent full reflection of waves from the lateral (numerical) boundaries. In many cases, this numerical absorption is designed to take into account physical dissipative processes (e.g. wave breaking or bottom friction) or simply to simulate fully open (radiative) boundary conditions without wave reflection. There are several methods used to absorb waves in numerical models, which can be classified into two main groups:

1. Wave absorption is located at the boundary and is achieved with adapted boundary conditions. It can be either a radiative boundary condition that allows waves to propagate out of the domain or “active” absorption that adapts the boundary condition such that a wave is generated to cancel out the incoming wave. These two options require knowing the characteristics of the waves to be absorbed (celerity, direction of propagation). These methods can be very efficient for regular waves but are difficult to extend and to optimize for irregular waves with a wide range of wavelengths and directions.
2. Wave absorption can be carried out in a zone leading up to the lateral boundary either by adding dissipative terms in the evolution equations (i.e. Kim et al., 2014; Koo and Kim, 2004;

Zhang et al., 2007) or by imposing a pressure opposing the waves (i.e. Clamond et al., 2005; Viotti and Dias, 2014). These terms are generally added progressively in space to avoid discontinuities and numerical instabilities. Another solution is to implement a relaxation zone where the solution obtained by the model is progressively modified to correspond to an imposed solution (i.e. Bingham and Agnon, 2005; Engsig-Karup, 2006). The efficiency of this second kind of method strongly depends on several parameters: the length of the relaxation zone, the mathematical formulation of the dissipative terms and its numerical parameters, and the shape of the spatial ramp function. The optimization of these characteristics might depend on the problem considered. Moreover, the lateral boundary condition at the end of the domain still needs to be defined. Generally it is a fully reflective condition or null normal velocity, but it may be a condition of type (1) to absorb long waves that might not have been absorbed well by methods of type (2) (i.e. Clément, 1996; Grilli and Horrillo, 1997; Zhang and Duan, 2012). The main drawbacks of this kind of method are that they require increasing the size of the computational domain and thus the computational time, and they may not be very efficient for absorbing very long waves.

The following paragraphs present a series of tests evaluating the implementation of methods of type (2) with first a relaxation zone and then with the addition of dissipative terms.

2.2.1.2 Relaxation zones

Relaxation zones are used to impose a known solution with a progressive transition in space to avoid the generation of shocks. The method is applied to both surface variables η and $\tilde{\Phi}$. Over the length of the relaxation zone, the solution obtained with the model ($\eta, \tilde{\Phi}$), at the end of each time step, is replaced by a linear combination of the obtained values and the imposed solution ($\eta_{imp}, \tilde{\Phi}_{imp}$). The linear combination is defined by the relaxation coefficient C_r , which is a monotonic positive function varying between 0 at the entrance of the relaxation zone ($x = x_{relax}$) and 1 at the boundary ($x = x_b$) such that:

$$\eta(x, t) = (1 - C_r(x)) \eta(x, t) + C_r(x) \eta_{imp}(x, t) \tag{2.10}$$

$$\tilde{\Phi}(x, t) = (1 - C_r(x)) \tilde{\Phi}(x, t) + C_r(x) \tilde{\Phi}_{imp}(x, t) \tag{2.11}$$

If the imposed solution is the null function, the relaxation zone can be used to absorb, but it can also be used in the case of wave generation with values of η and $\tilde{\Phi}$ calculated using linear (see Section 2.2.2) or nonlinear wave theory. As previously mentioned, this method depends on adjustable parameters that have to be tuned and may depend on each specific problem, mainly the length of the relaxation zone L_{relax} and the shape of the relaxation coefficient C_r . A good

choice of these parameters is necessary to have an efficient relaxation zone, and a series of tests are completed here to study the sensitivity to these parameters.

The first characteristic to be studied is the shape of the relaxation coefficient C_r . The condition to meet for C_r can be obtained for various shapes with different rates of transition from 0 to 1. A gradual change of the coefficient is important to avoid wave reflection from the relaxation zone. The first implementation of C_r in the model was made following [Bingham and Agnon \(2005\)](#), with $C_r(x) = \left(1 - 0.6 \frac{|x_b - x|}{|x_b - x_{relax}|}\right)^8$, and $|x_b - x_{relax}| = L_{relax}$. However, this shape of coefficient does not fulfill the condition $C_r(x = x_{relax}) = 1$, so it was adapted to $C_r(x) = \left(1 - \frac{|x_b - x|}{|x_b - x_{relax}|}\right)^\alpha$, with α a real number to be determined for the optimization of the relaxation zone. In [Engsig-Karup \(2006\)](#), relaxation zones for wave generation and absorption for high-order Boussinesq-type models based on unstructured grids are studied, and $\alpha = 5$ was suggested as the optimal value. In [Kim et al. \(2014\)](#), dissipative terms are added to the free surface boundary conditions. To avoid an abrupt change of the boundary conditions, they tested several ramp functions to increase gradually the magnitude of the damping coefficient. In the following set of tests, the ramp functions used by [Kim et al. \(2014\)](#) are considered. Finally, six shapes of the relaxation coefficient C_r are also tested:

$$C_{r1}(x) = \left(1 - \frac{|x_b - x|}{|x_b - x_{relax}|}\right)^5 \quad (2.12)$$

$$C_{r2}(x) = 1 - \frac{|x_b - x|}{|x_b - x_{relax}|} \quad (2.13)$$

$$C_{r3}(x) = 1 - \cos\left(\frac{\pi}{2} \frac{x - x_{relax}}{x_b - x_{relax}}\right) \quad (2.14)$$

$$C_{r4}(x) = \frac{1}{2} \left(1 - \cos\left(\pi \frac{x - x_{relax}}{x_b - x_{relax}}\right)\right) \quad (2.15)$$

$$C_{r5}(x) = \sin\left(\frac{\pi}{2} \frac{x - x_{relax}}{x_b - x_{relax}}\right) \quad (2.16)$$

$$C_{r6}(x) = 1 - e^{-20 \frac{x - x_{relax}}{x_b - x_{relax}}} \quad (2.17)$$

All the tests in this section and the following one are made with the linear version of the code for a regular wave of amplitude $a = 0.06$ m, wavelength $L = 6$ m and period $T = 1.96$ s that

propagates over a flat bottom ($h = 4$ m). The domain extends from 0 m to 36 m ($6L$) and is regularly meshed with $\Delta x = 0.7875$ m ($L/32$). The wave is propagated during $60T$ with a time step $\Delta t = 0.0613$ s ($T/32$), and a vertical resolution $N_T = 7$. Waves are generated in a $2L$ -long relaxation zone with a Dirichlet boundary condition at the left boundary. This relaxation zone is not varied in the simulations since the focus is on the relaxation zone added for wave absorption. Unless specified otherwise, the absorption relaxation zone is one wavelength (L) long. Figure 2.1 shows the shape of the factors $1 - C_r(x)$, by which the solution obtained by the model is multiplied in the relaxation zone.

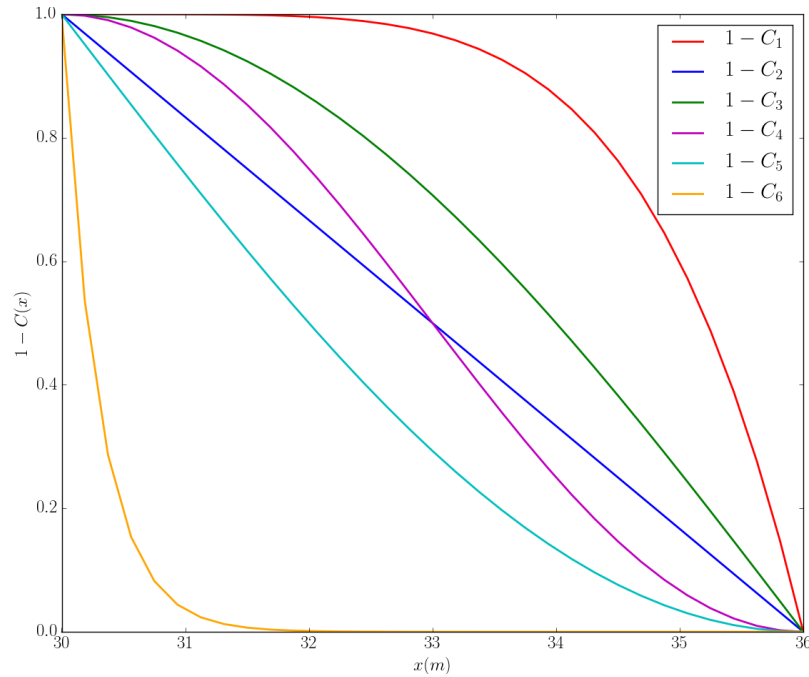


Figure 2.1: Shapes of the six $1 - C_r(x)$ coefficients considered in the first set of simulations for the absorption relaxation zone.

The efficiency of the relaxation zone is evaluated by the reflection measured inside the domain. If waves are fully absorbed, there should be no reflection of the incoming wave field. Once the periodic steady state is reached, the time series of the free surface elevation at 32 locations between $x = 18$ m and $x = 24$ m covering a domain of one wavelength are analyzed to obtain the average wave height at each location. If no reflection occurs (full absorption) the mean wave height is expected to be constant, but as can be seen in Figure 2.2, the resulting normalized wave height profiles obtained for the different shape of the relaxation coefficient vary along the domain. The wave height is modulated by the phase difference between the incoming H_I and the reflected H_R waves.

From the variations of the mean wave height profile, the reflection coefficient R can be computed

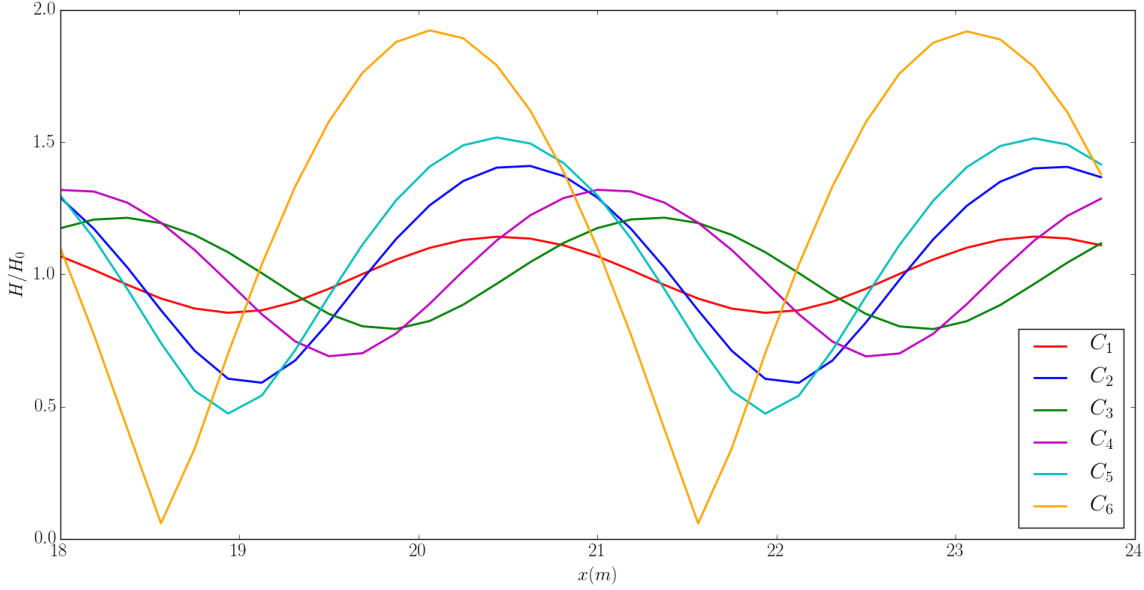


Figure 2.2: Comparison of the normalized wave height for $x \in [18, 24]$ m for different shapes of the relaxation coefficient. H_0 is the incident wave height, $H_0 = 2a = 0.12$ m.

(Table 2.1).

$$R = \frac{H_R}{H_I} = \frac{H_{max} - H_{min}}{H_{max} + H_{min}},$$

where H_{max} and H_{min} are the extreme values reached by the wave profile at each node. Reflections are minimum with the relaxation coefficient C_{r1} and maximum with C_{r6} . The coefficient C_{r6} makes the free surface elevation zero along a longer part of the relaxation zone in comparison with C_{r1} , but this does not seem to be the important characteristic to reduce reflections. The main difference between the studied relaxation coefficients is their derivatives at $x = x_{relax}$ (the beginning of the relaxation zone), and it appears that the steeper the slope at the entrance of the zone, the larger the reflection in the domain. Engsig-Karup (2006) showed that at the interface not only $C_r(x_{relax}) = 0$ must be satisfied but also $C'_r(x_{relax}) = C''_r(x_{relax}) = C'''_r(x_{relax}) = \dots = 0$ to avoid the generation of spurious waves. Among the options considered here, this is only the case for C_{r1} , explaining the high reflection coefficients obtained with the other C_r shapes.

Relaxation coefficient	C_{r1}	C_{r2}	C_{r3}	C_{r4}	C_{r5}	C_{r6}
Reflection coefficient R	0.14	0.40	0.21	0.32	0.52	0.94

Table 2.1: Reflection coefficients for the different shapes of the relaxation coefficients considered in the first set of simulations (Figure 2.1).

Based on this set of tests, a coefficient of the type of C_{r1} is used for the model implementation of relaxation zones. A sensitivity test on the value of the α parameter is carried out. As can be seen in Figure 2.3, this value has a non negligible influence on the shape of the relaxation coefficient.

As done previously, the mean wave height is computed from the time series of the free surface elevation for $x \in [18, 24]$ m. It is not constant and varies with x (Figure 2.4), showing that reflections occur for all values of α . The amplitude of the variations depends on the parameter α , with higher variations for extreme values of α (both low, $\alpha = 1$, and high, $\alpha = 9$). The reflection coefficients calculated from the wave height profiles are plotted in Figure 2.5 (blue line). The optimal value to minimize reflection is approximately $\alpha = 3.5$.

The same set of simulations was completed for longer relaxation zones of $1.5L$ and $2L$. The evolution of the reflection coefficients R as a function of α are plotted in Figure 2.5. The lengthening of the relaxation zone improves its efficiency for every α , and the dependence on α weakens. The optimal value of α seems to decrease with an optimal value around $\alpha = 3$ for $L_{relax} = 1.5L$ and $\alpha = 2.5$ for $L_{relax} = 2L$. With a relaxation zone of two wavelengths, the reflection is less than 5% for $\alpha > 2$ and decreases down to 1% in the best cases.

In all test cases where absorption is required, a relaxation zone of two wavelengths of the primary wave in the region is generally applied. The relaxation technique is applied at the end of each time step, making the results dependent on the time step. With a smaller time step, the reflection at the entrance of the absorption relaxation zone increases. When using the relaxation zone for wave generation, the leading waves have larger amplitudes than with a smaller time step, so reflections increase, and if the first waves are not correctly absorbed, this prevents convergence of the simulations as a function of the time step. For two simulations with different time steps,

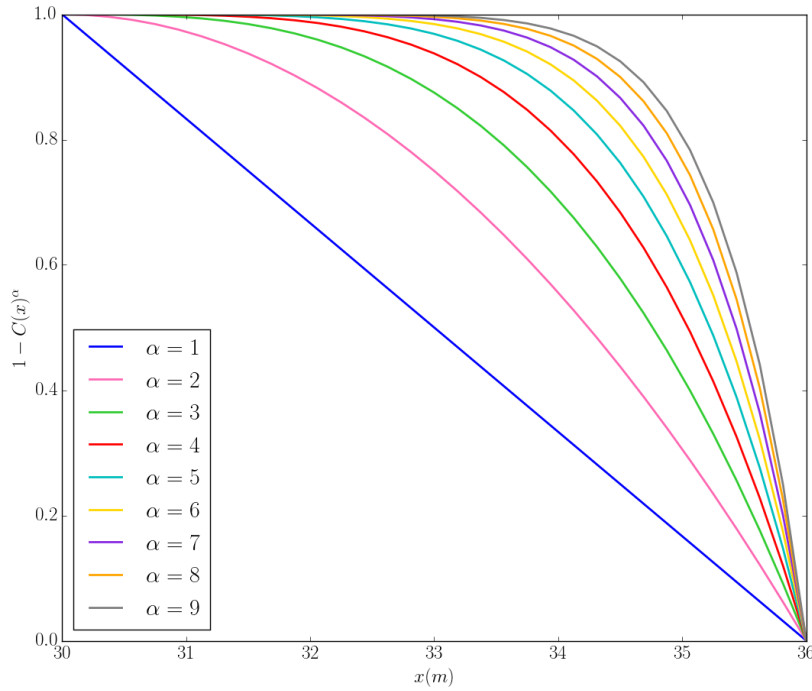


Figure 2.3: Shape of the coefficient $1 - C_r(x)$ for several values of the α parameter considered in the second set of simulations for the absorption relaxation zone.

if the relaxation zone is applied with the same frequency (i.e. applied every two time steps for $\Delta t_2 = \frac{\Delta t_1}{2}$), the convergence in time is recovered.

2.2.1.3 Adding dissipative terms

A second possibility for wave absorption is to include an artificial damping zone near the end of the domain. In this zone, artificial damping terms are progressively applied to the free surface boundary conditions. Kim et al. (2014) tested five different schemes to introduce wave absorption in their 3D numerical wave tank, where damping terms such as η -type, Φ -type or Φ_n -type (with $\Phi_n = \frac{\partial \Phi}{\partial n}$ the normal free surface velocity) were added to the KFSBC and/or the DFSBC. They concluded that adding a Φ_n -type term in the DFSBC and a η -type in the KFSBC (their method 5) was the solution minimizing reflections (with a ramp function with shape C_{r3}) in their work:

$$\begin{cases} \frac{\partial \tilde{\Phi}}{\partial t} = -g\eta - \mu_1 \frac{\partial \tilde{\Phi}}{\partial n} & \text{DFSBC} & (2.18a) \\ \frac{\partial \eta}{\partial t} = \tilde{w} - \mu_2 \eta & \text{KFSBC} & (2.18b) \end{cases}$$

In this system, the first damping term contributes to the damping of the water particle velocity, whereas the second one contributes to the damping of the free surface elevation. The coefficients μ_1 and μ_2 can be optimized through trial and error tests depending on wave characteristics. As the propagation equations are modified in the damping zone, a relation between the two damping coefficients is necessary to minimize the difference from the original boundary condition and to

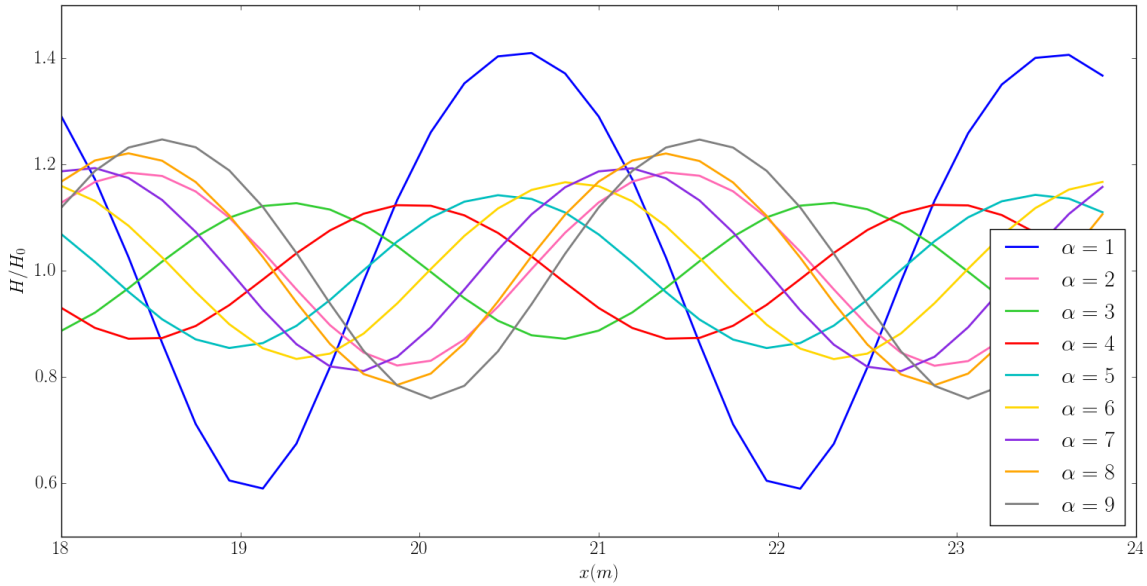


Figure 2.4: Comparison of the normalized wave height for $x \in [18, 24]$ m for several values of the parameter α . H_0 is the incident wave height, $H_0 = 2a = 0.12$ m.

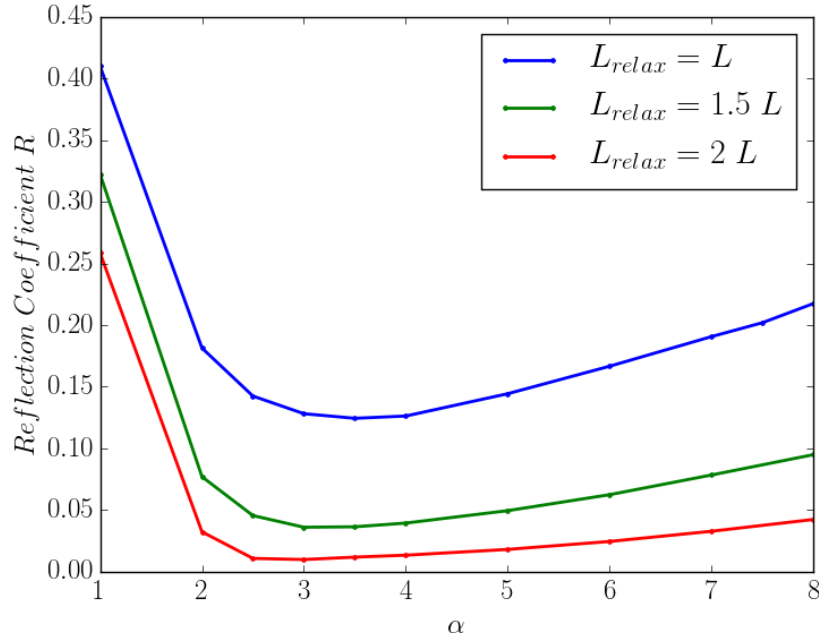


Figure 2.5: Reflection coefficient as a function of the parameter α for three different lengths of the relaxation zone ($L_{relax} = 1L$ (blue), $1.5L$ (green) and $2L$ (red)).

prevent wave dispersion and distortion. This relation is $\mu_2 = k\mu_1$ for deep water conditions, where k is the wave number. In their work, Kim et al. (2014) used a damping terms of $\mu_0 = 2.5$ such that $\mu_1 = \mu_0 C_r(x)$ and $\mu_2 = \mu_0 k C_r(x)$.

The set of equations (2.18) was implemented in the linear version of Misthyc with a ramp function corresponding to C_{r3} for a damping zone of one wavelength. A sensitivity test on the value of μ_0 was carried out. The mean wave height for several values of the parameter μ_0 , around the value of 2.5 used by Kim et al. (2014), are presented in Figure 2.6. The influence of the value of μ_0 is not negligible and the value $\mu_0 = 2.5$ is not the optimal one in that case.

The reflection coefficient as a function of μ_0 is plotted in Figure 2.7. A minimum in reflection is obtained for $\mu_0 \approx 1.75$. It is important to notice that the reflection coefficient is smaller than 5% for the range of values of μ_0 considered, with a damping zone of only one wavelength, whereas when using a relaxation zone of one wavelength, the reflection coefficient is over 10% (Figure 2.5). The relaxation zone has to be extended to two wavelengths to obtain comparable reflection coefficients.

2.2.1.4 Conclusion

From this study, it appears that the use of artificial damping terms may be more efficient for wave absorption than a relaxation zone since the same reflection coefficients are obtained for a shorter length of the damping zone, allowing a gain of computational time. However, with the chosen

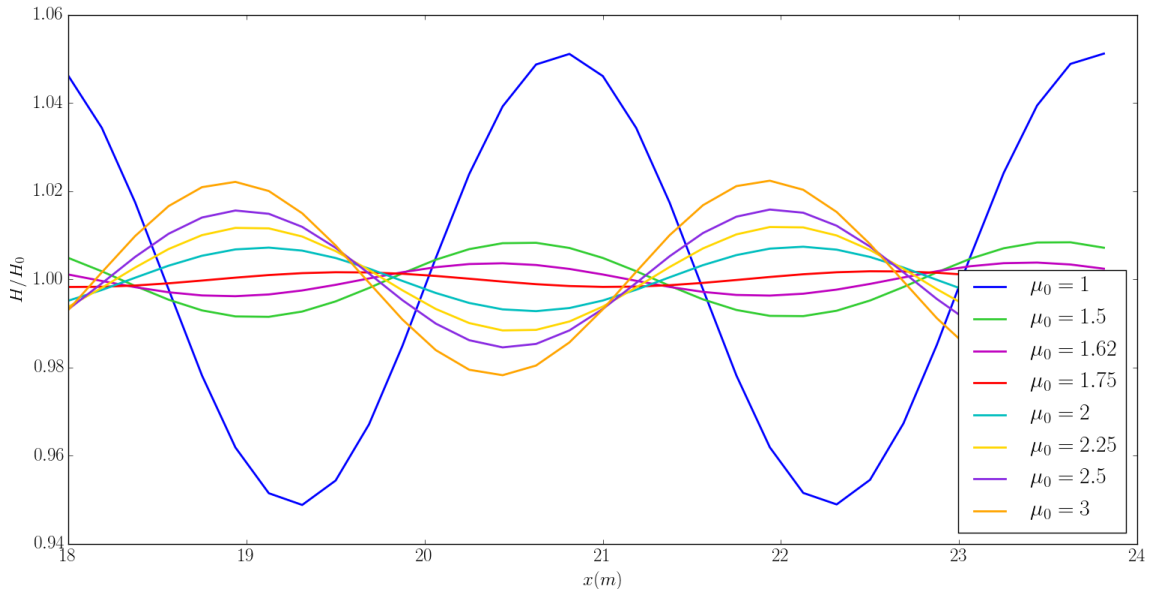


Figure 2.6: Comparison of the normalized wave height for $x \in [18, 24]$ m for several values of the parameter μ_0 . H_0 is the incident wave height, $H_0 = 2a = 0.12$ m.

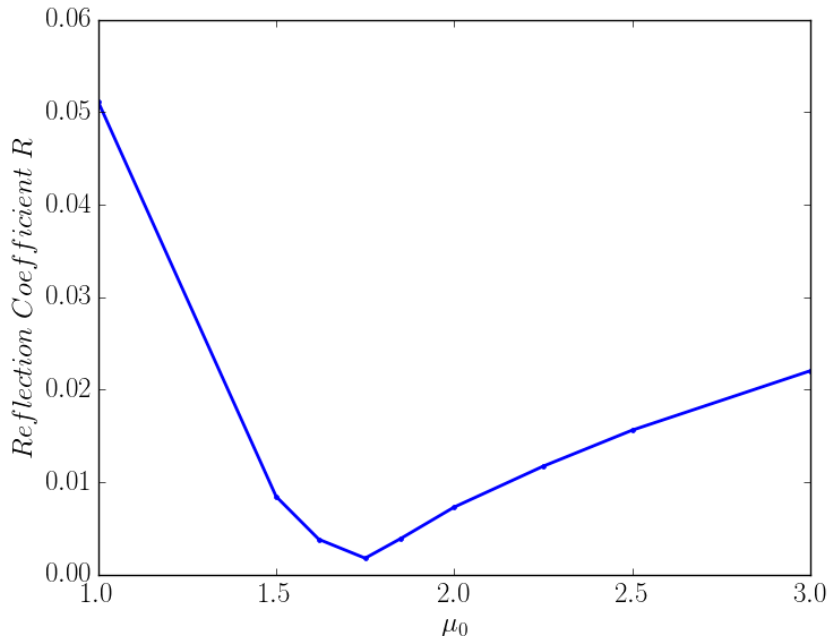


Figure 2.7: Reflection coefficient as a function of the parameter μ_0 for a damping zone of one wavelength.

artificial damping scheme a relation linking μ_1 to μ_2 is used, which relies on the wave number k . It is not clear that the efficiency of the damping terms is maintained for a range wavelengths, for example in the case of irregular waves. This has not been tested yet. Moreover, the relation between μ_1 and μ_2 is derived for deep water conditions only but what if this assumption is not

verified? The values of μ_1 and μ_2 then require being optimized, which may be more tedious than an optimization of μ_0 only. Thus the choice was made, in case where wave absorption is needed, to use a relaxation zone of generally two wavelengths long.

Finally, all the tests here were completed with the linear version of the model. Kim et al. (2014) studied the effects of non-linearity on the artificial damping scheme by applying it to waves of increasing steepness. They showed that even if the total energy ratio of nonlinear simulations to linear simulation diverged from one with the increase in wave steepness, it reaches a steady state indicating that the damping scheme is still efficient for nonlinear waves.

2.2.2 Wave generation

2.2.2.1 Brief review on wave generation in numerical models

When developing a numerical wave model, the focus is generally directed to the accurate representation of wave propagation and kinematics. However, the accurate generation of incident wave fields with specified characteristics (height, period, and direction) already presents a numerical challenge.

Wave generation methods can be implemented either by using a moving (impermeable) boundary, similar to what is done in experimental wave tanks (i.e. forcing the motion of fluid particles in a Lagrangian manner) (Contento, 2000; Ducroz et al., 2012b), or using numerical algorithms to create the desired wave field by adapting the lateral or free surface boundary conditions or the momentum equations. This second option can be divided into five main categories, most of which were compared and discussed in Schmitt and Elsaesser (2015), with respect to developing a model using the Volume of Fluid method:

1. lateral boundary forcing method: analytical solutions are prescribed at the incident, fixed boundary in an Eulerian manner, for example the incident velocity profile (Ning and Teng, 2007; Xiao et al., 2008). Variations of this method exist, and they are categorized based on how the wave conditions are imposed, including: Dirichlet-type conditions corresponding to imposing the unknown variable itself at the boundary, Neumann-type conditions corresponding to imposing its derivative (usually the normal derivative), or Robin-type conditions that are a mix of Dirichlet and Neumann conditions.
2. mass source method: based on the observation that the inflow and outflow of water in the domain can lead to a free surface displacement, the continuity equation is augmented with a source term in a given region of the domain (Liam et al., 2014).
3. impulse source method: similar to the mass source method, this method consists in adding source terms to the momentum equation (Lee and Suh, 1998).
4. surface pressure method: the wave motion is forced by applying a free surface pressure

term in the DFSBC (Clamond et al., 2005) that is variable in space and time.

5. relaxation method: similar to what was presented in Section 2.2.1.2, a relaxation zone can be implemented for wave generation using linear (or any high-order) wave theory to impose progressively over a given distance the reference solution Engsig-Karup (2006). This is done by replacing the computed solution at the end of each time step by a linear combination of this computed solution and the reference solution.

According to Schmitt and Elsaesser (2015), the relaxation method could lead to instabilities in the cases they studied, whereas mass and impulse source methods proved to be quite accurate and stable. Nevertheless, although the mass source method is simple to implement, it is limited in the range of wave heights that can be created. The impulse source method is more complex to implement and more computationally demanding, but it does not suffer from limitations on the maximum possible wave height. Finally, methods 2-5 require increasing the domain size to create a zone for waves to develop progressively, while method 1 (forcing at the boundary only) allows minimizing the size of the computational domain. For a more complete study, these methods could be compared with respect to the generation of spurious free waves, which can be a limitation factor.

Wave generation using a boundary forcing condition method is studied in the Misthyc model in the following section, in combination with the application of a relaxation zone.

2.2.2.2 Boundary conditions at the wave generator

To solve the Laplace problem, boundary conditions must be imposed at the lateral boundaries. At the wave maker boundary (located at $x = x_b$) either a Dirichlet condition (imposing the velocity potential Φ) or a Neumann condition (imposing the horizontal velocity u , which is the boundary normal velocity) can be used. In the following sections, the expression for both conditions applied at $x = x_b$ at time t are presented when linear theory is used to define Φ and u for a 1DH domain (x, z) .

Linear representation of incident waves

The simplest way to generate regular or irregular progressive waves is to consider a linear model such that the wave signal can be decomposed into N_c independent sinusoidal waves. Each component i is characterized by its height H_i , angular frequency ω_i , wave number k_i (obtained from the linear dispersion relation), phase speed C_i and phase ψ_i . Using linear wave theory, the phases ψ_i are assumed uncorrelated. Thus every component i can be treated separately as a solution of the linearized problem for a flat bottom (where h is the water depth). The free surface elevation $\eta(x, t)$, velocity potential $\Phi(x, z, t)$ and horizontal speed $u(x, z, t)$ of the wave train are obtained

by the superposition of each wave component.

$$\eta(x, t) = \sum_{i=1}^{N_c} \frac{H_i}{2} \cos(k_i x - \omega_i t + \psi_i), \quad (2.19)$$

$$\Phi(x, z, t) = \sum_{i=1}^{N_c} \frac{H_i}{2} \frac{g}{\omega_i} \frac{\cosh(k_i(z+h))}{\cosh(k_i h)} \sin(k_i x - \omega_i t + \psi_i), \quad (2.20)$$

$$u(x, z, t) = \sum_{i=1}^{N_c} \frac{H_i}{2} \frac{g}{C_i} \frac{\cosh(k_i(z+h))}{\cosh(k_i h)} \cos(k_i x - \omega_i t + \psi_i). \quad (2.21)$$

All of the results presented in this chapter use a linear representation of the incident wave field. Then during propagation, the waves adapt to be consistent with the nonlinear model. When the incident wave is too far from a linear wave, the linear generation can lead to the creation of parasitic waves and instabilities. In such cases, it is possible to generate second or higher-order regular waves (i.e. [Rienecker and Fenton, 1981](#)). It becomes more complicated when dealing with irregular waves because of nonlinear interactions between all of the components that have to be taken into account. Nevertheless, a second order generation is possible by using [Dalzell \(1999\)](#).

Dirichlet boundary condition

To derive the equations accounting for the Dirichlet boundary condition, the equality between the imposed velocity potential and the one given by the model is expressed at the boundary $x = x_b$ in the transformed (x, s) -plane. The imposed velocity potential $\varphi_I(x_b, s, t)$ given by linear theory is:

$$\varphi_I(x_b, s, t) = \sum_{i=1}^{N_c} A_i \cosh(B_i(1+s)), \quad (2.22)$$

where A_i and B_i are functions depending on x_b and t :

$$A_i = \frac{H_i}{2} \frac{g}{\omega_i \cosh(k_i h)} \sin(k_i x_b - \omega_i t + \psi_i), \quad i = 1, \dots, N_c \quad (2.23)$$

$$B_i = \frac{k_i h^+}{2} = \frac{k_i}{2} (h + \eta(x_b, t)), \quad i = 1, \dots, N_c. \quad (2.24)$$

At the same time, the spectral approach used in the vertical direction in the model, gives the following expression for the velocity potential:

$$\varphi(x, s) = \sum_{n=0}^{N_T} a_n(x) T_n(s), \quad (2.25)$$

Writing that at the wave maker boundary $x = x_b$, both expressions must be equal $\varphi_I = \varphi_{N_T}$:

$$\sum_{n=0}^{N_T} a_n(x_b) T_n(s) = \sum_{i=1}^{N_c} A_i \cosh(B_i(1+s)) \quad \forall s \in [-1; 1], \quad (2.26)$$

This expression is then projected on the Chebyshev polynomial basis by applying the operator $\langle f \rangle_p \equiv \frac{2}{\pi C_p} \langle f, T_p \rangle$ for $p = 0, 1, \dots, N_T$ to (2.26):

$$\sum_{n=0}^{N_T} a_n(x_b) \langle T_n \rangle_p = \sum_{i=1}^{N_c} A_i \langle \cosh(B_i(1+s)) \rangle_p, \quad p = 0, 1, \dots, N_T. \quad (2.27)$$

The left-hand-side of Eq.(2.27) can be rewritten as:

$$\sum_{n=0}^{N_T} a_n(x_b) \langle T_n \rangle_p = \sum_{n=0}^{N_T} a_n(x_b) \delta_{np} = a_p(x_b), \quad (2.28)$$

Moreover, it can be shown that the right-hand-side of Eq.(2.27) can be expressed using I_p , the modified Bessel function of the first kind of order p (Tian and Sato, 2008):

$$\sum_{i=1}^{N_c} \langle \cosh(B_i(1+s)) \rangle_p = \frac{2}{C_p} \sum_{i=1}^{N_c} I_p(B_i) \begin{cases} \cosh B_i & \text{if } p \text{ is even,} \\ \sinh B_i & \text{if } p \text{ is odd.} \end{cases} \quad (2.29)$$

Finally, combining Eq.(2.28) and Eq.(2.29), Eq.(2.27) is equivalent to:

$$a_p(x_b) = \sum_{i=1}^{N_c} A_i \frac{2}{C_p} I_p(B_i) \begin{cases} \cosh B_i & \text{if } p \text{ is even,} \\ \sinh B_i & \text{if } p \text{ is odd.} \end{cases} \quad (2.30)$$

Thus, the $a_p(x_b)$ coefficients can be computed analytically for any time t , for $p = 0, 1, \dots, N_T$.

When the incident waves cannot be decomposed as a sum of linear sinusoidal waves as in the case for a solitary wave, for instance, the modified Bessel function of the first kind (I_p) can no longer be used to compute the $a_p(x_b)$ for $p = 0, 1, \dots, N_T$. For more general cases, the vertical profile of the velocity potential $\phi(x_b, s, t)$, at $x = x_b$ for time t , has to be “directly” projected on the Chebyshev polynomial basis by applying the operator $\langle f \rangle_p$. A Gauss-Chebyshev quadrature (Eq.(2.31)) is used to compute the operator integral.

$$\langle f \rangle_p \equiv \frac{2}{\pi C_p} \int_{-1}^1 \frac{f(s) T_p(s)}{\sqrt{1-s^2}} ds \approx \sum_{k=1}^N w_k f(s_k) T_p(s_k) \quad (2.31)$$

with $s_k = \cos\left(\frac{(2k-1)\pi}{2N}\right)$, $w_k = \frac{\pi}{N}$, where N is the number of nodes discretizing the vertical profile of the velocity potential.

Thus the equivalent of Eq.(2.30) for an incident wave field that cannot be decomposed into sinu-

soidal waves is:

$$a_p(x_b) = \langle \phi(x_b, s, t) \rangle_p. \quad (2.32)$$

Neumann boundary condition

The method is used to obtain the expression for the Neumann boundary condition is quite similar to the one used for the Dirichlet boundary condition, but now the horizontal velocity profile u_I at the wave maker ($x = x_b$) is considered:

$$u_I(x_b, s, t) = \sum_{i=1}^{N_c} A_i \cosh(B_i(1 + s)), \quad (2.33)$$

with

$$A_i = \frac{H_i}{2} \frac{gk}{\omega_i \cosh(k_i h)} \cos(k_i x_b - \omega_i t + \psi), \quad i = 1, \dots, N_c \quad (2.34)$$

$$B_i = \frac{k_i h^+}{2} = \frac{k_i}{2} (h + \eta(x_b, t)) \quad i = 1, \dots, N_c. \quad (2.35)$$

The spectral approach in the vertical leads to the following expression for the horizontal velocity profile.

$$u(x, s) = \sum_{n=0}^{N_T} a'_n(x) T_n(s) + \sum_{n=1}^{N_T} a_n(x) \frac{h_x^- h^+ - s h_x^+ h^+}{h^{+2}} T'_n(s). \quad (2.36)$$

Similar to what was done previously for the velocity potential, the equality of the two expressions of the horizontal velocity at the wave maker boundary ($x = x_b$) gives:

$$\sum_{n=0}^{N_T} a'_n(x_b) T_n(s) + \sum_{n=1}^{N_T} a_n(x_b) \frac{h_x^- h^+ - s h_x^+ h^+}{h^{+2}} T'_n(s) = \sum_{i=1}^{N_c} A_i \cosh(B_i(1 + s)) \quad \forall s \in [-1; 1], \quad (2.37)$$

Then the operator $\langle f \rangle_p$ is applied to Eq.(2.37) for $p = 0, 1, \dots, N_T$:

$$\sum_{n=0}^{N_T} a'_n(x_b) \langle T_n \rangle_p + \sum_{n=1}^{N_T} a_n(x_b) \left[\frac{h_x^- h^+}{h^{+2}} \langle T'_n \rangle_p - \frac{h_x^+ h^+}{h^{+2}} \langle s T'_n \rangle_p \right] = \sum_{i=1}^{N_c} A_i \langle \cosh(B_i(1 + s)) \rangle_p, \quad p = 0, 1, \dots, N_T. \quad (2.38)$$

The left-hand side of Eq.(2.38) can be rewritten as:

$$\sum_{n=0}^{N_T} a'_n(x_b) \langle T_n \rangle_p + \sum_{n=1}^{N_T} a_n(x_b) \left[\frac{h_x^- h^+}{h^{+2}} \langle T'_n \rangle_p - \frac{h_x^+ h^+}{h^{+2}} \langle sT'_n \rangle_p \right] = 2a'_p(x_b) + \sum_{n=0}^{N_T} C_{pn} a_n(x_b), \quad p = 0, 1, \dots, N_T, \quad (2.39)$$

where $C_{pn} = \frac{m_{011} B_{p01N} + m_{111} B_{p11n}}{m_{020}}$ with $m_{011} = 2h^+ h_x^-$, $m_{111} = -2h^+ h_x^+$ and $m_{020} = h^{+2}$.

The right-hand side term is the same as in Eq.(2.29), so Eq.(2.38) can finally be rewritten as:

$$2a'_p(x_b) + \sum_{n=0}^{N_T} C_{pn} a_n(x_b) = 2 \sum_{i=1}^{N_c} A_i \frac{2}{C_p} I_p(B_i) \begin{cases} \cosh B_i & \text{if } p \text{ is even,} \\ \sinh B_i & \text{if } p \text{ is odd.} \end{cases} \quad (2.40)$$

The right-hand side of Eq.(2.40) can be analytically computed for any time t , for $p = 0, 1, \dots, N_T$. Just as for the Dirichlet boundary condition, if the incident waves cannot be decomposed as a sum of linear waves, the vertical profile of the horizontal velocity $u(x_b, s, t)$ has to be “directly” projected on the Chebyshev polynomial basis through the Gauss-Chebyshev quadrature (Eq.(2.31)).

2.2.2.3 Numerical implementation

Once the set of equations corresponding to Dirichlet or Neumann boundary conditions are derived, and in particular the associated right-hand side coefficients, the question is how to implement it. With the spectral approach in the vertical, the $N_T + 1$ coefficients of the decomposition on the Chebyshev polynomial basis have to be determined from a set of $N_T + 1$ equations. In the case of the nodes within the domain (not at the lateral boundary), the set of equations includes the projection of the main equation (Laplace equation) on the first $N_T - 2$ Chebyshev polynomials, completed with the Dirichlet boundary condition at the free surface, and the no-flux condition at the bottom.

Two initial options are considered to implement the lateral boundary conditions: the simpler option (option *A*) is to consider a set of equations consisting only of the boundary condition equations (Eq.(2.30) or Eq.(2.40)) for $p = 0, \dots, N_T$.

The second option of implementation (option *B*) is to do the same as for the interior nodes, by replacing the Laplace equation by Eq.(2.30) or Eq.(2.40) for $p = 0, \dots, N_T - 2$.

Two other options are also tested, based on the fact that the velocity potential is defined up to a

constant. In the case of option *B*, with a Dirichlet lateral boundary condition, the first $N_T - 2$ a_n coefficients are fixed leaving only two degrees of freedom through the a_n related to higher order polynomials to make the velocity potential to verify the free surface and the bottom condition. As it will be shown in the following part, this can lead to vertical oscillations in the profiles of the velocity potential. Here, the coefficient a_0 (related to the constant polynomial T_0) is left free so that the adaptation to the vertical boundary condition (particularly the free surface boundary condition) is mainly obtained through the a_0 coefficient. Thus, for the third option of implementation (option *C*), the set of equations for the node on the boundary includes Eq.(2.30) or Eq.(2.40) for $p = 1, \dots, N_T - 1$, supplemented by the free surface and the bottom boundary conditions. The last option (option *D*) only takes into account the free surface boundary condition and Eq.(2.30) or Eq.(2.40) for $p = 1, \dots, N_T$. All the four options tested for the implementation of the lateral boundary condition for wave generation are summarized in Table 2.2.

Another question concerning the implementation is the introduction of the lateral boundary condition in time. The goal here is to generate waves in a domain where the fluid is initially at rest ($\eta(x, t = 0) = 0, \tilde{\varphi}(x, t = 0) = 0$), but in linear theory, η and $\tilde{\varphi}$ have a phase difference of $\pi/2$ so when η reaches an extremum, $\tilde{\varphi}$ is zero. So, for a Dirichlet lateral boundary condition, the initial condition on $\tilde{\varphi}$ has to be set constant with a value consistent with the lateral condition. With proper initial conditions to assure the consistency with imposed lateral conditions, it is possible to apply “directly” the Dirichlet or the Neumann boundary condition at $x = x_b$. Nevertheless, it is an abrupt manner to introduce the lateral condition, and the discontinuity caused by the differences between the conditions applied at the boundary and the interior nodes can grow, causing the simulation to end prematurely or long waves can be generated that interfere with the primary wave if not absorbed properly.

One solution to reduce this phenomenon is to introduce the boundary condition progressively in time. The incident condition φ_I, u_I and η_I are multiplied by a coefficient varying linearly from 0 to 1 over a certain duration generally equal to one or two wave periods. Second solution is, instead of introducing the boundary conditions progressively in time, to introduce them progressively in space through the addition of a relaxation zone where the reference solution is given by linear wave theory.

These options for wave generation in a domain where the fluid is initially at rest are tested for regular waves propagating in deep water conditions.

option	set of equations for $x = x_b$
A	$a_p(x_b) = \langle \phi_I(x_b, s) \rangle_p \text{ for } p = 0, N_T \text{ (Dirichlet)}$ $2a'_p(x_b) + \sum_{n=0}^{N_T} C_{pn} a_n(x_b) = \langle u_I(x_b, s) \rangle_p \text{ for } p = 0, N_T \text{ (Neumann)}$
B	$a_p(x_b) = \langle \phi_I(x_b, s) \rangle_p \text{ for } p = 0, N_T - 2 \text{ (Dirichlet)}$ $2a'_p(x_b) + \sum_{n=0}^{N_T} C_{pn} a_n(x_b) = \langle u_I(x_b, s) \rangle_p \text{ for } p = 0, N_T - 2 \text{ (Neumann)}$ $\sum_{n=0}^{N_T} a_n(x_b) = \tilde{\Phi}(x_b) \text{ for } s = 1$ $\sum_{n=0}^{N_T} h^+ h_x (-1)^n a'_n(x_b) + \sum_{n=0}^{N_T} 2(1 + h_x^2) (-1)^{n-1} n^2 a_n(x_b) = 0 \text{ for } s = -1$
C	$a_p(x_b) = \langle \phi_I(x_b, s) \rangle_p \text{ for } p = 1, N_T - 1 \text{ (Dirichlet)}$ $2a'_p(x_b) + \sum_{n=0}^{N_T} C_{pn} a_n(x_b) = \langle u_I(x_b, s) \rangle_p \text{ for } p = 1, N_T - 1 \text{ (Neumann)}$ $\sum_{n=0}^{N_T} a_n(x_b) = \tilde{\Phi}(x_b) \text{ for } s = 1$ $\sum_{n=0}^{N_T} h^+ h_x (-1)^n a'_n(x_b) + \sum_{n=0}^{N_T} 2(1 + h_x^2) (-1)^{n-1} n^2 a_n(x_b) = 0 \text{ for } s = -1$
D	$a_p(x_b) = \langle \phi_I(x_b, s) \rangle_p \text{ for } p = 1, N_T \text{ (Dirichlet)}$ $2a'_p(x_b) + \sum_{n=0}^{N_T} C_{pn} a_n(x_b) = \langle u_I(x_b, s) \rangle_p \text{ for } p = 1, N_T \text{ (Neumann)}$ $\sum_{n=0}^{N_T} a_n(x_b) = \tilde{\Phi}(x) \text{ for } s = 1$

Table 2.2: Description of the four options considered to implement the lateral boundary condition for wave generation. The set of equations accounting for the node on the lateral boundary for the Laplace resolution is detailed.

2.2.2.4 Tests and analysis

To study and compare the different ways to generate waves, tests are conducted for the case of a small amplitude regular wave ($a = 0.001$ m, $L = 2$ m and $T \approx 1.132$ s) propagating in deep

water ($h = 10$ m). The wave steepness is small $2a/L = 0.1\%$, so linear theory should give a good approximation. The associated relative water depth $kh = 10\pi$ is ten times the usual limit taken for deep water conditions. For such a high relative water depth, a large value of N_T is selected to represent correctly the dispersion relation (here $N_T = 20$). The computational domain extends from $x = 0$ m to $x = 30$ m and is regularly meshed with $\Delta x = 0.02$ m ($\approx L/100$). From $x = 22$ m, a relaxation zone is applied to absorb waves arriving at the right boundary. The wave is propagated during $15 T$ with a constant time step $\Delta t = 0.01132$ s ($\approx T/100$). The steady state is not reached after $15 T$ but to have quantitative estimate of the representation of the wave by the model, an averaged absolute error is computed for η on the interval $x \in [0, 8]$ m.

Impact of the introduction in time of the lateral boundary condition

First the free surface elevation profiles at $t \approx 15T$ are compared to evaluate the impact of the introduction of the lateral boundary in time where the linear solution is used as a reference (Figure 2.8). Without a time ramp, option *A* does not work for the Dirichlet condition because a discontinuity appears at the node on the boundary inducing large derivatives that amplify and cause the simulation to blow up. Options *C* and *D* give very similar results for the Dirichlet condition with an error of $3.3 \cdot 10^{-5}$ m. Option *B* shows results with a slightly larger error of $5.9 \cdot 10^{-5}$ m. The wavelength of the first wave in the wave train is larger than the imposed wavelength. These long waves may not be well absorbed by absorption zone and create reflections in the domain. For the Neumann boundary condition, only options *A* and *B* work, giving very similar results with an error of $2.7 \cdot 10^{-5}$ m (Figure 2.8a, right). The long wave generated is smaller than that generated with Dirichlet boundary conditions. Options *C* and *D* do not work with Neumann boundary conditions because these options consist of not imposing the component of the horizontal speed component that is constant in the vertical, whose contribution may not be negligible. Hence, the imposed horizontal speed is not consistent with the wave characteristics and instabilities quickly develop. Then, applying a temporal ramp with Dirichlet boundary conditions improves the results obtained with option *B* (error $1.3 \cdot 10^{-5}$ m) but spurious oscillations with very short wavelengths appear and propagate in the domain. Option *A* still does not work, and the temporal ramp has almost no effect on the results of options *C* and *D*. For the Neumann boundary conditions both results for options *A* and *B* are improved (error $3.0 \cdot 10^{-6}$ m) and options *C* and *D* are now stable, giving similar results that are, however, quite far from the linear solution (Figure 2.8b, right). Using a relaxation zone in addition to Dirichlet or Neumann boundary conditions helps to generate stable waves. The four options of implementation of the boundary conditions work, giving very similar results for the Dirichlet condition with an error of $4.2 \cdot 10^{-6}$ m. For the Neumann condition, options *C* and *D* (error $1.8 \cdot 10^{-5}$ m) still show some small differences with options *A* and *B* (error $6.2 \cdot 10^{-6}$ m). The relaxation zone seems to dominate the wave generation in comparison with the lateral boundary conditions.

The results obtained with Dirichlet or Neumann boundary conditions do not appear qualitatively

different when looking at the free surface elevation. However, the option (A, B, C, D) of implementation for which the simulations finish without developing instabilities are different. The differences between the various implementation options are investigated in the following sections looking more particularly at the results at the boundary node $x = x_b$ when a linear ramp in time is applied.

Comparison of Dirichlet and Neumann boundary conditions with option B

The option B for the implementation of the boundary conditions is the only option producing stable simulations for both Dirichlet and Neumann conditions. In Figure 2.9, the a_n coefficients obtained at the end of the time step corresponding to $t \approx 15T$ are compared with the a_n given by the projection of the linear solution for the velocity potential on the 21 first Chebyshev polynomials (black dots). As expected, the a_n for $n = 0$ to 18 are exactly equal to those calculated with the linear solution since they are imposed. Differences are observed for the two last a_n , whose values are several orders of magnitude larger than those of the linear solution. This is a consequence of the need to satisfy the free surface and the bottom boundary conditions in addition to the Dirichlet lateral boundary condition. This leads to oscillations in the vertical profile of the velocity potential Φ (Figure 2.10, right), emphasized in the horizontal velocity u by the horizontal derivative. The two last a_n obtained with the Neumann condition also present larger values than the linear solution, but they are smaller than the ones from the Dirichlet condition. It also leads to oscillations in the vertical profile of u, w and Φ but with smaller amplitudes. Contrary to what is obtained with the Dirichlet condition, the first a_n are not rigorously equal those from the linear solution, resulting in a slightly different shape of the vertical profile of Φ (Figure 2.10, right). Thus, for option B , the largest difference between the Dirichlet and Neumann lateral boundary conditions is the fact that for the Neumann condition, the a_n related to lower orders can differ from the one from the linear solution not limiting the degrees of freedom to the two last a_n .

Comparison of options B, C and D for Dirichlet boundary conditions

In Figure 2.11, are shown the effects of the different options of implementing the Dirichlet conditions on the a_n . Options C and D produce almost the same a_n except for a_{20} , which is kept free for option C . The two main differences with option B are: (1) the value of a_0 resulting in a shift of Φ from the linear solution (Figure 2.12, right) and (2) the values of a_{19} and a_{20} lower than 10^{-8} where it is equal to 10^{-6} for option B (resulting in smaller oscillations of the u, w and Φ profiles). Even with options C and D , the horizontal velocity profile does not correspond exactly to the linear solution.

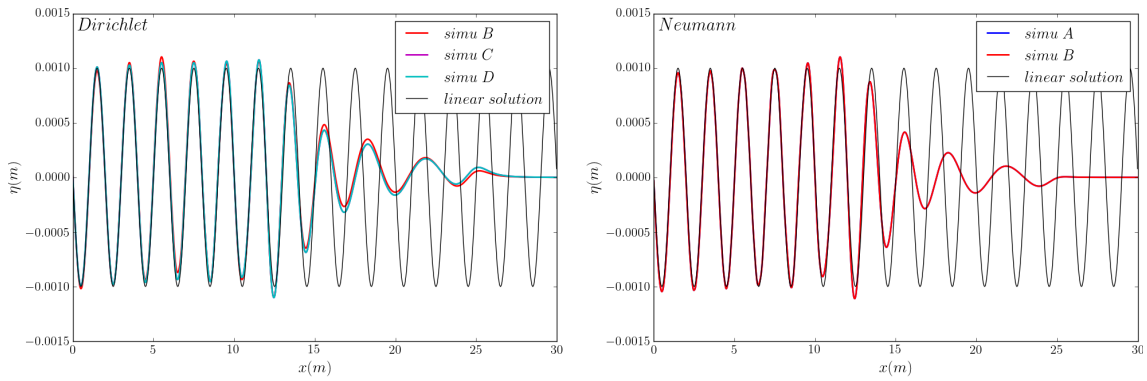
Comparison of options A and B for the Neumann boundary condition

Similarly, Figure 2.13 shows the effects of the different options of implementing the Neumann

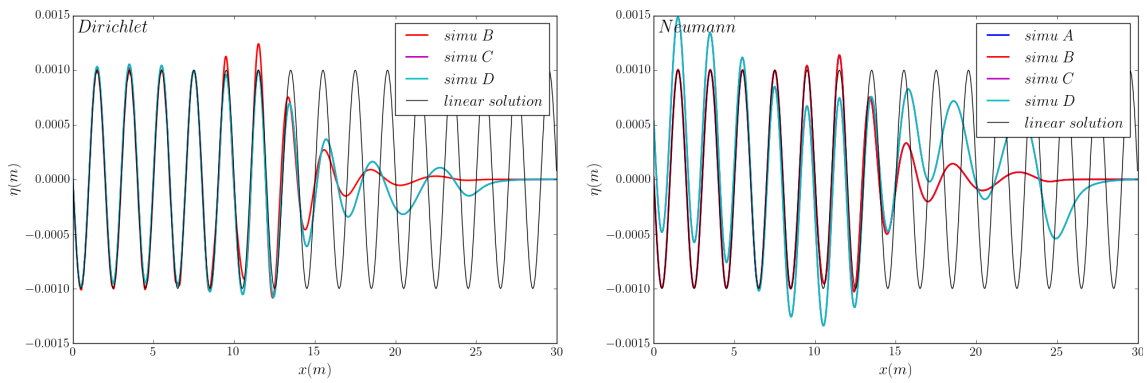
condition on the a_n . The difference between option A and B is only significant for the last two coefficients (a_{19} and a_{20}) which mainly results in larger oscillations of the Φ and u (in particular for option B) profiles. Even for option A , the a_n coefficients are not equal to those of the linear solution, indicating that the wave that propagates is not exactly a linear wave. This may be due to the propagation of an additional long wave involuntarily generated. The vertical profile of the horizontal velocity for option B has larger oscillations than the one obtained with option A . Nevertheless, the free surface profiles are very similar, because η and $\tilde{\Phi}$ and their propagation in time depend on the vertical velocity at the free surface \tilde{w} , which is very similar for both options.

Conclusion

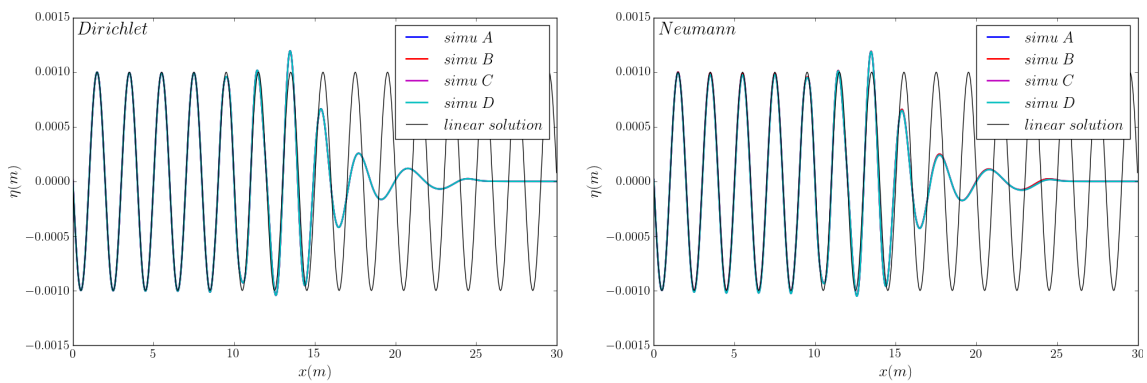
When applying a relaxation zone for the wave generation, similar results for the vertical profiles of u , v , and Φ are obtained. The four options (A , B , C and D) of implementation of the lateral boundary condition lead to nearly the same evolution of the free surface elevation. The effect of the relaxation zone dominates over the lateral boundary condition. Therefore, in the following test cases (unless otherwise specified), Dirichlet lateral boundary conditions are implemented with option B to generate waves, with a relaxation zone usually one wavelength long. For irregular wave cases, the wavelength is calculated using the peak frequency.



(a) without time ramping condition



(b) with a linear time ramping condition



(c) with a relaxation zone of one wavelength

Figure 2.8: Free surface elevation profile after 1500 time steps ($15T$). Comparison of the three methods to introduce the boundary condition in time, for the four implementation options (A , B , C , D), for Dirichlet boundary condition (left) and Neumann boundary conditions (right).

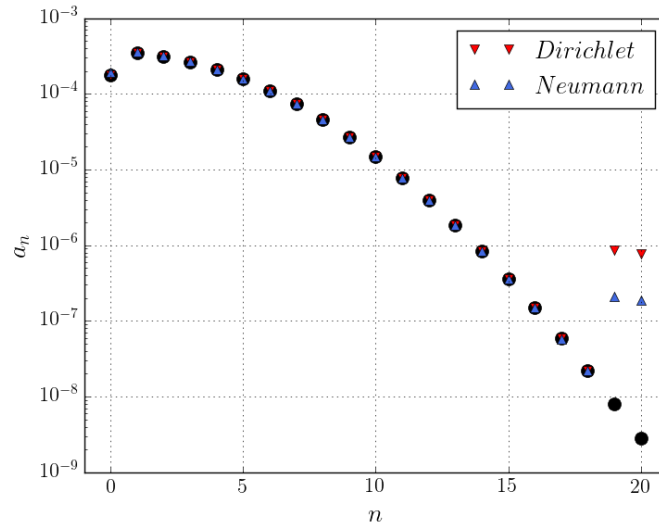


Figure 2.9: Comparison of the a_n coefficients computed at $t \approx 15T$, at $x = x_b$, for Dirichlet boundary conditions (red triangles) and Neumann boundary conditions (blue triangles). The coefficients corresponding to the linear potential expanded on the Chebyshev polynomial basis are presented for reference (black dots).

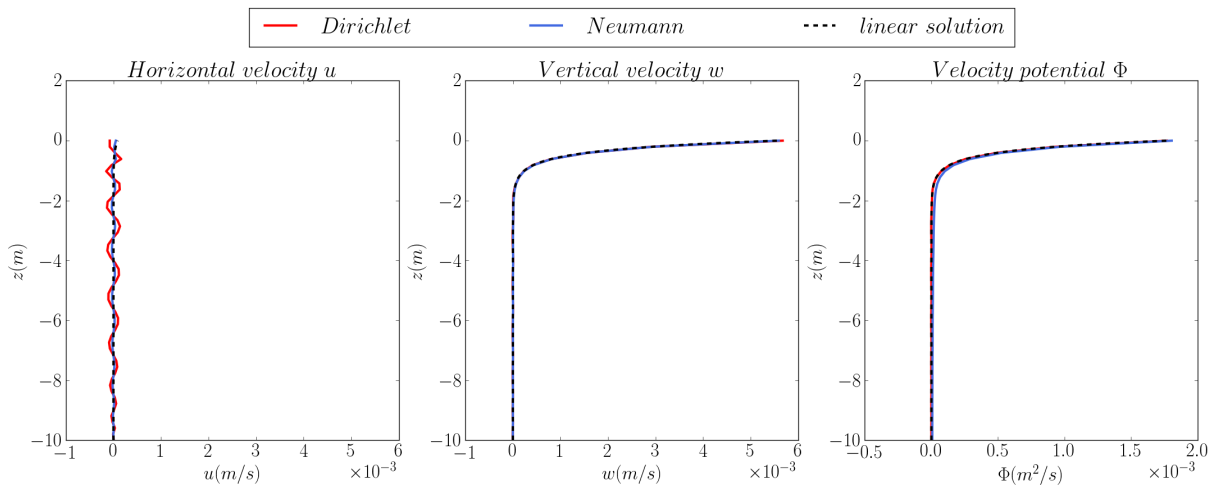


Figure 2.10: Comparison of the horizontal u and vertical w velocity profiles together with the velocity potential profile computed at $t \approx 15T$, at $x = x_b$, for Dirichlet boundary conditions (red) and Neumann boundary conditions (blue). The linear solution is presented for reference (black dashed line).

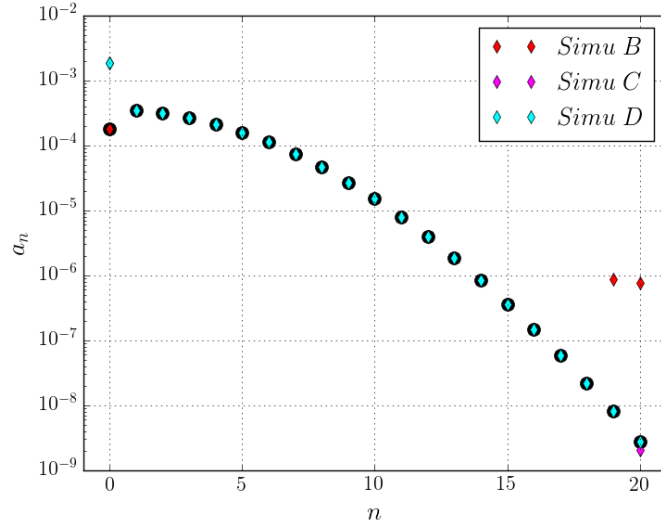


Figure 2.11: Comparison of the a_n coefficients computed at $t \approx 15T$, at $x = x_b$, for Dirichlet boundary conditions for options *B*, *C* and *D*. The coefficients corresponding to the linear potential expanded on the Chebyshev polynomial basis are presented for reference (black dots).

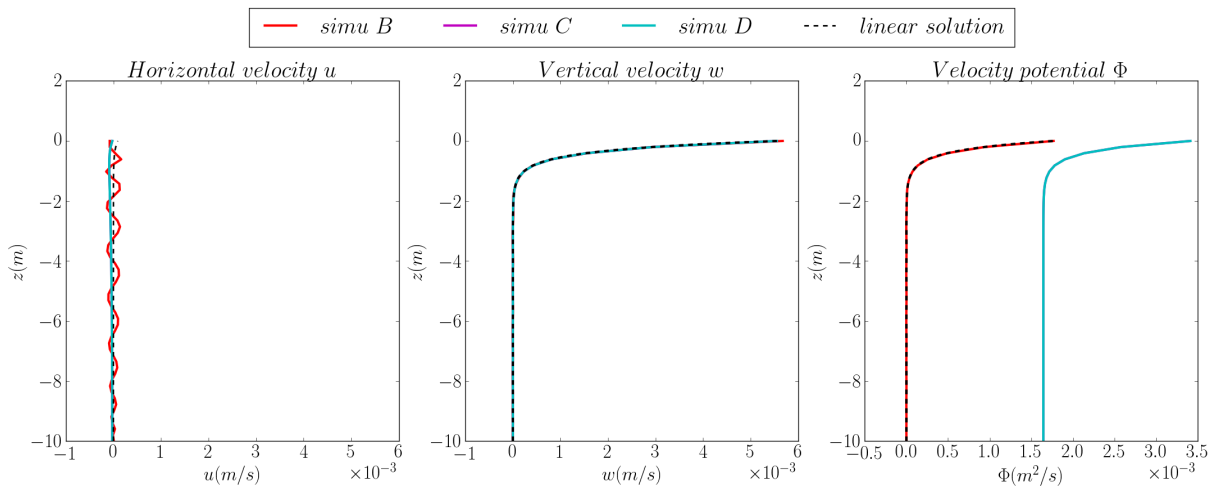


Figure 2.12: Comparison of the horizontal u and vertical w velocity profiles together with the velocity potential profile computed at $t \approx 15T$, at $x = x_b$, for Dirichlet boundary conditions for options *B*, *C* and *D*. The linear solution is presented for reference (black dashed line).

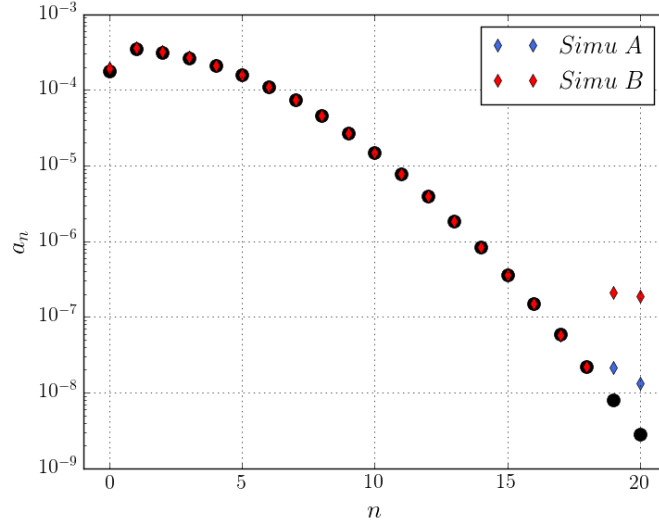


Figure 2.13: Comparison of the a_n coefficients computed at $t \approx 15T$, at $x = x_b$, for Neumann boundary conditions for options A and B . The coefficients corresponding to the linear potential expanded on the Chebyshev polynomial basis are presented for reference (black dots).

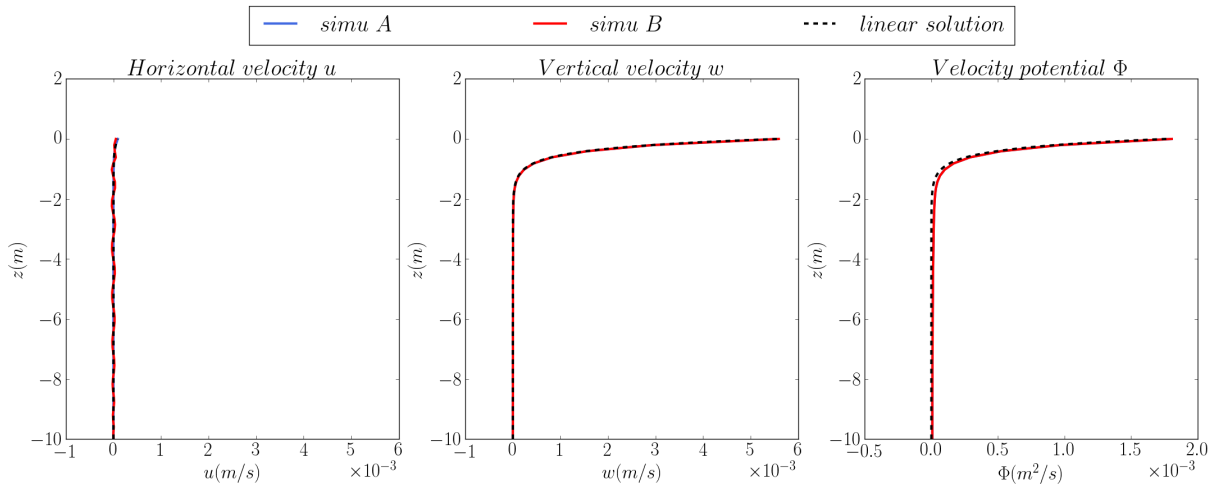


Figure 2.14: Comparison of the horizontal u and vertical w velocity profiles together with the velocity potential profile computed at $t \approx 15T$, at $x = x_b$, for Neumann boundary conditions for options A and B . The linear solution is presented for reference (black dashed line).

Chapter 3

Validation of the 1DH version of the model

Ce chapitre est consacré à la validation de la version 1DH du modèle à travers l'application à six cas tests. Tout d'abord, la version linéaire du modèle est utilisée pour simuler la réflexion et la transmission de vagues régulières lors de leur propagation au-dessus d'un profil bathymétrique défini par [Roseau \(1976\)](#), pour lequel une solution analytique est disponible. Ensuite, une étude de convergence approfondie, menée pour les trois paramètres numériques Δt , Δx et N_T , dans le cas d'une onde solitaire se propageant sur une longue distance, permet de montrer que les ordres de convergence en temps et en espace sont cohérents avec le schéma de Runge-Kutta d'ordre 4 utilisé pour l'intégration en temps et le schéma aux différences finies d'ordre 4 en espace pour la discrétisation des dérivées horizontales. La convergence exponentielle avec le paramètre N_T due à l'approche spectrale appliquée dans la direction verticale est également mise en évidence. Finalement, le modèle est comparé à des données expérimentales pour des cas de propagation de vagues non-déferlantes: la dynamique non-linéaire des composantes libre et liée de la seconde harmonique lors de la génération d'un train d'ondes par un générateur de vague de type piston ([Chapalain et al., 1992](#)), la génération de vagues par un mouvement impulsif du fond ([Hammack, 1973](#)), la propagation de vagues régulières au-dessus d'une barre submergée ([Dingemans, 1994](#)) et la propagation de vagues irrégulières au-dessus d'une plage présentant un haut-fond ([Becq-Girard et al., 1999](#)). L'ensemble de ces cas tests permet de montrer que le modèle est capable de représenter précisément les effets non-linéaires et dispersifs de génération et propagation d'harmoniques d'ordres supérieurs ainsi que les transferts d'énergie entre ces différentes composantes.

This chapter is devoted to the validation of the 1DH version of the model, with a series of six test cases.

The model is first validated by comparing the simulation results of the linear version to analytical solutions of the linearized problem for the reflection of regular waves propagating over a particular bathymetric profile proposed by [Roseau \(1976\)](#). Secondly, an advanced study of convergence is carried out for the case of a nonlinear solitary wave propagating over a flat bottom, for the three numerical parameters Δt , Δx and N_T controlling the accuracy of the solution. The model is then compared with measurements from four laboratory experiments of non-breaking waves: nonlinear dynamics of free and bound second-order components in a wave train generated by a piston-type wave maker in constant water depth ([Chapalain et al., 1992](#)), wave generation from an impulsive upthrust of the bottom ([Hammack, 1973](#)), propagation of a regular waves over a submerged bar ([Dingemans, 1994](#)), and propagation of irregular waves over a barred beach ([Becq-Girard et al., 1999](#)).

The majority of these test cases were presented in journal papers or conference proceedings. Case 2 (solitary waves) was presented at the conference Journées Nationales Génie Côtier Génie Civil 2014 in Dunkerque, while the third case was presented at the ICCE conference 2014 in Seoul ([Benoit et al., 2014](#)), and the last three test cases were published in Coastal Engineering ([Raoult et al., 2016](#)).

3.1 Reflection of linear waves propagating over Roseau-type bathymetric profile

In [Roseau \(1976\)](#), the propagation of gravity waves in a infinite channel of variable depth $h(x)$ is studied using the linear potential flow theory, in one horizontal dimension (x, z) . The bathymetry varies between two flat regions h_0 (for $x \rightarrow -\infty$) and h_1 (for $x \rightarrow +\infty$) with $h_0 > h_1$. Monochromatic waves are considered, with angular frequency ω . The motion is described by the velocity potential $\Phi(x, z, t) = Re[\phi(x, z)e^{i\omega t}]$ where ϕ satisfies the Laplace equation in the fluid domain, and a mixed condition at the (linearized) free surface ($z = 0$), and an impermeable boundary condition at the bottom ($z = -h(x)$):

$$\left\{ \begin{array}{ll} \phi_{xx} + \phi_{zz} = 0 & \text{for } -\infty < x < +\infty \text{ and } -h(x) \leq z \leq 0 \quad (3.1a) \\ -\frac{\omega^2}{g}\phi + \phi_z = 0 & \text{at } z = 0 \quad (3.1b) \\ h_x\phi_x + \phi_z = 0 & \text{at } z = -h(x) \quad (3.1c) \end{array} \right.$$

The fluid domain (x, z) is transformed using conformal mapping ($Z = F(\zeta)$) into a rectangular domain in the (ξ, χ) -plane, where $Z = x + iz$ and $\zeta = \xi + i\chi$. Thus $z = 0$ becomes $\chi = 0$, and $z = -h(x)$ becomes $\chi = -1$. The boundary value problem expressed in the (ξ, χ) -plane for $\varphi(\xi, \chi) = \phi(x, z)$ is then written as:

$$\left\{ \begin{array}{ll} \varphi_{\xi\xi} + \varphi_{\chi\chi} = 0 & \text{for } -\infty < \xi < +\infty \text{ and } -1 \leq \chi \leq 0 \quad (3.2a) \\ -\frac{\omega^2}{g}F'(\xi)\varphi + \varphi_\chi = 0 & \text{at } \chi = 0 \quad (3.2b) \\ \varphi_\chi = 0 & \text{at } \chi = -1 \quad (3.2c) \end{array} \right.$$

The choice of the conformal mapping function is important in the definition of the problem since it determines the family of the bottom topography in the (x, z) -plane that can be mapped. Here, the conformal mapping function is (following [Roseau \(1976\)](#)):

$$F(\zeta) = h_0 \left(\zeta + \frac{\epsilon - 1}{\pi\beta} \ln \left(1 + e^{\beta\pi\zeta} \right) \right), \quad (3.3)$$

where the parameter $\beta \in]0, 1[$, $\epsilon \in]0, 1[$ since it is assumed that $h_0 > h_1$, and $\epsilon = h_1/h_0$ is the far field depth ratio. This conformal mapping corresponds to a bottom profile varying smoothly from the depth h_0 to h_1 . The width of the transition zone is controlled by the parameter β . The bed slope steepens when β increases. Thus the bottom profile is defined by the two non dimensional quantities ϵ and β .

The bottom elevation is defined parametrically using the conformal mapping function $F(\zeta)$ for ξ describing $] -\infty, +\infty[$:

$$\begin{cases} \frac{x(\xi)}{h_0} = \operatorname{Re} \left[\frac{1}{h_0} F(\xi - i) \right] = \xi - \frac{1 - \epsilon}{\beta \pi} \operatorname{Re} \left[\ln \left(1 + e^{\beta \pi (\xi - i)} \right) \right], \\ \frac{y(\xi)}{h_0} = \operatorname{Im} \left[\frac{1}{h_0} F(\xi - i) \right] = -1 - \frac{1 - \epsilon}{\beta \pi} \operatorname{Im} \left[\ln \left(1 + e^{\beta \pi (\xi - i)} \right) \right]. \end{cases}$$

This particular form of the mapping was chosen by [Roseau \(1976\)](#) because it gives an explicit and exact expression for the modulus of the reflection coefficient R due to the bottom transition:

$$R = \left| \frac{\sinh \left(\frac{k_0 h_0 - k_1 h_1}{\beta} \right)}{\sinh \left(\frac{k_0 h_0 + k_1 h_1}{\beta} \right)} \right|, \quad (3.4)$$

where k_i are calculated from the linear dispersion relation $\omega^2 = g k_i \tanh(k_i h_i)$.

The transmission coefficient T is obtained by conserving the energy flux:

$$T = \frac{\cosh(k_1 h_1)}{\cosh(k_0 h_0)} \sqrt{(1 - R^2) \frac{2k_0 h_0 + \sinh(2k_0 h_0)}{2k_1 h_1 + \sinh(2k_1 h_1)}}. \quad (3.5)$$

To study the accuracy of Misthyc for the representation of wave propagation over a bottom profile with a sharp transition between two flat regions of different depths, the linear version of the code is applied to two bathymetric profiles. The choice was made to use the linear version of Misthyc to compare to [Roseau \(1976\)](#)'s analytical results. The first bottom profile is defined by $\epsilon = 1/3$ and $\beta = 0.25$ and the second profile presents a sharper transition for a larger "step" with $\epsilon = 0.1$ and $\beta = 0.5$ (Figure 3.1).

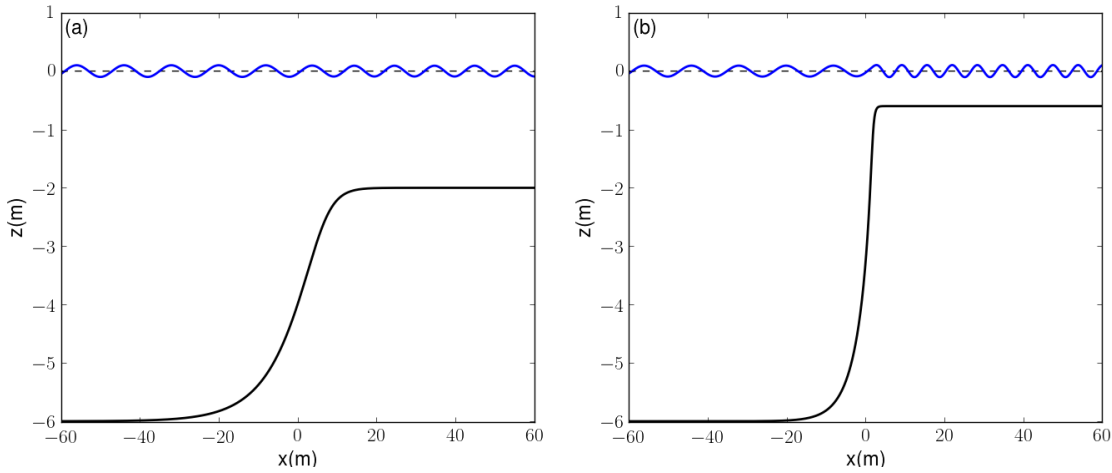


Figure 3.1: Bottom profiles and snapshots of free surface elevation (at an arbitrary time) for the two sets of (ϵ, β) considered: (a) $\epsilon = 1/3$ and $\beta = 0.25$, and (b) $\epsilon = 0.1$ and $\beta = 0.5$.

The reflection and transmission properties depend on the wave frequency. Two conditions for the incident wave are therefore considered: one corresponding to a small relative water depth ($k_0 h_0 \approx 0.87$), and a second one corresponding to deep water condition ($k_0 h_0 = 3.14$). The impact of the bathymetric variation on wave propagation is expected to be more important in the case with smaller relative depth. Nevertheless, the case with larger relative water depth is more challenging. Finally, four configurations are tested, the corresponding parameters are shown in Table 3.1.

case	Wave characteristics				Bottom	
	T (s)	L (m)	$k_0 h_0$	$k_1 h_1$	ϵ	β
1	6.28	43.27	0.87	0.47	1/3	0.25
2	2.78	12	3.14	1.23	1/3	0.25
3	6.28	43.27	0.87	0.25	0.1	0.5
4	2.78	12	3.14	0.59	0.1	0.5

Table 3.1: Physical parameters for the four simulations of regular waves propagating over a Roseau-type bottom profile.

Athanassoulis and Belibassakis (1999) (hereafter A&B1999) proposed an extension of the mild slope equation to study the propagation of linear waves over a variable bathymetry using a variational formulation of the linear wave problem. At each horizontal position, the velocity potential is described by the vertical eigenfunctions associated with the propagating mode and all of the evanescent modes. An additional mode is introduced to satisfy the bottom boundary condition exactly. Simulations of the four cases are also made with this model (Matlab version of the code presented in A&B1999, provided by Pr. K. Belibassakis) to compare with the Misthyc simulation results.

For the simulations, the domain is regularly meshed with $\Delta x = 0.4$ m ($\approx L/108$) for the longer wave and $\Delta x = 0.1$ m ($\approx L/120$) for the shorter wave. The origin of the horizontal axis is taken where the bottom elevation is $z = -(h_0 + h_1)/2$. Waves are generated at the left end of the domain in a relaxation zone that is two wavelength long. The right end of the domain is extended so that the waves never reach the boundary to avoid reflections on the right side where an impermeable boundary condition is imposed. The time step is chosen so that $CFL \approx 1$ with $CFL = \frac{C_0 \Delta t}{\Delta x}$ for $C_0 = L_0/T$, which gives $\Delta t = 0.057$ s and $\Delta t = 0.023$ s, for the longer and shorter waves respectively. Waves are propagated during a period long enough to reach a steady state over the zone encompassing the bottom transition. The vertical resolution is set to $N_T=7$. This choice of N_T is validated by the convergence study of the reflection and transmission coefficient as a function of N_T for cases 3 and 4 (presented below). The same horizontal discretization of the domain was used for the coupled-mode model of A&B1999 and 5 modes were found to be sufficient to represent accurately the vertical variation of the velocity potential.

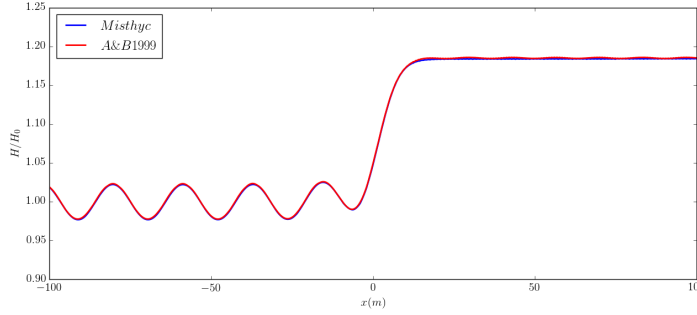
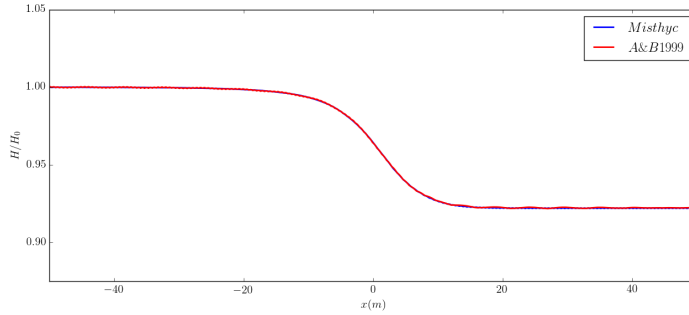
(a) case 1 : $\epsilon = 1/3$, $\beta = 0.25$ and $k_0 h_0 = 0.87$ (b) case 2 : $\epsilon = 1/3$, $\beta = 0.25$ and $k_0 h_0 = 3.14$

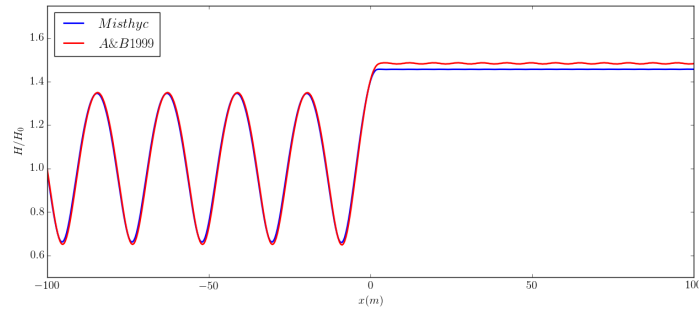
Figure 3.2: Normalized wave height profiles for cases 1 and 2, for the first bathymetric profile ($\epsilon = 1/3$, $\beta = 0.25$). Comparison between Misthyc (blue) linear version with $N_T = 7$ and the coupled-mode model of Athanassoulis and Belibassakis (1999) (red).

Once the steady state is obtained, the wave height is computed from free surface elevation time-series at each node in the domain. The wave height profiles are compared with those obtained with the coupled-mode model of A&B1999 (Figures 3.2 and 3.3). For the four cases with different physical parameters, both models give comparable results. They produce the same oscillation pattern of the wave height before the transition caused by the reflection at the transition except for case 2 where the reflection is very small and hardly visible (Figure 3.2b). The incident wave height H_I is modulated because of its interaction with the reflected wave (H_R) traveling in the opposite direction. After the bathymetric transition, the wave height becomes homogeneous, and is denoted as H_T . Small differences are mainly visible for case 3 (Figure 3.3a) where the model of A&B1999 gives a higher transmitted wave height than Misthyc. On the contrary, for case 4 (Figure 3.3b), the wave height profile from the Misthyc simulations is slightly shifted vertically, showing larger wave heights than A&B1999.

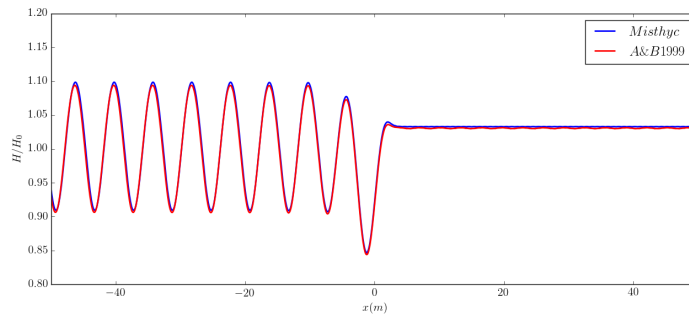
From the wave height profile, the reflection (R) and transmission (T) coefficients can be calculated as:

$$R = \frac{H_R}{H_I} = \frac{H_{max} - H_{min}}{H_{max} + H_{min}} \quad \text{and} \quad T = \frac{H_T}{H_I}$$

where H_{max} and H_{min} are the extremum values reached by the wave profile before the bottom



(a) case 3 : $\epsilon = 0.1$, $\beta = 0.5$ and $k_0 h_0 = 0.87$



(b) case 4 : $\epsilon = 0.1$, $\beta = 0.5$ and $k_0 h_0 = 3.14$

Figure 3.3: Normalized wave height profiles for cases 3 and 4, for the second bathymetric profile ($\epsilon = 0.1$, $\beta = 0.5$). Comparison between Misthyc (blue) linear version with $N_T = 7$ and the coupled-mode model of Athanassoulis and Belibassakis (1999) (red).

transition.

A convergence study of these two coefficients as a function of N_T was carried out for cases 3 and 4 with the more reflective bottom profile ($\epsilon = 0.1$ et $\beta = 0.5$). For both cases, the values obtained for the reflection and transmission coefficients appear to have converged (Figure 3.4 and Figure 3.5, respectively) for $N_T = 6$, validating the choice of $N_T = 7$ in the previous simulations.

The reflection and the transmission coefficients are then compared with those obtained with the model of A&B1999 and those obtained with the analytical expression Eq.(3.4) and Eq.(3.5) (Table 3.2). The reflection coefficient for case 2 was too small (only about 0.005%) to be determined accurately from the wave height profile obtained with Misthyc using the method described above. For the first bathymetric profile, both models produce coefficients close to the analytical ones. For the second bathymetric profile, Misthyc shows more accurate results for long waves, whereas the model of A&B1999 is more accurate for short waves.

This first test case shows that the linear version of the model (with $N_T = 7$) reproduces well the reflection and transmission phenomena occurring when waves propagate over a steep transition between two flat regions. Some differences with the analytical solution are obtained for the steepest slope for the smallest wavelength, but the differences remain small.

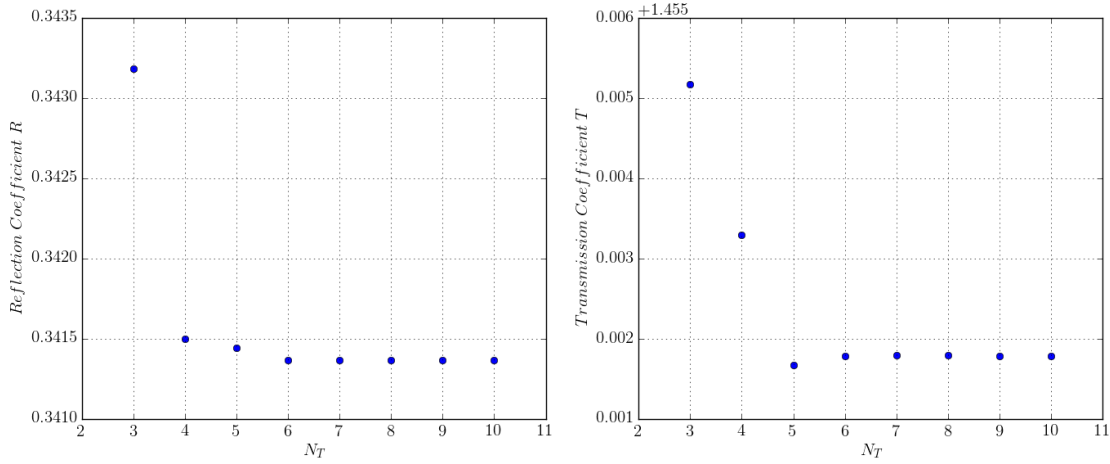


Figure 3.4: Convergence with N_T of the reflection coefficient (R) and the transmission coefficient (T) obtained with Misthyc for case 3.

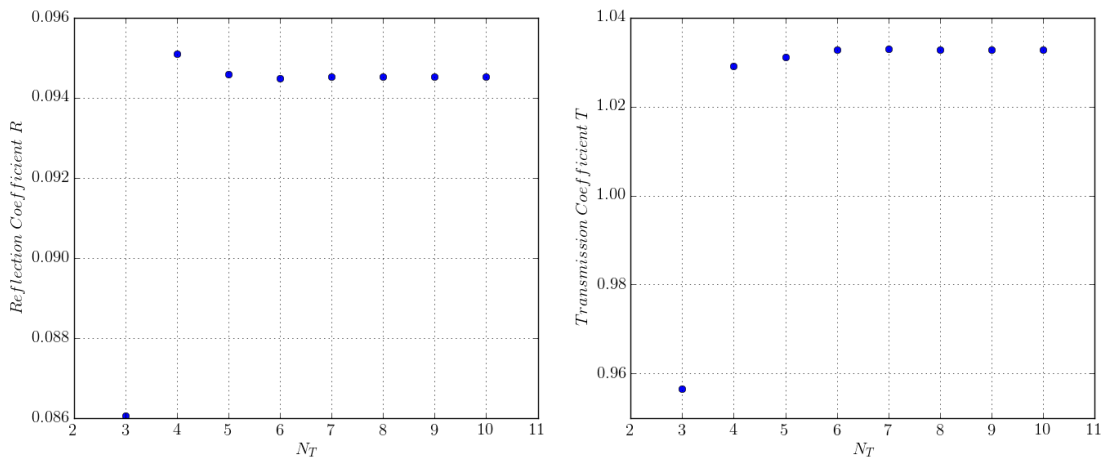


Figure 3.5: Convergence with N_T of the reflection coefficient (R) and the transmission coefficient (T) obtained with Misthyc for case 4.

case	Analytical results		Misthyc		A&B1999	
	R	T	R	T	R	T
1	0.02282	1.185	0.02273	1.184	0.02262	1.185
2	0.000051	0.9221	X	0.9222	0.00011	0.9222
3	0.3413	1.452	0.3414	1.457	0.3497	1.482
4	0.09428	1.029	0.09453	1.033	0.09415	1.030

Table 3.2: Analytical and simulated (with Misthyc and with the coupled-mode model of Athanassoulis and Belibassakis (1999)) reflection and transmission coefficients for the four cases of regular wave propagating over Roseau bathymetry profile. The reflection coefficient for case 2 was too small to be determined accurately from the wave height profile obtained with Misthyc.

3.2 Solitary wave propagation over a flat bottom

3.2.1 Objectives

The goal of this test case is to propagate a solitary wave over a flat bottom over a long distance with minimum distortion or phase difference.

Solitary waves, which are composed of a single hump of water, are a particular solution of a set of mathematical models. They propagate with constant shape and celerity as a result of balance between the effects of dispersion and nonlinearity. The expression and form of a solitary wave is closely related to the selected mathematical model, and different mathematical systems such as the Korteweg-De Vries (KdV) equations, various formulations of Boussinesq, Serre, or Green-Naghdi equations, etc. exhibit different solitary wave profiles.

Solitary waves are also a particular solution of the Euler equations with nonlinear free surface boundary conditions in the constant depth case. The expression of the wave can not be given in closed analytical form, but it can be computed with high accuracy using specific numerical algorithms (see e.g. [Tanaka \(1986\)](#), [Clamond and Dutykh \(2013\)](#))

Solitary waves are characterized by a single parameter, the nondimensional height $\delta = H/h$, which is the ratio of the wave height (H) to the water depth (h). In this study, three values of δ are investigated, from the least nonlinear to the most nonlinear: $\delta = 0.3, 0.5$, and 0.7 .

3.2.2 Description

3.2.2.1 Model domain and numerical parameters

In these tests, the water depth is uniform ($h = 1$ m) and the horizontal length of the model domain (L_x) is $700h$ ($= 700$ m). The horizontal domain extends from $x/h = -25$ to $x/h = 675$, and the solitary wave is initially centered at $x/h = 0$ (e.g. [Figure 3.6](#)). The height H of each solitary wave is determined from $\delta = H/h = 0.3, 0.5$ or 0.7 .

The horizontal domain consists of a regularly-spaced mesh of size Δx , and the simulations are advanced in time with a fixed time step Δt . The spatial and temporal discretizations are controlled by the parameters M_x and M_t , respectively, such that $\Delta \tilde{x} \equiv \Delta x/h \equiv 1/M_x$ and $\Delta \tilde{t} \equiv \Delta t \sqrt{g/h} = 1/M_t$.

Each wave is propagated during a nondimensional time $\tilde{T} \equiv T \sqrt{g/h}$ set to $\tilde{T} = 500$, corresponding to a physical time $T \approx 159.64$ s. The distance traveled by the wave at the end of the simulation (d) is theoretically $d = CT$, where C is the speed of the solitary wave. The wave thus covers a nondimensional distance $\tilde{d} \equiv d/h = F\tilde{T}$, where F is the Froude number defined as $F \equiv C/C_0$, with $C_0 = \sqrt{gh}$. Depending on the value of δ , this corresponds to d varying between about $569h$ ($\delta = 0.3$) and $639h$ ($\delta = 0.7$).

The CFL number is defined here as $\text{CFL} \equiv C_0 \Delta t / \Delta x$, which can be rewritten as $\text{CFL} = M_x / M_t$.

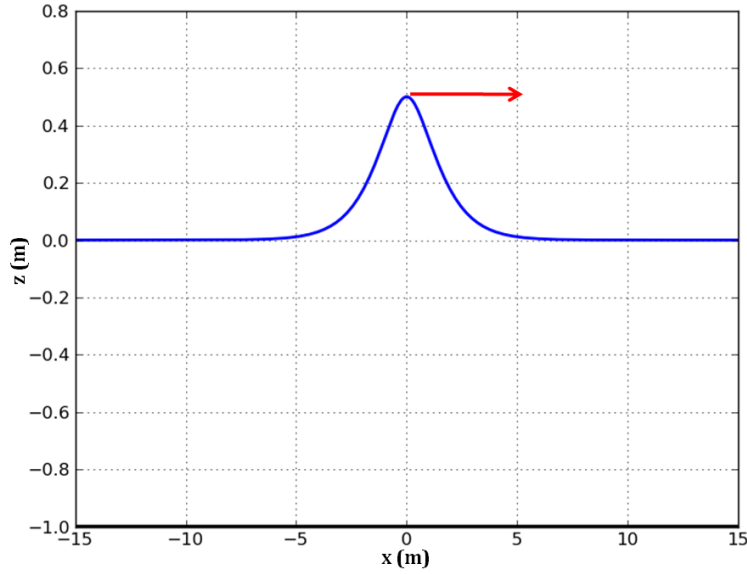


Figure 3.6: Bathymetry and free surface profile at $\tilde{t} = 0$ for a solitary wave with nondimensional height $\delta = 0.5$ (the intermediate nonlinear case).

3.2.2.2 Boundary conditions

In the vertical, the bottom boundary condition is a fixed, impermeable bottom at $z = -h$ (constant depth). The lateral boundary conditions are impermeable vertical walls at the domain extremities ($x/h = -25$ and $x/h = 675$).

3.2.2.3 Initial conditions

To initialize the model, it is necessary to calculate the free surface elevation (η) and the free surface velocity potential ($\tilde{\phi} = \phi|_{z=\eta}$) corresponding to the Euler equations with nonlinear boundary conditions at the surface. The algorithm of [Clamond and Dutykh \(2013\)](#) is adapted to calculate these parameters and the Froude number F using the nondimensional height δ as an input parameter.

3.2.3 Simulations and evaluation criteria

3.2.3.1 Simulation parameters

The ability of the model to simulate accurately the propagation of a solitary wave depends on the horizontal spacing of the model grid (characterized by Δx or M_x), time step size (characterized by Δt or M_t), and the maximum order N_T of the Chebyshev polynomials used to resolve the vertical variations.

To evaluate the impact of these parameters on the simulation results, three convergence studies were carried out:

1. convergence as a function of the size of the time step, with M_t varying from 4 to 12 ($M_x = 10$ and $N_T = 7$ held constant),
2. spatial convergence at a constant CFL number with M_x varying from 5 to 30, (CFL = 1.25 and $N_T = 7$ held constant), and
3. convergence as a function of the maximum order of the Chebyshev polynomials with N_T varying from 3 to 15 ($M_x = 10$ and $M_t = 8$ held constant).

3.2.3.2 Quantities analyzed from model results

The performance of the model is evaluated as a function of four quantities that can be computed at each time step:

1. the total volume of the fluid domain (V),
2. the total mechanical energy of the fluid domain (E),
3. the solitary wave crest height (η_{max}),
4. the phase difference, or difference between the simulated and theoretical wave crest positions x_{max} (as $\eta_{max} = \eta(x_{max})$).

The simulated wave crest height (η_{max}) and position (x_{max}) do not in general occur at grid points. Therefore, they are estimated by fitting a quadratic polynomial to node with the maximum free surface elevation and the two neighboring nodes.

3.2.3.3 Errors as a function of time

The first three quantities should be conserved during the simulation, and relative errors are calculated in comparison to the values at the initial time:

$$Err_{Y(t)} = \frac{Y(t) - Y_0}{Y_0},$$

where $Y = V, E, \eta_{max}$.

The phase difference at time t is calculated by comparing the simulated wave crest position to the theoretical wave crest position calculated using the wave celerity given by the algorithm of [Clamond and Dutykh \(2013\)](#):

$$Err_{phase(t)} = \left| \frac{x_{max}(t) - Ct}{Ct} \right|.$$

3.2.3.4 Global errors

As described above, errors in four different quantities are calculated as a function of time during the simulation period. Global errors are then defined to quantify the total error for each simulation.

For the temporal and horizontal step size convergence tests, global volume and energy errors are calculated as the arithmetic mean of the relative volume and energy evolution:

$$Errr_Y = \left| \left\langle \frac{Y(t) - Y_0}{Y_0} \right\rangle_t \right| = \left| \frac{\langle Y(t) \rangle_t - Y_0}{Y_0} \right|,$$

where $\langle Y(t) \rangle_t = \frac{1}{NDT} \sum_{i=1}^{NDT} Y(t_i)$, NDT is the number of time steps, and $Y = E$ or V .

The wave amplitude and phase errors are calculated relative to the initial amplitude and to the theoretical position of the wave at the end of the simulation (at $t = T$):

$$Errr_{ampl} = \left| \frac{\eta_{max}(T) - H}{H} \right|, \quad Errr_{phase} = \left| \frac{x_{max}(T) - CT}{CT} \right|.$$

For the vertical convergence tests, the maximum order N_T of the Chebyshev polynomial is varied from $N_T = 3$ to 15, and the relative error is calculated using the results of the simulation with the highest order as the reference value (here $N_T = 15$). In this case, the relative volume and energy errors are given by:

$$Errr_Y = \left| \frac{\langle Y(t) \rangle_t - \langle Y_{15}(t) \rangle_t}{\langle Y_{15}(t) \rangle_t} \right|,$$

where $Y = E$ or V . Likewise, the relative wave amplitude and wave errors at the final time step are defined as:

$$Errr_{ampl} = \left| \frac{\eta_{max}(T) - \eta_{max15}(T)}{\eta_{max15}(T)} \right|, \quad Errr_{phase} = \left| \frac{x_{max}(T) - x_{max15}(T)}{x_{max15}(T)} \right|.$$

3.2.4 Results

The simulation results are evaluated with respect to the convergence as a function of the time step Δt , horizontal grid spacing Δx , and maximum order of the Chebyshev polynomial N_T for three relative wave heights $\delta = 0.3, 0.5, \text{ and } 0.7$. The efficiency of the model is also evaluated by quantifying the dependence of the CPU time on these three parameters.

3.2.4.1 Convergence as a function of the time step Δt

For these simulations, the horizontal and vertical resolution are held constant, with $M_x = 10$ and $N_T = 7$. M_t is varied from 12 to 4, giving a time step varying in the range $\Delta t \approx 0.0266 - 0.0798$ s, corresponding to a CFL number ranging from 0.8333 to 2.5 (Table 3.3).

M_t	$\Delta \tilde{t}$	$\Delta t(s)$	CFL
12	$1/12 \approx 0.0833$	≈ 0.0266	$5/6 \approx 0.833$
10	$1/10 = 0.1$	≈ 0.0319	1
8	$1/8 = 0.125$	≈ 0.0399	1.25
7	$1/7 \approx 0.143$	≈ 0.0456	≈ 1.429
6	$1/6 \approx 0.167$	≈ 0.0532	≈ 1.667
5	$1/5 = 0.2$	≈ 0.0639	2
4	$1/4 = 0.25$	≈ 0.0798	2.5

Table 3.3: Selected time steps Δt and associated quantities for convergence runs as a function of Δt ($M_x = 10$ and $N_T = 7$)

Final free surface profiles. The free surface profile at end of the simulation ($\tilde{T} = 500$) are plotted in Figure 3.7 for the three values of nonlinearity. For the least nonlinear case ($\delta = 0.3$), varying the time step within this range of values has only a small impact on the wave crest height and phase difference at the end of the simulation (Figure 3.7(a)), and the four presented curves ($M_t = 4, 6, 8, 12$) are nearly superimposed on the reference solution.

For the more nonlinear cases, a decrease in the wave crest height is observed at the end of the simulations for larger time steps (e.g. $M_t = 4, 5$ in Figure 3.7(b) and $M_t = 5, 6, 8$ in Figure 3.7(c)). In addition, phase differences, caused by an underestimation of the wave celerity (which is directly related to the underestimation of the wave height), are also observed for these cases.

As a function of the time step, the more nonlinear waves require a smaller time step to represent accurately the wave height and propagation speed. For the case with $\delta = 0.7$ (Figure 3.7(c)), there is a small phase and wave height difference in comparison to the reference solution even for the smallest tested time step ($\Delta t \approx 0.0266$ s for $M_t = 12$).

All simulations were stable for the length of the simulation period ($\tilde{T} = 500$), except for the case with $\delta = 0.7$ and CFL = 2.5, which became unstable before reaching the end.

Conservation of volume and energy. Energy and volume are conserved well during the simulations with the smallest errors for the smallest time steps. Both quantities decrease monotonically throughout the simulation period, with a more rapid decrease for larger time steps (Figure 3.8). For the largest time step, the final relative volume errors are of the order 10^{-11} , 10^{-8} and 10^{-6} , and the final relative energy errors are of the order 10^{-3} , 10^{-2} , and 10^{-2} for $\delta = 0.3$, $\delta = 0.5$ and $\delta = 0.7$, respectively.

Evolution of global errors as a function of the time step. To summarize the convergence properties as a function of the time step, the four global errors are calculated for each simulation. All four measures (relative volume, energy, phase, and amplitude) of simulation errors increase both with increasing time step size and with increasing relative wave height (Figure 3.9), with algebraic convergence rate. The slopes of the linear regression curves are similar for each test case, ranging from 4 to 5 for $\delta = 0.3$ and $\delta = 0.5$, and 3.3-4.1 for $\delta = 0.7$, the most nonlinear test case. These values are in agreement with the fourth-order Runge-Kutta temporal integration scheme used in the model, demonstrating the fourth-order, algebraic temporal convergence of the model.

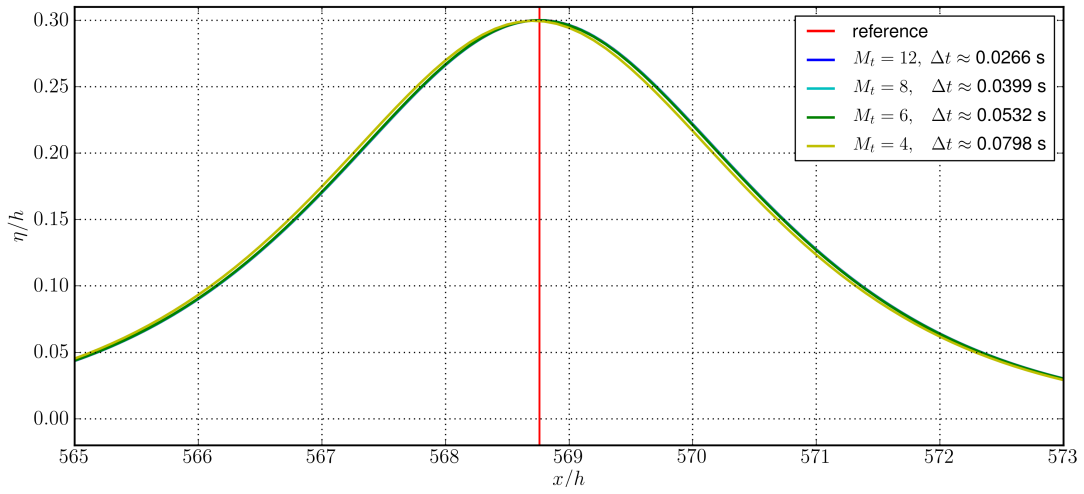
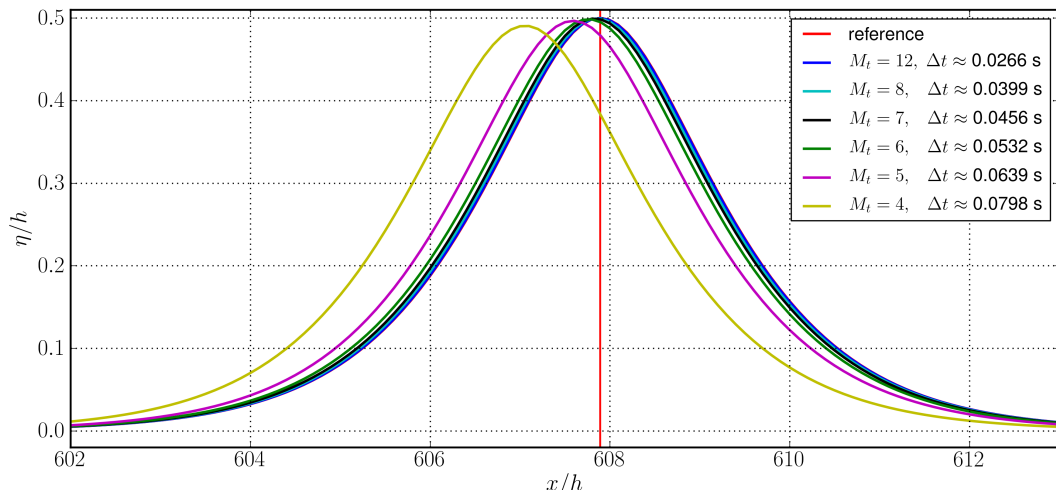
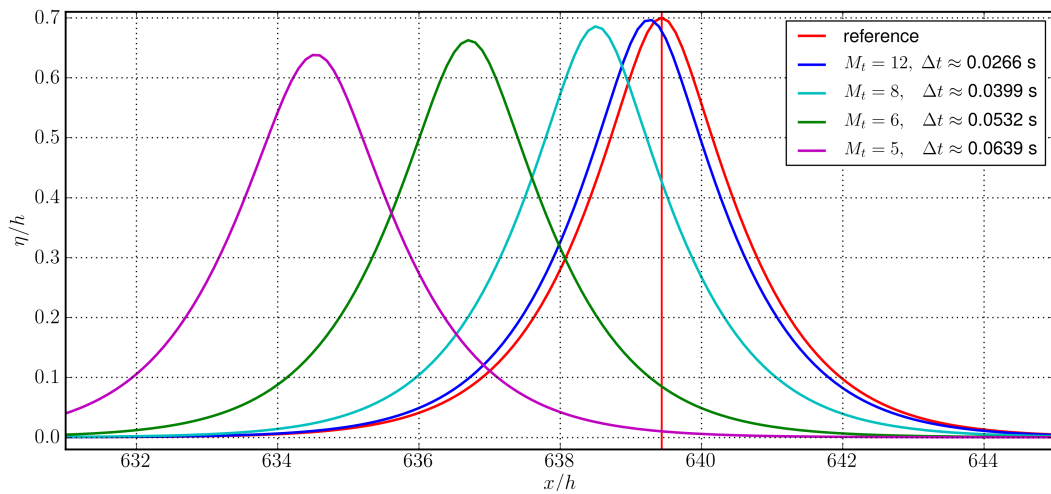
(a) $\delta = 0.3$ (b) $\delta = 0.5$ (c) $\delta = 0.7$

Figure 3.7: Free surface profiles at $\tilde{T} = 500$ for a range of Δt values ($M_x = 10$ and $N_T = 7$) for (a) $\delta = 0.3$, (b) $\delta = 0.5$ and (c) $\delta = 0.7$.

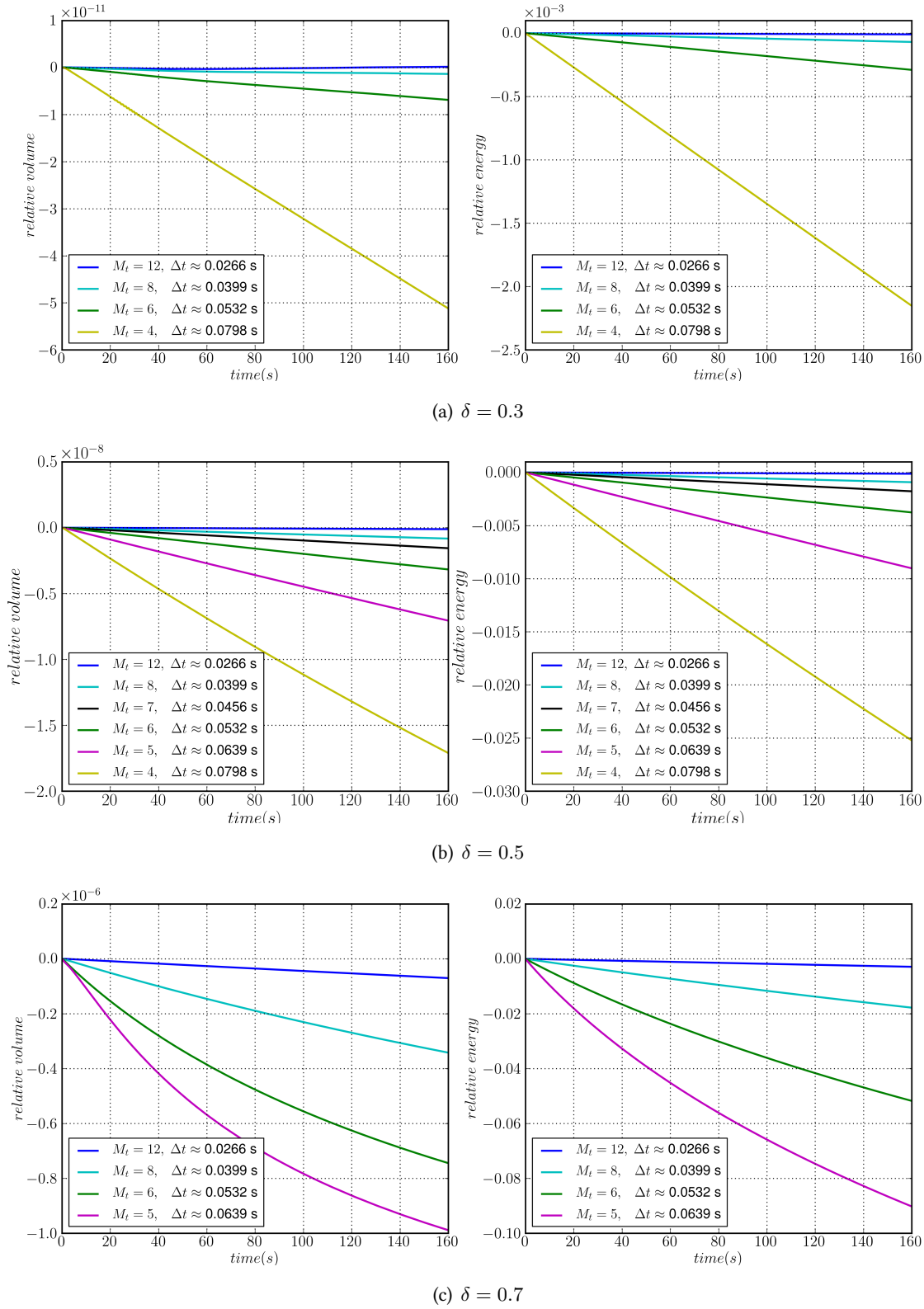


Figure 3.8: Relative volume (left) and relative energy (right) time series for a range of Δt values ($M_x = 10$ and $N_T = 7$) for (a) $\delta = 0.3$, (b) $\delta = 0.5$ and (c) $\delta = 0.7$. Note that the axis scales change for each value of δ .

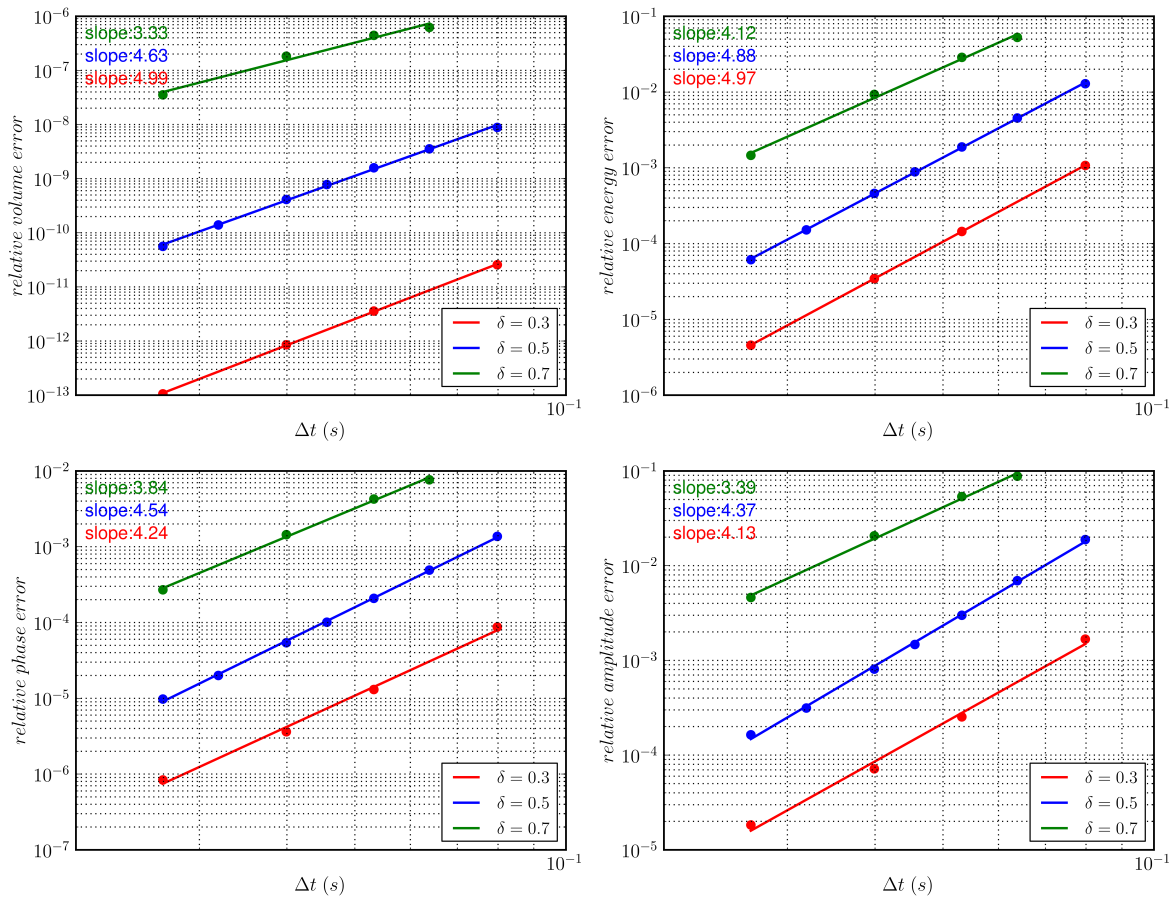


Figure 3.9: Convergence as a function of the time step Δt and wave nonlinearity δ for $N_T = 7$ and $M_x = 10$.

3.2.4.2 Convergence as a function of the spatial resolution Δx

To evaluate the convergence of the model as a function of the horizontal spatial resolution, a series of simulations were run with M_x varying from 30 to 5, corresponding to Δx varying from 0.033 to 0.2 m. For each simulation, the time step was calculated to maintain a constant CFL number equal to 1.25, and $N_T = 7$ was held constant (Table 3.4).

M_x	$\Delta\tilde{x}$	$\Delta x(m)$	M_t	$\Delta\tilde{t}$	$\Delta t(s)$
30	$1/30 \approx 0.0333$	≈ 0.0333	24	$1/24 \approx 0.417$	≈ 0.0133
25	$1/25 = 0.04$	0.04	20	$1/20 = 0.05$	≈ 0.0160
20	$1/20 = 0.05$	0.05	16	$1/16 = 0.0625$	≈ 0.0200
15	$1/15 \approx 0.0667$	≈ 0.0667	12	$1/12 \approx 0.0833$	≈ 0.0266
10	$1/10 = 0.1$	0.1	8	$1/8 = 0.125$	≈ 0.0399
5	$1/5 = 0.2$	0.2	4	$1/4 = 0.25$	≈ 0.0798

Table 3.4: Selected spatial steps Δx and associated quantities for convergence runs as a function of Δx (CFL = 1.25 and $N_T = 7$)

Final free surface profiles. The free surface profiles at the end of the simulation period agree well with the expected results for $\delta = 0.3$ (Figure 3.10(a)). As the wave nonlinearity increases, decreases in the amplitude and wave phase speed become apparent for larger Δx or smaller M_x (e.g. for $\Delta x = 0.2$ with $\delta = 0.5$ in Figure 3.10(b) and for $\Delta x > 0.04$ with $\delta = 0.7$ in Figure 3.10(c)).

Conservation of volume and energy. The relative energy error time series show that energy conservation improves with finer horizontal resolution, as expected (Figure 3.11, right column). For $\delta = 0.3$ and $\delta = 0.5$, the energy appears to decrease nearly linearly in time. However, for $\delta = 0.7$ and large values of Δx , the errors increase more rapidly and have larger final errors than for smaller Δx , but the rate of increase in error slows in time (e.g. Figure 3.11(c), right).

The relative volume error time series also show that volume conservation improves with finer horizontal resolution, as expected, but only for the most nonlinear case with $\delta = 0.7$ (Figure 3.11, left column). For smaller values of δ , there are several exceptions where simulations with larger Δx conserve volume better than those with smaller Δx . For example, errors in volume conservation for $\Delta x = 0.04$ m are larger than for $\Delta x = 0.1$ m and $\Delta x = 0.05$ m, for $\delta = 0.3$ and $\delta = 0.5$, respectively. The reason for these exceptions is unknown.

Evolution of global errors as a function of the spatial resolution. Global errors in relative volume, energy, phase, and amplitude summarize the error trends as a function of Δx and the relative wave height δ (Figure 3.12). With the exception of the anomalies in the volume errors, with minima reached for intermediate values of Δx for $\delta = 0.3$ and $\delta = 0.5$, the global errors decrease with decreasing Δx and with decreasing relative wave height δ . As a function of the

horizontal resolution, the trends are linear in log-log plots, with slopes ranging from 4 to 5 for $\delta = 0.3$ and $\delta = 0.5$ and from 3 to 4 for $\delta = 0.7$, as would be expected for the fourth-order finite difference schemes used in the model, confirming the fourth-order, algebraic spatial convergence of the model.

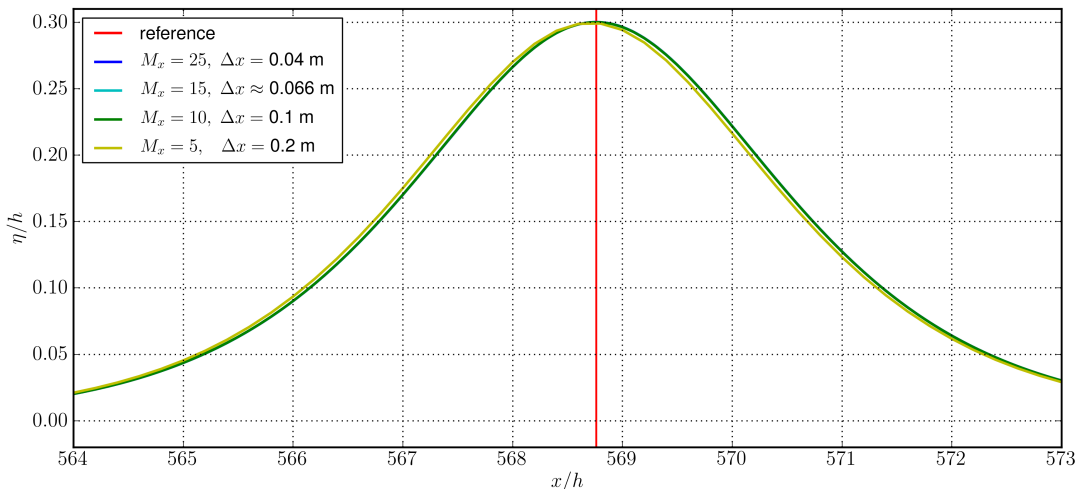
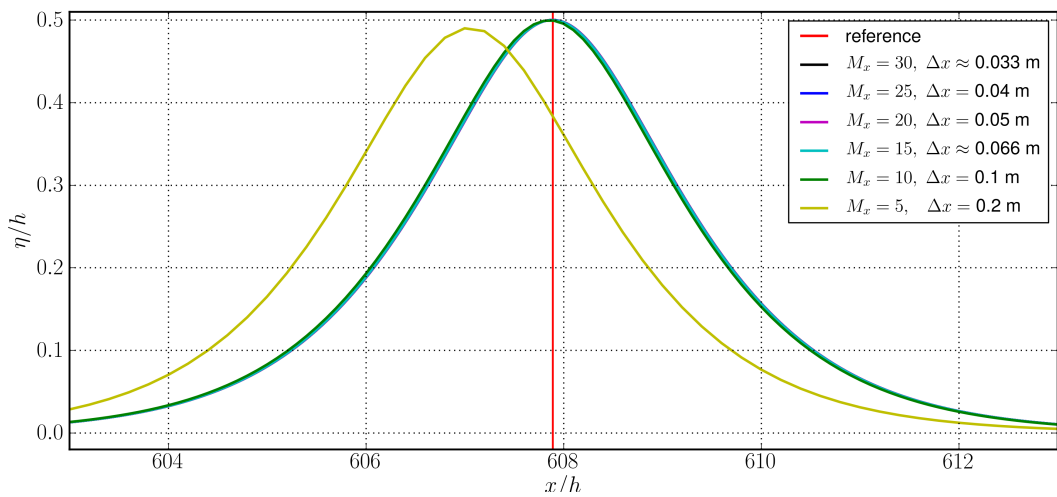
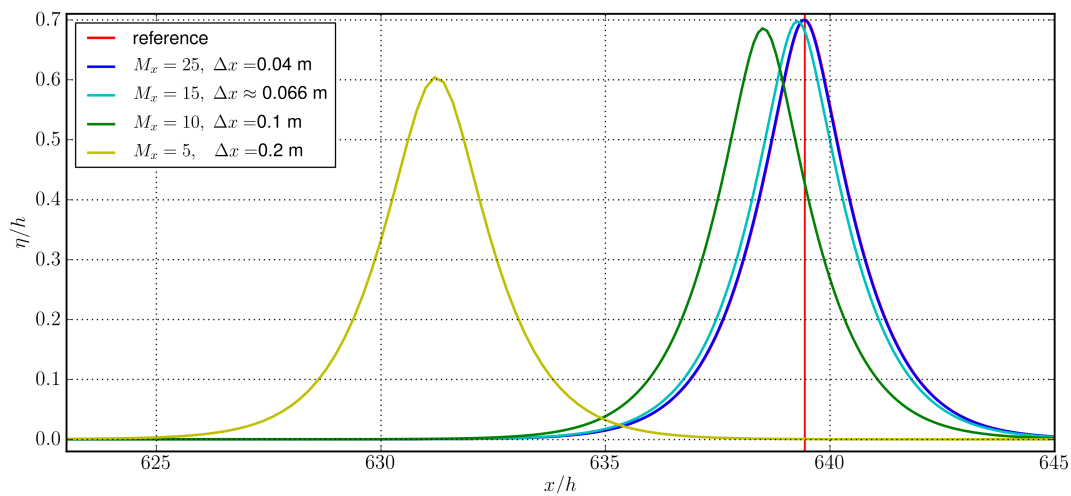
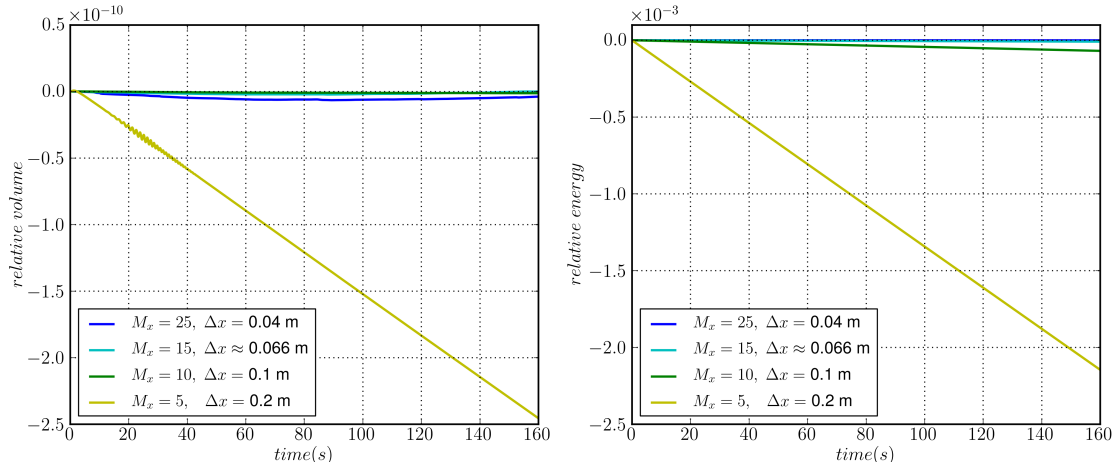
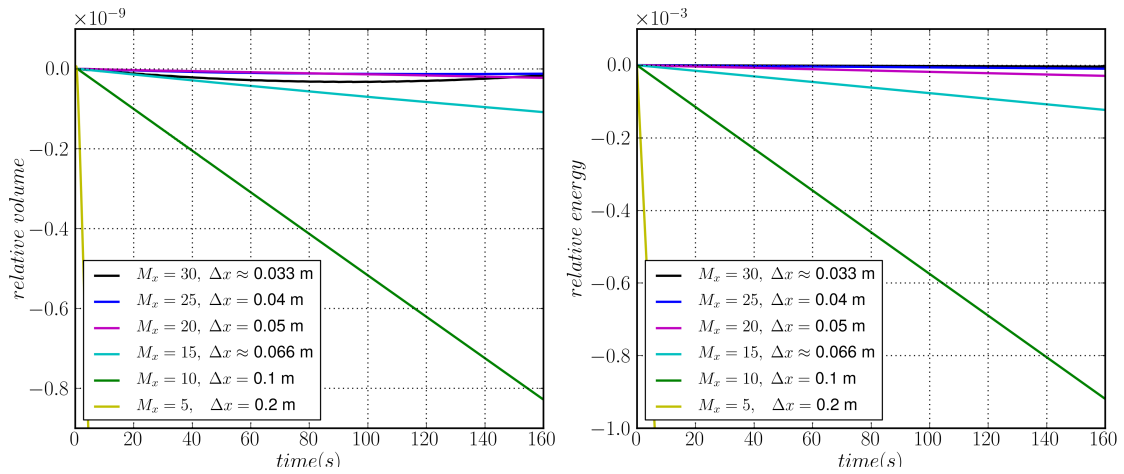
(a) $\delta = 0.3$ (b) $\delta = 0.5$ (c) $\delta = 0.7$

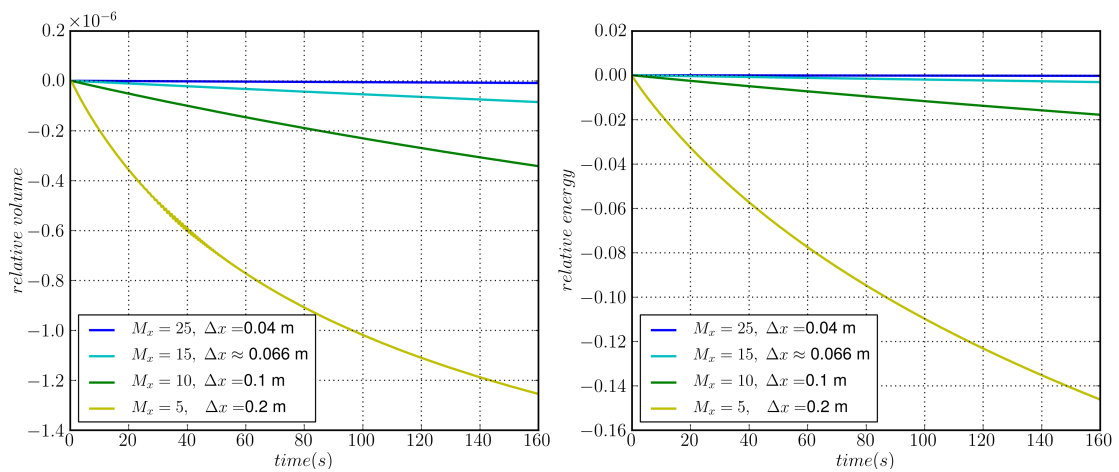
Figure 3.10: Free surface profiles at $\tilde{T} = 500$ for a range of Δx ($CFL = 1.25$ and $N_T = 7$) for (a) $\delta = 0.3$, (b) $\delta = 0.5$ and (c) $\delta = 0.7$.



(a) $\delta = 0.3$



(b) $\delta = 0.5$



(c) $\delta = 0.7$

Figure 3.11: Relative volume (left) and relative energy (right) time series for a range of Δx values (CFL = 1.25 and $N_T = 7$) for (a) $\delta = 0.3$, (b) $\delta = 0.5$ and (c) $\delta = 0.7$. Note that the axis scales change for each value of δ .

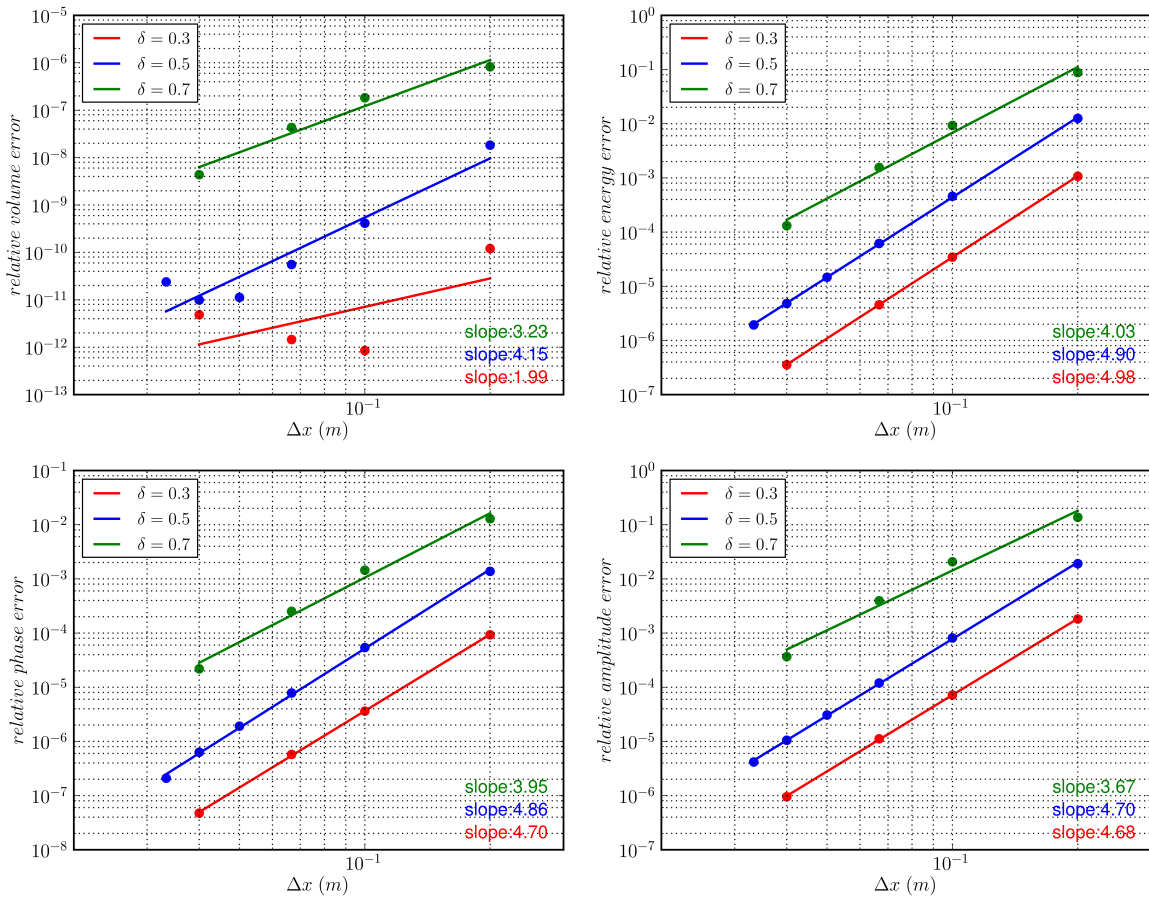


Figure 3.12: Convergence as a function of the horizontal resolution Δx and wave nonlinearity δ for $N_T = 7$ and CFL = 1.25.

3.2.4.3 Convergence as a function of the Chebyshev polynomial order N_T

To evaluate the convergence as a function of the order of the maximum Chebyshev polynomial used to resolve the vertical variation in ϕ , a series of simulations were run with N_T ranging from 3 to 15, with a constant CFL = 1.25 ($M_x = 10$ and $M_t = 8$).

Final free surface profiles. The final (at $\tilde{T} = 500$) free surface profiles converges for intermediate values of N_T , and the particular value of N_T increases with increasing δ (Figure 3.13). For example, the curves converge for $N_T \geq 4$ for $\delta = 0.3$, and for $N_T \geq 7$ for $\delta = 0.5$ and 0.7 . For $\delta = 0.3$ and $\delta = 0.5$, the free surface profile converges to the reference solution. However, for $\delta = 0.7$, the most nonlinear test case, the free surface profile converges to a solution with a slightly smaller wave height and slower propagation speed than the reference solution. This difference is caused by the choice of Δx and Δt , which appear to be the limiting factors for large values of N_T . One can observe that the smallest value $N_T = 3$ results in a wave propagating faster than the theoretical solution, while larger values of N_T result in waves propagating slower than the theoretical solution.

Conservation of volume and energy. The relative energy time series show a decrease in both of these quantities as a function of time, with larger final errors for smaller values of N_T , as expected (Figure 3.14, right column). The relative volume time series also show similar trends, with an unexplained exception in which the volume conservation is better for $N_T = 4$ than for $N_T = 5$, for $\delta = 0.5$ and $\delta = 0.7$ (Figures 3.14(b) and 3.14(b), left).

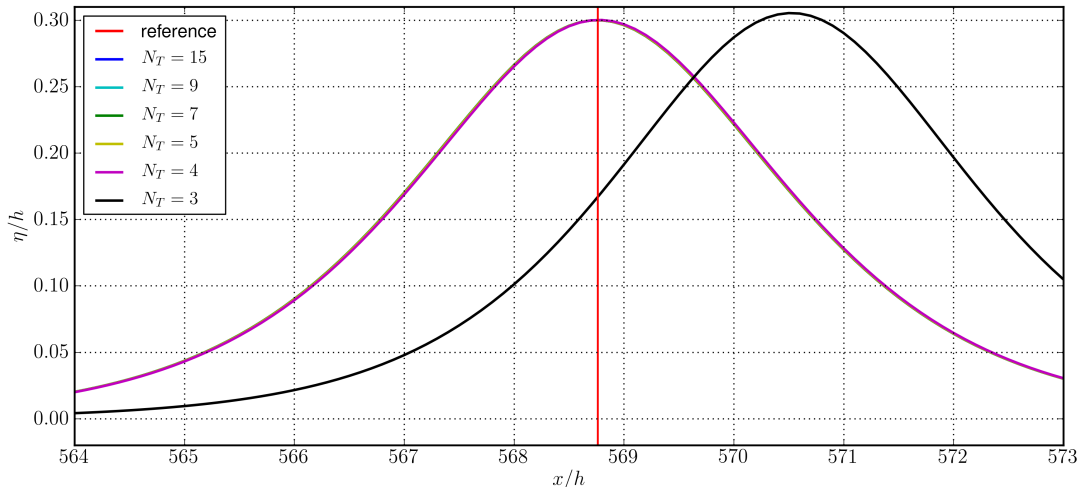
Evolution of global errors as a function of N_T . The global errors in the relative volume, energy, phase, and amplitude as a function of N_T and the relative wave height δ are shown in semi-log plots in Figure 3.15. The linear error trends decreasing with N_T demonstrate the exponential convergence of the model as a function of N_T . The model results converge exponentially to the value obtained with $N_T = 15$, such that $\text{Error} \propto \exp(aN_T)$. This is an appealing property of the model since small errors can be attained with small to intermediate values of N_T .

The relative energy error does not show the same trend for $\delta = 0.3$ as for $\delta = 0.5$ and 0.7 : for $\delta = 0.3$ the convergence is more rapid for values of N_T smaller than 7, and then the convergence rate decreases rapidly. For this case, however, the relative phase and amplitude errors are equal to 0 for $N_T > 9$ (and are thus not visible in Figure 3.15), which indicates that the model has converged to a solution (for the given Δx and Δt).

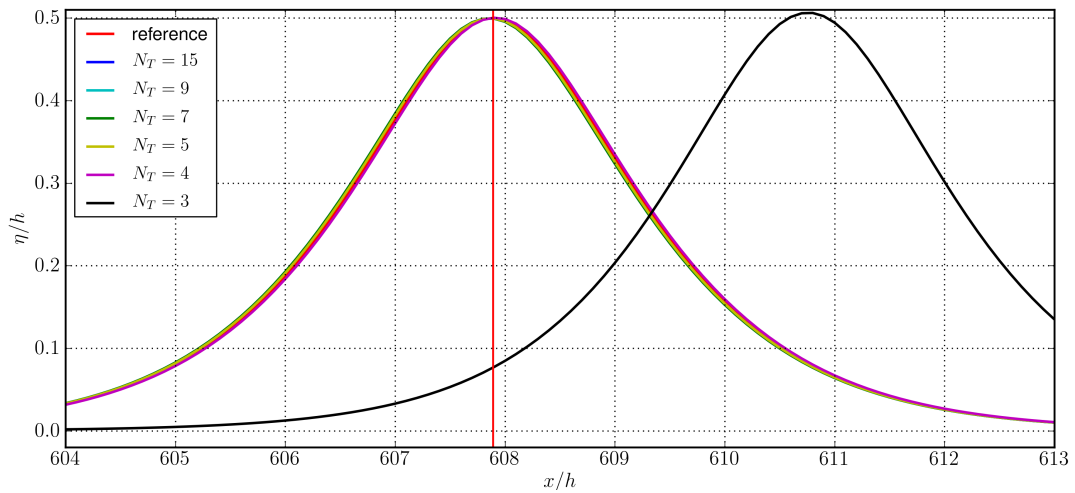
For the test case with $\delta = 0.5$, the energy error decreases monotonically with N_T for $N_T \leq 14$, but the errors in relative phase and amplitude appear to reach a plateau for $N_T > 12$. This behavior is similar to that with $\delta = 0.3$, but with a higher threshold of N_T above which the error is only marginally decreased by an increase of N_T . Again, in this range, the error is likely dependent on the choice of Δx and Δt .

The volume errors also present an unusual trend as a function of N_T , such that for a given

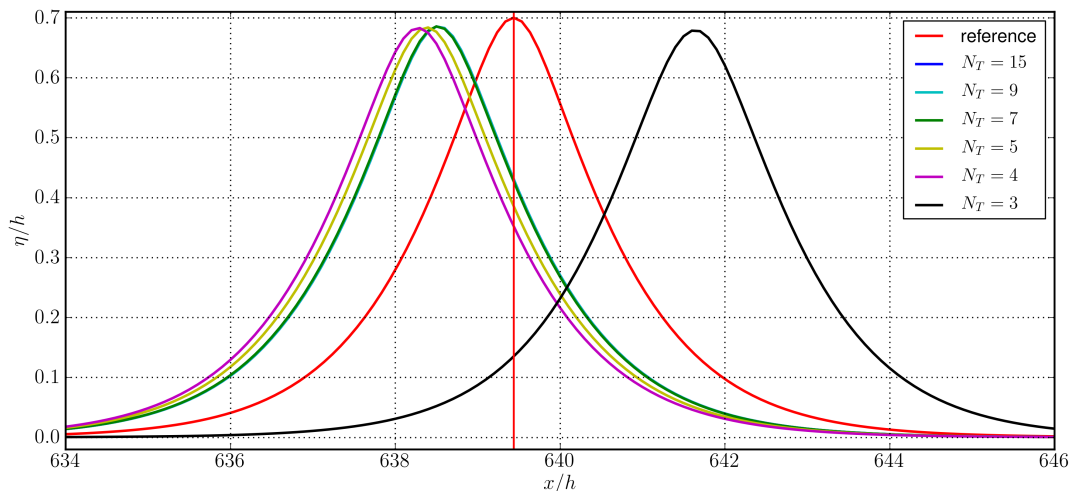
even value of N_T , the error is lower than for $N_T + 1$. This is hypothesized to be related to the method used to calculate the relative volume error, which is essentially a simple arithmetic mean of the difference in the free surface elevation profile for a given value of N_T and $N_T = 15$. Therefore, positive and negative errors compensate partially over the length of the domain. This compensation varies as a function of N_T , leading to the observed step-like behavior in volume errors.



(a) $\delta = 0.3$



(b) $\delta = 0.5$



(c) $\delta = 0.7$

Figure 3.13: Free surface profiles at $\tilde{T} = 500$ for several values of N_T (CFL = 1.25, with $M_x = 10$ and $M_t = 8$) for (a) $\delta = 0.3$, (b) $\delta = 0.5$ and (c) $\delta = 0.7$.

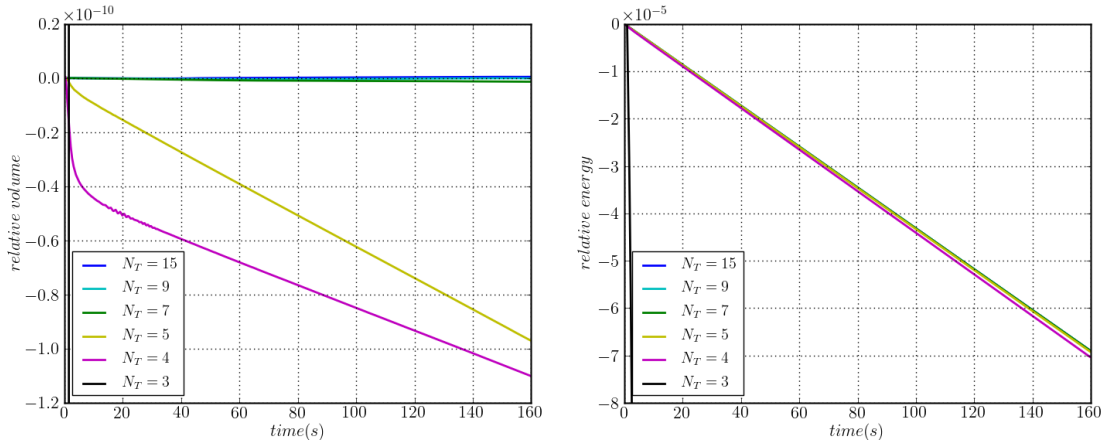
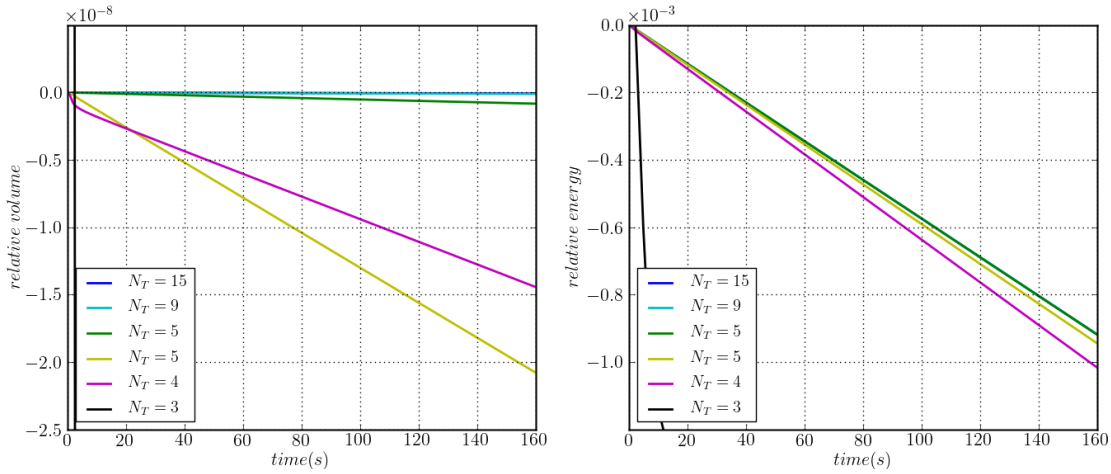
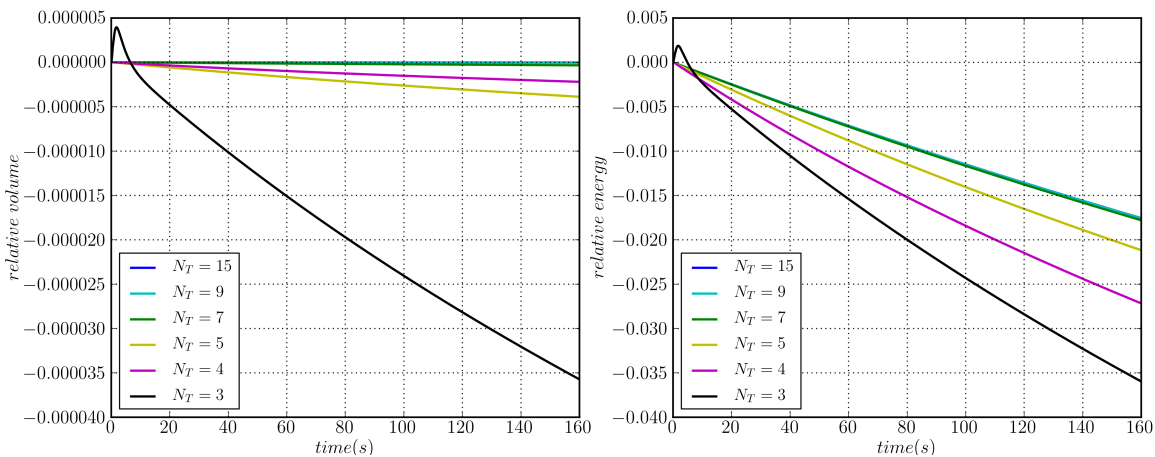
(a) $\delta = 0.3$ (b) $\delta = 0.5$ (c) $\delta = 0.7$

Figure 3.14: Relative volume (left) and relative energy (right) time series for a range of N_T values (CFL = 1.25, with $M_x = 10$ and $M_t = 8$) for (a) $\delta = 0.3$, (b) $\delta = 0.5$ and (c) $\delta = 0.7$. Note that the vertical axis scales change for each value of δ .

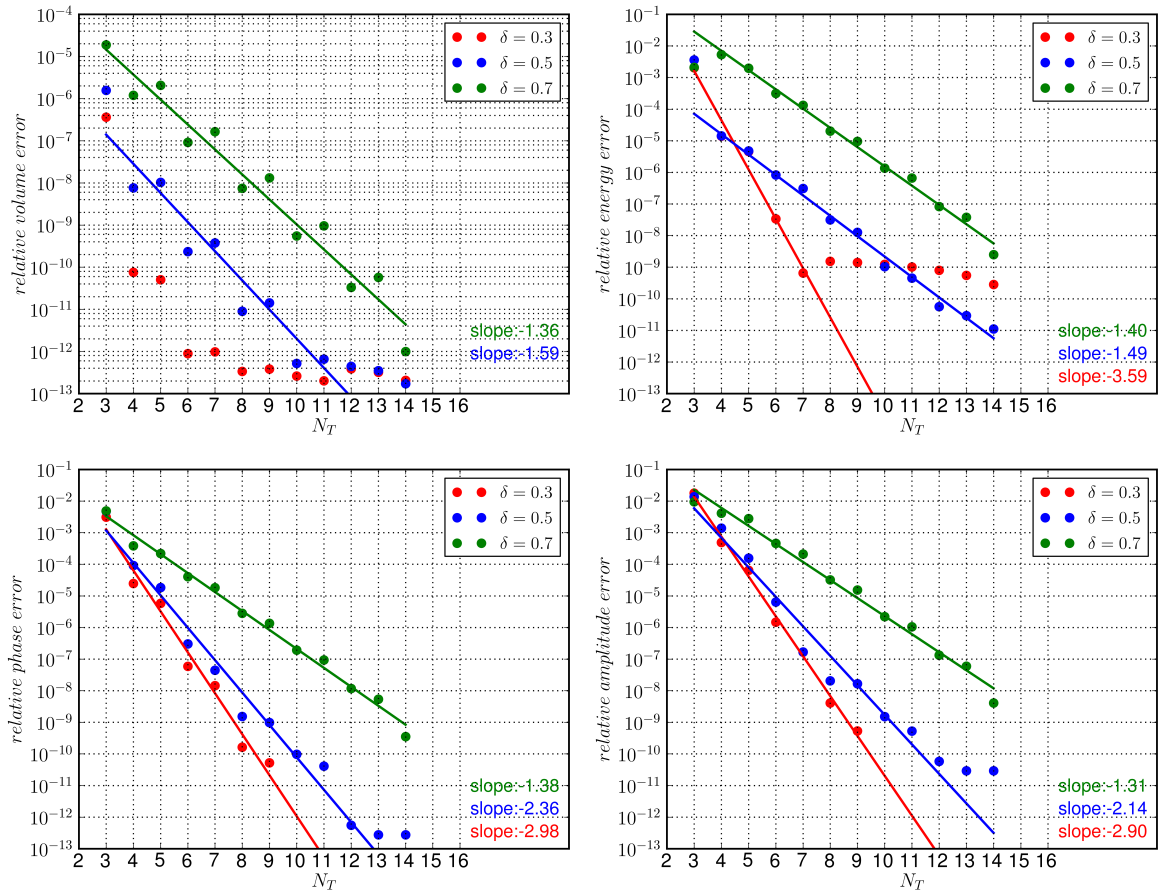


Figure 3.15: Convergence as a function of the Chebyshev polynomial order N_T (vertical space convergence) and wave nonlinearity δ with CFL = 1.25 ($M_X = 10$ and $M_t = 8$).

3.2.4.4 Analysis of CPU time

The efficiency of the current version of the model is evaluated by recording the CPU time necessary for each of the convergence studies:

1. convergence as a function of the time step Δt (Figure 3.16(a)),
2. convergence as a function of the horizontal spatial resolution Δx (Figure 3.16(b)),
3. convergence as a function of the Chebyshev polynomial order N_T (Figure 3.16(c)).

For the three values of δ , the simulation times for the same values of Δt , Δx , or N_T are very similar, as expected. The CPU time depends on Δt , Δx and N_T , and it is observed that this dependence has the following form:

$$T_{CPU} \approx \Delta t^\alpha \Delta x^\beta N_T^\gamma.$$

In the log-log plots (Figure 3.16), the CPU time is linearly dependent on Δt , Δx , and N_T , with slopes of approximately -1, -2, and 1.5, respectively. Therefore, the CPU time is proportional to :

$$T_{CPU} \approx \frac{N_T^{1.5}}{\Delta t \Delta x^2}.$$

showing the importance in minimizing N_T and that the dependency on Δx is stronger than the dependency on Δt and N_T .

3.2.5 Conclusions

This test case shows that the model is very accurate even in the limit of highly nonlinear waves ($\delta = H/h$ up to 0.7). For the same value of Δx , Δt or N_T , relative errors in volume, energy, phase and amplitude increase with increasing nonlinearity. This may be explained partly by the fact that for a given CFL number as defined here, the true CFL number (taking into account the actual wave celerity) is larger for $\delta = 0.7$ than for $\delta = 0.3$ due to the difference in the corresponding Froude number.

The order of temporal and spatial convergence are approximately 4-5 for $\delta = 0.3$ and 0.5 and 3-4 for $\delta = 0.7$, in good agreement with the fourth-order Runge-Kutta temporal integration scheme and the fourth-order finite difference schemes used in the model. The model shows exponential convergence in the vertical dimension due to the applied spectral approach, which enables obtaining highly accurate results for small to moderate values of the maximum order of Chebyshev polynomials N_T (typically smaller than 10).

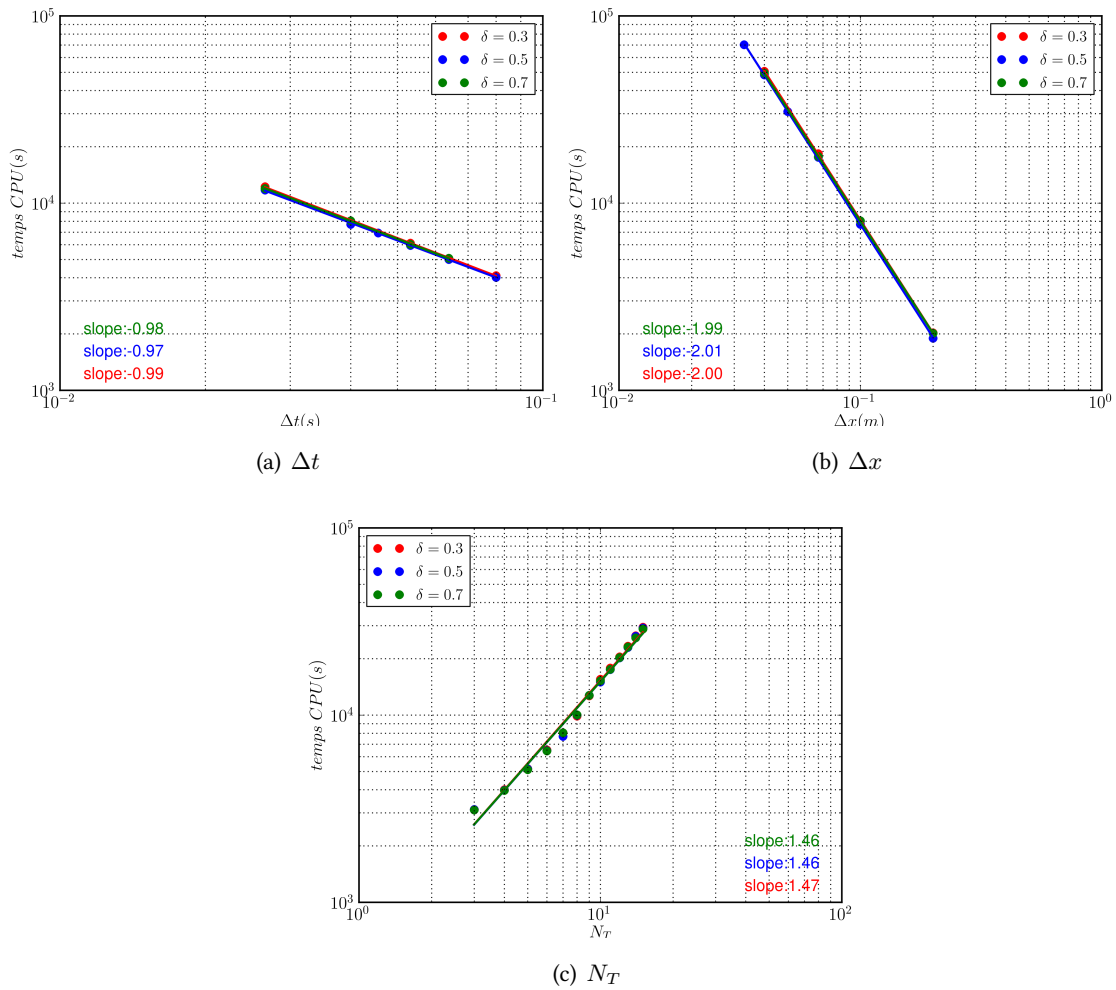


Figure 3.16: Simulation time as a function of (a) the time resolution Δt , (b) the spatial resolution Δx , and (c) the maximum order of the Chebyshev polynomial N_T (for $\delta = 0.3$ in red, $\delta = 0.5$ in blue, and $\delta = 0.7$ in green)

3.3 Nonlinear wave dynamics in constant water depth

The third test case consists of simulating the propagation of waves generated by the sinusoidal movement of a piston-type wavemaker over a flat bottom, based on the flume experiments of [Chapalain et al. \(1992\)](#) (hereafter C92). The results presented here correspond to trial A (piston stroke amplitude $e = 7.8$ cm and period $T = 2.5$ s), with a constant water depth $h = 0.4$ m. The wavelength of the fundamental component is $L = 4.74$ m from the linear dispersion relation, corresponding to long waves with $\mu = 0.53$. The model domain is regularly meshed with $\Delta x = 0.1$ m ($\approx L/47$) and extends far enough to prevent reflection from the right boundary. The waves were propagated during 16 periods (i.e. 40 s) with a time step $\Delta t = T/40 = 0.0625$ s, with maximum order of the Chebyshev polynomial $N_T = 7$. The model is forced by imposing at the left boundary a sinusoidal time varying horizontal velocity that is uniform in the vertical. A harmonic analysis of free surface elevation time series (after steady state is reached) decomposes the signal into a discrete sum:

$$\eta(t) = a_0 + \sum_{n=1}^N a_n \cos(n\omega t + \varphi_n), \quad (3.6)$$

where $\omega = \frac{2\pi}{T}$ is the angular frequency of the wavemaker, and a_n and φ_n are the amplitude and phase of the harmonic component n . The phase difference between the first and the second harmonic is defined as $\Delta \varphi_{1,2} \equiv \varphi_2 - 2\varphi_1$, following [Chapalain et al. \(1992\)](#). The simulated spatial evolution of the amplitudes of the first four harmonics agrees well with the experiments (Figure 3.17a). Overall, the model correctly represents the energy transfers between the different harmonic components, as well as the resultant beat lengths. However, a decrease in the second harmonic amplitude (after $x = 19$ m) is observed in the experimental data but is not reproduced in the simulations. This could be explained by dissipation in the experiments that is not taken into account in the model. This phenomenon is more noticeable for short waves, hence more visible for the higher harmonics. The spatial evolution of the phase difference between the first and second harmonic is also reproduced well (Figure 3.17b). The phase difference oscillates between $-\pi/2$ and $+\pi/2$ with the same periodicity as the harmonic amplitudes. Zero phase difference occurs when either the first harmonic is maximum and the second harmonic is minimum, or the contrary.

The variation of the free surface elevation thus depends on the position in the wave channel, as shown in Figure 3.18 at $x = 4$ m, 7 m, 10 m and 14 m (the simulated free surface position qualitatively agrees well with the measurements, when compared to Figure 3 of [Chapalain et al. \(1992\)](#)). When the first and second harmonics are in phase, the free surface profile is either quasi-sinusoidal when the first harmonic is maximal and the second minimal (e.g. $x = 14$ m), or cnoidal when the second harmonic is maximal and the first minimal (e.g. $x = 7$ m). However, when the first and second harmonics are out of phase, the waves are vertically asymmetrical with either a

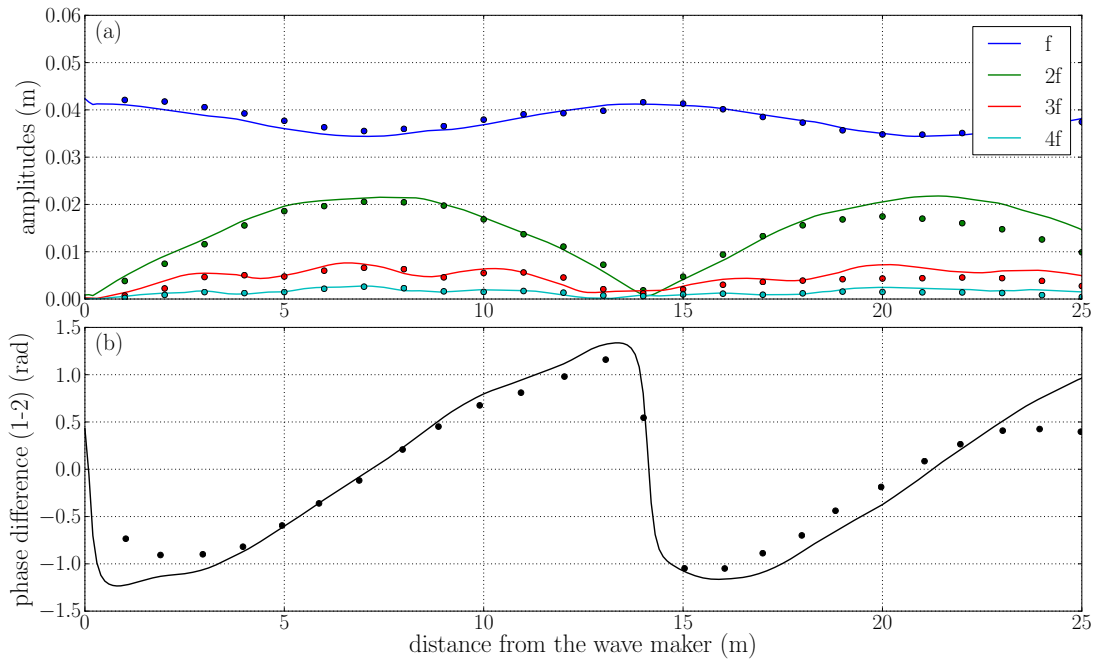


Figure 3.17: a) Spatial evolution of the first four harmonic amplitudes for test case A of [Chapalain et al. \(1992\)](#): experimental (circles) and Misthyc simulation (solid line) results. b) Spatial evolution of the phase difference between the first and second harmonic: experimental (circles) and Misthyc simulation (solid line) results.

steeper (gentler) wave front and a gentler (steeper) rear slope if the phase difference is positive (negative) (e.g $x = 10$ m and $x = 4$ m).

This test case demonstrates the ability of the model to simulate accurately the nonlinear resonant interactions occurring when waves are generated with a piston-like wavemaker and propagate over a flat bottom. The transfer of energy from the principal wave to the second harmonic was reproduced well, including the beat length of the resonant interaction.

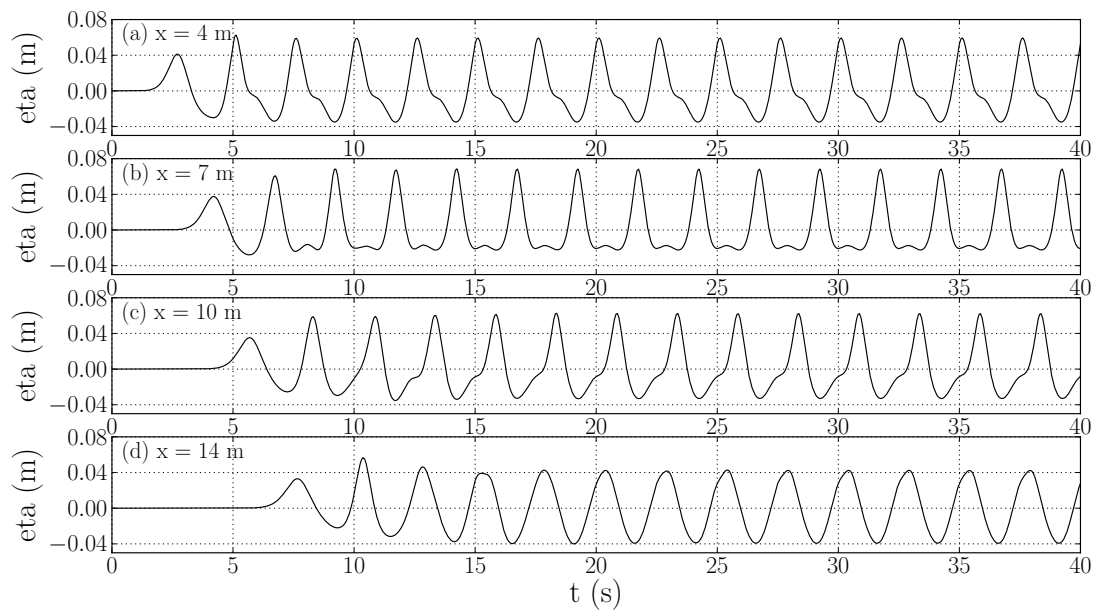


Figure 3.18: Misthyc simulated free surface elevation η at four different positions in the wave channel for the test case A of [Chapalain et al. \(1992\)](#).

3.4 Waves generated by an impulsive bottom motion

The fourth test case simulates waves generated by an impulsive vertical motion of the bottom to study tsunami-like wave dynamics. Hammack (1973) studied the case of a moving bottom with laboratory experiments, an analytical study of the linear solution, and numerical simulations with a KdV (Korteweg-de Vries) model. Fuhrman and Madsen (2009) (abbreviated F&M09 hereafter) also tried to reproduce numerically these experiments with a high-order Boussinesq model. Both upthrust and downthrust of the bottom were studied using different expressions for the temporal evolution of the bottom. Here, impulsive exponential bed upthrust is first simulated with the linear version of Misthyc and compared to the linear solution, and then simulated with the nonlinear version of Misthyc and compared to the experimental data and to the results of F&M09. The fluid domain is initially motionless, with an undisturbed water depth $h_0 = 1$ m. During the simulation, a step in the bottom between $x = 0$ m and $x = b$ m is rapidly upthrust (Figure 3.19, for $b/h_0 = 12.2$), and the water depth ($h(x, t)$) evolves following:

$$h(x, t) = h_0 - \zeta(x, t) \quad \text{with} \quad \zeta(x, t) = \zeta_0(1 - e^{-\alpha t})H(b - x), \quad (3.7)$$

where H is the Heaviside step function. The step is upthrust over a total vertical distance of $\zeta_0/h_0 = 0.1$, and the exponential decay constant and critical time are respectively $\alpha = 1.11/t_c$ and $t_c = 0.148b/\sqrt{gh_0}$. The domain is discretized on a regular grid extending from 0 to $2500h_0 = 2500$ m, with a spatial step $\Delta x = h_0/5 = 0.20$ m (12501 nodes). The simulation length is the nondimensional time $t\sqrt{g/h_0} = 2375$ (i.e. $t \approx 75828$ s), with nondimensional time step $\Delta t\sqrt{g/h_0} = 0.20$ (i.e. $\Delta t \approx 0.0638$ s). The resulting CFL number is $\text{CFL} = \sqrt{gh_0}\Delta t/\Delta x = 1$. Fully reflective vertical boundaries are applied at both ends of the domain. The maximum order of the Chebyshev polynomial is $N_T = 7$.

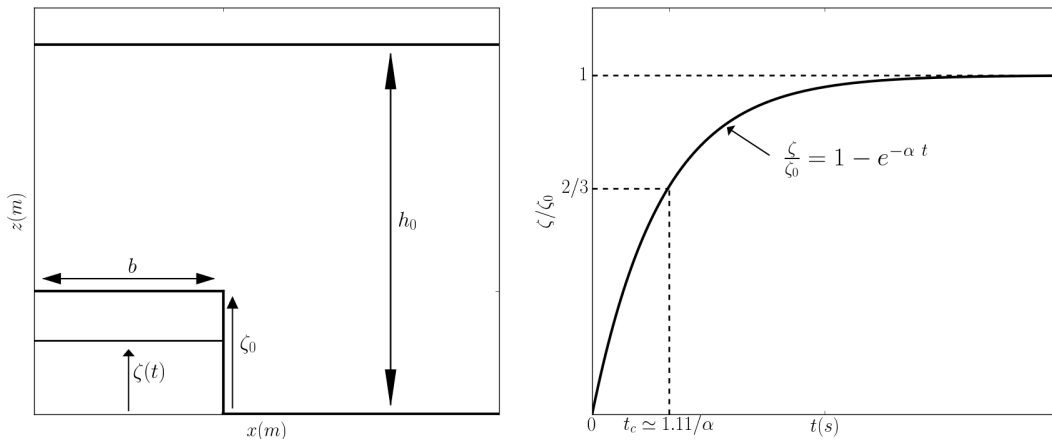


Figure 3.19: (left) Bathymetry at time t ($\zeta(t)$) and final bathymetry (ζ_0), and (right) temporal evolution of the bottom deformation.

3.4.1 The linear solution

Hammack (1973) derived an analytical solution for the associated linearized potential flow problem. The free surface elevation resulting from an exponential bed movement is given by Eq.(22) of Hammack (1973):

$$\eta(x, t) = -2 \frac{\zeta_0}{\pi} \int_0^\infty \frac{\cos(kx) \sin(kb)}{k \cosh(kh_0)} \frac{\alpha^2}{\alpha^2 + \omega^2} \left[e^{-\omega t} - \cos(\omega t) - \frac{\omega}{\alpha} \sin(\omega t) \right] dk \quad (3.8)$$

This solution is numerically computed using the trapezoidal rule to estimate the integral to obtain the free surface elevation time series at four positions in the domain ($(x - b)/h_0 = 0, 20, 180, \text{ and } 400$), where experimental data are available. The results obtained with the linear version of Misthyc for different values of N_T are compared to the linear solution in Figure 3.20. The simulated free surface elevations are nearly superimposed on the linear solution, except for the smaller values of N_T tested ($N_T = 3 \text{ and } 4$). For these values of N_T , small differences with the theoretical solution can be observed in the oscillatory trailing wave train following the main wave, in particular at the last two stations. The results with $N_T = 7 \text{ and } 10$ cannot be distinguished visually from the theoretical solution at all four stations.

To quantify the convergence of the results with the vertical discretization (N_T), the averaged absolute error over the interval $[-20, 100]$ (as shown in Figure 3.20) is computed at each of the four positions considered in the domain. The error is defined as:

$$\text{Averaged error} = \frac{1}{n} \sum_{i=1}^n |\eta(i) - \eta_{ref}(i)|. \quad (3.9)$$

The evolution of this error as a function of N_T shows that a constant value is reached for $N_T \geq 6$ (Figure 3.21). For $N_T = 3$, the error is larger for the two last probes where the effects of dispersion become apparent, and the dispersion relation obtained with $N_T = 3$ is less accurate (as shown in Section 1.4.3).

3.4.2 Comparison with the experimental data

Here, the simulated time series of the free surface elevation obtained with the nonlinear version of Misthyc and $N_T = 7$ are compared to the experimental measurements (red line) at four positions in the domain ($(x - b)/h_0 = 0, 20, 180, \text{ and } 400$), and to the linear analytical solution (Eq.3.8) (dotted blue line) in Figure 3.22.

Near the generation zone (Figure 3.22a and b), the simulated free surface position (black line) agrees well with the global trend of the experimental data, with a slight overestimation at $(x - b)/h_0 = 0$ and with larger oscillations at $(x - b)/h_0 = 20$. These results are similar to those obtained by F&M09 (their Figure 2). Farther from the generation zone (Figures 3.22c and d), the differences are more significant. The linear solution diverges from the experimental measurements, showing that a model with nonlinear properties is required to simulate properly this

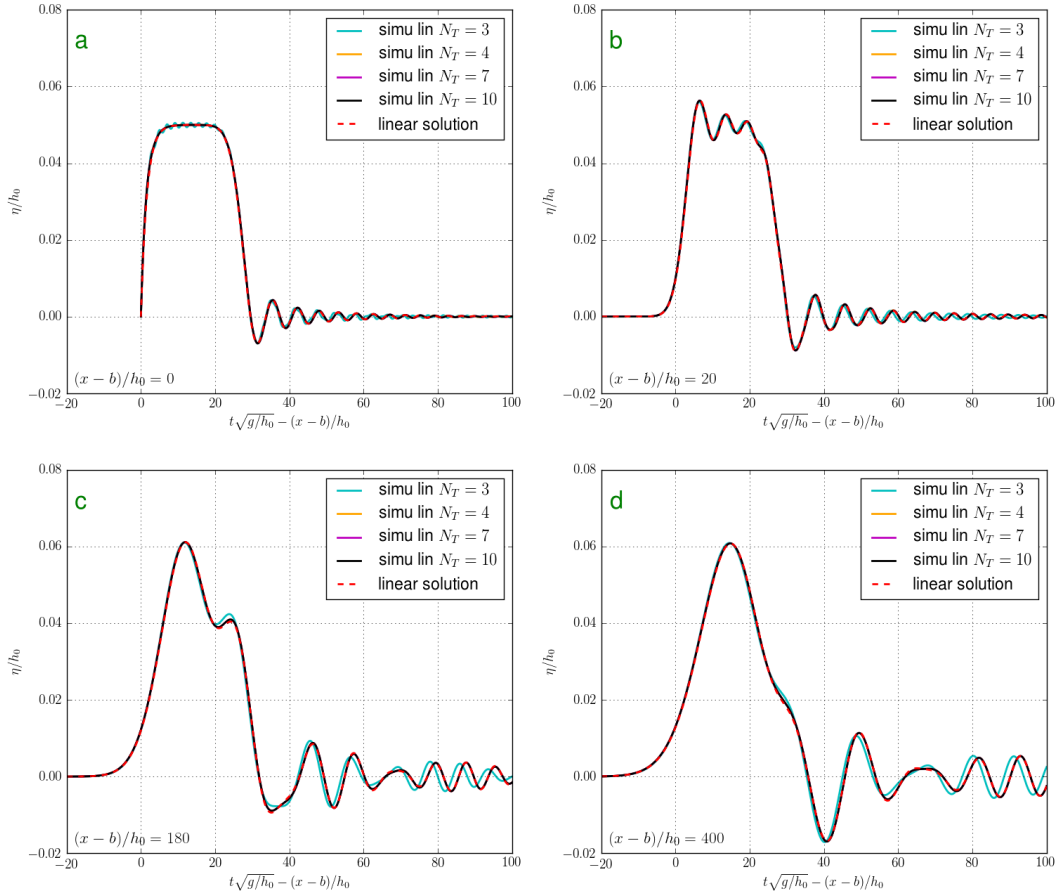


Figure 3.20: Free surface time series at four locations: $(x - b)/h_0 =$ (a) 0, (b) 20, (c) 180, and (d) 400. Comparison between the linear solution (red dashed line) and results of the linear version of the model for $N_T = 3, 4, 7$ and 10.

case. The simulated results (with the present model) are closer to the measurements than to the linear solution, demonstrating the nonlinear properties of the model. A comparison of the far-field waves (Figure 3.22c and d) shows that the free surface deformations have the same global shape, but that the model predicts faster wave propagation speeds (relative rightward shift in the time series), which is consistent with the overprediction of the wave amplitude. Hammack (1973), who obtained the same type of differences with a KdV model, suggested that differences in the simulated and measured wave amplitudes could be due to viscous energy losses occurring in the experiments that were neglected in both numerical models. The high-order (non-dissipative) Boussinesq model of F&M09 produces results in close agreement to Misthyc, which suggests that the differences with the experiments can be attributed to dissipative effects.

When the wave train propagates over long distances (up to 2500 times the water depth), the leading waves separate into two solitary waves (Figure 3.23). These solitary waves then propagate with constant shape, with the first wave (larger amplitude) traveling faster, as observed by F&M09. In Figure 3.23, the free surface profiles at $t\sqrt{g/h_0} = 2375$ obtained with Misthyc for

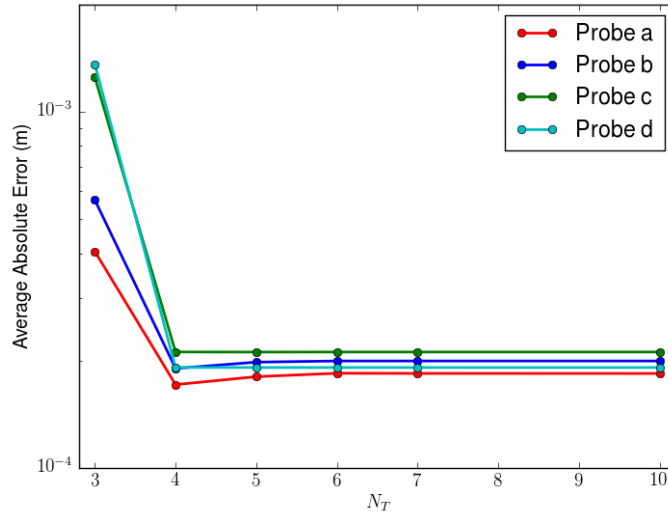


Figure 3.21: Averaged absolute error Eq.(3.9) as a function of N_T for the four probes located at $(x - b)/h_0 = 0, 20, 180, \text{ and } 400$, and shown in Figure 3.20.

several values of N_T are compared to the corresponding final results of F&M09 (dashed black line). The Misthyc simulation results (converged for $N_T \geq 5$) predict slightly faster propagation speeds of slightly larger amplitude solitary waves. In F&M09, the simulation had a spatial resolution of $\Delta x = 0.25$ m. More recently, D. Fuhrman provided (personal communication) new results obtained with a finer spatial resolution of $\Delta x = 0.2$ m (black line), to resolve accurately the step upthrust with an integer number of grid spaces cells. In comparison to the simulation results presented in F&M09, these new results are closer to those obtained with Misthyc, some small discrepancies likely due to the different mathematical models and numerical schemes used.

Comparisons of the simulated free surface time series with the experimental results of Hammack (1973) confirm the ability of the model to reproduce accurately the wave disturbance dynamics, including the formation of leading waves leaving the generation zone and their separation from the wave train after a sufficient length of time, as observed by F&M09.

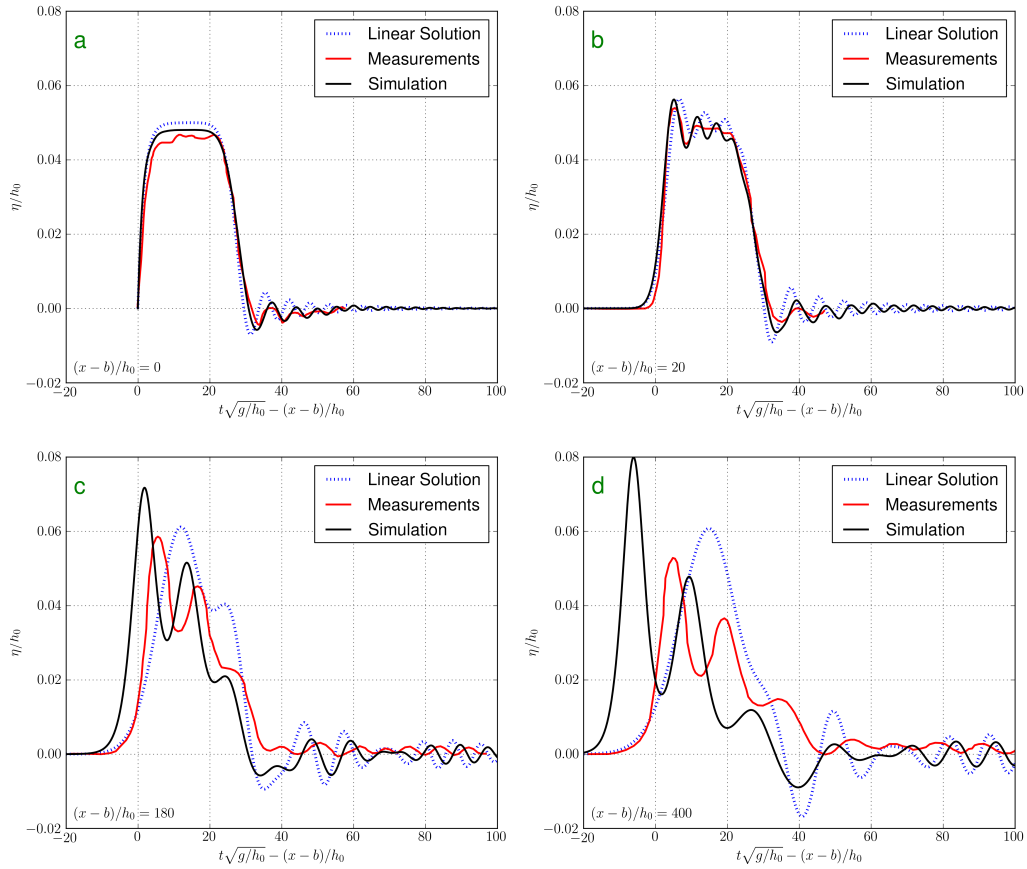


Figure 3.22: Free surface time series at four nondimensional positions in the domain: $(x-b)/h_0 =$ (a) 0, (b) 20, (c) 180, and (d) 400. Comparison between the present model simulations (black line) and Hammack (1973) measurements (red line). The associated linear solution (blue dotted line) is also shown.

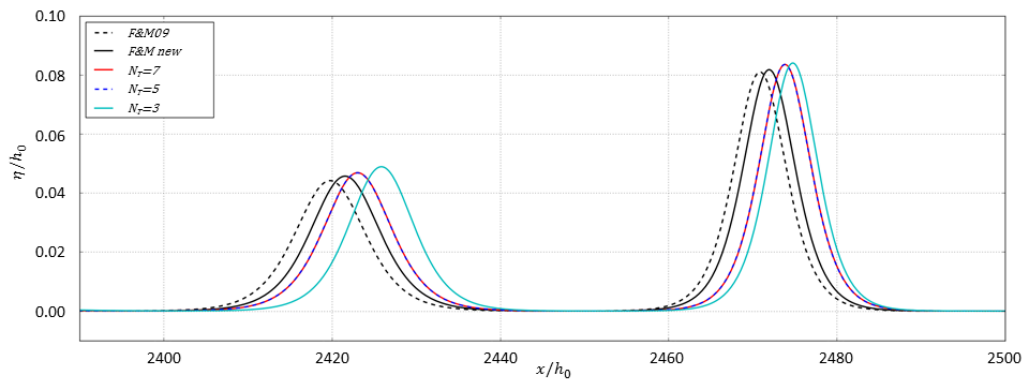


Figure 3.23: Free surface profiles at $t\sqrt{g/h_0} = 2375$. Comparison between F&M09 final results (corresponding to their figure 3) with a resolution $\Delta x = 0.25$ m (dashed black line), a more recent simulation using the same model but with a resolution $\Delta x = 0.2$ m (solid black line), and Misthyc simulation results for several values of N_T ($N_T = 3$ light blue, $N_T = 5$, dashed blue and $N_T = 7$, red).

3.5 Regular waves over a submerged bar

Beji and Battjes (1993) and then Dingemans (1994) (D94) performed a series of experiments of regular wave propagation over a submerged trapezoidal bar. These experiments are now a standard test case for wave models since both nonlinear and dispersive effects are important when waves propagate over the top of the bar. The bottom profile is shown in Figure 3.24. The water depth is $h = 0.40$ m offshore and reduces to a minimum of 0.10 m on top of the bar. The front slope of the bar is 1:20, and the rear slope is 1:10. Eleven wave probes recorded the free surface elevation time series in the experiments (see positions in Figure 3.24).

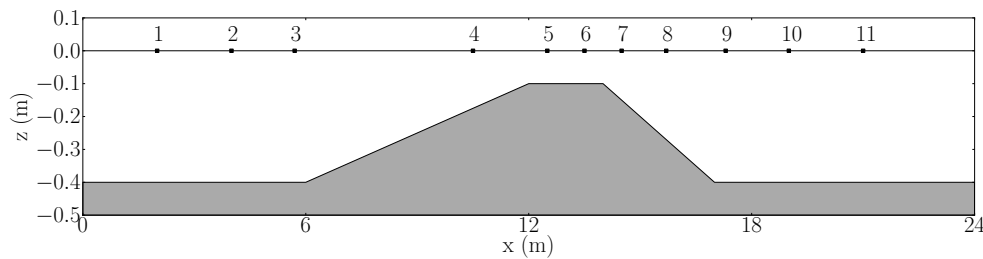


Figure 3.24: Bathymetry and position of wave probes in the Beji and Battjes (1993) experiments.

Here, case A is studied with an incident wave height $H = 2.0$ cm and period $T = 2.02$ s, corresponding to long waves with $\mu = 0.67$ (or $h/L = 0.107$) offshore of the bar and relatively small wave steepness $\epsilon = 0.017$ (or $H/L = 0.53\%$). Under these conditions, the incident wave train is significantly affected during the propagation over the submerged bar, with transfers of energy toward higher harmonics.

The model domain has a regularly spaced grid with $\Delta x = 0.05$ m (i.e. about $L/75$ offshore of the bar) and extends from $x = -6$ m to 30 m (721 nodes along the x axis). Waves are generated in an 8-m wide relaxation zone at the left boundary of the domain ($-6 \leq x \leq 2$ m) using, here, a second-order Stokes solution to impose the free surface elevation and the velocity potential. Waves are absorbed in a 5-m wide relaxation zone ($25 \leq x \leq 30$ m) applied in front of the fully reflective right boundary to avoid reflections. Waves are propagated during 25 wave periods (i.e. 50.5 s) with a time step $\Delta t = T/100 = 0.0202$ s.

Times series of the free surface elevation computed with $N_T = 7$ are presented at probes 4 to 11 in Figure 3.25. The choice of this value of N_T will be discussed at the end of this section. When waves propagate over the front slope of the bar, the wave height and steepness increase due to shoaling effects (probes 4 to 6, Figure 3.25(a-c)). The wave profile becomes asymmetric due to nonlinear wave-bottom interactions that create higher frequency bound harmonic components. These harmonics are released in the shallowest region and on the rear slope of the bar and then propagate at their own phase speed (probes 7 and 8, Figure 3.25(d-e)). After the bar, the measured wave profiles vary significantly between the probes due to the differences in celerity of the free wave components. At the last three probes (probes 9 to 11, Figure 3.25(f-h)), the model reproduces

well the complex wave profiles, including the dispersive (high frequency) components.

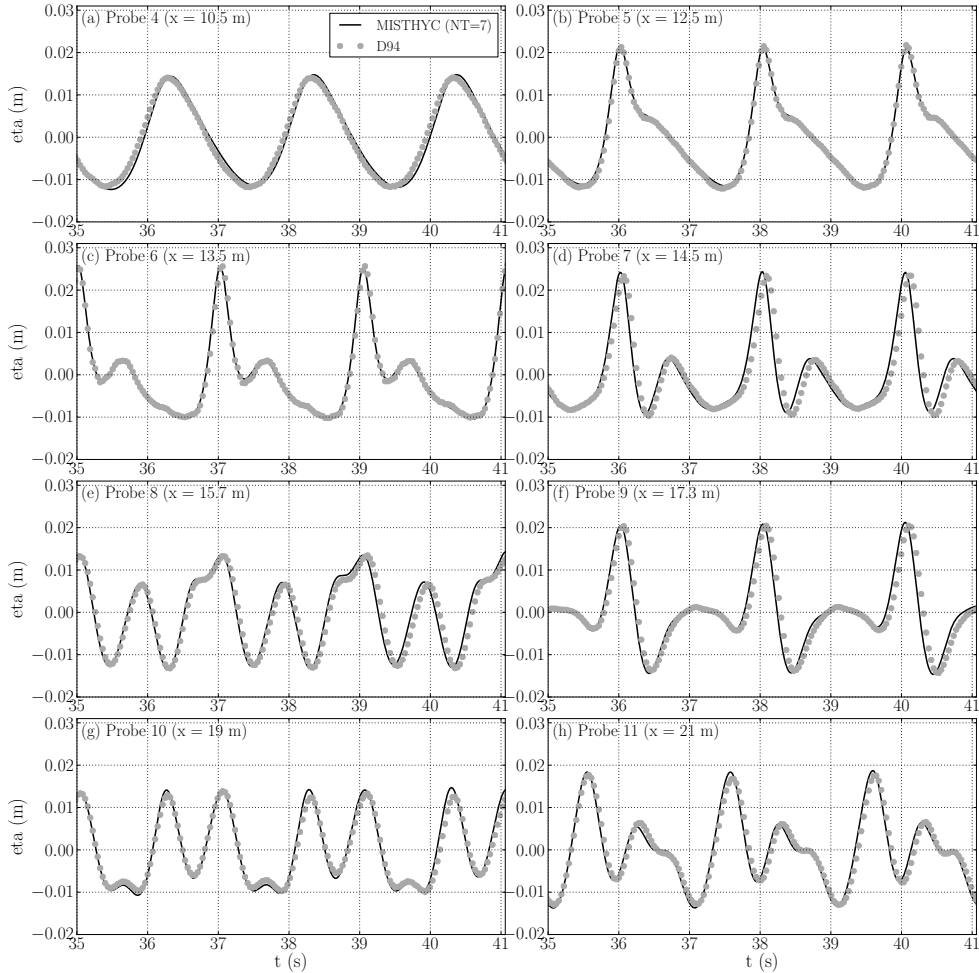


Figure 3.25: Comparison of measured and simulated (with $N_T = 7$) free surface elevation time series at probes 4 to 11 for case A of Dingemans (1994) (probe locations shown in Figure 3.24).

In order to examine more closely the energy transfers between harmonics, a Fourier analysis of the measured and computed wave signals was completed. The model accurately reproduces the spatial evolution of the amplitudes of the first six harmonics, corresponding to frequencies $f = 1/T$ (fundamental component) to $6f$ (Figure 3.26). The amplitude of the fundamental wave increases due to shoaling on the submerged bar up to the bar's crest and then decreases (starting from about $x = 12$ m) due to transfers of energy to higher harmonics. The observed oscillations (of ≈ 2 -2 m wavelength) are hypothesized to be caused by reflections in the wave channel. The amplitude of the second harmonic ($2f$) increases as the waves shoal on the front slope of the bar, and continues increasing until $x = 16$ m, after which its amplitude fluctuates. The higher harmonics start increasing in amplitude at shallower depths and have the largest amplitudes around the bar crest ($12 \leq x \leq 15$ m). Harmonics $4f$ to $6f$ decrease after the bar, which is not the case for harmonics $2f$ and $3f$. In addition, after the bar, the second harmonic has the largest

amplitude, and the amplitude of the third harmonic is nearly comparable to (though smaller than) that of the fundamental wave. The model results agree well with the data up to the sixth harmonic, with the exception of slight differences in the amplitude of the second harmonic at some locations (e.g. at $x = 19$ m).

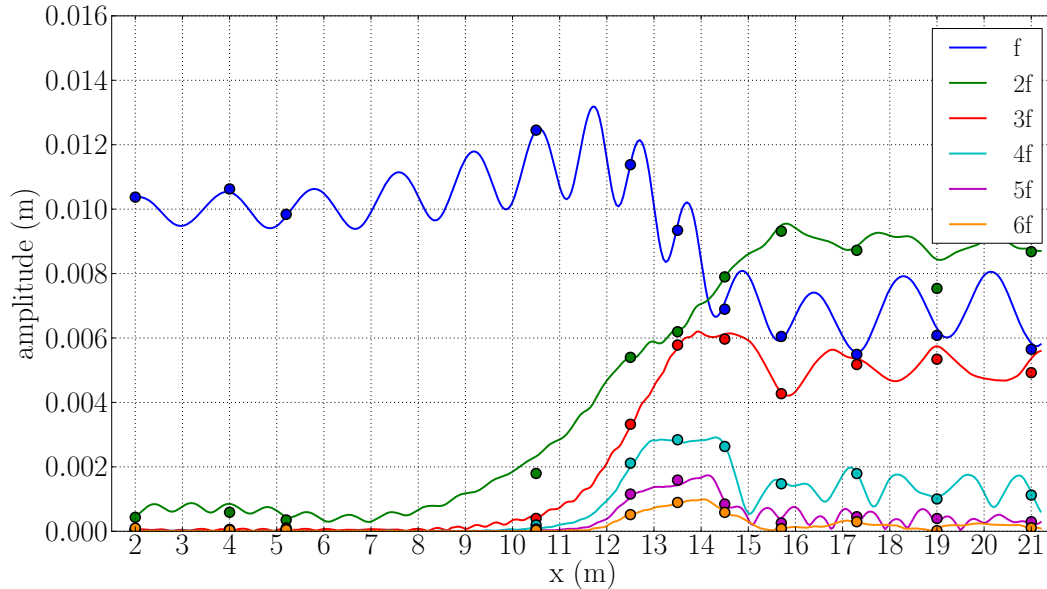


Figure 3.26: Spatial evolution of the first six harmonic amplitudes (at frequencies f , $2f$, ..., $6f$) of the free surface elevation for case A of Dingemans (1994): observations (circles) and Misthyc simulation results (solid lines).

To test the sensitivity of the model to the parameter N_T , simulations were run with $N_T = 3, 4, 5, 7$ and 10 (all other parameters were kept constant) and compared to the observations (Figure 3.27). In the offshore part of the flume and up to the submerged bar (i.e. up to probe 8), only the simulation results with $N_T = 3$ differ significantly from those with higher N_T , which are superimposed and agree well with the measured time series. At the last three probes, where dispersive effects are more important, the results with $N_T = 3, 4$ and 5 show increasing differences with the measurements. Results with $N_T = 7$ and 10 remain superimposed and in good agreement with the measurements at all probes. Therefore, $N_T = 7$ was chosen to optimize model's accuracy and efficiency.

In this test case, the model reproduces well the propagation of regular waves over a submerged bar, including the generation and propagation of higher harmonics. Dispersive effects become important after the bar, and time series of the free surface elevation differ significantly along the wave channel depending on the phase of the harmonic components. Values of $N_T \geq 7$ allow reproducing accurately the free surface elevation in the lee of the submerged bar, where dispersive effects are most important.

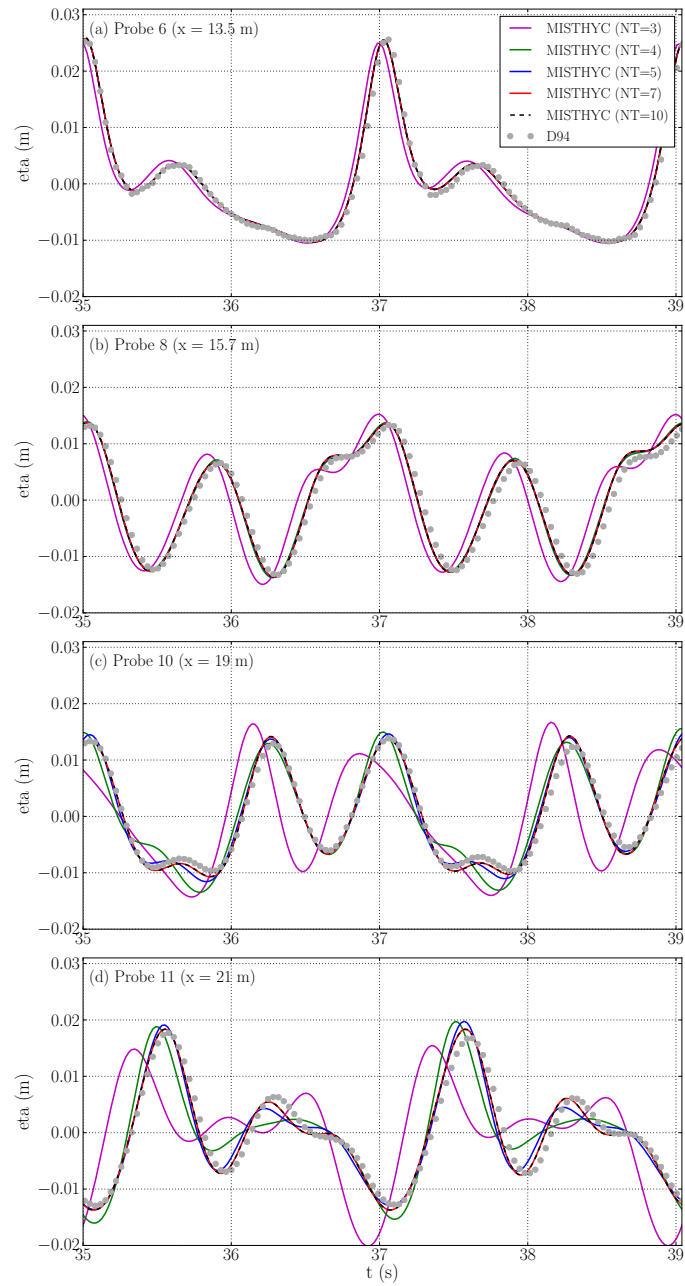


Figure 3.27: Comparison of measured and simulated free surface elevation time series at probes 6, 8, 10 and 11 for case A of Dingemans (1994). Results of simulations with 5 values of N_T (3, 4, 5, 7, 10) are compared (all other numerical parameters are constant).

3.6 Random waves over a barred beach

The last 1DH test case simulates the propagation of irregular nonlinear waves over a barred beach, reproducing the wave flume experiments of [Becq-Girard et al. \(1999\)](#) (B99). The bathymetric profile of these experiments (Figure 3.28) was specifically designed to study nonlinear wave interactions in shallow water. Irregular waves were generated with a piston-type random wavemaker using a JONSWAP wave spectrum with a peak-enhancement factor of $\gamma = 3.3$. The bottom profile was created with smooth metal sheets to minimize bottom friction dissipation, and a beach absorber was included on the upper part of the beach to reduce wave reflection. Resistive-type wave probes measured the free surface elevation at 16 locations in the wave flume (black dots, Figure 3.28) during the 40-minute experiment with a sampling time step $\Delta t = 0.07$ s.

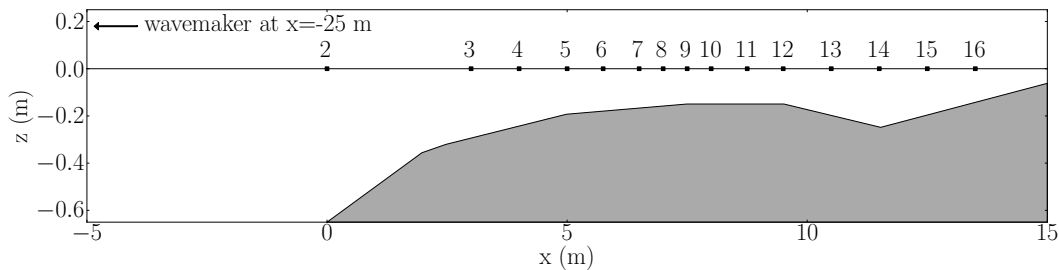


Figure 3.28: Bathymetry and wave probe positions for the [Becq-Girard et al. \(1999\)](#) experiments.

The model computational grid extends from $x = -5$ m to $x = 25$ m (with the foot of the bar at $x = 0$ m). Waves are generated in a 5-m relaxation zone by imposing the velocity potential at the left boundary and correcting the free surface position and velocity potential in the relaxation zone. Non-breaking irregular waves are simulated with significant wave height $H_{m0} = 3.4$ cm and peak period $T_p = 2.39$ s in the deepest part of the domain ($h = 0.65$ m). Waves are absorbed in a 10-m long relaxation zone at the right boundary. Time series of these variables are reconstructed using linear wave theory to sum the components of the wave spectrum obtained from the free surface measurements at probe 2 (located at the foot of the submerged bar). The computational grid is regularly meshed with $\Delta x = 0.05$ m, and $N_T = 7$. The total simulation time is 2380 s (approximately 39.7 min), with a time step equaling the sampling time step of the free surface elevation probes, $\Delta t = 0.07$ s.

The measured and simulated wave variance spectra agree well (Figure 3.29, spectra shown for probes 2, 5, 7, 9, 11, 13, 15, and 16). The main spectral peak increases from probes 2 to 5 due to wave shoaling. In addition, energy is transferred from lower to higher frequencies, particularly from the peak frequency to its super-harmonics. This phenomenon is visible at probe 5 with the appearance of the second harmonic peak ($2f_p$). When the water depth becomes nearly constant (probes 7, 9, and 11), the second and higher harmonic peaks become more pronounced. A peak at the fifth harmonic ($5f_p$) becomes visible in the spectra at probes 9 and 11, and its amplitude

is reproduced well by the model. On the back side of the bar, the energy transfer reverses back to the lower harmonics (in particular to the second harmonic). At probe 13, the peak of the fifth harmonic has disappeared, and at probe 15, the peaks of the third and fourth harmonics have also nearly disappeared. Only the second harmonic and main spectral peaks remain visible in the trough. Finally, at probe 16, the third harmonic ($3f_p$) peak reappears due to the new decrease in the water depth.

The simulated spatial evolution of the first five harmonic amplitudes agrees well with the experimental observations (Figure 3.30). In the deepest region, the amplitude of the first harmonic is dominant, and between 0 m and 5 m, its amplitude increases due to shoaling, while the higher harmonic amplitudes remain constant. After 5 m, the first harmonic amplitude decreases while the higher harmonic amplitudes increase due to transfers of energy from lower to higher frequencies. Around 9 m, the water depth increases again, the first harmonic amplitude continues decreasing, and the third, fourth, and fifth harmonic amplitudes also begin to decrease, with an energy transfer to the second harmonic. Finally, in the shallowest part of the domain, the energy transfer from the second to the third harmonic begins again. The oscillations visible in the first and second harmonic amplitudes are likely caused by reflections from the lateral boundaries.

To further evaluate the spatial spectral evolution, a set of integral wave parameters are calculated. From the variance density spectrum $E(f)$, the significant wave height $H_{m0} = 4\sqrt{m_0}$ and mean wave period $T_e = T_{m-1,0} = \frac{m-1}{m_0}$ or $T_{m0,2} = \left(\frac{m_0}{m_2}\right)^{\frac{1}{2}}$ can be expressed in terms of the n -th moment (m_n) of the variance density spectrum:

$$m_n = \int_0^{\infty} f^n E(f) df \quad (3.10)$$

The 0^{th} moment corresponds to the free surface elevation variance or $\sigma^2 = \langle(\eta - \langle\eta\rangle)^2\rangle$ where $\langle-\rangle$ denotes the time-average operator.

Nonlinear effects are also visible in the spatial evolution of these parameters, which are globally estimated well by the model (Figure 3.31). The significant wave height evolves similarly to the first harmonic amplitude shown in Figure 3.30. It increases as the waves shoal, decreases in the trough and finally increases again as the water depth decreases approaching the beach. The simulated H_{m0} agrees well with the measured values, with only a slight overestimation for $x > 7$ m, and a maximum difference of 8.8%. The evolution of the mean wave period is similar for the two definitions considered ($T_{m-1,0}$ and $T_{m0,2}$). The mean period initially decreases when a reduction in the energy in the low frequency range of the spectrum is compensated for by an increase in the high frequency range. The subsequent release of higher harmonics in the trough leads to an increase in the mean wave period that persists along the tank. The largest differences in mean period occur near the end of the tank, with errors of less than 3.5% and 7% for $T_{m-1,0}$ and $T_{m0,2}$, respectively.

To further analyze the simulated wave nonlinearity, higher order statistical moments were cal-

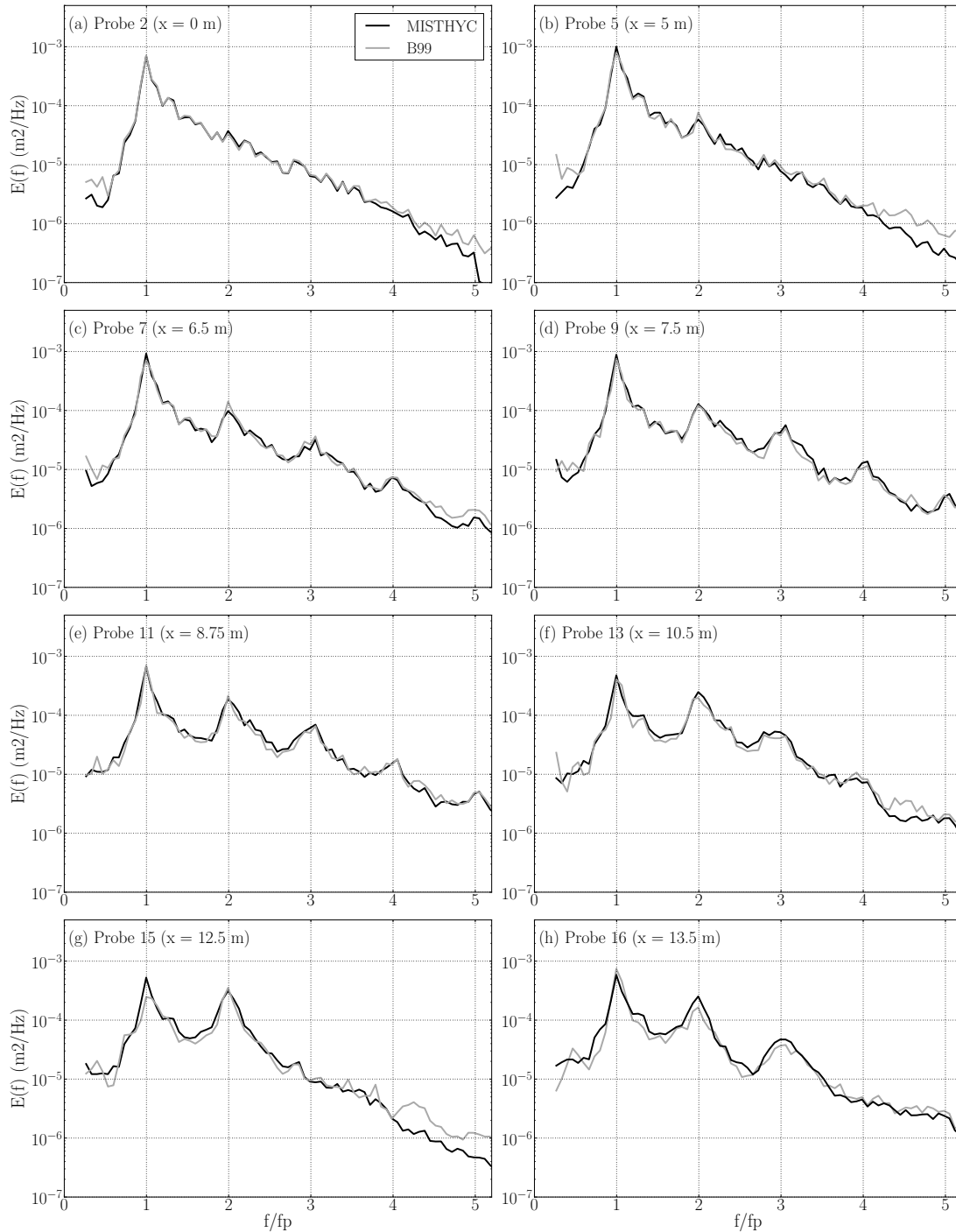


Figure 3.29: Comparison of the measured and simulated variance spectra of the free surface position at probes 2, 5, 7, 9, 11, 13, 15 and 16 for the [Becq-Girard et al. \(1999\)](#) experiments (probe positions, [Figure 3.28](#)). The frequency scale is normalized by the peak frequency (f_p) to identify clearly the harmonic peaks (e.g. $2f_p$, $3f_p$, ...).

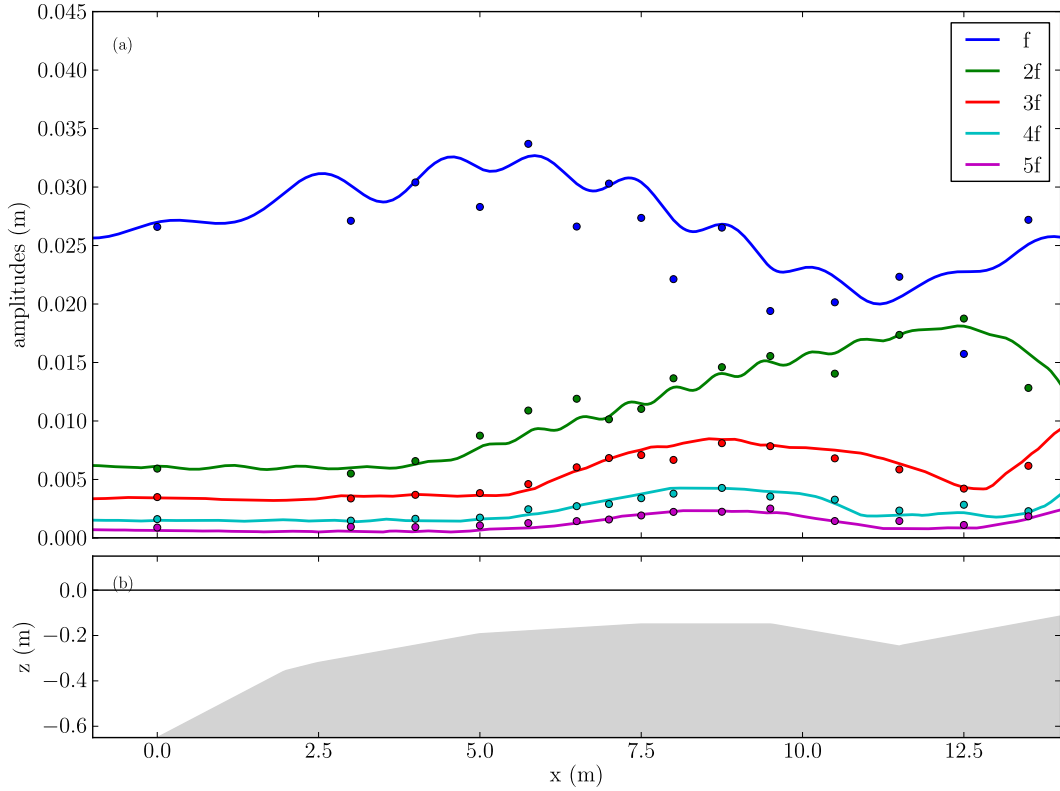


Figure 3.30: (a) Spatial evolution of the first five harmonic amplitudes for the [Becq-Girard et al. \(1999\)](#) experiments: observations (circles) and simulation results (Misthyc, solid lines). (b) Bathymetry.

culated from the free surface elevation time series, including:

- the skewness (S) or horizontal asymmetry coefficient, defined as the normalized, centered, third-order moment of the free surface elevation:

$$S = \frac{\langle (\eta - \langle \eta \rangle)^3 \rangle}{\sigma^3}. \quad (3.11)$$

It can also be defined as:

$$S = \frac{\sum_{m=-\infty}^{+\infty} \sum_{n=-\infty}^{+\infty} \text{Re}[B_{m,n}]}{m_0^{3/2}}, \quad (3.12)$$

where $B_{m,n}$ is the complex bispectrum.

- the vertical asymmetry coefficient (A):

$$A = \frac{\sum_{m=-\infty}^{+\infty} \sum_{n=-\infty}^{+\infty} \text{Im}[B_{m,n}]}{m_0^{3/2}}, \quad (3.13)$$

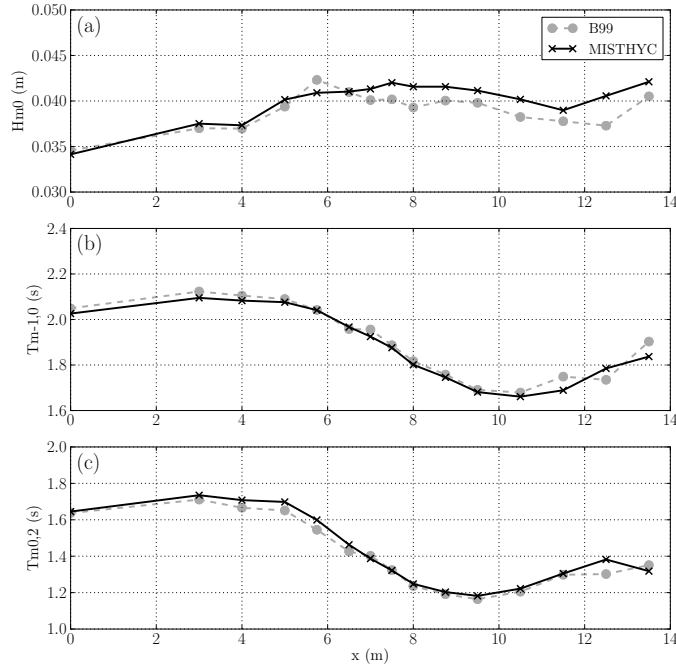


Figure 3.31: Comparison of simulated and measured sea state parameters along the bathymetric profile for the [Becq-Girard et al. \(1999\)](#) experiments: (a) significant wave height (H_{m0}), (b) mean wave period ($T_{m-1,0}$), and (c) mean wave period ($T_{m0,2}$).

- the kurtosis, which measures the flatness of the free surface elevation distribution and is related to the probability of occurrence of high waves, is defined as the normalized, centered, fourth-order moment of the free surface elevation:

$$K = \frac{\langle (\eta - \langle \eta \rangle)^4 \rangle}{\sigma^4}. \quad (3.14)$$

For a linear sea state, both the horizontal and vertical asymmetries are zero. Here (Figure 3.32), the simulated skewness and vertical asymmetry are approximately zero in the deepest part of the domain and evolve along the bathymetric profile in close agreement with the measurements. The spatial evolution of the kurtosis also begins with a value of approximately 3, typical of a linear (Gaussian) sea state, and then increases in shallower water, reaching a maximum in the shallowest zone. The model reproduces well the spatial evolution of the kurtosis, only slightly underestimating the maximum.

This last test case validates the ability of the model to simulate the generation, propagation, and absorption of irregular, non-breaking waves, including wave shoaling and nonlinear wave interactions causing the transfer of energy between higher and lower harmonics.

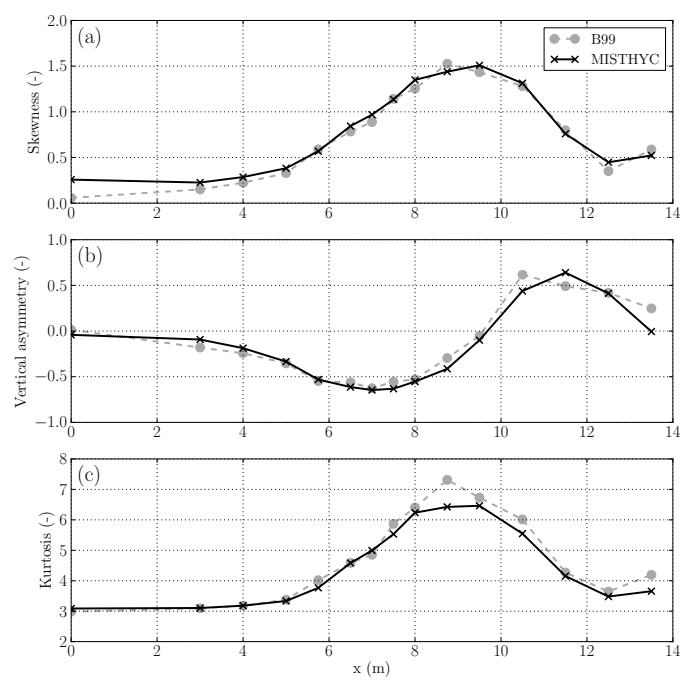


Figure 3.32: Comparison of simulated and measured sea state parameters along the bathymetric profile for the Becq-Girard et al. (1999) experiments: (a) skewness (or horizontal asymmetry), (b) vertical asymmetry, and (c) kurtosis.

Chapter 4

Modeling viscous dissipation: the visco-potential approach

Ce chapitre, consacré à la prise en compte des effets visqueux dans le modèle potentiel développé, commence par un bref aperçu des différentes sources de dissipation de l'énergie des vagues avec un accent mis sur les effets dissipatifs dus à la viscosité et les différentes approches existantes pour prendre en compte ces effets dans les modèles potentiels. Dans le modèle visco-potentiel retenu, la dissipation interne est prise en compte par l'ajout de deux termes dissipatifs dans les conditions aux limites à la surface libre provenant de la contribution principale de la composante rotationnelle de la vitesse. L'approximation de couche limite au niveau du fond, permet la dérivation d'un terme venant modifier la condition d'imperméabilité, modélisant la dissipation par frottement sur le fond. Ces développements sont ensuite validés par l'application à quatre cas tests. Les deux premiers cas consistent à comparer les résultats obtenus par la version linéaire du modèle avec des solutions analytiques pour la décroissance de vagues régulières se propageant dans un domaine périodique en profondeur infinie et d'une onde stationnaire pour différentes valeurs de profondeur relative (Antuono and Colagrossi, 2013). Le troisième cas test simule l'atténuation d'une onde solitaire se propageant sur un fond plat qui se termine par une pente, où l'effet combiné du shoaling et du frottement sur le fond est bien représenté par le modèle (Liu et al., 2006). Enfin, le dernier cas test consiste à reproduire les expériences réalisées récemment à l'ESPCI à petite échelle de vagues se propageant au-dessus d'une marche submergée. Dans ce cas, du fait du gradient important de bathymétrie, la validité du terme de frottement sur le fond n'est plus assurée. L'utilisation des termes de dissipation interne avec une valeur de viscosité plus élevée que celle de l'eau permet néanmoins d'obtenir des résultats proches des expériences.

4.1 Introduction

4.1.1 Review of sources of wave energy dissipation

Many mechanisms contribute to the dissipation of wave energy. Wave breaking is the most important sink of wave energy in the open ocean and in the coastal zone by dissipating energy through turbulence (e.g. [Ardhuin, 2012](#)). When the wave crest velocity exceeds the phase velocity of the wave, the wave becomes unstable and the crest collapses. Depending on the wave conditions (L , H) and bathymetry, different kinds of wave breaking may occur: spilling, collapsing, plunging and surging. The amplification of wave steepness leading to breaking can be induced by different processes. One must differentiate between depth-induced breaking occurring in shallow water caused by the convergence of the energy flux through shoaling (H/h) and deep water wave breaking (so-called white-capping) that is caused by the relative steepness of a wave (H/L) exceeding a threshold. Deep water wave breaking is often caused by interactions with the wind, or currents or between waves.

Aside from wave breaking, wave amplitudes decrease during propagation in the open ocean as well as in laboratory experiments. For non-breaking waves, three main processes lead to energy dissipation ([Lighthill, 1978](#)).

1. **Near-surface dissipation** is related to the difference between the instantaneous and equilibrium surface tension. This effect is usually negligible when the water surface is clean, but when it is fully contaminated (e.g. film of oil,...), the presence of a thin film at the surface changes the attenuation properties of the free surface (zero tangential velocity), and energy dissipation may become significant. The damping rate due to near surface dissipation can be even more important for partial contamination when a resonance occurs between capillary-gravity waves and elastic waves (Marangoni waves) on the surface film ([Henderson and Segur, 2013](#); [Przadka et al., 2015](#)). In laboratory experiments, the pollution of the water surface from ambient air conditions can modify the nature of the physical processes at the origin of the damping and may explain extra dissipation occurring in experiments where dissipation rates are too large to be attributed only to boundary layer effects ([Henderson and Segur, 2013](#); [Nicolás and Vega, 2000](#)). This can be avoided by cleaning the surface. When considering the dissipation of ocean swell, [Henderson and Segur \(2013\)](#) showed that a linear inextensible film model produces a better decay rate prediction than a clean surface model (i.e. [Lamb, 1932](#)) or a two-phase model (taking into account the air-water interface). The stress due to the action of the wind at the surface may induce additional energy dissipation ([Dore, 1978](#)).
2. **Internal dissipation by viscous stresses** acting throughout the water volume (also called bulk viscosity) is generally small for water waves but may be comparable with boundary layer damping in some cases ([Miles and Henderson, 1998](#)). These internal viscous effects can be estimated from the decrease in the wave height of deep water waves propagating

over long distance in the absence of wind.

3. **Interaction with solid boundaries** (i.e. bottom and lateral wall friction when considering laboratory experiments in a wave tank) also cause dissipation due to friction. The rotational motion induced in the oscillatory boundary layers that develop close to solid boundaries dissipates energy. Bottom friction becomes important when the water depth is shallow enough such that waves induce significant horizontal motions near the bottom.

According to [Dutykh \(2009a\)](#), the rate of viscous dissipation is $O(\nu^{3/2})$ in the free-surface boundary layer (for a clean water surface), $O(\nu)$ in the fluid interior from bulk viscosity, and $O(\nu^{1/2})$ in the bottom boundary layer, where ν is the kinematic viscosity of the fluid ($[m^2/s]$). The largest energy dissipation mechanism in the absence of wave breaking is bottom friction, when this phenomenon becomes important in intermediate and shallow water conditions.

4.1.2 Review of wave attenuation due to viscous effects

Different theoretical estimations of the wave damping have been derived depending on which sources of energy dissipation are taken into account: in infinite depth, only bulk viscosity is important, whereas in finite depth, solid boundary interactions must be also considered.

First, [Lamb \(1932\)](#) derived the decay rate for a wave amplitude a in infinite depth, assuming small viscosity, using two methods: first by a dissipation calculation and then by a direct calculation using the linearized Navier-Stokes equations, and obtained the same result. When the wave amplitude varies in time but is homogeneous in the entire domain (i.e. periodic waves in space), he estimated the following decay rate:

$$\frac{da}{dt} = -2\nu k^2 a \quad (4.1)$$

where k is the wave number. The wave amplitude at time t is therefore $a(t) = a(t=0) e^{-2\nu k^2 t}$. The amplitude decrease is exponential in time and faster for shorter waves (i.e. large k).

Later, [Biesel \(1949\)](#) considered the finite depth case, using zero normal pressure and zero tangential stress free surface boundary conditions, plus zero velocity at the bottom to derive an expression of the decay rate for the wave amplitude assuming very small viscosity and laminar flow. The obtained dispersion relation, expressing the complex angular frequency is expanded as a function of the viscosity ν , and only the terms of order $O(\sqrt{\nu})$ and $O(\nu)$ are kept. Surprisingly, [Biesel \(1949\)](#) found that in deep water conditions, even when the movement close to the bottom is very weak, the effect of bottom friction is not negligible.

[Hunt \(1952\)](#) then derived an expression for wave damping in a finite and uniform width b channel, in shallow water, to be able to estimate the total energy dissipation observed in laboratory

experiments. He took into account the dissipation of energy in the boundary layers near the bottom and the lateral walls.

$$a(t) = a(t = 0) e^{-\alpha t} \quad \text{with} \quad \alpha = \frac{2k}{b} \sqrt{\frac{\nu}{2\omega}} \left(\frac{kb + \sinh(2kh)}{2kh + \sinh(2kh)} \right) \quad (4.2)$$

In [Hunt \(1952\)](#), the case where the bottom has a mild slope is also considered.

More recently, [Behroozi \(2004\)](#) used the conservation of energy flux to derive a relationship between the fluid viscosity and waves attenuation, for a wave amplitude that varies in space, contrary to [Lamb \(1932\)](#). He considered that the wave amplitude is constant in time at a given location but varies in space as the waves propagate in the domain by using a complex wave number. The power loss per unit area due to viscous dissipation was estimated and equated to the power loss per unit area of the spatial decay in wave amplitude. The results were generalized to take into account the effects of surface tension.

With the objective of extending Lamb's results, [Antuono and Colagrossi \(2013\)](#) derived a new approximation of the decay rate of gravity waves in viscous fluid using the linearized Navier-Stokes equations. The objective was to both remove the assumption of infinite depth, making the approximation valid for waves propagating in intermediate and shallow water, and to relax the assumption of small viscosity. They completed a perturbation expansion of the angular frequency as a function of the Reynolds number Re ($Re = UL/\nu$, dimensionless quantity defined as the ratio of inertial forces to viscous forces) to obtain a complex expression for the wave damping. In deep water and at first order their decay rate corresponds to the one obtained by [Lamb \(1932\)](#). However, the second order term in their development is negative, such that Lamb's first-order solution overestimates the decay rate. In finite depth, the differences with Lamb's solution are even larger since Lamb's solution does not consider dissipation through bottom friction.

4.1.3 On the inclusion of viscous dissipation in potential modeling approaches

Potential flow theory (inviscid fluid and irrotational flow) reproduces well water wave propagation and is therefore a commonly used approach. However, it does not contain natural dissipation terms, as shown in the corresponding set of equations repeated from Section 1.1.2 (here, neglecting surface tension and with $p_{atm} = 0$):

$$\left\{ \begin{array}{ll} \Delta\Phi = 0 & \text{in the fluid domain} \quad (4.3) \\ \frac{\partial\Phi}{\partial t} + \frac{1}{2}(\nabla\Phi)^2 + g\eta + \frac{p_{atm}}{\rho} = 0 & \text{at } z = \eta(x, y, t) \quad (4.4) \\ \frac{\partial\eta}{\partial t} + \nabla_H\Phi \cdot \nabla_H\eta - \frac{\partial\Phi}{\partial z} = 0 & \text{at } z = \eta(x, y, t) \quad (4.5) \\ \nabla_H\Phi \cdot \nabla_H h + \frac{\partial\Phi}{\partial z} = 0 & \text{at } z = -h(x, y) \quad (4.6) \end{array} \right.$$

Here, the bottom is assumed to be fixed in time (but is variable in space).

In certain cases (long propagation times, shallow water...), viscous effects cannot be neglected to reproduce correctly wave evolution during propagation. Viscosity causes a decrease in the wave amplitude but also alters the speed and shape of the wave. Moreover, to estimate accurately the bottom shear stress and to compute sediment transport fluxes and the induced changes in the bathymetry, viscous effects must be taken into account. One alternative is to resolve the full Navier-Stokes equations using a three-phase (air, water and sediment) model, but this approach is generally computationally expensive and only allows simulating a few wavelengths. [Lu et al. \(2010\)](#) studied the resonance of incident waves in narrow gaps between identical bodies. They compared the results obtained with (i) a viscous fluid model and (ii) a potential flow model including artificial viscous damping, and showed that the results obtained with both models are similar. The wave height in the narrow gap can be predicted correctly as long as the damping coefficient is properly calibrated. Two important questions are then, how to narrow the gap between the Navier-Stokes equations and the potential flow equations, and what kind of physically relevant dissipative terms should be included?

In infinite depth, potential flow is a solution of the Navier-Stokes equations, but to take into account the effects of viscosity, the boundary conditions of the potential flow problem have to be modified. The zero normal stress condition at the free surface can be still satisfied with irrotational flow. This is not the case for the zero tangential stress condition, thus vorticity has to be introduced in the model. [Dias et al. \(2008\)](#), following the work of [Lamb \(1932\)](#), introduced a Helmholtz decomposition of the velocity in the linearized Navier-Stokes equations to separate the vortical and potential flow contributions. They showed that the vortical velocity can be expressed asymptotically as a function of the velocity potential and the free surface elevation. A new set of equations was derived with viscous correction terms added in the KFSBC and DFSBC. They extended their set of equations with the addition of nonlinear terms by conjecturing that the expression of the dissipative term as a function of the surface elevation in the KFSBC is still valid when the viscosity is small. By deriving the Non Linear Schrödinger (NLS) equation from their model, they obtained the widely used damped NLS equation. This set of equations has been used by [Chen and Dias \(2010\)](#) to study time harmonic ship waves (after deriving a new

boundary condition only satisfied by the velocity potential by combining the linear KFSBC and DFSBC of [Dias et al. \(2008\)](#) and introducing the effects of surface tension). In the limit of small viscosity, the solution of [Chen and Dias \(2010\)](#) leads to the same decay rate as that of [Lamb \(1932\)](#).

[Longuet-Higgins \(1992\)](#) also re-derived the same decay rate but with another physical interpretation. By assuming that viscous effects are confined to a vortical boundary layer close to the free surface, the zero tangential stress condition at the free surface leads to an increase in the surface elevation that contributes to the normal stress, in addition to the classic viscous component of the normal stress. Thus, the zero normal stress condition applied at the free surface boundary corresponds to a pressure correction that is twice the one obtained when not taking into account the vortical boundary layer at the free surface.

[Joseph and Wang \(2004\)](#) first derived the decay rate of gravity waves by solving the stability problem corresponding to the set of equations formed by the Laplace equation in the domain, the Bernoulli equation at the free surface and the normal stress balance at the free surface. The decay rate obtained with this method is half the one found by [Lamb \(1932\)](#) in the limit of long waves. The authors discovered that for long waves, a vorticity layer is created close to the surface, and a correction to the irrotational pressure is needed to satisfy the zero shear stress boundary condition and compensate for the irrotational shear stress. With this correction, [Joseph and Wang \(2004\)](#) obtained the same decay rate as Lamb.

In the case of finite depth, a boundary layer approach is applied at the bottom. In this boundary layer, vorticity is introduced to satisfy the no-slip (zero velocity) boundary condition at the bottom. The boundary layer is assumed laminar, and the flow is assumed irrotational outside the boundary layer. [Liu and Orfila \(2004\)](#) derived a new kinematic bottom boundary condition for the velocity potential with a non local term in time (convolution integral) scaling as $O(\sqrt{\nu})$. This condition can be seen as a correction of the vertical velocity at the bottom, corresponding to the potential flow problem, due to the vertical rotational velocity induced in the boundary layer. The derived model with the Boussinesq approximation has been validated with comparison to experimental data to study viscous damping and shoaling of a solitary wave in a wave tank ([Liu et al., 2006](#)). For this study the derived expression was extended from constant water depth to slowly varying water depth. The study of the laminar bottom boundary layer flow under a solitary wave ([Liu et al., 2007](#)) shows that the nonlinear advection terms have a weak impact on the results. The model was further improved to take into account a turbulent bottom boundary layer ([Simarro et al., 2009](#)). In parallel, [Dutykh and Dias \(2007\)](#) derived the same bottom boundary condition with the addition of to bulk viscosity dissipative terms scaling as $O(\nu)$. The study of the time-dependent dispersion relation associated with the long wave model derived from the new potential flow equations first is complete assuming a slowly varying rotational frequency with time ([Dutykh, 2009a](#)), and then with a relaxation of this assumption ([Dutykh, 2009b](#)). The

last paper showed that the local dissipative terms in the KFSBC and the DFSBC have a stabilizing effect, whereas the non-local term in the bottom boundary layer creates modes with a positive imaginary part that have a destabilizing effect.

Generally, the new sets of visco-potential equations (Dutykh and Dias, 2007; Liu and Orfila, 2004) are not solved directly. Boussinesq-type “lighter” long wave models are often derived, since the derivation from the inviscid potential equations is easier than that from the complete Navier-Stokes equations. A review of the derivation of asymptotic models taking into account viscosity is presented in Le Meur (2015). He pointed out two difficulties in completing a rigorous derivation of the asymptotic model: (i) matching the boundary layer solution and the potential flow solution in the interior of the domain, and (ii) the resolution of Cauchy problem with an initial condition. He then presented the derivation of a Boussinesq model from the Navier-Stokes equations without the irrotationality assumption, with special care dedicated to the treatment of the initial solution for the half derivative.

Kakleas and Nicholls (2010) restate the set of equations from Dias et al. (2008) in terms of the free surface quantities (η and $\tilde{\phi}$) to obtain a Zakharov-like set of equations taking into account viscosity in infinite depth. They developed the related Dirichlet-to-Neumann operator up to the second order in nonlinearity to obtain a weakly nonlinear model for small values of viscosity.

In this chapter, the dissipative terms to be added to the classical potential flow equations (Eq.(4.3)-Eq.(4.6)) are re-derived to take into account the dissipation due to both bulk viscosity and bottom friction. Then the implementation of the free surface dissipative terms and of the non-local term in the bottom boundary condition is presented. With a linear version of the code, the damping rate is studied for two cases: (1) regular waves propagating over a flat bottom with only the bulk viscosity contribution to the dissipation, and (2) standing waves evolving in several relative depths and Reynolds numbers following Antuono and Colagrossi (2013). The nonlinear version of the code augmented with viscous terms derived under the linear assumption is then validated with a comparison to laboratory experiments for the propagation of a solitary wave attenuated by bottom friction in Liu et al. (2006). Finally the model is used to study the dissipation of regular waves propagating over a step to small-scale experiments performed by Monsalve et al. (2015).

4.2 Mathematical modeling of visco-potential flows

4.2.1 Linearized Navier-Stokes system

The derivation of the dissipative terms is carried out for the simplified case of linear theory. In this context, the free surface flow in a fluid layer of constant depth (h), whose free surface displacement is denoted by η , can be described by the continuity equation and the linearized 3D

incompressible Navier-Stokes equations in the fluid domain (Ω):

$$\begin{cases} \nabla \cdot \underline{v} = 0 \\ \frac{\partial \underline{v}}{\partial t} = -\frac{\nabla p}{\rho} + \underline{g} + \nu \Delta \underline{v} \end{cases} \quad (4.7)$$

$$(4.8)$$

where \underline{v} is the velocity vector. These equations are supplemented by appropriate boundary conditions:

- a no-slip condition at the bottom : $\underline{v}(z = -h) = \underline{0}$,
- a linearized kinematic condition at the free surface $\frac{\partial \eta}{\partial t} = w$, and
- a dynamic condition at the free surface $[\underline{\sigma} \cdot \underline{n}] = 0$, where $\underline{\sigma} = -p\underline{n} + \underline{\tau} \cdot \underline{n}$ is the stress tensor and $\underline{\tau} = (\tau_{i,j}) = \rho\nu(\partial v_i/\partial x_j + \partial v_j/\partial x_i)$ is the viscous tensor. $[f]$ denotes the jump of the function f across the interface, and \underline{n} is the unit vector normal to the interface. The dynamic condition at the free surface is decomposed into three conditions corresponding to the tangential components (σ_{xz} and σ_{yz}) and the normal component (σ_{zz}) of the stress at the free surface.

4.2.2 Dissipation due to bulk viscosity

In this section, the derivation of dissipative terms to model dissipation due to bulk viscosity in potential flow equations is shown, following the work of [Dias et al. \(2008\)](#), who derived this new set of equation for 1DH cases in infinite depth, and of [Dutykh and Dias \(2007\)](#) who extended it to 3D cases in finite depth. The main contribution of the vortical component of the velocity in the KFSBC can be expressed as a dissipative term that depends only on the free surface elevation, and is negligible in comparison to the velocity potential contribution in the DFSBC.

4.2.2.1 Velocity decomposition

In order to decouple the problem, the Helmholtz-Leray decomposition is applied to the velocity field $\underline{v} = (u, v, w)$ dividing it into a potential (irrotational) component and a rotational component:

$$\underline{v} = \nabla \Phi + \nabla \wedge \underline{\Psi} \quad \text{with} \quad \underline{\Psi} = (\Psi_1, \Psi_2, \Psi_3) \quad (4.9)$$

$$(4.10)$$

$$\text{hence } \underline{v} = \begin{pmatrix} \frac{\partial \Phi}{\partial x} + \frac{\partial \Psi_3}{\partial y} - \frac{\partial \Psi_2}{\partial z} \\ \frac{\partial \Phi}{\partial y} + \frac{\partial \Psi_1}{\partial z} - \frac{\partial \Psi_3}{\partial x} \\ \frac{\partial \Phi}{\partial z} + \frac{\partial \Psi_2}{\partial x} - \frac{\partial \Psi_1}{\partial y} \end{pmatrix} \quad (4.11)$$

where Φ is the velocity potential and $\underline{\Psi}$ the vector stream function. Substitution of this decomposition (Eq.(4.11)) into the continuity equation (Eq.(4.7)) gives:

$$\nabla \cdot (\nabla \Phi + \nabla \wedge \underline{\Psi}) = 0$$

$$\Delta \Phi + \underbrace{\nabla \cdot (\nabla \wedge \underline{\Psi})}_{=0 \text{ by def}} = 0,$$

$$\Delta \Phi = 0. \quad (4.12)$$

Similarly, the momentum equation (Eq.(4.8)) can be rewritten as:

$$\frac{\partial(\nabla \Phi + \nabla \wedge \underline{\Psi})}{\partial t} = -\frac{\nabla p}{\rho} + \underline{g} + \nu \Delta(\nabla \Phi + \nabla \wedge \underline{\Psi})$$

$$\frac{\partial \nabla \Phi}{\partial t} + \frac{\nabla p}{\rho} + \nabla gz + \nu \Delta(\nabla \Phi) = -\frac{\partial \nabla \wedge \underline{\Psi} + \nu \Delta(\nabla \wedge \underline{\Psi})}{\partial t}$$

$$\frac{\partial \nabla \Phi}{\partial t} + \frac{\nabla p}{\rho} + \nabla gz + \nu [\underbrace{\nabla \cdot (\nabla \Phi)}_{=0 \text{ by (4.12)}} - \nabla \wedge \underbrace{(\nabla \wedge (\nabla \Phi))}_{=0 \text{ by def}}] = -\nabla \wedge \frac{\partial \underline{\Psi}}{\partial t} + \nu \nabla \wedge (\Delta \underline{\Psi})$$

$$\nabla \left(\frac{\partial \Phi}{\partial t} + \frac{p}{\rho} + gz \right) = \nabla \wedge \left(-\frac{\partial \underline{\Psi}}{\partial t} + \nu \Delta \underline{\Psi} \right) \quad (4.13)$$

One can notice that Eq.(4.13) is satisfied, if Φ and $\underline{\Psi}$ also satisfy:

$$\begin{cases} \frac{\partial \Phi}{\partial t} + \frac{p}{\rho} + gz = 0 & \text{(a)} \\ \frac{\partial \underline{\Psi}}{\partial t} - \nu \Delta \underline{\Psi} = \underline{0} & \text{(b)} \end{cases} \quad (4.14)$$

To determine the structure of Φ and $\underline{\Psi}$, the Fourier-Laplace transform of Eq.(4.12) and Eq.(4.14b)

is taken to work in (\underline{k}, s) space. The Fourier-Laplace transform is defined as:

$$L_F = L \circ F \text{ such that } f(\underline{x}, t) \longrightarrow \hat{f}(\underline{k}, s), \text{ with } \underline{k} = (k_x, k_y) \text{ and } k = |\underline{k}|$$

Applying the Fourier-Laplace transform to the continuity equation gives:

$$\Delta \hat{\Phi} = 0 \longrightarrow -k^2 \hat{\Phi} + \frac{\partial^2 \hat{\Phi}}{\partial z^2} = 0$$

The solution to this equation can be written as:

$$\hat{\Phi}(\underline{k}, s) = \hat{\varphi}_0^+(\underline{k}, s)e^{kz} + \hat{\varphi}_0^-(\underline{k}, s)e^{-kz},$$

where $\hat{\varphi}_0^+$ and $\hat{\varphi}_0^-$ are unknown functions of \underline{k} and s .

The Fourier-Laplace transform applied to Eq.(4.14b) gives:

$$\frac{\partial \underline{\Psi}}{\partial t} = \nu \Delta \underline{\Psi} \longrightarrow s \hat{\underline{\psi}} = \nu(-k^2 \hat{\underline{\psi}} + \frac{\partial^2 \hat{\underline{\psi}}}{\partial z^2}),$$

whose solution is:

$$\hat{\psi}_i(\underline{k}, s) = \hat{\psi}_{i0}(\underline{k}, s) \left(e^{|m|z} + C_i(\underline{k}, s)e^{-|m|z} \right),$$

with $m^2 = k^2 + s/\nu$, and $\hat{\psi}_{i0}$ ($i = 1, 3$) and C_i ($i = 1, 3$) are unknown functions that will be determined by using the initial and boundary conditions.

4.2.2.2 Modification of the kinematic free surface condition

Now the goal is to investigate how the vortical term impacts the KFSBC. With the velocity decomposition presented in 4.2.2.1, the KFSBC becomes:

$$\frac{\partial \eta}{\partial t} = w = \frac{\partial \Phi}{\partial z} + \frac{\partial \Psi_2}{\partial x} - \frac{\partial \Psi_1}{\partial y} \text{ on } z = 0$$

When applying the Fourier-Laplace transform, this expression becomes:

$$s \hat{\eta} = k(\hat{\varphi}_0^+ - \hat{\varphi}_0^-) + ik_y \hat{\psi}_{10}(1 + C_1) - ik_x \hat{\psi}_{20}(1 + C_2) \quad (4.15)$$

To see if the vortical term in Eq.(4.15) can be expressed as a function of Φ and η only, the tangential stresses at the free surface must be continuous across the interface (here at $z = 0$, following linear theory):

$$\sigma_{xz} = \rho \nu \left(\frac{\partial w}{\partial x} + \frac{\partial u}{\partial z} \right) = 0 \quad (4.16)$$

$$\sigma_{yz} = \rho\nu\left(\frac{\partial w}{\partial y} + \frac{\partial v}{\partial z}\right) = 0 \quad (4.17)$$

After substitution of the decomposition of \mathbf{v} , the Fourier-Laplace transform of Eq.(4.16) and Eq.(4.17) are:

$$-2ik_x \frac{\partial \hat{\varphi}}{\partial z} - k_x^2 \hat{\psi}_2 + k_x k_y \hat{\psi}_1 - ik_y \frac{\partial \hat{\psi}_3}{\partial z} - \frac{\partial^2 \hat{\psi}_2}{\partial z^2} = 0 \quad (4.18)$$

$$-2ik_y \frac{\partial \hat{\varphi}}{\partial z} - k_x k_y \hat{\psi}_2 + k_y^2 \hat{\psi}_1 + \frac{\partial^2 \hat{\psi}_1}{\partial z^2} + ik_x \frac{\partial \hat{\psi}_3}{\partial z} = 0 \quad (4.19)$$

Combining these two equations as $(-ik_x)(4.18) + (-ik_y)(4.19)$ produces an expression relating the vortical term of Eq.(4.15) and the irrotational velocity.

$$ik_y \hat{\psi}_{10}(1 + C_1) - ik_x \hat{\psi}_{20}(1 + C_2) = -\frac{2k^3(\hat{\varphi}_0^+ - \hat{\varphi}_0^-)}{k^2 + m^2} \quad (4.20)$$

Eq.(4.15) and Eq.(4.20) can be combined and rearranged to express of the vortical part of the KFSBC as a function of $\hat{\eta}$ only:

$$ik_y \hat{\psi}_{10}(1 + C_1) - ik_x \hat{\psi}_{20}(1 + C_2) = -2\nu k^2 \hat{\eta}. \quad (4.21)$$

Substituting Eq.(4.20) in Eq.(4.15) gives a KFSBC expressed only as a function of the potential flow problem variables:

$$s\hat{\eta} = k(\hat{\varphi}_0^+ - \hat{\varphi}_0^-) - 2\nu k^2 \hat{\eta}. \quad (4.22)$$

By taking the inverse Fourier-Laplace transform of Eq.(4.22), this expression becomes:

$$\frac{\partial \eta}{\partial t} = \frac{\partial \Phi}{\partial z} + 2\nu \Delta_H \eta. \quad (4.23)$$

This expression is the KFSBC of the irrotational linearized Euler problem with an additional diffusive term coming from the vortical velocity contribution.

4.2.2.3 Modification of the dynamic free surface condition

The condition for the normal stress at the free surface ($\sigma_{zz} = 0$ at $z = 0$) gives the following expression for the pressure at the free surface:

$$p = 2\rho\nu \left(\frac{\partial^2 \Phi}{\partial z^2} + \frac{\partial^2 \Psi_2}{\partial z \partial x} - \frac{\partial^2 \Psi_1}{\partial z \partial y} \right) \quad \text{at } z = 0. \quad (4.24)$$

The Fourier-Laplace transform of this equation is:

$$\hat{p} = 2\rho\nu \left(-k^2(\hat{\varphi}_0^+ - \hat{\varphi}_0^-) + m(-ik_x\hat{\psi}_{20}(1 - C_2) + ik_y\hat{\psi}_{10}(1 - C_1)) \right). \quad (4.25)$$

Now the order of each term is evaluated. Eq.(4.21) shows that $(-ik_x\hat{\psi}_{20}(1 + C_2) + ik_y\hat{\psi}_{10}(1 + C_1)) = O(\nu)$. [Dutykh and Dias \(2007\)](#) argue that the second term of the right-hand side of Eq.(4.25) is $O(\nu^{3/2})$, which is negligible in comparison with the first term which is $O(\nu)$, when weak dissipation is considered (typically $\nu \in [10^{-6}; 10^{-3}] m^2/s$). In the following developments, terms of the order of $o(\nu)$ will be neglected. Inferring this from Eq.(4.21) is not so immediate but considering both extreme cases where C_1 and C_2 are either $\ll 1$ or $\gg 1$, $-ik_x\hat{\psi}_{20}(1 - C_2) + ik_y\hat{\psi}_{10}(1 - C_1)$ can be considered as $O(\nu)$. Since $m = O(\nu^{-1/2})$, the second term of the right hand side of Eq.(4.25) is actually $O(\nu^{3/2})$. Taking the inverse Fourier-Laplace transform of Eq.(4.25), the pressure at the free surface at the leading order in ν is thus:

$$p = 2\rho\nu \frac{\partial^2 \Phi}{\partial z^2} \quad \text{at } z = 0. \quad (4.26)$$

This pressure can be considered as a correction of the pressure in the Bernoulli equation, which is the DFSBC of the potential flow approach. Therefore the new DFSBC can be written as:

$$\frac{\partial \Phi}{\partial t} + g\eta + 2\nu \frac{\partial^2 \Phi}{\partial z^2} = 0 \quad \text{at } z = 0. \quad (4.27)$$

Finally, the two free surface conditions of the linearized irrotational Euler problem can be completed with dissipative terms to take into account the effects of bulk viscosity:

$$\frac{\partial \eta}{\partial t} = \frac{\partial \Phi}{\partial z} + 2\nu \Delta_H \eta \quad \text{at } z = 0, \quad (4.28)$$

$$\frac{\partial \Phi}{\partial t} = -g\eta - 2\nu \frac{\partial^2 \Phi}{\partial z^2} \quad \text{at } z = 0. \quad (4.29)$$

[Dias et al. \(2008\)](#) obtained these equations for the linear case, and extended them heuristically to the nonlinear case by keeping the same expressions of the additional dissipative terms in the nonlinear DFSBC and KFSBC (by conjecturing that the expression of the dissipative term as a function of η in the KFSBC is still valid when the viscosity is small).

4.2.3 Dissipation due to bottom friction

The two dissipative terms added to the irrotational Euler free surface boundary conditions, derived in the previous section, account for the dissipation due to the bulk viscosity. However, the predominant source of dissipation in shallow water is bottom friction. To take into account this dissipation source, a boundary layer correction is introduced at the bottom. This correction estimates the impacts of the rotational part of the vertical velocity induced in the boundary layer

on the flow in the interior (Dutykh and Dias, 2007; Liu and Orfila, 2004). Although the fluid motion is described well by potential theory in the interior of the fluid domain, this is not the case anymore close to the bottom, due to viscous effects. In potential flow theory, the condition of impermeability at the bottom implies a tangential velocity component, whereas when considering the boundary layer, this condition is replaced by a no-slip condition at the bottom. To fulfill this condition, a horizontal rotational velocity component of the same order of magnitude as the horizontal velocity in the interior of the fluid domain appears in the bottom boundary layer, which generates a vertical velocity component that persists outside the boundary layer (Liu and Orfila, 2004). It is this vertical rotational component that is evaluated hereafter to determine the correction of the impermeability condition of the potential problem at the bottom boundary.

4.2.3.1 Nondimensional equations

Based on the work of Liu and Orfila (2004), a wave train with surface displacement η , with amplitude a and wavelength l , in a constant water depth h is considered. The following dimensionless variables (denoted by $*$) are defined:

$$\begin{aligned} (x^*, y^*) &= \frac{(x, y)}{l} & z^* &= \frac{z}{h} & t^* &= \frac{t\sqrt{gh}}{l} & \eta^* &= \frac{\eta}{a} & p^* &= \frac{p}{\rho gh} \\ (u^*, v^*) &= \frac{(u, v)}{\sqrt{gh}} & w^* &= \frac{w}{\mu\sqrt{gh}}, \end{aligned}$$

where $\mu = h/l$ is a parameter quantifying the dispersion. In comparison to Liu and Orfila (2004), some slight differences in the nondimensionalization may be noticed. The small parameter $\epsilon = a/h$ does not appear here since the problem was already linearized. In addition, here $O(w^*) = O(\mu u^*)$ which is, in our opinion, more consistent with the physics than the choice of $O(w^*) = O(u^*/\mu)$ by Liu and Orfila (2004). While the intermediate steps differ, this nondimensionalization leads to the same bottom correction term in dimensional space as in Liu and Orfila (2004) and Dutykh and Dias (2007). In the following, the dimensionless equations are considered, after dropping the $*$ to facilitate reading. The dimensionless continuity equation remains unchanged:

$$\nabla_H \cdot \underline{u} + \frac{\partial w}{\partial z} = 0 \quad (4.30)$$

with $\underline{u} = (u, v)$. The dimensionless linear Navier-Stokes equations are:

$$\frac{\partial \underline{u}}{\partial t} = -\nabla_H p + \alpha^2 \left(\Delta_h \underline{u} + \frac{1}{\mu^2} \frac{\partial^2 \underline{u}}{\partial z^2} \right), \quad (4.31)$$

$$\mu^2 \frac{\partial w}{\partial t} = -\frac{\partial p}{\partial z} - 1 + \mu^2 \alpha^2 \left(\Delta_h w + \frac{1}{\mu^2} \frac{\partial^2 w}{\partial z^2} \right), \quad (4.32)$$

where Δ_h is the horizontal Laplacian operator and $\alpha^2 = \frac{\nu}{l\sqrt{gh}}$ is the dimensionless viscosity (i.e. equivalent to the inverse of a Reynolds number).

4.2.3.2 Bottom boundary layer approximation

The Helmholtz decomposition is again applied to the velocity: $\underline{v} = \nabla\Phi + \underline{v}^r$, where the vortical component is now expressed as $\underline{v}^r = (\underline{u}^r, w^r)$, such that $\nabla \cdot \underline{v}^r = 0$. The rotational part of the velocity is assumed to vary rapidly in the direction normal to the bottom, in the boundary layer of thickness $O(\alpha)$, and the potential flow needs to be corrected at order $O(\alpha)$. Thus the following perturbation expansions of the potential and the velocities are introduced:

$$\Phi = \Phi_0 + \alpha\Phi_1 + o(\alpha), \quad (4.33)$$

$$\underline{u}^r = \underline{u}_0^r + \alpha\underline{u}_1^r + o(\alpha), \quad (4.34)$$

$$w^r = w_0^r + \alpha w_1^r + o(\alpha). \quad (4.35)$$

To focus on the flow inside the bottom boundary layer, a new vertical coordinate is introduced:

$$\xi = \frac{z+1}{\alpha}, \quad (4.36)$$

where $\xi = 0$ corresponds to the solid boundary. This change of coordinate is only applied for the vortical velocity.

Substituting the expansion of the rotational part of the velocity in the continuity equation gives at zero and first order in α :

$$O(1) : \frac{\partial w_0^r}{\partial \xi} = 0 \quad (4.37)$$

$$O(\alpha) : \nabla_H \underline{u}_0^r + \frac{\partial w_1^r}{\partial \xi} = 0 \quad (4.38)$$

Eq.(4.37) shows that w_0^r is independent of the vertical coordinate, and thus with the no-slip condition at the bottom ($\underline{v} = \underline{0}$), the following relations at the zero and first order in α can be written:

$$O(1) : \nabla_H \Phi_0 = -\underline{u}_0^r \quad \text{and} \quad \frac{\partial \Phi_0}{\partial z} = -w_0^r \quad (4.39)$$

$$O(\alpha) : \nabla_H \Phi_1 = -\underline{u}_1^r \quad \text{and} \quad \frac{\partial \Phi_1}{\partial z} = -w_1^r \quad (4.40)$$

The no-flux condition at the bottom of the potential flow problem implies that $\frac{\partial \Phi_0}{\partial z} = 0$. Therefore, $w_0^r = 0$ at the bottom and throughout the whole boundary layer because of Eq.(4.37). The correction to the bottom boundary condition is thus the term $-w_1^r$. Looking for the leading order

in α of the momentum equation for the horizontal rotational velocity gives:

$$\frac{\partial \underline{u}_0^r}{\partial t} = \frac{1}{\mu^2} \frac{\partial^2 \underline{u}_0^r}{\partial \xi^2}. \quad (4.41)$$

After the coordinate change $\beta = \mu\xi$, Eq.(4.41) becomes:

$$\frac{\partial \underline{u}_0^r}{\partial t} = \frac{\partial^2 \underline{u}_0^r}{\partial \beta^2}. \quad (4.42)$$

The boundary conditions for the horizontal rotational flow are known: Eq.(4.39) at the bottom, and $\underline{u}_0^r \rightarrow 0$ as $\beta \rightarrow +\infty$. Following Liu and Orfila (2004) and Dutykh and Dias (2007), the solution of Eq.(4.42) is:

$$\underline{u}_0^r = -\frac{\beta}{\sqrt{4\pi}} \int_0^t \frac{\nabla_H \Phi(\underline{x}, z = -1, \tau)}{\sqrt{t-\tau}^3} e^{-\frac{\beta^2}{4(t-\tau)}} d\tau. \quad (4.43)$$

Then, from the continuity equation (Eq.(4.38)) and with substitution for β :

$$w_1^r(\xi = 0) = -\frac{1}{\mu\sqrt{\pi}} \int_0^t \frac{\nabla_H^2 \Phi(\underline{x}, z = -1, \tau)}{\sqrt{t-\tau}} d\tau. \quad (4.44)$$

From the no-flux bottom boundary condition (Eq.(4.40)), the expression of the correction of the potential vertical velocity at the bottom is obtained:

$$\frac{\partial \Phi}{\partial z}(z = -1) = -\alpha w_1^r = \frac{\alpha}{\mu\sqrt{\pi}} \int_0^t \frac{\Delta_h \Phi(\underline{x}, z = -1, \tau)}{\sqrt{t-\tau}} d\tau. \quad (4.45)$$

In dimensional space, using the continuity equation, Eq.(4.45) becomes:

$$\frac{\partial \Phi}{\partial z}(z = -h) = -\sqrt{\frac{\nu}{\pi}} \int_0^t \frac{\frac{\partial^2 \Phi}{\partial z^2}(\underline{x}, z = -h, \tau)}{\sqrt{t-\tau}} d\tau. \quad (4.46)$$

This term enables accounting for the viscous effects created by bottom friction in the bottom boundary layer, in the interior of the flow region. As it is a diffusion process, the influence of viscosity is not instantaneous, and a time dependent term appears. The effect of the boundary layer is cumulative in time but weighted in favor of the current time (through the term $1/\sqrt{t-\tau}$ in the time integral).

4.2.3.3 Bottom boundary condition for an uneven bottom

The previous correction term was derived for the constant depth case. For an uneven bottom, the bottom boundary condition has to be modified to take into account the slope ($\gamma = O(\nabla_H h)$). As done by Liu et al. (2006), a local orthonormal coordinate system is introduced (\underline{x}', z') with

\underline{x}' parallel and z' normal to the bottom. In this new system of coordinates, \underline{u}' and w' are the velocities parallel and normal to the bottom, and the non dimensional continuity and momentum equations for the horizontal speed \underline{u}' are:

$$\nabla'_H \underline{u}' + \frac{\partial w'}{\partial z'} = 0, \quad (4.47)$$

$$\frac{\partial \underline{u}'}{\partial t} = -\nabla'_H p - \frac{1}{\mu} \frac{\nabla'_H h}{1 + (\nabla'_H h)^2} + \alpha^2 \left(\Delta'_u \underline{u}' + \frac{1}{\mu^2} \frac{\partial^2 \underline{u}'}{\partial z'^2} \right). \quad (4.48)$$

The same methodology as in 4.2.3.2 is then applied: first a stretched coordinate is defined in the direction perpendicular to the bottom ($\xi' = z'/\alpha$) to focus on the variation of the vortical part of the velocity in the boundary layer, then a Helmholtz decomposition of the velocity field is completed, followed by a perturbation expansion. The expression of the vortical part of the velocity is substituted in the continuity equation giving at zero and first order in α the same expressions as Eq.(4.37) and Eq.(4.38). When substituted in the momentum equation, the leading order in α gives:

$$\frac{\partial \underline{u}'_0}{\partial t} = \frac{1}{\mu^2} \frac{\partial^2 \underline{u}'_0}{\partial \xi'^2} - \frac{1}{\mu} \frac{\nabla'_H h}{1 + (\nabla'_H h)^2} = \frac{1}{\mu^2} \frac{\partial^2 \underline{u}'_0}{\partial \xi'^2} + O\left(\frac{\gamma}{\mu}\right). \quad (4.49)$$

The solution of this equation is known and given by Eq.(4.43). The expression of $w'_1(\xi = 0)$ can then be deduced (Eq.(4.44)). The no-flux condition at the bottom gives the bottom condition correction term to apply to the potential flow problem in the local coordinate system:

$$\frac{\partial \Phi}{\partial z'}(z' = 0) = -\alpha w'_1 = \frac{\alpha}{\mu\sqrt{\pi}} \int_0^t \frac{\Delta'_h \Phi(\underline{x}', z' = 0, \tau)}{\sqrt{t - \tau}} d\tau + O\left(\frac{\gamma}{\mu}\right). \quad (4.50)$$

In the global coordinate system (\underline{x}, z) , this new bottom condition is written as:

$$\frac{\partial \Phi}{\partial z}(z = -h) = \frac{\alpha}{\mu\sqrt{\pi}} \int_0^t \frac{\Delta_h \Phi(\underline{x}, z = -h, \tau)}{\sqrt{t - \tau}} d\tau - \nabla_H h \cdot \nabla_H \Phi + O\left(\frac{\gamma}{\mu}, \alpha \frac{\gamma^2}{\mu}\right) \quad (4.51)$$

According to Liu et al. (2006) this equation is valid under the assumption that the bottom slope satisfies $O(\gamma) \sim O(\mu^3)$, necessary for the linearization of the boundary layer momentum equation.

4.3 Numerical implementation of the viscous terms

4.3.1 Numerical implementation of the terms in the free surface boundary condition

To take into account of the effects of bulk viscosity, the two dissipative terms in Eq.(4.28) and (4.29), derived in the linear case, are added to the nonlinear Zakharov equations resolved by the

code:

$$\frac{\partial \eta}{\partial t} = -\nabla_H \tilde{\Phi} \cdot \nabla_H \eta + \tilde{w}(1 + (\nabla_H \eta)^2) + 2\nu \Delta_H \eta, \quad (4.52)$$

$$\frac{\partial \tilde{\Phi}}{\partial t} = -g\eta - \frac{1}{2}(\nabla_H \tilde{\Phi})^2 + \frac{1}{2}\tilde{w}^2(1 + (\nabla_H \eta)^2) - 2\nu \frac{\partial^2 \Phi}{\partial z^2}. \quad (4.53)$$

The first term $\Delta_H \eta$ is computed with finite difference schemes whereas the second term $\frac{\partial^2 \Phi}{\partial z^2}(x, z = \eta)$ is computed at the end of each resolution of the Laplace BVP from the $a_n(x)$ coefficients according to:

$$\frac{\partial^2 \Phi}{\partial z^2}(x, z = \eta) = s_z^2 \varphi_{ss}(s = +1) = \frac{4}{h^{+2}} \sum_{n=2}^{N_T} (-1)^n n^2 (n^2 - 1) a_n(x) \quad (4.54)$$

4.3.2 Numerical implementation of the bottom friction term

The bottom friction condition (Eq.(4.46) or Eq.(4.51)) includes a term with an integral in time of the following form:

$$B(t, x) = \int_0^t \frac{\partial^2 \Phi}{\partial z^2}(\tau, x) \frac{1}{\sqrt{t - \tau}} d\tau. \quad (4.55)$$

The evaluation of $A(t)$ is carried out assuming that $\frac{\partial^2 \Phi}{\partial z^2}(\tau, x)$ is constant over each (small) time step Δt . Under this assumption Eq.(4.55) can be evaluated knowing the value of $\frac{\partial^2 \Phi}{\partial z^2}(\tau, x)$ at each half-time step ($t = k\Delta t/2$, with $k = 0, 1, \dots$), as needed by the fourth-order Runge-Kutta algorithm (RK4).

$$\begin{aligned} B(t) \approx B(k\frac{\Delta t}{2}) \approx & \frac{\partial^2 \Phi}{\partial z^2}(0) \int_0^{\frac{\Delta t}{4}} \frac{1}{\sqrt{k\frac{\Delta t}{2} - \tau}} d\tau + \frac{\partial^2 \Phi}{\partial z^2}(\frac{\Delta t}{2}) \int_{\frac{\Delta t}{4}}^{\frac{3\Delta t}{4}} \frac{1}{\sqrt{k\frac{\Delta t}{2} - \tau}} d\tau + \\ & \frac{\partial^2 \Phi}{\partial z^2}(\Delta t) \int_{\frac{3\Delta t}{4}}^{\frac{5\Delta t}{4}} \frac{1}{\sqrt{k\frac{\Delta t}{2} - \tau}} d\tau + \dots + \frac{\partial^2 \Phi}{\partial z^2}(k\frac{\Delta t}{2}) \int_{k\Delta t - \frac{\Delta t}{4}}^{k\Delta t} \frac{1}{\sqrt{k\frac{\Delta t}{2} - \tau}} d\tau \end{aligned} \quad (4.56)$$

By defining:

$$\alpha_0 = 2\sqrt{\frac{\Delta t}{2}} \quad \text{and} \quad \alpha_p = 2 \left(\sqrt{(2p+1)\frac{\Delta t}{4}} - \sqrt{(2p-1)\frac{\Delta t}{4}} \right) \quad p \geq 1, \quad (4.57)$$

$$\beta_p = 2 \left(\sqrt{(2p+2)\frac{\Delta t}{4}} - \sqrt{(2p+1)\frac{\Delta t}{4}} \right) \quad p \geq 0. \quad (4.58)$$

Eq.(4.56) can then be rewritten as:

$$B\left(k\frac{\Delta t}{2}\right) = \beta_{k-1} \frac{\partial^2 \Phi}{\partial z^2}(0) + \sum_{p=1}^{k-1} \alpha_p \frac{\partial^2 \Phi}{\partial z^2} \left((k-p)\frac{\Delta t}{2} \right) + \alpha_0 \frac{\partial^2 \Phi}{\partial z^2} \left(k\frac{\Delta t}{2} \right). \quad (4.59)$$

In Eq.(4.59), the last term is the only one depending on the potential at current time t , which then has to be expanded on the Chebyshev polynomial basis. The other terms in Eq.(4.59) are evaluated from the values of $\frac{\partial^2 \Phi}{\partial z^2}(\tau, x)$ computed for the previous time steps and constitute the right-hand side of the bottom boundary condition. In terms of $a_n(x, t)$, Eq.(4.46) can be written:

$$\frac{2}{h^+} \sum_{n=1}^{N_T} a_n n^2 (-1)^{n-1} + \alpha_0 \sqrt{\frac{\nu}{\pi}} \frac{4}{h^{+2}} \sum_{n=1}^{N_T} a_n (-1)^n \frac{n^2(n^2-1)}{3} = -\sqrt{\frac{\nu}{\pi}} \int_0^{t-\frac{\Delta t}{4}} \frac{\partial^2 \Phi}{\partial z^2} \frac{dt}{\sqrt{t-\tau}} \quad (4.60)$$

The implementation of this term requires storing the values of $\frac{\partial^2 \Phi}{\partial z^2}(\tau, x)$ at each sub-time step of the RK4 algorithm at all the nodes of the domain, which may be computationally expensive in terms of both memory and CPU time if the domain is large and the integration time long. To reduce the memory requirement, [Torsvik and Liu \(2007\)](#) proposed estimating $A(t)$ from the values of $\frac{\partial^2 \Phi}{\partial z^2}(\tau, x)$ for the most recent N time steps only, by applying a correction term to compensate for the truncated series. The correction term is computed from the residual term (accumulation of the discarded values), and a coefficient that has to be calibrated. This method will not be used for the presented test cases since the goal was first to study the relevance of the additional viscous terms to reproduce physical processes occurring in the experiments. To optimize the inclusion of this term, one must analyze the impact of this approximation of $B(t)$ on the quality of the results, the sensitivity to free parameters in this method, and the computational gain is.

To implement viscous effects in a domain without any relaxation zones for wave generation, viscous terms are applied in the entire domain. Additional complexities appear when there are relaxation zones, because the solution imposed in the relaxation zone does not take into account viscous effects. One way to avoid this problem, associated with wave generation, is to apply the viscous terms only outside the relaxation zones. To smooth the discontinuity at the transition, the viscous terms are applied progressively in space. Nevertheless, in areas where the bottom friction is large (in shallow water or for large values of the viscosity), the simulations tend to become unstable at the end of the transition zone. The limit of stability depending on the viscosity value and the water depth is not yet defined, and it would require additional attention.

4.4 Validation test cases

4.4.1 Bulk viscosity terms in the linear regime

The first goal is to determine the bulk viscosity damping rate as a function of time for a regular wave in a periodic domain of constant water depth (h). The wavelength is fixed (k is real), and the angular frequency ω is complex (here denoted by the underlined variable): $\underline{\omega} = a - ib$, where the real part a is the temporal frequency of the signal and the imaginary part b is the coefficient of the damping factor e^{-bt} . Again, the linearized system of equations describing the problem will be considered here. Both the KFSBC (Eq.(4.28)) and the DFSBC (Eq.(4.29)) free surface boundary conditions are supplemented by terms accounting for the bulk dissipation, which are proportional to the kinematic viscosity of the fluid ν . In the following, the viscosity appearing in each of these equations is differentiated by ν_1 and ν_2 to evaluate their respective contributions:

$$\frac{\partial \eta}{\partial t} = \frac{\partial \Phi}{\partial z} + 2\nu_1 \Delta \eta \quad \text{at } z = 0 \quad (4.61)$$

$$\frac{\partial \Phi}{\partial t} = -g\eta - 2\nu_2 \frac{\partial^2 \Phi}{\partial z^2} \quad \text{at } z = 0 \quad (4.62)$$

The solution of these equations for a progressive wave of initial complex amplitude \underline{A} is:

$$\underline{\eta}(x, t) = \underline{A} e^{i(kx - \underline{\omega}t)} \quad (4.63)$$

$$\underline{\Phi}(x, z, t) = -\frac{ig\underline{A}}{\underline{\omega} + i2\nu_2 k^2} \frac{\cosh(k(h+z))}{\cosh(kh)} e^{i(kx - \underline{\omega}t)} \quad (4.64)$$

together with the dispersion relation:

$$\underline{\omega}^2 \left(1 + i2\nu_1 \frac{k^2}{\underline{\omega}}\right) \left(1 + i2\nu_2 \frac{k^2}{\underline{\omega}}\right) = \omega_0^2 \quad (4.65)$$

with $\omega_0^2 \equiv gk \tanh(kh)$.

Depending on the values of ν_1 and ν_2 , three cases can be considered to obtain $\underline{\omega}$ as the roots of Eq.(4.65):

- case 1 : $\nu_1 = \nu > 0$ and $\nu_2 = 0$: $\underline{\omega} = \omega_0 \sqrt{1 - \left(\frac{\nu_1 k^2}{\omega_0}\right)^2} - i\nu_1 k^2$
- case 2 : $\nu_1 = 0$ and $\nu_2 = \nu > 0$: $\underline{\omega} = \omega_0 \sqrt{1 - \left(\frac{\nu_2 k^2}{\omega_0}\right)^2} - i\nu_2 k^2$

- case 3 : $\nu_1 = \nu > 0$ and $\nu_2 = \nu > 0$: $\underline{\omega} = \omega_0 - i 2 \nu k^2$

In the third case where the dissipative term is added in both free surface boundary conditions, the dispersion relation corresponds to that of Lamb (1932), and the damping rate is twice that when the dissipation is present in only one boundary condition (case 1 and 2). Thus both terms contribute equally to the damping of the amplitude of the wave. When either ν_1 or ν_2 is equal to zero, the angular frequency (real part of $\underline{\omega}$) is slightly reduced, whereas it remains unchanged when both dissipative terms are present.

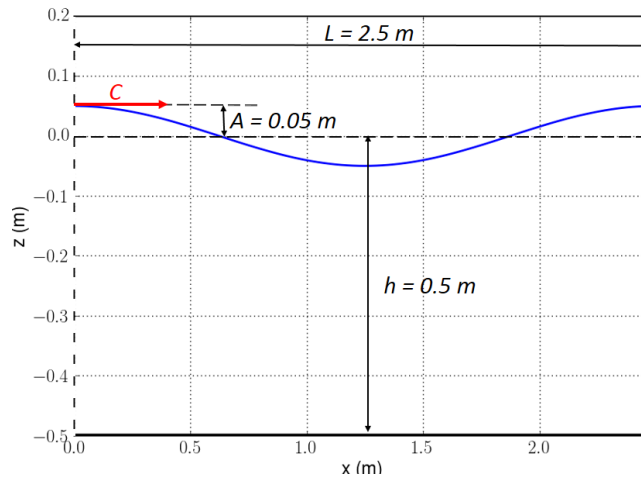


Figure 4.1: Set-up of the simulations of regular waves of amplitude $A = 0.05$ m, propagating in a periodic domain equal to one wavelength ($L = 2.5$ m), in constant water depth $h = 0.5$ m. The blue line is the initial free surface position and the red arrow indicates the direction of propagation of the wave.

To verify the numerical implementation of the viscous terms in the code and to evaluate the contribution of each term, a linear regular wave, of wavelength $L = 2.5$ m, period $T_0 = 2\pi/\omega_0 \approx 1.3724$ s and amplitude $A = 0.05$ m is propagated in a periodic domain of constant depth ($h = 0.5$ m) for 10 periods (about 13.7 s) (Figure 4.1). The linear version of the model is used with $\Delta x = 0.025$ m ($\approx L/100$), $\Delta t = 0.001372$ s ($\approx T/1000$) for the two smallest values of viscosity and $\Delta t = 0.0001372$ s ($\approx T/10000$) for the largest viscosity, and $N_T = 7$. At time $t = 0$ s, the free surface elevation is maximal at the left end of the domain. The time evolution of the free surface elevation at this point is compared to the envelop (Eq.(4.66)) for $\nu = 10^{-6}$, 10^{-3} , and 0.2263 m²/s in Figures 4.2-4.4, respectively.

$$f(\nu, x, t) = \pm \eta_{max}(x, t = 0)e^{-bt} \quad (4.66)$$

In these figures the envelop corresponding to cases 1 and 2 is the black dashed line and the one corresponding to case 3 is the dark blue dashed line. For small values of the viscosity ($\nu =$

$10^{-6} \text{ m}^2/\text{s}$, see Figure 4.2), the amplitude decrease is hardly visible during the simulated period. The differences between the three cases are very small but by zooming in one can see that the amplitude decreases faster for case 3 than for cases 1 and 2, and that the decay rate is the same for cases 1 and 2, in agreement with the theory. The decrease of the local maxima follows well the predicted envelop for the three cases. For a 1000-times higher value of the viscosity ($\nu = 10^{-3} \text{ m}^2/\text{s}$, see Figure 4.3) these effects are even more visible.

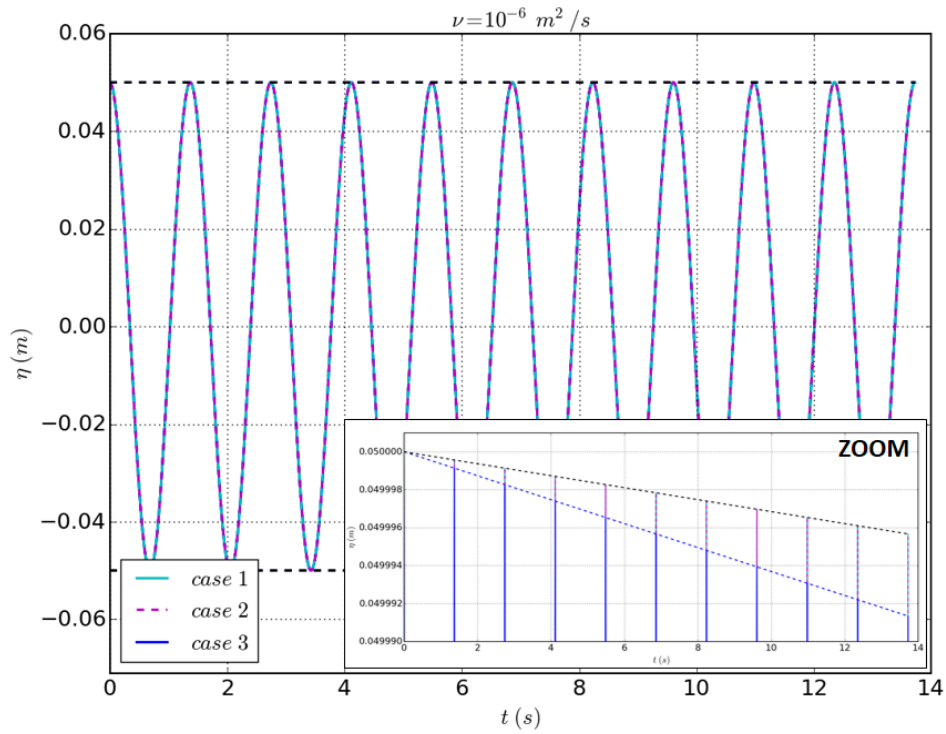


Figure 4.2: Amplitude decay at the first node of the domain as a function of time with viscosity $\nu = 10^{-6} \text{ m}^2/\text{s}$, for cases 1-3.

According to the theory, the angular frequency is reduced for case 1 and case 2. However, the value of the viscosity needed to obtain a significant reduction in the angular frequency is large. To obtain an angular frequency $\omega = \alpha\omega_0$ ($\alpha \in [0, 1]$), the viscosity must be $\nu = \nu_{max}\sqrt{1 - \alpha^2}$, with $\nu_{max} = \omega_0/k^2$. For the wave characteristics considered here, the viscosity therefore must be $\nu = 0.2263 \text{ m}^2/\text{s}$ (as $\nu_{max} = 0.7248 \text{ m}^2/\text{s}$) to obtain a 5% reduction of the angular frequency, which is not a physically realistic value. However, in order to check the correct implementation of the dissipative terms in the code, the results of the simulations of the three cases with this value of viscosity are presented in Figure 4.4. The period estimated from Figure 4.4 for cases 1 and 2 is $T = 1.444596 \text{ s}$, which is in good agreement with the theoretical value of $T = 1.444635 \text{ s}$. Note the very rapid reduction of the amplitude of the free surface with this high value of viscosity (consequently the extent of the time interval in the horizontal axis of this figure was reduced compared to Figures 4.2 and 4.3).

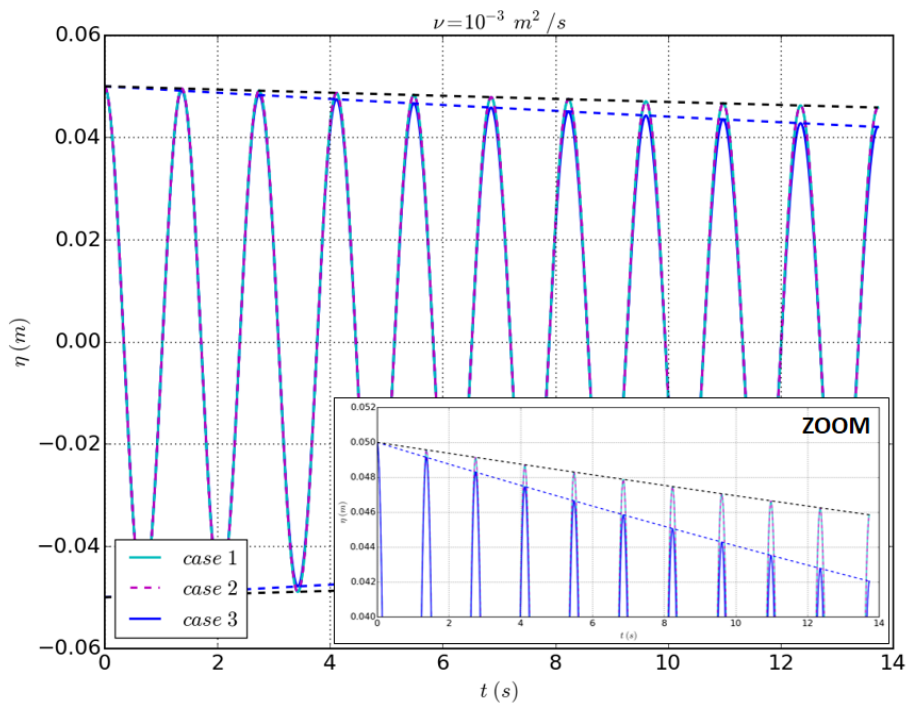


Figure 4.3: Amplitude decay at the first node of the domain as a function of time with viscosity $\nu = 10^{-3} \text{ m}^2/\text{s}$, for cases 1-3.

This test case shows the ability of the model to take into account the effects of bulk viscosity, showing good agreement with Lamb's theory (Lamb, 1932). Moreover, it is shown theoretically and verified numerically that the viscous terms contribute equally to the damping of the amplitude of the wave.

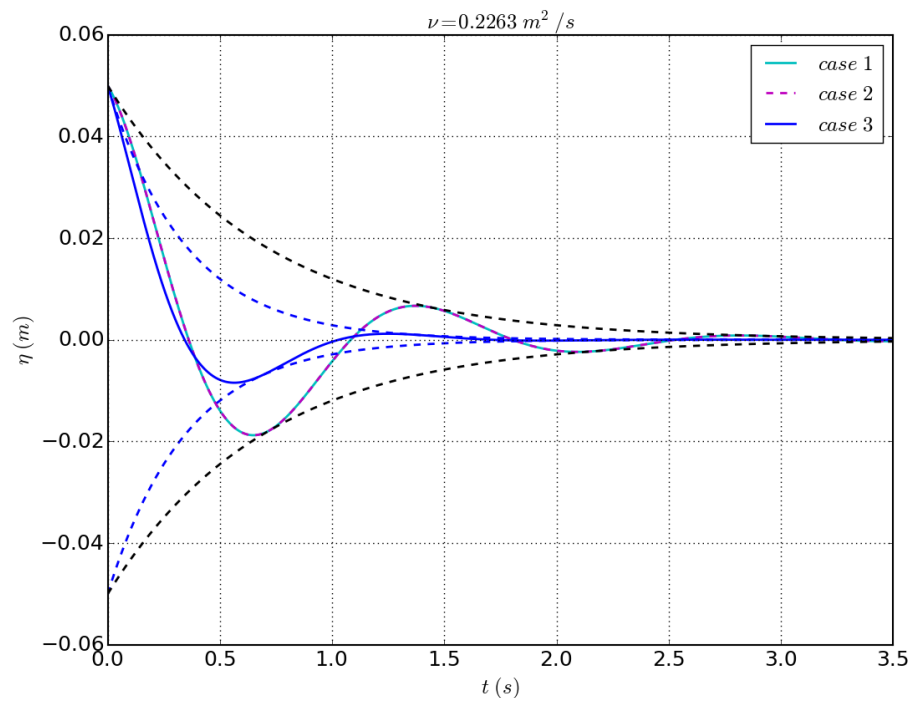


Figure 4.4: Amplitude decay at the first node of the domain as a function of time with viscosity $\nu = 0.2263 \text{ m}^2/\text{s}$, for cases 1-3. (Note that the time interval in this figure is shorter than the simulated duration, contrary to Figures 4.2 and 4.3).

4.4.2 Viscous standing wave in the linear regime

The energy loss due to bulk viscosity following Lamb's theory (Lamb, 1932) is well reproduced by the model. Nevertheless, this theory is only valid for high Reynolds numbers. In the case of finite depth, additional energy losses may exist due to bottom friction, which are not taken into account with Lamb's damping coefficient. As an extension of Lamb's theory, Antuono and Colagrossi (2013) (AC2013 hereafter) considered waves propagating in finite depth in a viscous fluid for a wide range of Reynolds numbers (as low as $Re = 50$), and they derived an approximate formula for the damping rate using a solution of the linearized Navier-Stokes equations.

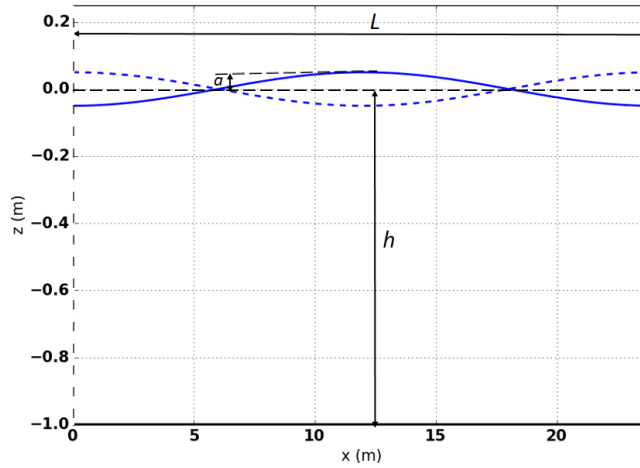


Figure 4.5: Set-up of the simulations of standing waves of amplitude a , oscillating in a periodic domain equal to one wavelength (L), in constant water depth h . Blue solid and dashed lines indicate the extreme positions of the free surface.

Here, the simulations of standing waves, using the linear version of Misthyc, will be compared to this theory. The standing wave has an amplitude $a = 0.05$ m in depth $h = 1$ m (Figure 4.5). The periodic domain is one wavelength long (L). The temporal evolution of the total kinetic energy of the fluid, normalized by its value at initial time, is defined as:

$$E_c(t) = \frac{1}{2} \rho \left[\int_x \int_y \phi(z = \eta, t) \frac{\partial \eta}{\partial t}(t) dx dy + \int_x \int_y \phi(z = -h, t) \frac{\partial \phi}{\partial z}(z = -h, t) dx dy \right], (4.67)$$

where the first term is the free surface contribution and the second term is the bottom contribution.

Several values of the viscosity (ν) or Reynolds number, here defined as $Re = h\sqrt{gh}/\nu$ and relative water depth (kh), are considered. Five combinations of (Re , kh) from deep to shallow water (see Table 4.1) were tested. For each combination, two linear simulations were completed by activating, (1) only the bulk viscosity, (2) the bulk viscosity and bottom friction terms. The second series of simulations allows evaluating when bottom friction is negligible. Simulations 1, 2 and 3

can be compared to assess the effects of viscosity in deep water ($kh = \pi$), which are expected to be small since bulk viscosity is the only source of dissipation. Large values of the viscosity (up to $\nu = 0.06264 \text{ m}^2/\text{s}$) are tested for this analysis to emphasize the viscous effects. Simulations 2, 4 and 5, can be compared to assess the impacts of the relative water depth. The dissipation is expected to increase as the relative water depth decreases, and the bottom friction term become predominant. The results are plotted in Figures 4.6-4.11 as a function of the nondimensional time $t^* = t\sqrt{g/h}$.

Simulation	kh	$L(m)$	Re	$\nu \text{ (m}^2/\text{s)}$
1	π	2	50	0.06264
2	π	2	500	0.006264
3	π	2	2500	0.001253
4	$\pi/3$	6	500	0.06264
5	$\pi/12$	24	500	0.06264

Table 4.1: Nondimensional and physical parameters for the five simulations.

In some cases, instabilities develop in time when the bottom friction term is present (e.g. Figure 4.6). Small wavelength oscillations in the free surface elevation appear and grow during the simulation. Looking at the time evolution of the amplitude spectra as a function of k (not shown here), the increase of energy for high values of k is clearly visible. In simulation 4, for which time instabilities develop, a series of tests of the numerical parameters (Δt , Δx and N_T) were completed for the simulation with bottom friction (see Figure 4.6). The default parameters are $\Delta t = T/1000 = 0.00222 \text{ s}$, $\Delta x = L/100 = 0.06 \text{ m}$ and $N_T = 7$ (dark blue line). With these numerical parameters, the kinetic energy diverges from the approximated solution proposed by AC2013 around $t^* \approx 28$. Decreasing the time step by a factor of 100 (dashed red line) does not delay the divergence. A finer spatial resolution (light blue line) leads to an earlier divergence around $t^* = 24$, and the increase of the vertical resolution to $N_T = 12$ (purple line) also leads to an even earlier divergence at $t^* = 12$. The simulations were stabilized by applying a low-pass filter on the variable $\partial^2\Phi/\partial z^2(z = -h)$ which is integrated in time in the bottom friction condition (Eq.(4.46)). At each time step, the Fast Fourier Transform of $\partial^2\Phi/\partial z^2(z = -h)$ is computed and only the first 10 modes are kept. With filtering (orange line), the evolution of the kinetic energy agrees with AC2013. The frequency of the filtering was also tested. For this simulation, applying the filter only every 6 time steps is sufficient to avoid the growth of instabilities. However, this is not a general result, and the optimal filtering frequency may vary for each simulation. Thus, the filter is applied at every time step in the following simulations.

Unexpectedly, the time instability develops even more rapidly in the case of deep water ($kh = \pi$) when the bottom friction term should be negligible, and the simulations with and without bottom friction should produce nearly the same results. For simulation 1, filtering the $\partial^2\Phi/\partial z^2(z = -h)$ term is not sufficient. Previous results without viscosity showed that the model accuracy

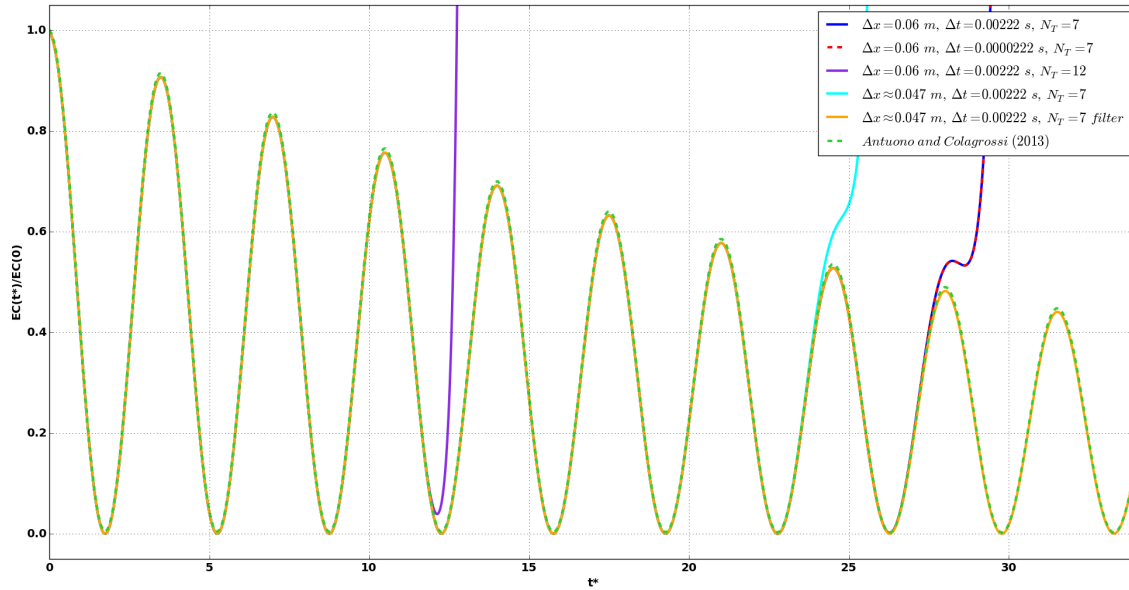


Figure 4.6: Evolution of the normalized kinetic energy of the system as a function of nondimensional time for $kh = \pi/3$ and $Re = 500$ ($\nu = 0.06264 \text{ m}^2/\text{s}$), for different values of Δx , Δt and N_T (see legend).

increases for deep water cases with larger N_T (Yates and Benoit (2015)), but increasing the value of N_T only caused the divergence to occur earlier (as seen for simulation 4). On the contrary, by decreasing N_T to $N_T = 5$, the simulation with bottom friction shows the same kinetic energy evolution as the simulation with only the bulk viscosity (Figure 4.7). In deep water, the simulated vertical profile of the velocity potential varies significantly, and adding higher order polynomials in the decomposition increases the creation of small oscillations in the profile that are amplified by taking the second derivative. These instabilities occur for high values of the viscosity, above the range of validity of the theory (which is roughly $\nu \in [10^{-6}, 10^{-3}] \text{ m}^2/\text{s}$). Higher order terms ($O(\nu)$) that were neglected for small viscosities may become important and their absence could destabilize the system. In real application cases, the viscosity will be of maximum value e.g. $10^{-3} \text{ m}^2/\text{s}$. For this range of viscosities, the simulations are stable even without filtering (simulation 3).

It is also important to note that filtering enables increasing the simulation time step to that of the same order as the one used for the simulations without viscosity. For example, simulation 5 with bottom friction is stable for $\Delta t = T/10000$ without filtering, and $\Delta t = T/100$ with filtering, producing visually identical curves of the kinetic energy evolution. Table 4.2 shows the maximum nondivergent time step for the five simulations with bottom friction, with and without filtering. The time step used for the simulation with bulk viscosity only is the same as the one for the simulation with bottom friction and filtering.

The results for the deep water cases ($kh = \pi$) for several values of viscosity are compared to

Simulation	Δt_{min} no filter	Δt_{min} filter
1	X	$T/2000 = 0.000567$ s ($N_T = 5$)
2	X	$T/200 = 0.00567$ s
3	$T/100 = 0.01134$ s	$T/100 = 0.01134$ s
4	X	$T/100 = 0.0222$ s
5	$T/10000 = 0.000775$ s	$T/100 = 0.0775$ s

Table 4.2: Maximum time steps for the simulations with and without a low-pass filter on the 10 first modes of $\partial^2\Phi/\partial z^2(z = -h)$ at each time step. X means that the simulation diverged even for the smallest time step tested $\Delta t = T/10000$.

the solution proposed by AC2013 (green dashed line) and Lamb's solution (black dashed line) in Figures 4.7 to 4.9. For this set of simulations, the results of the simulation with and without bottom friction are superimposed, since in infinite depth the effects of bottom friction are negligible. Lamb's solution overestimates the energy dissipation in comparison with the solution proposed by AC2013, especially for small Reynolds numbers (high viscosity). The leading order term of the damping rate obtained by AC2013 coincides with Lamb's damping coefficient, and the negative higher order terms in AC2013 thus explains the overestimation of Lamb's solution. The simulation results follow Lamb's solution since the bulk viscous terms have been derived using the same assumptions by considering small viscosity values to neglect terms of order $o(\nu)$. For the smallest value of viscosity ($\nu = 0.001253$ m²/s), the difference between the two solutions is hardly visible, but, according to AC2013, for long propagation times, these differences could become important.

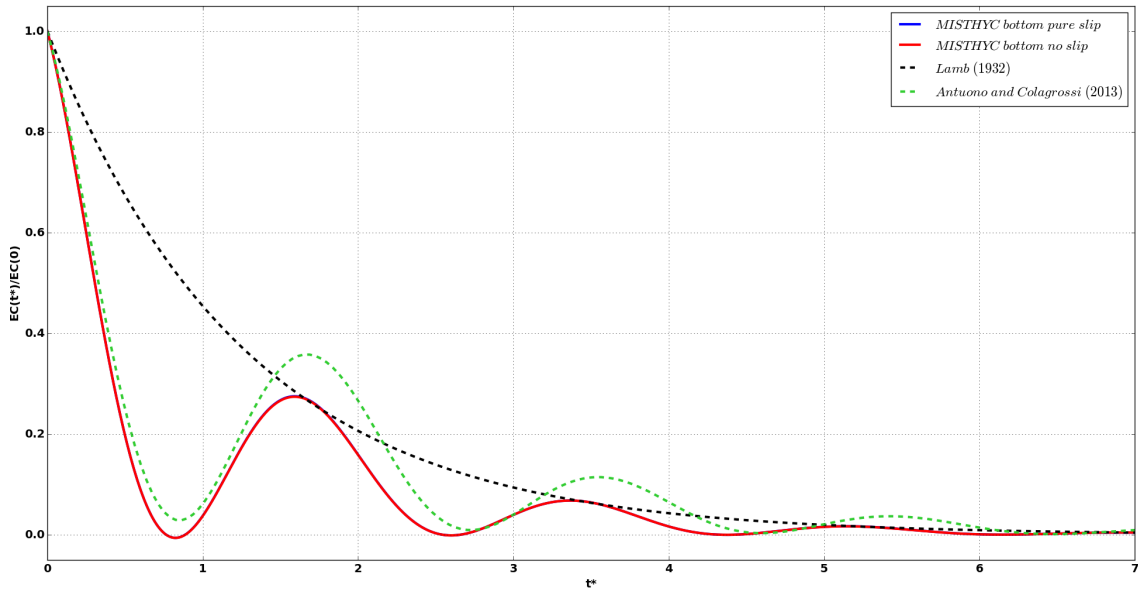


Figure 4.7: Evolution of the normalized kinetic energy of the system as a function of nondimensional time for $kh = \pi$ and $Re = 50$ ($\nu = 0.06264$ m²/s).

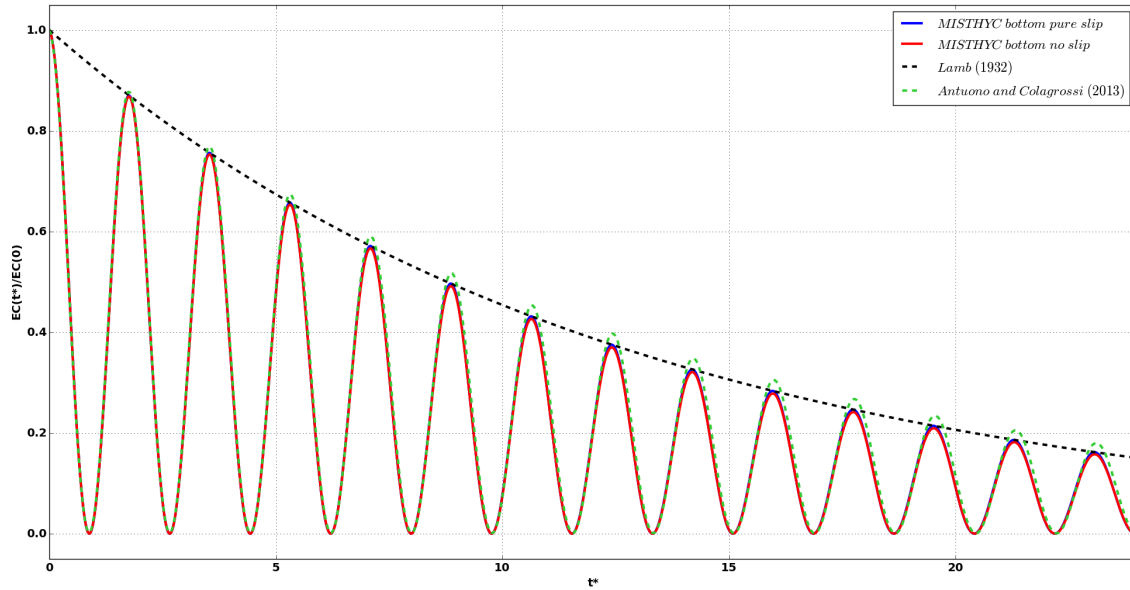


Figure 4.8: Evolution of the normalized kinetic energy of the system as a function of nondimensional time for $kh = \pi$ and $Re = 500$ ($\nu = 0.006264 \text{ m}^2/\text{s}$).

In cases 4 and 5 where the relative water depths are no longer in the infinite depth limit, the differences between the simulation with and without bottom friction increase when the relative water depth decreases (Figures 4.10 and 4.11). The damping is more important with bottom friction and has consequences on the wave amplitude and propagation speed, as seen in the phase shift between the two curves. The simulations with bulk viscosity only follow Lamb's solution, while the simulations that also include bottom friction are in good agreement with the solution proposed by AC2013. For intermediate and small relative water depths, the bottom friction term becomes non negligible and contributes significantly to the dissipation. It is necessary to take into account the effect of bottom friction to reproduce correctly the damping of a standing wave during in finite depth.

In comparison to the solution proposed by AC2013, it is necessary to use the bottom friction term to reproduce correctly the decay of the kinetic energy in intermediate and shallow water. However, in deep water, the numerical model overestimates the decay of the kinetic energy for small Reynolds numbers since it follows Lamb's theory.

This set of simulations will be presented in a a publication currently being prepared on taking into account viscosity in water waves models. The visco-potential flow model is compared to a model based on the linear free surface Stokes equations and a model resolving the full nonlinear free surface Navier-Stokes equations.

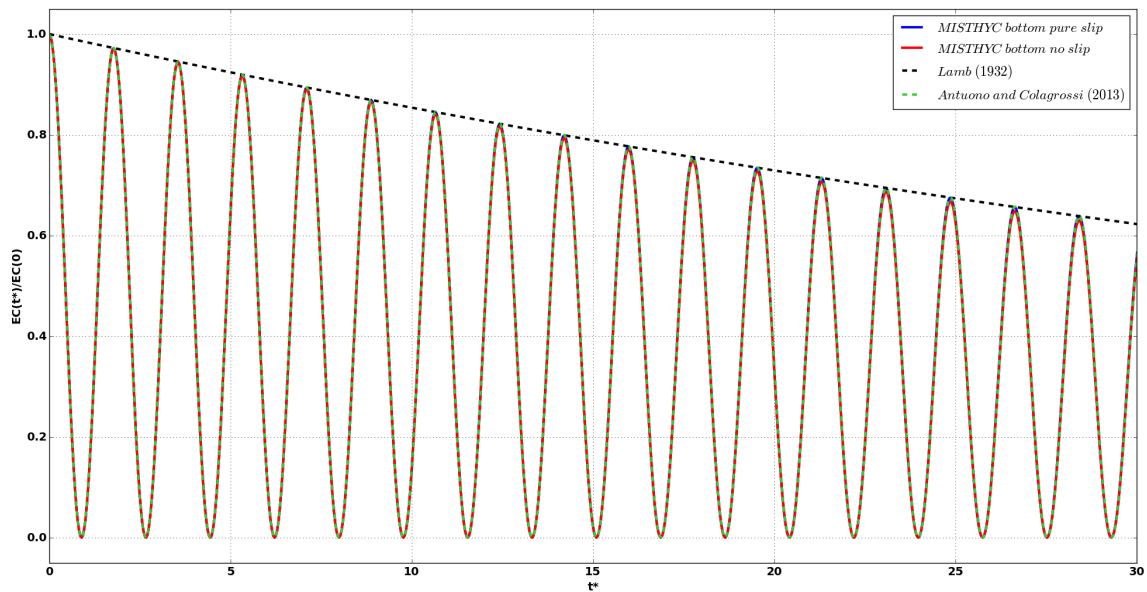


Figure 4.9: Evolution of the normalized kinetic energy of the system as a function of nondimensional time for $kh = \pi$ and $Re = 2500$ ($\nu = 0.001253 \text{ m}^2/\text{s}$).

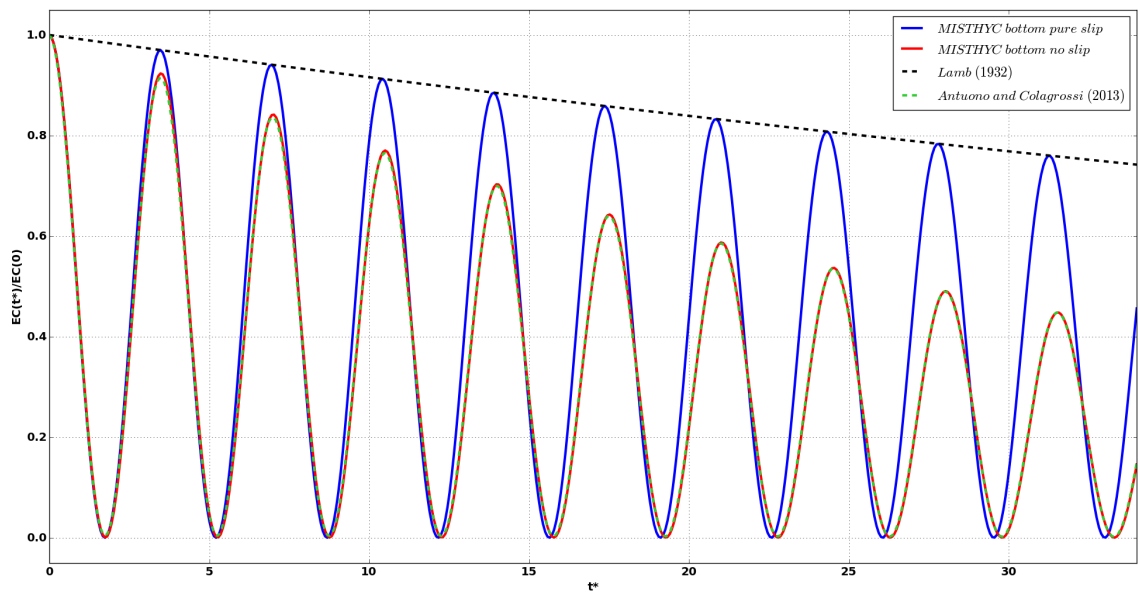


Figure 4.10: Evolution of the normalized kinetic energy of the system as a function of nondimensional time for $kh = \pi/3$ and $Re = 500$ ($\nu = 0.06264 \text{ m}^2/\text{s}$).

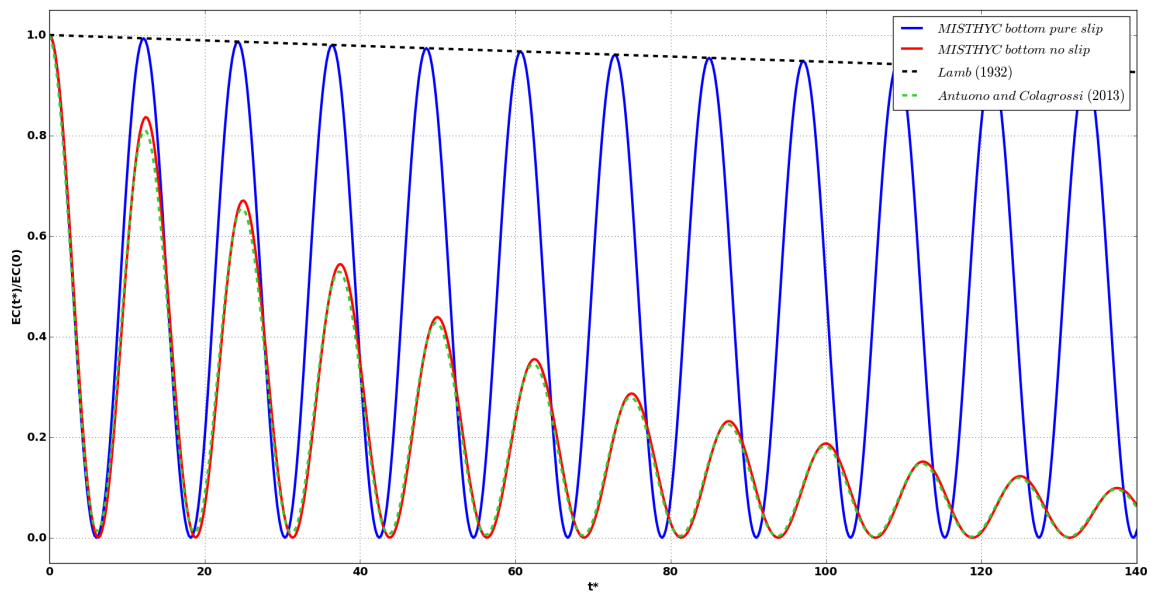


Figure 4.11: Evolution of the normalized kinetic energy of the system as a function of nondimensional time for $kh = \pi/12$ and $Re = 500$ ($\nu = 0.06264 \text{ m}^2/\text{s}$).

4.4.3 Attenuation of a solitary wave in a wave flume

The third test case simulates the propagation of a solitary wave over a flat bottom ($h_0 = 0.15$ m) and then up a gentle slope (1/20), based on the experiments of Liu et al. (2006). In the experiments, the wave is generated by a piston-type wavemaker. Acoustic gauges in the wave flume record the evolution of the free surface elevation in the flat-bottom zone and in the shoaling zone (black triangles in Figure 4.12). The domain for the numerical simulation extends from $x = 0$ m to $x = 25$ m (with the slope beginning at $x = 19.88$ m), with a regular mesh with $\Delta x = 0.0075$ m, and $N_T = 7$. Since the numerical model is not able to simulate run-up on the slope, a minimum depth of $h_1 = 0.01$ m is set, and the simulations are stopped before the wave arrives at the reflective right boundary. Facing stability problems at the right boundary for high values of N_T due to the very small water depth, the impermeable wall boundary condition is slightly modified, using its projection on the $N_T + 1$ first Chebyshev polynomials instead of only on the $N_T - 1$ supplemented by the Dirichlet condition at the free surface and the slip or no-slip condition on the bottom as done usually.

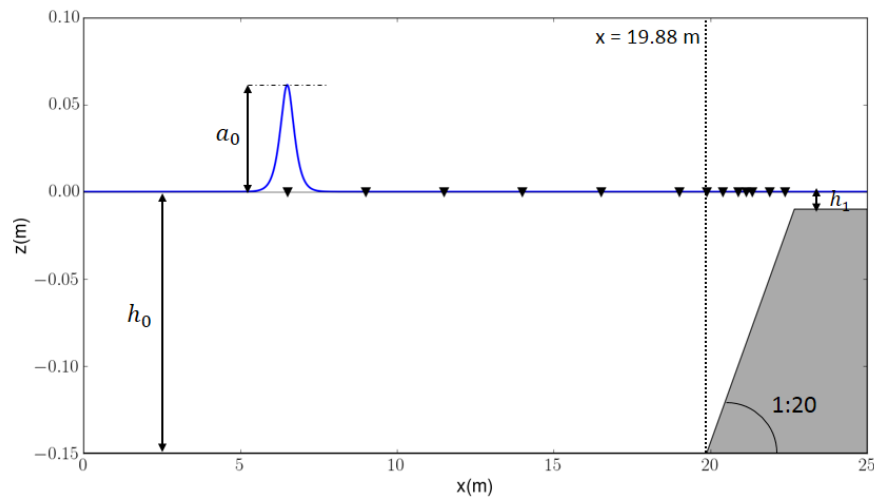


Figure 4.12: Bathymetry, initial free surface elevation, and positions of wave gauges (black triangles) in the Liu et al. (2006) experiments.

The initial condition is the solution of the fully nonlinear Euler equations obtained with the algorithm of Clamond and Dutykh (2013), computed using the solitary wave amplitude measured at the first gauge ($x = 6.5$ m). Among the five wave amplitudes tested by Liu et al. (2006), the smallest ($a = 0.01365$ m) and the largest ($a = 0.06135$ m) are simulated here, corresponding to non-linearities of $\epsilon = a/h_0 = 0.091$ and $\epsilon = 0.409$, respectively. The time step is calculated such that $CFL = 1$ with $CFL = C\Delta t/\Delta x$ (using the velocity C given by the algorithm of Clamond and Dutykh (2013)). For the smallest wave, $\Delta t = 0.006$ s and for the largest wave $\Delta t = 0.0052$ s. The simulation parameters are shown in Table 4.3.

a (m)	ϵ	Δt (s)	CFL
0.01365	0.091	0.006	1
0.06135	0.409	0.0052	1

Table 4.3: Simulation parameters for the two solitary waves.

The nonlinear version of the model is used for this test case, simply by adding the linear viscous correction terms to the basic nonlinear equations (Eq.4.5) and (Eq.4.4), and using the no-slip boundary condition at the bottom (Eq.4.51). As noted by [Dutykh and Dias \(2007\)](#), the derivation of these viscous terms was completed for the linear regime, and it is merely hypothesized that these terms can be generalized directly to the fully nonlinear equations. The application to a case with small ($\epsilon = 0.091$) and moderate ($\epsilon = 0.409$) nonlinearities is a good test of the limits of this hypothesis.

The domain can be decomposed into two zones of interest where different physical processes are important. First, over the flat bottom ($x \leq 19.88\text{m}$), wave dissipation is caused by bulk viscosity and bottom friction. Second, on the slope, the effects of wave shoaling (increase of the wave amplitude due to the water depth decrease) become important and compete with the energy dissipation ($19.88\text{m} \leq x \leq 25\text{m}$). Over the flat bottom, the amplitude of the solitary waves decreases (Figure 4.13 a and b for $\epsilon = 0.091$ and $\epsilon = 0.409$, respectively) due to these dissipative processes. The results of four simulations for each value of ϵ are presented in Figure 4.13 to evaluate the influence of the different sources of energy dissipation on the decay rate. Without viscosity (light blue line), the wave amplitude remains constant. The simulations with only the bulk viscosity terms (slip bottom condition) and with $\nu = 7.10^{-6} \text{ m}^2/\text{s}$ show only a weak amplitude decay and are close to the simulations without viscosity ($\nu = 0 \text{ m}^2/\text{s}$). When the bottom friction term (no-slip bottom condition) is added, the soliton amplitudes decrease significantly. The primary source of energy dissipation is bottom friction. This effect becomes more pronounced for larger wave heights that have larger horizontal velocities at the bottom. The value of the viscosity required to best fit the experimental data is slightly higher ($\nu = 7.10^{-6} \text{ m}^2/\text{s}$) than the kinematic viscosity of water ($\nu = 10^{-6} \text{ m}^2/\text{s}$). Using a Boussineq model to simulate these experiments, [Liu et al. \(2006\)](#) found the same decay rate with a viscosity of $10^{-6} \text{ m}^2/\text{s}$ when taking into account the boundary layers on the walls of the wave flume. Here this dissipation is not taken into account, which could explain the higher value of ν adjusted to obtain the same decay rate as in the experiments. The same value of viscosity is used to fit the experimental data for the two wave heights, showing the insensitivity of this value to the wave non-linearity, for the considered range of conditions.

Over the sloping bottom, two processes are competing: energy dissipation that decreases the wave amplitude, and wave shoaling that increases the wave amplitude with a decrease in water

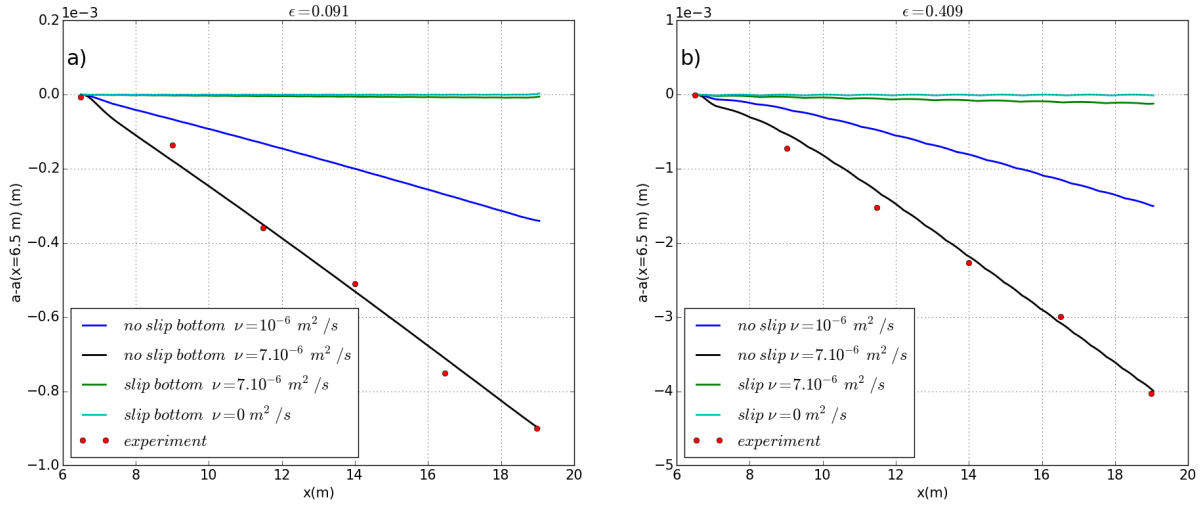


Figure 4.13: Decrease of the amplitude of the soliton along the wave flume, for a) $\epsilon = 0.091$ and b) $\epsilon = 0.409$, comparing the experimental data (red dots), and numerical results without viscosity (light blue), with $\nu = 10^{-6} \text{ m}^2/\text{s}$ bottom pure slip condition (green), with $\nu = 10^{-6} \text{ m}^2/\text{s}$ no-slip bottom condition (blue), and with $\nu = 7.10^{-6} \text{ m}^2/\text{s}$ no-slip bottom condition (black) .

depth. The shoaling effects appear stronger than the dissipative effects for these two simulations since the amplitude of the wave increases as the wave propagates over the slope. This increase is reproduced well by the simulations with the bottom friction term using $\nu = 7.10^{-6} \text{ m}^2/\text{s}$ (Figure 4.14). Here, it is essential to use the modified bottom friction term for a non flat bottom (Eq.4.51), otherwise the dissipation due to bottom friction is overestimated by the numerical model.

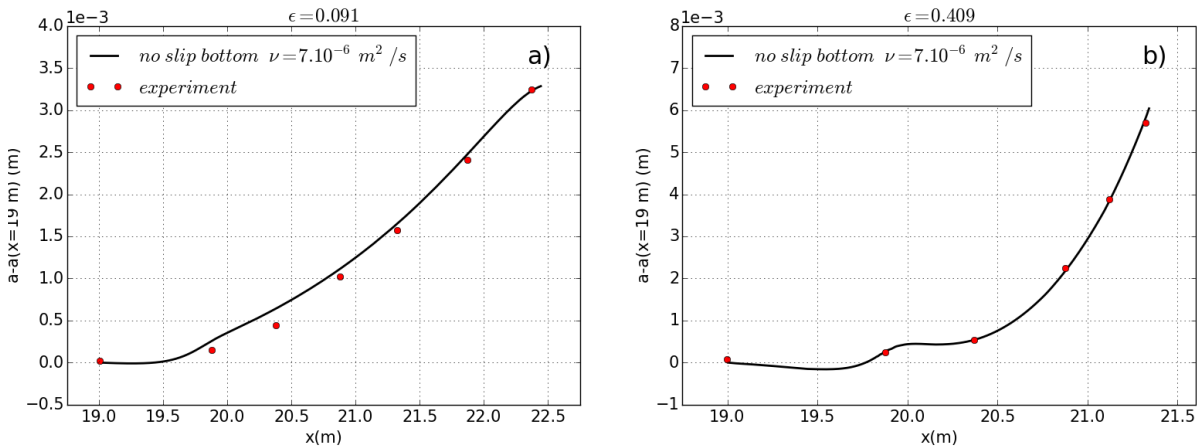


Figure 4.14: Evolution of the amplitude of the soliton in the shoaling zone, for a) $\epsilon = 0.091$ and b) $\epsilon = 0.409$, comparing the experimental data (red dots), and the numerical results with $\nu = 7.10^{-6} \text{ m}^2/\text{s}$ (black).

This third test case shows that the introduction of the linear viscous terms in the nonlinear version of the model allows reproducing well the experiments with non negligible nonlinear effects. When the bottom friction term is modified to take into account the bottom slope, the model reproduces correctly the equilibrium between the effects of dissipation and shoaling on the wave amplitude as the soliton propagates up the slope.

4.4.4 Dissipation of waves propagating over a step

The last test case simulates the propagation of regular waves over a vertical submerged step, based on a series of small-scale experiments performed by E. Monsalve in the PMMH laboratory, at the ESPCI (Ecole Supérieure de Physique et de Chimie Industrielle de la ville de Paris) (Monsalve et al., 2015). The goal of these experiments is to study the nonlinearities occurring when waves pass over a submerged obstacle and to compare the observations with Massel's theory (Massel, 1983) for a wide range of incident wave frequencies $f_1 \in [1 \text{ Hz}; 4 \text{ Hz}]$. Massel developed a second order theory to explain the generation of a second harmonic over a step (zone (II), Figure 4.16). The second harmonic can be decomposed into two components: (1) bound waves that propagate at the same celerity as the fundamental mode with frequency f_1 but with a wave number twice the fundamental wave number ($2k_1^{(II)} = 2k(f_1, h^{(II)})$), and (2) free waves with the wave number corresponding to the linear dispersion relation for the frequency $2f_1$ ($k_2^{(II)} = k(2f_1, h^{(II)})$) that propagate at the corresponding celerity. These two components interact, creating a beating of the second harmonic amplitude. The beat length is estimated by (Massel, 1983):

$$D^- = \frac{2\pi}{k_2^{(II)} - 2k_1^{(II)}} \quad (4.68)$$

In the experiments, the nonlinearities are created by the transition between the deep water region ($h^{(I)} = 6.5 \text{ cm}$) and the shallow water region ($h^{(II)} = 2.0 \text{ cm}$) at a vertical step located at $x = 0 \text{ m}$ (Figure 4.16). Waves are generated by a flap wavemaker at $x = -0.38 \text{ m}$. At the right end of the domain, beginning at $x = 0.85 \text{ m}$, an absorbing beach of slope 8% is constructed to prevent wave reflection. The free surface deformation is measured through a non-intrusive method, called Fourier Transformed Profilometry (Cobelli et al., 2009). A sinusoidal pattern is projected on the water surface made opaque by adding TiO_2 particles (Figure 4.15). The free surface is reconstructed from the phase difference between the deformed fringe pattern due to wave propagation, and the reference pattern measured when the water is at rest. This provides accurate spatial (2D) and temporal measurements of the free surface.

The 1DH nonlinear version of the model (Eq.(1.25) and Eq.(1.26)) that does not include the effects of viscous dissipation was first used to simulate the experiments. The vertical step is modeled with a hyperbolic tangent, with a transition of slope 85 degrees in order to avoid creating a discontinuity at the step (see inset in Figure 4.16). The numerical domain is the same as that of the experiments ($x \in [-0.38 \text{ m}; 0.85 \text{ m}]$), with the addition of a L_{gen} -long relaxation zone for wave generation and a L_{abs} -long relaxation zone for wave absorption (Figure 4.16). Waves are generated with a Dirichlet boundary condition for the potential computed using linear theory. The amplitude of the incident wave was not measured in the experiments (only the motion of the wave maker was prescribed), so the amplitude used in the numerical simulation is determined

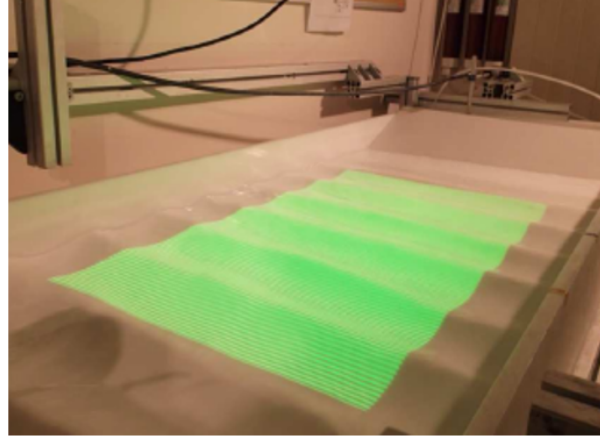


Figure 4.15: Experimental set-up. ESPCI credit.

by qualitatively fitting the amplitude of the simulation results to the experimental data before the step.

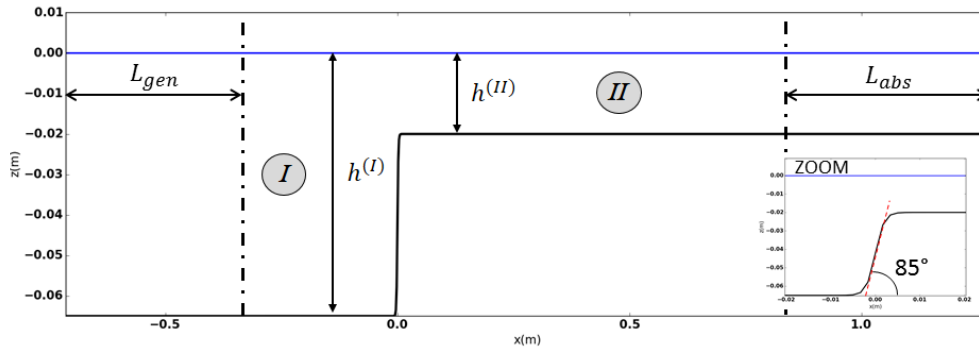


Figure 4.16: Bathymetry used in the numerical simulations, showing a zoom of the hyperbolic tangent form of the step transition in the bottom elevation.

The first simulations were completed for an incident wave frequency of $f_1 = 1.9837$ Hz. The associated wavelength depending on the water depth is given by the linear dispersion relation: $L_1^{(I)} = 0.334$ m in depth $h^{(I)}$ and $L_1^{(II)} = 0.2112$ m in depth $h^{(II)}$. In this case $N_T = 7$, and the domain was irregularly meshed with a spatial step of $\Delta x = L_1^{(I)}/100$ far from the step, and a refinement of $\Delta x/2$ near the step. The time step was $\Delta t = 0.025$ s $\approx T_1/200$ in order to have a maximum CFL=1. The amplitude of the wave was set to $a = 3.2$ mm. The relaxation zones were of length $L_{gen} = L_1^{(I)}$ and $L_{abs} = 2L_1^{(II)}$.

The simulated space-time evolution of the free surface elevation shows wave crests in red and wave troughs in deep blue (Figure 4.17). The slope of the line following a wave crest is proportional to the inverse of its celerity: the steeper the slope, the slower the wave propagation. Two phenomena are visible: (1) The reflection on the step causes an amplitude modulation in the deeper part of the domain. (2) Passing over the step, the slope of the line following a wave crest in-

creases, showing the decrease in wave propagation associated with a decrease in the water depth. A secondary crest (in light blue) forms between the two main crests from ($x \in [0.2 \text{ m}; 0.4 \text{ m}]$). In addition, the slope of the secondary crest is even steeper, corresponding to the free component of the second harmonic, which propagates more slowly than the fundamental wave.

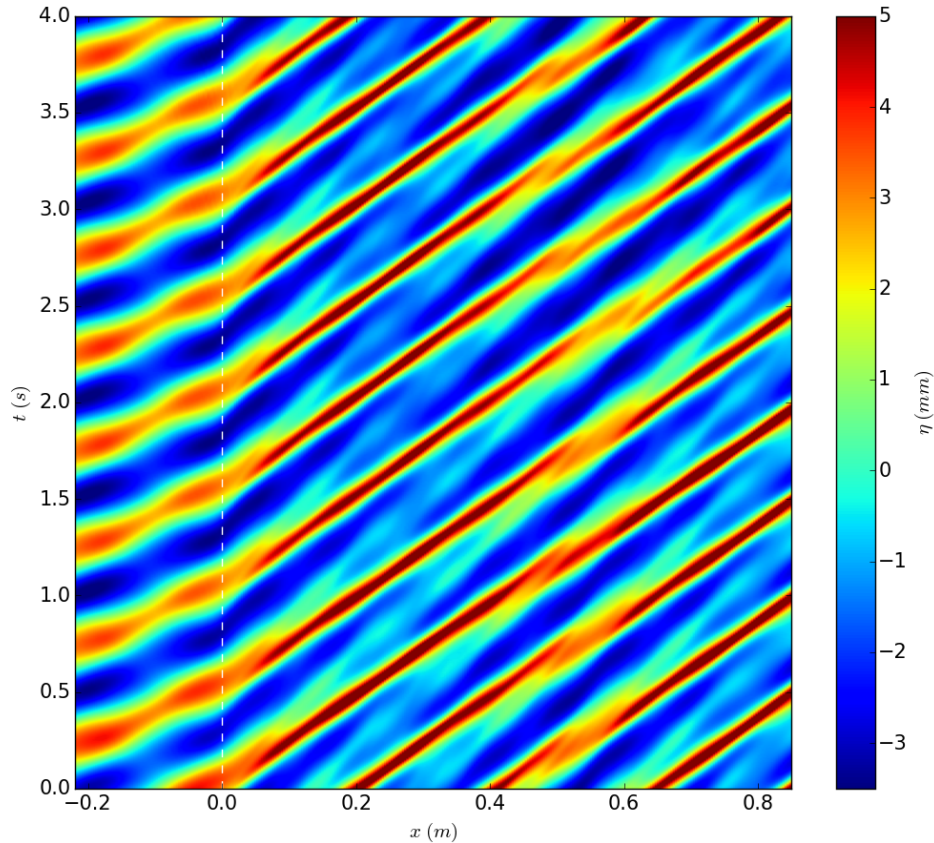


Figure 4.17: Simulated space-time profile of the free surface elevation (in mm) for $f_1 = 1.9837$ Hz. The position of the step is indicated by the vertical white dashed line. The slope of the crest and trough lines show the wave celerity.

The free surface elevation time series were decomposed into the amplitudes of the first five harmonics. The spatial evolution of these amplitudes were then compared to those obtained from the measurements. In the experiments, the bi-dimensional measurements of the free surface show that transverse variations are not always negligible. Here the simulation results are compared to the transverse average of the amplitudes (dashed lines), and the standard deviation is indicated by the shaded zone. For $f_1 = 1.9837$ Hz, in the deeper region of the domain before the step, the simulation results agree well with the experiments (Figure 4.18). However, in the shallower water part over the step, the harmonic amplitudes from the experimental data (dashed lines) show significant dissipation that is not reproduced by the simulations (that do not include

viscous effects). In addition, the beat length of the second harmonic in the simulations is smaller than in the experiments.

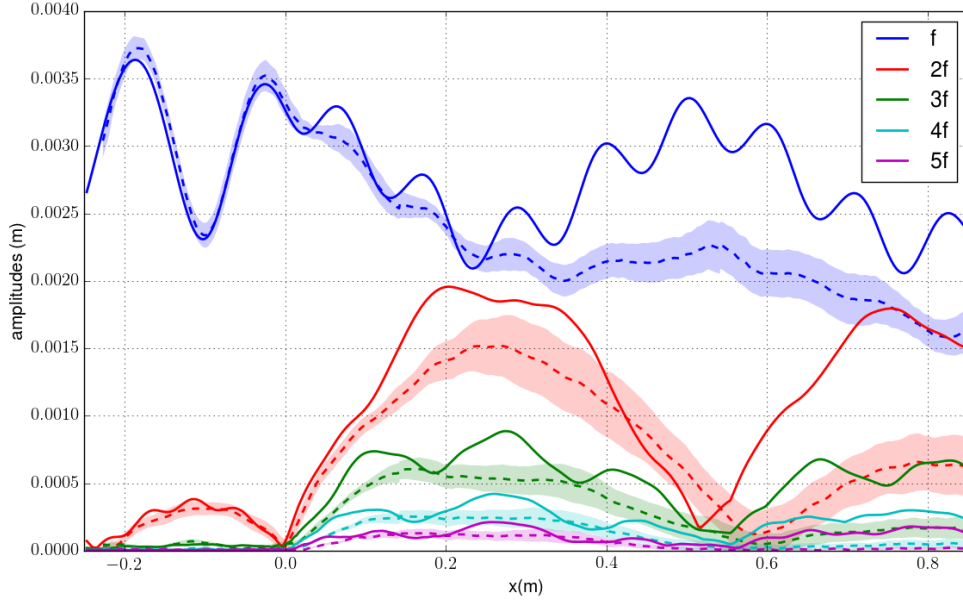


Figure 4.18: Simulated (solid line) and measured (dashed line) spatial evolution of the first five harmonic amplitudes for $f_1 = 1.9837$ Hz without including viscosity or surface tension in the simulations. The dashed line is the transversal mean of the measurements and the shaded zone is the standard deviation.

To evaluate the importance of viscous effects, first, the bulk viscosity terms were added to the model and the optimal value of the bulk viscosity was sought to reproduce the amplitude of the second harmonic (Figure 4.19). The optimal value $\nu = 4.10^{-5} \text{ m}^2/\text{s}$ is higher than the viscosity of pure water. This is likely due to the fact that only dissipation through internal friction was included whereas the effects of bottom friction may also be important. However, adding bulk viscosity to the simulations improves the agreement with the experimental data, but the model still overestimates the harmonic amplitudes for $x > 0.2$ m. The bulk viscosity terms have no effect on the beat-length of the second harmonic.

The beat length of the second harmonic is expressed as a function of the difference between the wave numbers of the free and bound components (Eq.(4.68)), which depend on the dispersion relation for waves. The surface tension (σ) modifies the linear dispersion relation such that (Dingemans, 1997a):

$$\omega^2 = \left(1 + \frac{1}{Bo}\right) gk \tanh(kh), \quad (4.69)$$

where $Bo = \rho g/(\sigma k^2)$ is the Bond number quantifying the ratio between gravity effects and surface tension effects. If $Bo \gg 1$, surface tension effects can be neglected and the classical

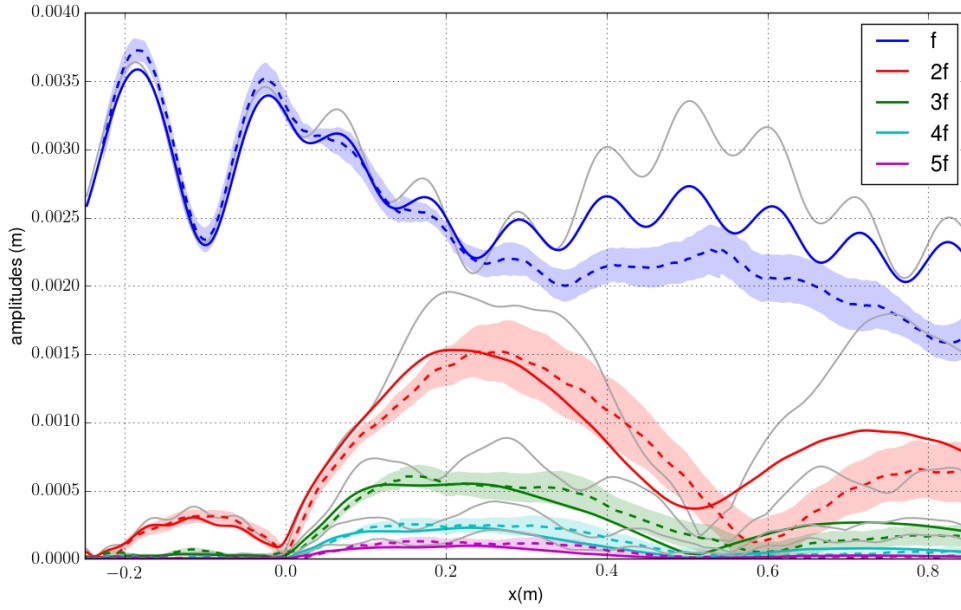


Figure 4.19: Simulated (solid line) and measured (dashed line) spatial evolution of the first five harmonic amplitudes for $f_1 = 1.9837$ Hz with bulk viscosity $\nu = 4.10^{-5}$ m^2/s , but without the effects of surface tension. For comparison, the results from the simulation without the effects of viscosity or surface tension are shown by the gray lines.

relation dispersion is recovered. For small Bo , surface tension effects become important causing an increase in the wavelength for a given wave frequency. According to the values in Table 4.4, for the water depth $h^{(II)}$, the Bond numbers corresponding to $k_1^{(II)}$ and $k_2^{(II)}$ are respectively $Bo = 158$ and $Bo = 29$.

Surface tension impacts short waves with wavelengths on the order of centimeters. The wave lengths associated with the second harmonic over the step are less than 10 cm, so the influence of surface tension on their associated wavelength is small (Table 4.4), but important enough to modify the beat length.

σ (N/m)	$k_1^{(II)}$ (rad/m)	$L_1^{(II)}$ (m)	$k_2^{(II)}$ (rad/m)	$L_2^{(II)}$ (m)	D^- (m)
0	29.65	0.2118	70.95	0.08855	0.5393
0.071	29.54	0.2127	69.11	0.0909	0.6264

Table 4.4: Wave number and wavelength of the first and second harmonics with the associated beat length for the water depth $h^{(II)} = 2.0$ cm, and for surface tension $\sigma = 0$ N/m and $\sigma = 0.071$ N/m.

To take into account the effects of surface tension, the dynamic free surface boundary condition is modified with a term proportional to the curvature of the free surface (e.g. [Dias and Kharif](#),

1999), Eq.(1.26) becomes:

$$\frac{\partial \tilde{\Phi}}{\partial t} = -g\eta - \frac{1}{2} \left(\frac{\partial \tilde{\Phi}}{\partial x} \right)^2 + \frac{1}{2} \tilde{\omega}^2 \left(1 + \left(\frac{\partial \eta}{\partial x} \right)^2 \right) - 2\nu \frac{\partial^2 \tilde{\Phi}}{\partial z^2} + \frac{\sigma}{\rho} \frac{\partial}{\partial x} \left(\frac{\frac{\partial \eta}{\partial x}}{\sqrt{1 + \left(\frac{\partial \eta}{\partial x} \right)^2}} \right). \quad (4.70)$$

With surface tension ($\sigma = 0.071 \text{ N/m}$), the simulated beat length of the second harmonic (red curves, Figure 4.20) is close the measured value. Thus, even with wavelengths at the limit of the range for which surface tension has significant effects, the influence is visible.

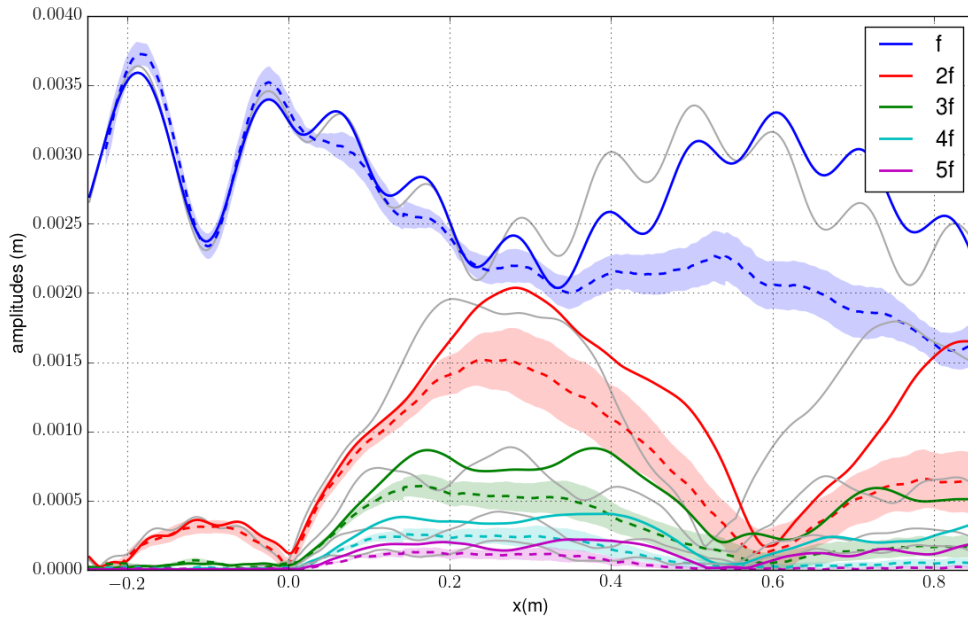


Figure 4.20: Simulated (solid line) and measured (dashed line) spatial evolution of the first five harmonic amplitudes for $f_1 = 1.9837 \text{ Hz}$ without the effects of viscosity but with surface tension $\sigma = 0.071 \text{ N/m}$. For comparison, the results from the simulation without the effects of viscosity or surface tension are shown by the gray lines.

Finally, by simulating the combined effects of bulk viscosity ($\nu = 4.10^{-5} \text{ m}^2/\text{s}$) and surface tension ($\sigma = 0.071 \text{ N/m}$), the simulation results agree well with the experiments (Figure 4.21). The amplitude of the second harmonic reaches a minimum around $x = 0.59 \text{ m}$, that is larger in the simulations than measured in the experiments. This minimum is proportional to the amplitude difference between the bound and free waves. The free wave has a smaller wavelength than the bound wave, and is thus more dissipated by the bulk viscosity. Therefore, the difference between the two amplitudes increases, explaining the increase of the minimum attained by the second harmonic amplitude. The space-time profiles of the free surface elevation of the simulation (Figure 4.22) and the experiments (Figure 4.23) show that in the simulation, the dissipation is still underestimated in comparison with the experiments. Note that the experimental space-time free

surface profile is made with the free surface elevation at the center of the wave tank, which may explain some differences in wave amplitude attenuation when compared with Figure 4.21.

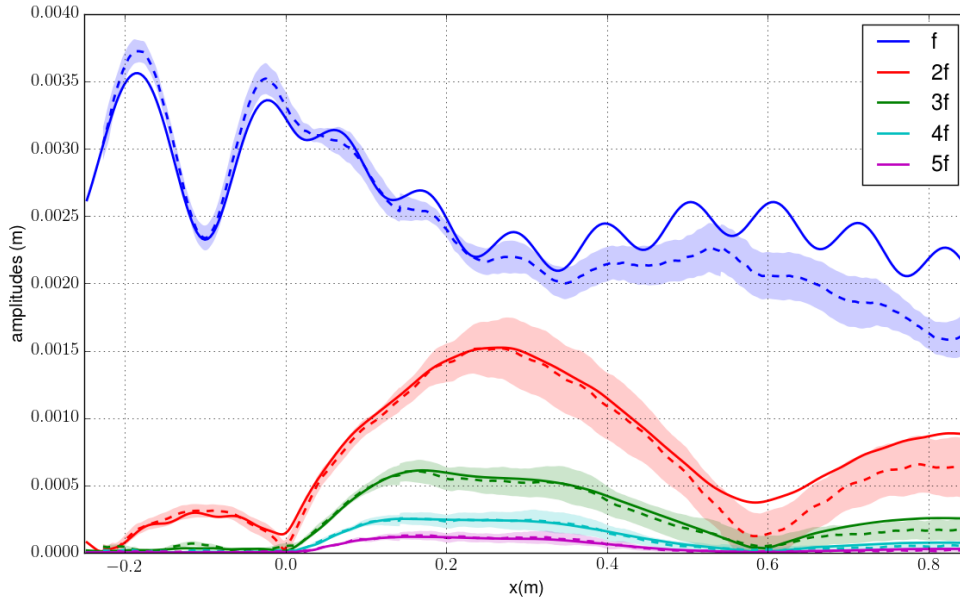


Figure 4.21: Simulated (solid line) and measured (dashed line) spatial evolution of the first five harmonic amplitudes for $f_1 = 1.9837$ Hz with viscosity $\nu = 4.10^{-5} \text{ m}^2/\text{s}$ and surface tension $\sigma = 0.071 \text{ N/m}$.

Additional experiments were completed with higher incident wave frequencies. Using the same value of the bulk viscosity ($\nu = 4.10^{-5} \text{ m}^2/\text{s}$) in the simulations produces good results for frequencies up to 3 Hz. For higher frequencies, the simulated dissipation is too strong, and the amplitudes decrease even before the step. This is likely due to the fact that the dominant source of energy dissipation is bottom friction.

Bottom friction may become a significant source of dissipation for lower frequency waves (L) (since the dissipation is stronger for longer wavelengths). By taking into account the effects of bottom friction, the optimal viscosity will likely be reduced. Therefore, a series of tests were run including the bottom friction term. The no-slip condition was first applied everywhere in the domain, except the generation relaxation zone. However, this did not give satisfactory results in the region around the step. Since the bottom friction term is derived assuming small gradients in the water depth, the theory is likely no longer valid when simulating abrupt changes in depth like a bottom step.

Finally, the no-slip condition was only applied in the shallow water region. To prevent an abrupt change of the bottom boundary condition, the viscosity in the bottom friction term increase slowly in space to reach the targeted value. However, for value of the viscosity required to re-

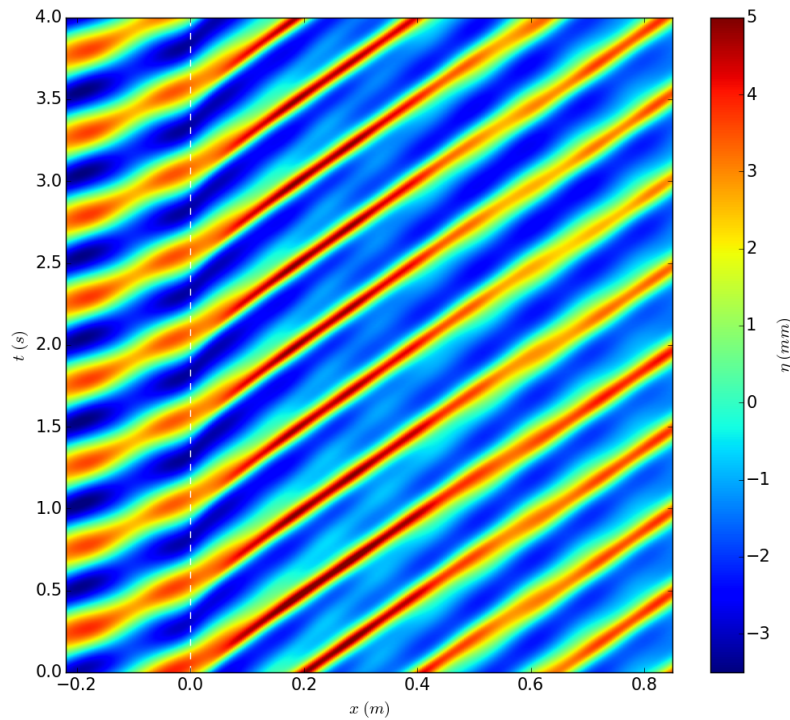


Figure 4.22: Simulated space-time profile of the free surface elevation (in mm) for $f_1 = 1.9837$ Hz, with viscosity $\nu = 4.10^{-5} \text{ m}^2/\text{s}$ and surface tension $\sigma = 0.071 \text{ N/m}$. The position of the step is indicated by the vertical white dashed line.

produced the observed amplitude decay, oscillations occur in the viscosity transition zone making the simulation unstable. Therefore, only simulations taking into account the effects of bulk dissipation are shown here.

In the numerical model, only two sources of energy dissipation are represented. Prządka et al. (2015) show that the white pigments added to the water were chosen to avoid surface film effects contrary to most other paint pigments that contain surfactants. But if the water is not perfectly clean, a surface film can form, which changes the attenuation properties at the surface of the fluid and increases the damping. This effect can increase significantly owing to a resonance effect between capillary-gravity waves and elastic waves (also called) Marangoni waves. Thus, the high dissipation observed in the experiments may also be due to the presence of dust on the water surface. This contribution to energy dissipation is not taken into account in the numerical model and may be one additional explanation for the differences between the experiments and simulations.

With the bulk viscosity and surface tension terms, the model reproduces well the experimental data for a given frequency of the incident wave (e.g. Figure 4.21). However, the value of the bulk

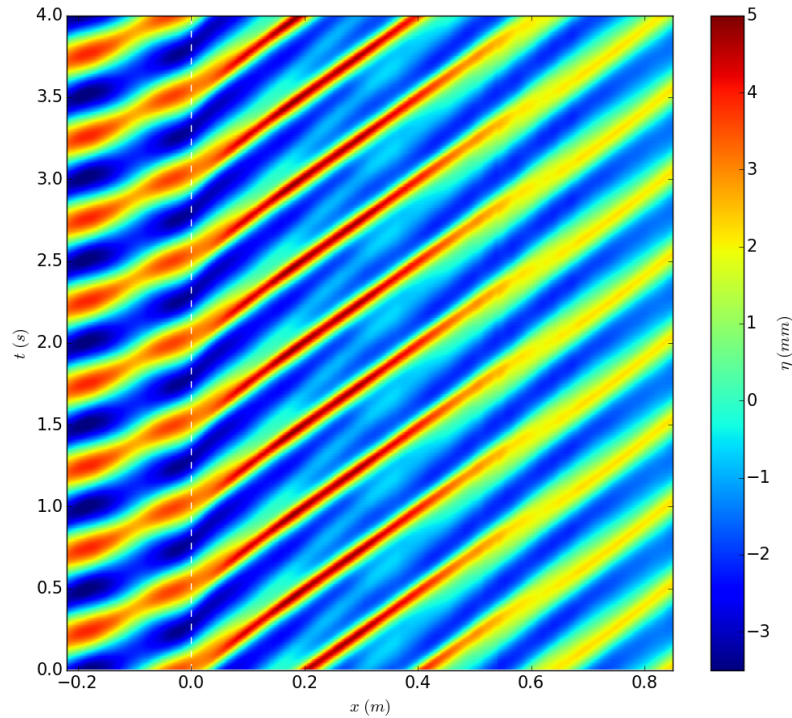


Figure 4.23: Experimental space-time profile of the free surface elevation (in mm) for $f_1 = 1.9837$ Hz. The position of the step is indicated by the vertical white dashed line.

viscosity has to be adapted for each frequency. The model is not able to take into account the effects of bottom friction in this specific case (too steep bottom slope) nor surface film effects that may be an important mechanisms for energy dissipation in the experiments.

4.5 Conclusions

Dissipation has been introduced into the potential flow model deriving a visco-potential system of equations that contains: (1) two additional terms in the free surface boundary conditions to take into account the predominant contribution of the vortical component of the velocity representing the effects of bulk viscosity, and (2) the modification of the bottom boundary condition to take into account the presence of a boundary layer representing the effects of bottom friction. The simulation results agree well with the developed theories and experimental data when applied to cases respecting the model assumptions (i.e. $\nu < 10^{-3}$, small bottom slope).

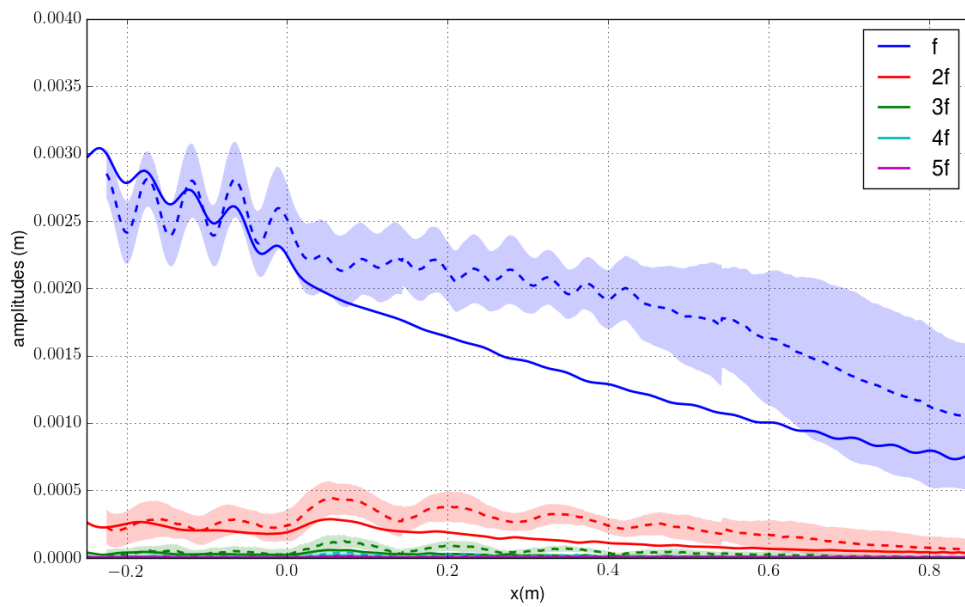


Figure 4.24: Simulated (solid line) and measured (dashed line) spatial evolution of the first five harmonic amplitudes for $f_1 = 3.8$ Hz with viscosity $\nu = 4.10^{-5} \text{ m}^2/\text{s}$ and surface tension $\sigma = 0.071 \text{ N/m}$. The dashed line is the transversal mean of the measurements and the shaded zone is the standard deviation.

Chapter 5

Development and implementation of the 2DH version of the model using Radial Basis Functions (RBF)

Ce chapitre traite de l'extension du modèle en deux dimensions dans le plan horizontal. Avec l'objectif de modifier le moins possible la structure du code 1DH (i.e. en gardant un schéma explicite de Runge-Kutta d'ordre 4 pour l'intégration en temps et la résolution spectrale du problème de Laplace sur la verticale), et de pouvoir traiter des domaines irréguliers, une méthode basée sur les Fonctions de Base Radiales (en Anglais RBF) est utilisée pour estimer les dérivées horizontales en deux dimensions pour des nuages de points distribués de façon irrégulière et non-structurée. Après une revue des différentes utilisations et caractéristiques des RBFs, le choix se porte sur la méthode RBF-FD, qui consiste à estimer la dérivée d'une fonction en un point comme une combinaison linéaire des valeurs de la fonction en ses points voisins. Les RBF centrées en ces points sont ensuite utilisées pour déterminer les pondérations. La formulation mathématique de la méthode ainsi que sa mise en œuvre numérique sont présentées. La précision de l'estimation des dérivées premières et secondes est testée pour une fonction sinusoidale en faisant varier les différents paramètres de la méthode: type de RBF, valeur du paramètre de forme C , taille du stencil N_{sten} , degré du polynôme augmenté l . L'objectif étant d'appliquer les poids déterminés pour chaque type de dérivée à toutes les variables du modèle, la recommandation pour une telle utilisation serait de privilégier des RBFs ne dépendant pas de paramètre de forme. En effet, la valeur optimale de celui-ci apparaissant fortement dépendante de la fonction considérée, il peut s'avérer compliqué de trouver une valeur adéquate pour l'ensemble des fonctions utilisées. Pour une taille de stencil fixée entre 20 et 30 points, la PHS (Polyharmonic Spline) r^7 augmentée d'un polynôme de degré 3 semble un bon compromis entre précision de l'estimation et temps de calcul.

For the extension of the model to two horizontal dimensions, our aim in the frame of the current PhD work was to modify as little as possible the 1DH version of the code, keeping the RK4 scheme for time integration (section 2.1.1) and the spectral resolution in the vertical dimension (section 1.2). Nevertheless, for the estimation of the horizontal derivatives, finite-difference schemes are hardly generalizable for two or higher dimensions since polynomial unisolvency is no longer assured. In cases where the geometry of the domain is simple, horizontal dimensions can be treated separately with 1D schemes but then, the model cannot be applied to complex domains requiring geometric flexibility with scattered node layout. Here, a meshless method based on the Radial Basis Functions (RBF) is tested and implemented in Misthyc to avoid these kind of restrictions.

5.1 Presentation of the RBF method

5.1.1 General context

5.1.1.1 RBF to interpolate scattered data fields

RBF were first introduced by Hardy (1971) for interpolation purposes. He wanted to construct a continuous surface representative of the topography of a given zone, from a set of scattered elevation measurements. After trying to use Fourier and polynomial series methods that he found unsatisfactory, Hardy finally obtained good results using a basis composed of radially symmetric functions $\phi(\|\underline{x} - \underline{x}_k\|)$, with one centered at each data point \underline{x}_k (where the norm is the standard Euclidean distance function). Thus the interpolant $s(\underline{x})$ knowing the data values f_k at N nodes $\underline{x}_k, k = 1, 2, \dots, N$ can be written as:

$$s(\underline{x}) = \sum_{k=1}^N \lambda_k \phi(\|\underline{x} - \underline{x}_k\|) \quad (5.1)$$

The coefficients λ_k in the RBF interpolant can be found by enforcing $s(\underline{x}_k) = f_k$, which results in the system of linear equations:

$$\begin{bmatrix} \phi(\|\underline{x}_1 - \underline{x}_1\|) & \phi(\|\underline{x}_1 - \underline{x}_2\|) & \cdots & \phi(\|\underline{x}_1 - \underline{x}_N\|) \\ \phi(\|\underline{x}_1 - \underline{x}_2\|) & \phi(\|\underline{x}_2 - \underline{x}_2\|) & \cdots & \phi(\|\underline{x}_2 - \underline{x}_N\|) \\ \vdots & \vdots & \ddots & \vdots \\ \phi(\|\underline{x}_N - \underline{x}_1\|) & \phi(\|\underline{x}_N - \underline{x}_2\|) & \cdots & \phi(\|\underline{x}_N - \underline{x}_N\|) \end{bmatrix} \begin{bmatrix} \lambda_1 \\ \lambda_2 \\ \vdots \\ \lambda_N \end{bmatrix} = \begin{bmatrix} f_1 \\ f_2 \\ \vdots \\ f_N \end{bmatrix} \quad (5.2)$$

Hardy (1971) used the multiquadric (MQ) radial function $\phi(r) = \sqrt{r^2 + C^2}$ with C a strictly positive shape parameter to have a continuously differentiable basis function (even when $r = 0$). C controls the sharpness of the RBFs: large values of C give rise to flat basis functions, whereas intermediate values lead to bowl-like basis functions, and small values to narrow cone-like basis functions. Franke (1982) led a study on scattered data interpolation, testing 29 interpolation

methods for 6 different test functions, and the MQ function was among the most accurate, together with the inverse multiquadric (IMQ), and the thin plate spline (TPS). Despite the good results obtained with the multiquadric RBF, [Franke \(1982\)](#) still raised concerns because the non-singularity of the associated interpolation matrix had not been proven at the time of the study.

Many different RBFs can be used, the most common choices are presented in [Table 5.1](#).

Name (Acronyme)	Function $\phi(r)$	Condition	Regularity
Polyharmonic Spline (PHS)	r^m	m odd integer	piecewise-smooth
Thin Plate Spline (TPS)	$r^m \log r$	m even integer	piecewise-smooth
Multiquadric (MQ)	$\sqrt{r^2 + C^2}$	$C \in \mathbb{R}$	infinitely-smooth
Inverse Multiquadric (IMQ)	$\frac{1}{\sqrt{r^2 + C^2}}$	$C \in \mathbb{R}$	infinitely-smooth
Inverse Quadratic (IQ)	$\frac{1}{r^2 + C^2}$	$C \in \mathbb{R}$	infinitely-smooth
Gaussian (GA)	e^{-r^2/C^2}	$C \in \mathbb{R}$	infinitely-smooth

Table 5.1: Commonly used RBFs including the form of the function, the necessary constraints on the free parameter, and the regularity of the function.

For infinitely smooth RBFs (typically those with a shape parameter C), the interpolation system will never be singular if the scattered nodes are distinct, and they lead to spectral accuracy. For GA , IQ and IMQ RBFs, it can be shown that because they have a positive Fourier transform, their interpolation matrices are positive definite and thus non-singular ([Fornberg and Flyer, 2015](#)), but it is not the case with the MQ . However, [Micchelli \(1986\)](#) proved that the interpolation matrix for MQ has one positive and $N - 1$ negative eigenvalues, ensuring its non-singularity.

Piecewise smooth RBFs do not depend on a shape parameter, but they present a singularity at the origin leading to algebraic rather than spectral convergence. To assure the unique solvability of the linear system for interpolation with piecewise smooth RBF, the interpolant has to be modified slightly by including polynomial terms:

$$s(\mathbf{x}) = \sum_{k=1}^N \lambda_k \phi(\|\mathbf{x} - \mathbf{x}_k\|) + \sum_{j=1}^M \beta_j p_j(\mathbf{x}), \quad (5.3)$$

with $p_j(\underline{x})_{j=1}^{\binom{l+d}{d}}$ a basis for polynomials up to degree l in \mathbb{R}^d (where $\binom{l+d}{d}$ is the binomial coefficient $\binom{l+d}{d} \equiv \frac{(l+d)!}{d!l!}$). For *PHS* of degree m , [Barnett \(2015\)](#) showed that a polynomial of degree at least $l = (m - 1)/2$ must be added to meet this condition. The addition of polynomial terms requires additional constraints for the linear system to be well-posed, which tend to minimize far-field growth (reducing the divergence order when $r \rightarrow \infty$):

$$\sum_{i=1}^N \lambda_i p_j(\underline{x}_i) = 0 \quad j = 1, 2, 3, \dots, M. \quad (5.4)$$

In this case, the non-singularity of the matrix becomes more restrictive since it requires the nodes not just to be distinct but also unisolvent with regard to the appended polynomial space ([Fornberg and Flyer, 2015](#)).

5.1.1.2 Use of RBF to solve partial differential equations (PDE)

The good interpolation results obtained with the RBF method made it of interest for partial derivative estimates on scattered nodes. [Stead \(1984\)](#) compared partial derivatives obtained from the *MQ* interpolant and from the least square quadratic approximation. Because RBF interpolants have no polynomial precision (except when adding polynomial terms Eq.(5.3)), [Stead \(1984\)](#) recommended the *MQ* method for surfaces with significant curvature. Later, [Kansa \(1990\)](#) was the first to use the *MQ* method (with a modified scheme) to solve PDEs (namely a Poisson equation) with the straight collocation method, by applying the PDE derivative operators to interior nodes and boundary conditions to the nodes on the boundary. The resulting matrix is not symmetric and not proved to be unisolvent. [Hon and Schaback \(2001\)](#) showed that it was possible to find very rare cases where the matrix was singular and so a general proof of unisolvency is impossible. That is why, [Fasshauer \(1997\)](#) tried to recover the symmetry of the matrix, to ensure non-singularity, by modifying the basis functions following a method based on Hermite interpolation. Another improvement was made by [Fedoseyev et al. \(2002\)](#), imposing both the PDE and the boundary conditions at boundary nodes. [Larsson and Fornberg \(2003\)](#) compared these three collocation methods to solve a Poisson equation for several functions. They found that for infinitely-smooth RBFs, symmetric collocation gave the best results whereas, for piecewise smooth RBFs, extra boundary collocation worked better.

5.1.2 Condition number of the interpolation matrix

The RBF interpolation method is known for generating ill-conditioned interpolation matrices. The matrix condition number measures how sensitive the solution of the system is to changes in the interpolation matrix. The computation of a solution of a linear system associated with an ill-conditioned matrix is prone to large numerical errors. The interpolation coefficients become oscillatory with large magnitudes that may lead to a poor evaluation of the interpolation

because of numerical cancellations. Practically, the matrix is almost singular because the matrix coefficients become very similar. In the case of the global RBF method, the matrix becomes ill-conditioned either when the size of the matrix increases (i.e. when the number of nodes N in the domain increases) or when the shape parameter C of the infinitely smooth RBFs becomes very large leading to matrix coefficients that depend strongly on C . Overcoming the problem of an ill-conditioned matrix is an important part of the work on RBFs (i.e. [Kansa and Hon, 2000](#)). Depending on the causes of the ill-conditioned matrix, several types of solutions have been proposed, which are presented briefly in the following sub-sections.

5.1.2.1 Numerical methods

Even without knowing the cause of an ill-conditioned matrix, some numerical approaches can be used to solve ill-conditioned systems. The first idea is to increase the arithmetic precision of the calculation, but it is computationally costly and is not usually retained as a “good” solution. Other methods such as using a preconditioner or doing block partitioning have also been tested ([Kansa and Hon, 2000](#)). Additionally, filtering techniques, using the Singular Value Decomposition (SVD) method, which neglects the smallest singular values, is also suggested by [Boyd \(2010\)](#).

5.1.2.2 Reduction of the size of the matrix

The interpolation method was first introduced as a global method taking into account all the nodes of the domain, leading to a full matrix. When the size of the matrix becomes too large, it often becomes ill-conditioned appears. In this case, the size of the matrix can be reduced by considering smaller domains using domain decomposition algorithms ([Beatson et al., 2001](#); [Wong et al., 1999](#); [Zhou et al., 2003](#)). By extending this idea to the other limit, one can switch to a local approach, defining stencils centered at each node of the domain, including only its $N_{sten} - 1$ nearest neighbors, for a total of N_{sten} nodes in each stencil. [Tolstykh and Shirobokov \(2003\)](#) were the first to consider this method to estimate derivatives with a finite difference approach, followed shortly by [Wright \(2003\)](#) and [Shu et al. \(2003\)](#). [Wright and Fornberg \(2006\)](#) improved the accuracy of this method by including a linear combination of derivatives of the function f at the surrounding nodes. This local method also presents the advantage of reducing considerably the computational time in comparison with the global method, and offers the possibility of being easily parallelized. The construction of approximate formulas for the derivatives using RBF interpolants, also called the RBF-FD method, will be presented in more detail in Section 5.2.

5.1.2.3 Nearly flat basis functions ($C \rightarrow \infty$)

The interpolation matrix becomes ill-conditioned when $C \rightarrow \infty$, i.e. in the limit of flat basis functions, generally leading to a trade-off between accuracy and numerical conditioning. Nevertheless, according to [Fornberg and Flyer \(2015\)](#), the interpolation problem is not itself ill-conditioned in the flat basis function limit; it is the numerical algorithm corresponding to the “direct” application of the method that leads to an ill-conditioned procedure, whereas the problem is completely well-conditioned. Work has been done to develop stable algorithms to reach accurate results even for high values of C . For example, the Contour Padé algorithm ([Fornberg and Wright, 2004](#)) allows numerically stable computations of MQ RBF interpolants for all C values. The interpolant is written as the sum of a rational function and a power series in C whose coefficients are determined in a complex C -plane, removing the restriction that C is real. This method is not really adapted for a large data set. Another stable algorithm valid for larger node sets, called RBF-QR, was developed by [Fornberg and Piret \(2007\)](#) for data points distributed over the surface of a sphere. It consists in finding an alternative well-conditioned RBF basis spanning exactly the same space. In this case, the new equivalent bases converge to the spherical harmonic basis as $C \rightarrow \infty$. The RBF-QR method has been extended to more general domains from 1 to 3 dimensions ([Fornberg et al., 2011](#)) mainly for GA RBF (Table 5.1). More recently a simpler and faster algorithm, the RBF-GA algorithm has been developed ([Fornberg et al., 2013](#)), particularly well-suited for RBF-FD applications. Use of a stable algorithm not only improves the accuracy by allowing the use of larger values of C , but also makes the choice of optimal C less critical. Nevertheless, the modified RBFs have much more complicated expressions.

5.1.3 Accuracy of the estimates and choice of the RBF

The choice of RBF to obtain the most accurate estimates is not straightforward. Some trade-offs must be considered. RBFs can be divided into two categories: the infinitely smooth and the piecewise smooth functions. Two characteristics mainly differentiate these two categories: (1) the type of convergence when reducing the typical node distance, and (2) the dependency on a shape parameter C .

5.1.3.1 Spectral convergence vs algebraic convergence

Considering global RBF methods, infinitely-smooth RBFs have a spectral convergence when piecewise smooth RBFs only have algebraic convergence, which often leads to a preference for infinitely smooth RBFs ([Fornberg and Flyer, 2015](#)). Nevertheless, when considering local methods (i.e. RBF-FD method), the spectral accuracy of infinitely smooth RBFs is lost, minimizing its advantage with respect to convergence. Moreover, infinitely smooth RBFs feature stagnation errors, meaning that when the inter-node spacing is reduced, the error is not improved indefinitely but reaches a plateau because the matrix becomes ill-conditioned. To counteract this

problem, the value of C is generally increased while the inter-node distance is decreased to keep the condition number of the matrix constant. However this increase in C tends to degrade the accuracy and prevents convergence (Fornberg and Flyer, 2015). The addition of a polynomial of variable degree (at least a constant) to the RBF interpolant may reduce these errors producing a convergence rate corresponding to the degree of the added polynomial. *PHS* RBFs need the addition of a polynomial to the interpolant to guarantee the unisolvency of the system, thus they do not present this kind of stagnation error. Flyer et al. (2016) recommended for simple local interpolation problems with *PHS* to increase the degree of the polynomial close the maximum value allowed by the size of the stencil, but for more complex applications, the degree of the added polynomial should be such that there are twice as many RBFs as polynomial terms in the interpolant (i.e. $N_{sten} \approx 2M$) (Barnett, 2015).

5.1.3.2 Optimal value for the shape parameter C

With infinitely smooth RBFs, the estimation error is very dependent on the value of the shape parameter C : for small values of C , the error is generally quite high and decreases with an increase of C , often reaching a minimum for an intermediate value of $C = C_{opt}$ (called in the following the optimal value of C). Increasing C beyond this optimal value, the error increases and large oscillations may be observed if the matrix becomes ill-conditioned. However, the matrix may already become ill-conditioned for values of C smaller than C_{opt} : in this case, the minimal error is just at the limit of ill-conditioning. In the limit of $C \rightarrow \infty$, Fornberg et al. (2004) showed that when the limit exists, the interpolant tends to a multivariate polynomial. Except for *GA* RBF, the existence of the limit depends on the unisolvency of the node setting with regard to multivariate polynomials. Concerning the estimation of derivatives, Bayona et al. (2010) showed that the formulas obtained with the RBF-FD method approached conventional finite-difference formulas in the limit of infinitely flat RBFs, and that there is a range of values of C that produce more accurate estimates than standard finite difference schemes.

However, finding C_{opt} is a difficult task. For global methods, there is no mathematical theory to help with the choice of C . Usually, the choice of C is based on the inter-node spacing, for convenience, but Carlson and Foley (1991) concluded that (according to their tests), the value of optimal shape parameter depended on the value of the function interpolated and not on the node spacing or the node positions. This was also observed by Rippa (1999). For interpolation, the value of C is chosen by cross-validation methods, for example Rippa (1999) developed a method based on the minimization of a cost function that was the sum over each node of the errors between the interpolant and the function when each node is removed from the initial set. Fasshauer and Zang (2007) adapted Rippa's algorithm for the resolution of PDEs with RBF pseudospectral method. For RBF-FD, Bayona et al. (2010) derived an expression of the error estimate as a function of C , showing that C_{opt} depends on the value of the function and its derivatives, and is independent of

the node spacing at first order, but can vary with node locations in 2D. Knowing the expression of the error estimate, [Bayona et al. \(2011\)](#) proposed an algorithm to find the optimal value of C . However, this required solving the problem twice, since the values of the derivative of the function are necessary to compute the error estimates.

Several studies show that the accuracy of the estimations could be greatly improved by making the shape parameter vary with the location of the center. For example, [Kansa and Carlson \(1992\)](#) used a strictly monotonic function to vary C at each node by several orders of magnitude, depending on its index in the node set. Later, [Kansa and Hon \(2000\)](#) varied the shape parameter as a function of the local curvature radius of the function being solved. According to [Fornberg and Zuev \(2007\)](#), C should be proportional to the distance to the nearest neighbor and should be increased at the edge of the domain. Even if varying the shape parameter seems to improve the accuracy, the optimal way in which C must vary from one node to another is yet not very clear, except in the RBF-FD method. Indeed, with the analytical expression of the error estimates, [Bayona et al. \(2012\)](#) developed an algorithm to find the C_{opt} for each node (a generalized MQ is for nodes without C_{opt}) and improve significantly the accuracy in comparison with a constant shape parameter. With a variable shape parameter the proof of the non-singularity of the interpolation matrix is no longer valid, but it seems that singular systems still are not likely to arise ([Fornberg and Flyer, 2015](#)). Moreover, this approach produces more variable matrix coefficients, reducing the condition number.

The selection of a “good” value for the shape parameter can be challenging, which is why RBFs without shape parameters such as *PHS*, recently have become more and more attractive, noting furthermore that they produce relatively well-conditioned matrices.

5.1.3.3 Stencil size for the RBF-FD method

In the case of local methods, the size of the stencil also enters into consideration when looking at the accuracy of the estimation. [Bayona et al. \(2010\)](#) and [Ding et al. \(2005\)](#) study, among other parameters, the convergence of the error as a function of the number of nodes in the stencil (N_{sten}). They showed that the accuracy is generally increased when the size of the stencil increases, with some jumps occurring at certain values of N_{sten} . [Bayona et al. \(2010\)](#) gave the threshold value of N_{sten} for which the error is significantly smaller than the error for $N_{sten} - 1$: $N_{sten} = (p - 1)^2 + 4$ (where p is an even integer) for equispaced nodes and $N_{sten} = (p + 2)(p + 3)/2$ (where p is any integer) for non-equispaced nodes. As a consequence, the order of convergence as a function of the node spacing also varies in phase with the number of nodes in the stencil, which is different for equispaced nodes and non-equispaced nodes. For example with $N_{sten} = 13$, the convergence is of order $p = 4$ for equispaced nodes, but only of order $p = 2$ for non-equispaced nodes, ac-

according to [Bayona et al. \(2010\)](#). For *PHS* RBFs, increasing the stencil size decreases the error, but the order of convergence is controlled by the degree of the added polynomials, not by the stencil size itself.

5.1.4 Runge phenomenon and boundary errors

Approximations near the boundary usually present larger errors than in the interior due to the one-sided nature of the stencil. It is a problem of major concern since for time-dependent PDEs, the errors at the boundary can contaminate the solution across the entire domain or simply grow quickly and cause the solution to diverge. That is why it is particularly important to find solutions to minimize boundary errors. [Fornberg et al. \(2002\)](#) studied four edge enhancement techniques: inclusion of low degree polynomials (here first degree), node clustering (with higher density of nodes near the boundary), Not-a-knot (Nak) and Super Not-a-knot (Snak) methods. The last two techniques consist in moving some RBF centers from the inside to the outside of the domain: nodes from the first row inside the domain for Nak, and nodes on the boundary are added for Snak. Their conclusions are that the four correction methods are efficient with a preference for the Nak type of correction that is more “local” and may be more adapted for complex geometry domains than the addition of low degree polynomials.

Moreover, in the near-flat limit, infinitely smooth RBF may tend to a multivariate polynomial, but polynomial interpolation on an equispaced grid is known to present large oscillations of the interpolated function at the edges of the domain. This effect, usually called the Runge phenomenon, can be prevented by node clustering close to the boundaries. Nevertheless, with the RBF method, this phenomenon can be also triggered by node refinement in the interior of the domain. It is then advantageous to let the shape parameter vary spatially ([Fornberg and Zuev, 2007](#)). Increasing the value of C for nodes on the boundary may significantly improve the accuracy.

Finally, another possibility to reduce the one-sided nature of the stencil for nodes on the boundary, is to add a layer of nodes just outside the boundary. No equations are enforced at their location, which is why they are usually called ghost nodes, but they become part of the stencil of boundary and near boundary interior nodes. These additional nodes allow enforcing, in addition to the boundary condition, the PDE at the boundary nodes. The function values at the ghost nodes are found by enforcing either a non-Dirichlet condition or the PDE at the boundary nodes.

5.1.5 Stability for the resolution of time-dependent PDEs

The RBF-FD method allows obtaining sparse differentiation matrices (DM), that then can be used to solve PDEs. The analysis of the distribution of the DM eigenvalues gives important information concerning the capacity of the method to solve time-dependent PDEs with an explicit time-stepping algorithm. For purely convective PDEs, as energy should be constant for all time-stepping, all eigenvalues of the DM should be purely imaginary. Nevertheless, because of the irregularity of the stencils, eigenvalues of the DM are scattered into the right half of the com-

plex plane, which can cause severe instabilities if no natural dissipation occurs. This effect is emphasized by large stencils since the scatter of the eigenvalues increases with N_{sten} . Thus the resolution of time-dependent PDE without a diffusive operator is quite challenging.

To prevent numerical instabilities, the stencil size is often limited to relatively small values between 5 and 15. To control the eigenvalues, a hyperviscosity approach can be implemented (Fornberg and Lehto, 2011). This method acts like a filter, by adding higher order derivatives of the Laplacian to the right hand side of the governing equations. The effect will be a damping of the spurious high frequencies by moving the corresponding eigenvalues to the left side of the complex plane, while leaving the relevant modes intact. As a consequence, larger stencils can be used allowing approximations of higher accuracy. For *PHS* RBFs, the implementation is quite simple since the Laplacian operator can be expressed as a function of another *PHS* RBF (Barnett, 2015).

For more details on RBF methods and numerous application examples, see the recently published book of Fornberg and Flyer (2015).

5.2 Implementation of the RBF-FD method

In the extension of the model to two horizontal dimensions, the horizontal derivatives will be approximated with the local RBF-FD method. This method seems to be a good compromise between:

- an easy implementation, with an algorithm similar to finite-difference methods,
- accuracy close to pseudo-spectral methods and global RBF methods,
- flexibility with a scattered nodes distribution and possibilities of local refinement,
- potential for high computational speed with sparse DM and parallelization due to the local definition of the stencil.

5.2.1 Theory

In this section, the estimation of derivatives with the RBF-method is described following Barnett (2015). The goal is to estimate the value of $Lf(\underline{x}_1)$, where $\underline{x}_1 = (x_1, y_1)$ is any point in the domain, f is any function expressed at each node, and L the desired linear differential operator (i.e. $\frac{\partial}{\partial x}$, $\frac{\partial}{\partial y}$, $\frac{\partial^2}{\partial x^2}$, $\frac{\partial^2}{\partial y^2}$, etc.).

Here, the local RBF method is applied, so a stencil of N_{sten} nodes, formed by the node of interest \underline{x}_1 (center of the stencil) and its $N_{sten} - 1$ nearest neighbors ($\underline{x}_2, \underline{x}_3, \dots, \underline{x}_{N_{sten}}$), is considered. In Figure 5.1, an example of a RBF-FD stencil in 2D corresponding to $N_{sten} = 9$ is shown. The

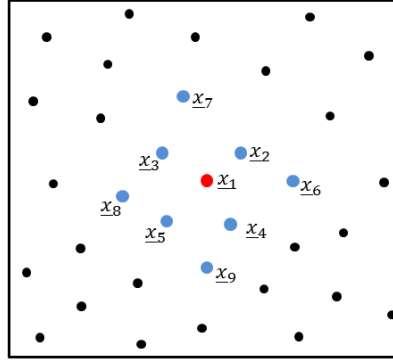


Figure 5.1: Definition of a stencil with $N_{sten} = 9$ nodes. The node in red (\underline{x}_1) is the center of the stencil and the blue dots are its supporting nodes. Black dots are non-supporting nodes.

corresponding function values are $f_1, f_2, \dots, f_{N_{sten}}$. Weights $\{w_i\}_{i=1}^{N_{sten}}$ are sought so that:

$$Lf(\underline{x}_1) \approx \sum_{i=1}^{N_{sten}} w_i f_i. \quad (5.5)$$

In matrix formalism this becomes:

$$Lf(\underline{x}_1) \approx \begin{bmatrix} \underline{w} & \underline{v} \end{bmatrix} \begin{bmatrix} \underline{f} \\ \underline{0} \end{bmatrix}, \quad (5.6)$$

where

$$\underline{w} = [w_1 \quad w_2 \quad \dots \quad w_{N_{sten}}] \quad \text{and} \quad \underline{v} = [v_1 \quad v_2 \quad \dots \quad v_M]$$

with

$$\underline{f} = [f_1 \quad f_2 \quad \dots \quad f_{N_{sten}}]^T. \quad (5.7)$$

The M weights contained in \underline{v} are added here in order to facilitate the derivation made using a matrix formalism (explained further below). But they will be discarded once the system is resolved.

To derive these weights, a RBF interpolant supplemented with a polynomial of degree l (general case) is considered :

$$s(\underline{x}) = \sum_{k=1}^{N_{sten}} \lambda_k \phi(\|\underline{x} - \underline{x}_k\|) + \sum_{j=1}^M \beta_j p_j(\underline{x}) \quad (5.8)$$

with $p_j(\underline{x})_{j=1}^{\binom{l+2}{2}}$ a basis of polynomials up to degree l in \mathbb{R}^2 and $M = \binom{l+2}{2}$.

The interpolation coefficients $(\{\lambda_k\}_{k=1}^{N_{sten}}, \{\beta_j\}_{j=1}^M)$, are found by enforcing:

- N_{sten} constraints corresponding to forcing the interpolant to have the value of the function for all nodes in the stencil: $s(\underline{x}_k) = f_k$, for $k = 1, \dots, N_{sten}$,
- M constraints to minimize the far-field growth due to the addition of polynomial terms: $\sum_{i=1}^{N_{sten}} \lambda_i p_j(\underline{x}_i) = 0 \quad j = 1, 2, 3, \dots, M$.

The addition of the M polynomial terms increases the size of the system in Eq.(5.2), leading to the following linear system:

$$\begin{bmatrix} A & P \\ P^T & 0 \end{bmatrix} \begin{bmatrix} \underline{\lambda} \\ \underline{\beta} \end{bmatrix} = \begin{bmatrix} f \\ 0 \end{bmatrix} \Rightarrow \begin{bmatrix} \underline{\lambda} \\ \underline{\beta} \end{bmatrix} = \begin{bmatrix} A & P \\ P^T & 0 \end{bmatrix}^{-1} \begin{bmatrix} f \\ 0 \end{bmatrix} \quad (5.9)$$

where

$$A = \begin{bmatrix} \phi(\|\underline{x}_1 - \underline{x}_1\|) & \phi(\|\underline{x}_1 - \underline{x}_2\|) & \cdots & \phi(\|\underline{x}_1 - \underline{x}_{N_{sten}}\|) \\ \phi(\|\underline{x}_1 - \underline{x}_2\|) & \phi(\|\underline{x}_2 - \underline{x}_2\|) & \cdots & \phi(\|\underline{x}_2 - \underline{x}_{N_{sten}}\|) \\ \vdots & \vdots & \ddots & \vdots \\ \phi(\|\underline{x}_{N_{sten}} - \underline{x}_1\|) & \phi(\|\underline{x}_{N_{sten}} - \underline{x}_2\|) & \cdots & \phi(\|\underline{x}_{N_{sten}} - \underline{x}_{N_{sten}}\|) \end{bmatrix},$$

$$P = \begin{bmatrix} p_1(\underline{x}_1) & p_2(\underline{x}_1) & \cdots & p_M(\underline{x}_1) \\ p_1(\underline{x}_2) & p_2(\underline{x}_2) & \cdots & p_M(\underline{x}_2) \\ \vdots & \vdots & \ddots & \vdots \\ p_1(\underline{x}_{N_{sten}}) & p_2(\underline{x}_{N_{sten}}) & \cdots & p_M(\underline{x}_{N_{sten}}) \end{bmatrix},$$

$$\underline{\lambda} = [\lambda_1 \quad \lambda_2 \quad \cdots \quad \lambda_{N_{sten}}]^T \quad \text{and} \quad \underline{\beta} = [\beta_1 \quad \beta_2 \quad \cdots \quad \beta_M]^T.$$

Evaluating the derivative of the interpolant (Eq.(5.8)) at \underline{x}_1 gives:

$$\begin{aligned} Ls(\underline{x}_1) &= \sum_{k=1}^{N_{sten}} \lambda_k L\phi(\|\underline{x}_1 - \underline{x}_k\|) + \sum_{j=1}^M \beta_j Lp_j(\underline{x}_1) \\ &= \begin{bmatrix} \underline{b} & \underline{c} \end{bmatrix} \begin{bmatrix} \underline{\lambda} \\ \underline{\beta} \end{bmatrix} \\ &= \left(\begin{bmatrix} \underline{b} & \underline{c} \end{bmatrix} \begin{bmatrix} A & P \\ P^T & 0 \end{bmatrix}^{-1} \right) \begin{bmatrix} f \\ 0 \end{bmatrix} \end{aligned} \quad (5.10)$$

where

$$\underline{b} = \left[L\phi(\|\underline{x}_1 - \underline{x}_1\|) \quad \cdots \quad L\phi(\|\underline{x}_1 - \underline{x}_{N_{sten}}\|) \right] \quad \text{and} \quad \underline{c} = \left[Lp_1(\underline{x}_1) \quad \cdots \quad Lp_M(\underline{x}_1) \right].$$

By equating Eq.(5.6) and Eq.(5.10), it is found that:

$$\begin{bmatrix} \underline{b} & \underline{c} \end{bmatrix} \begin{bmatrix} A & P \\ P^T & 0 \end{bmatrix}^{-1} = \begin{bmatrix} \underline{w} & \underline{v} \end{bmatrix} \quad (5.11)$$

Finally, taking the transpose of Eq.(5.11) leads to the following system for the unknown weights \underline{w} and \underline{v} of Eq.(5.6):

$$\begin{bmatrix} A & P \\ P^T & 0 \end{bmatrix} \begin{bmatrix} \underline{w}^T \\ \underline{v}^T \end{bmatrix} = \begin{bmatrix} \underline{b}^T \\ \underline{c}^T \end{bmatrix} \quad (5.12)$$

Notice that the system can be simplified in this manner because the matrix A is symmetric. Thus the matrix arising in the system to find the derivative weights is the same as for the interpolation problem. Otherwise, if A is not symmetric, the matrix $\begin{bmatrix} A & P \\ P^T & 0 \end{bmatrix}$ has to be replaced by its transposed matrix. The application of the method depends on the non-singularity of the matrix $\begin{bmatrix} A & P \\ P^T & 0 \end{bmatrix}$, which was discussed in Section 5.1.

5.2.2 Numerical implementation

The calculation of the approximation weights of Eq.(5.6) has to be done at all nodes of the domain for each differential operator L required for the discretization of the PDE. In the Misthyc model, first and second-order derivatives in the two horizontal dimensions are needed. The resolution of the linear system Eq.(5.12) is achieved with a LU decomposition with a threshold of 10^{-16} . Once the weights are computed, they are stored in tables (differentiation matrices) and can be used whenever a derivative is estimated in the model. They are applied to evaluate the derivatives of any function in the model, such as the bottom profile h , the free surface elevation η , the a_n coefficients of the decomposition of the velocity potential Φ on the Chebyshev polynomial basis. The calculation of the weights is completed only once at the beginning of the simulation, and is therefore a part of the pre-processing phase.

Before the weights in Eq.(5.6) are calculated, it is necessary to determine the $N_{sten} - 1$ nearest neighbors. The size of the stencil is defined at the beginning of the simulation, and is often defined either as a fixed number of nodes or as a fixed radius including a variable number of nodes.

For all the simulations presented in the two following chapters, the size of the stencil is constant for all the nodes as N_{sten} . In the code, an algorithm that calculates the Euclidean distance between two nodes (developed by Michel Benoit) is implemented to identify the $N_{sten}-1$ nearest neighbors. Some faster algorithms could have been used such as the k-dimensional tree algorithm (Fornberg and Flyer, 2015). Nevertheless, it is a pre-processing task whose computational time is relatively small in comparison to the resolution of the Laplace problem. Note that with this algorithm, the final set of nodes defining the stencil depends on the index of the nodes: since the stencil size is imposed to determine the nodes belonging to the stencil, (rather than a characteristic distance to the center), several nodes separated by the same distance to the center (for example, for regular grid) may be selected depending on the order in which they are evaluated.

Another characteristic of the code is the possibility to normalize the stencil. The physical length of the stencil is different for randomly scattered nodes, and the optimal value of the shape parameter that depends on the scale of the supporting region may vary from one node to another. Shu et al. (2003) proposed, similarly to finite element methods, to transform the local support to a unit circle by applying the following coordinate transformation:

$$(x', y') = \left(\frac{x}{D_i}, \frac{y}{D_i} \right), \quad (5.13)$$

where (x, y) are the coordinates in the physical space, (x', y') the coordinates in the unit circle, and D_i is the diameter of the smallest circle enclosing all nodes belonging to the stencil of node center i . This normalization is equivalent to considering a traditional RBF with a modified shape parameter $C' = CD_i$. Thus, when D_i changes, the equivalent C in the physical space also changes. Considering a set of evenly distributed scattered nodes, for a given stencil size N_{sten} , nodes located at the interior of the domain display a centered stencil whereas nodes located at the boundary have only a one-sided stencil. As a consequence, the D_i of a node at the boundary will be larger than the one for a node from the interior of the domain, as well as the equivalent C . Knowing that the estimation error generally decreases with an increase in C , the goal of the normalization is to reduce the difference in accuracy between interior nodes (with centered stencil) and boundary nodes with asymmetric or one-sided stencils. Note that the value of C used to estimate the weighting coefficients is constant for all the RBFs of a given stencil. It does not vary with the centers of the RBF contrary to what was tested by Fornberg and Zuev (2007).

The implementation of the RBF-FD method is first tested for the approximation of spatial derivatives. A series of tests are completed to verify that the main characteristics of the RBF-FD method described in the literature review (Section 5.1) are well reproduced.

5.3 Tests on the estimation of derivatives with the RBF-FD method.

This section is dedicated to a series of tests to evaluate the capabilities and limitations of the RBF-FD method to estimate first and second-order spatial derivatives, before implementing it in the time-stepping Misthyc code. The test function is first presented with the results of the tests designed to make numerical experiments with RBF-FD and to help evaluate the choice of several parameters of the method (RBF, shape parameter, added polynomial, stencil size N_{sten} , and stencil normalization).

5.3.1 Presentation of the test functions

Different types of functions have been tested to evaluate the performance of RBF methods for interpolation and derivative estimations in the literature. These functions were usually chosen arbitrarily, displaying more or less complex spatial variations (i.e. steep gradients, flat functions,...). Here, the tests are completed for a sinusoidal function because it is the first step to represent waves, and the free surface in the model will generally present oscillatory variations:

$$f(x, y) = A \cos \left(\frac{2\pi}{L} (x \cos \theta + y \sin \theta) \right), \quad (5.14)$$

where $L = 0.5$ m is the characteristic length of variation (or wavelength), A is the wave amplitude such that $A/L = 0.05$ and $\theta = 20^\circ$ is the direction of wave propagation with respect to the x axis (Figure 5.2). The domain of interest is defined by $0 \leq x \leq 1$ m and $0 \leq y \leq 1$ m.

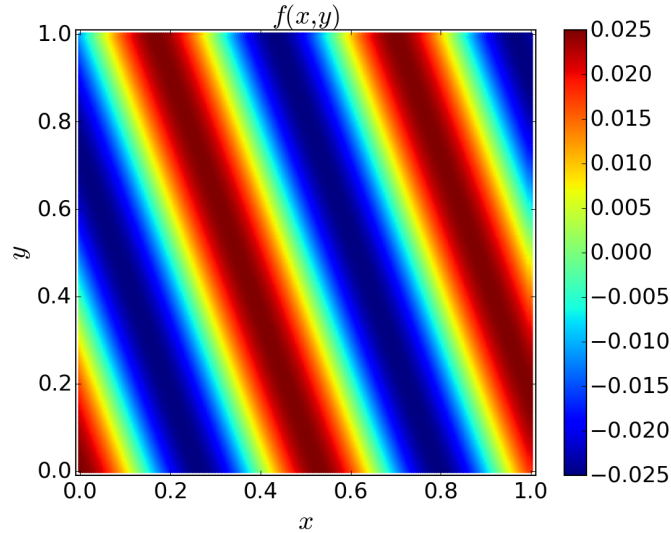


Figure 5.2: Test function $f(x, y) = A \cos \left(\frac{2\pi}{L} (x \cos \theta + y \sin \theta) \right)$ with $L = 0.5$ m, $A/L = 0.05$, and $\theta = 20^\circ$.

First and second-order derivatives in both horizontal dimensions are computed with the RBF-FD method, and the results are compared to the analytical derivatives (Figure 5.3). These derivatives

feature sinusoidal variations with different amplitudes: the largest are obtained for $f_{xx} = \frac{\partial^2 f}{\partial x^2}$ and the smallest for $f_y = \frac{\partial f}{\partial y}$.

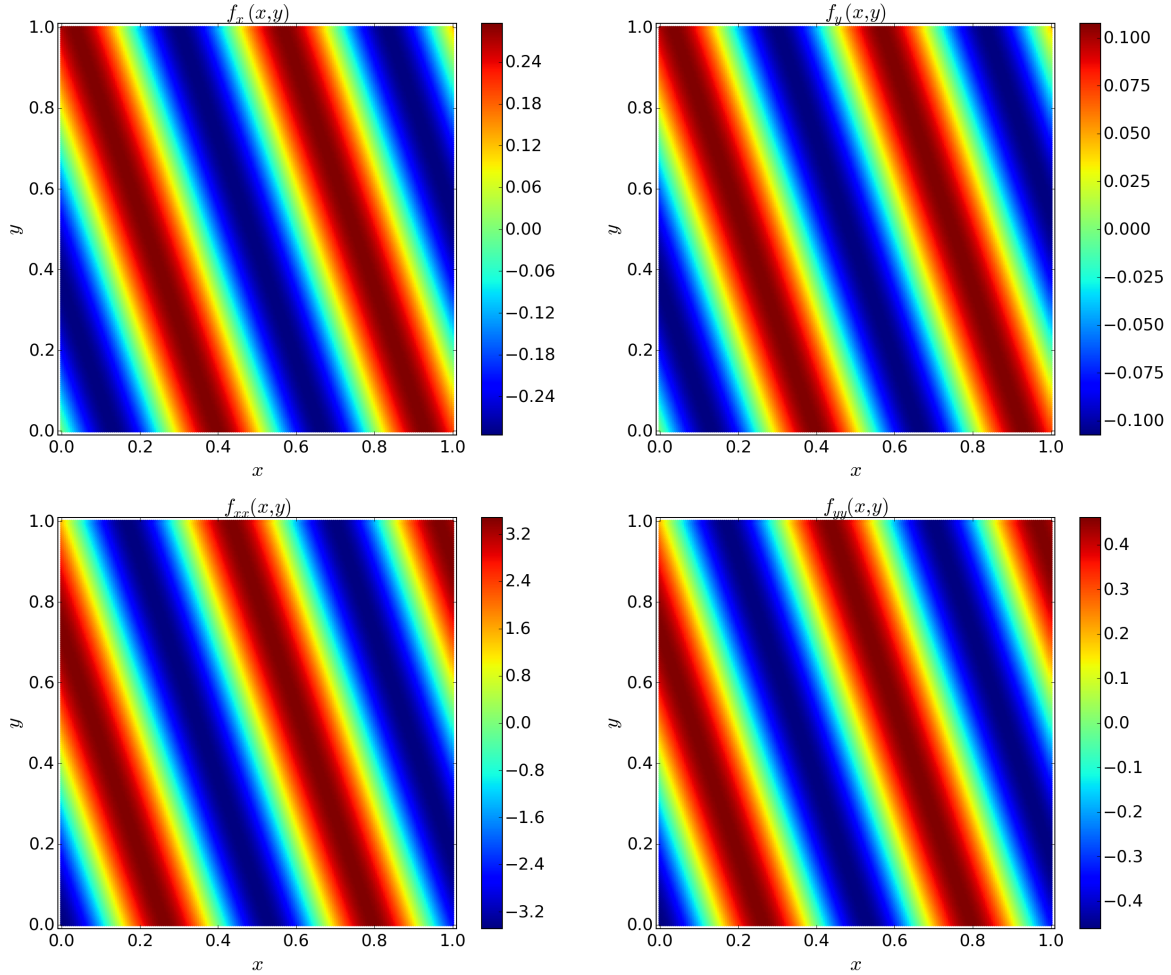


Figure 5.3: Analytical first and second-order derivatives of the test function $f(x, y)$.

Although the literature review showed that the accuracy of the method, and especially the value of the optimal shape parameter C , may vary with the function considered, the tests have been completed primarily for a sinusoidal function. The RBF-FD method is aimed to be used to estimate the derivatives of any variable occurring in the model (i.e. free surface elevation, velocity potential, bottom profile and a_n coefficients), which may have spatial variations quite different from sinusoidal variations. Therefore, some limited tests have also been carried out using a flat function, since in some test cases, the bottom bathymetry presents large flat areas. The results of the present tests may not be directly extended to all functions, they enable evaluating the advantages and disadvantages of the RBF-FD method.

5.3.2 Presentation of the tests

RBF methods rely on several parameters: the choice of RBF, the shape parameter, the degree of the added polynomial, and the size of the stencil. From the series of tests carried out to study the sensitivity of the accuracy to these parameters, one initial question is “Which RBF to choose?”, and the values for the other parameters will result from this first choice.

In the case of RBFs depending on a shape parameter, the following tests were completed:

- four infinitely smooth RBFs: MQ , IMQ , IQ and GA (see Table 5.1 for the expressions of the functions),
- variation of the shape parameter in the range $C \in [0, 30]$,
- added polynomials up to second degree,
- three stencil sizes $N_{sten} = 5, 13$ and 21 , corresponding to the thresholds defined by Bayona et al. (2010) (see Section 5.1.3.3) (with corresponding node sets for interior nodes plotted in Figure 5.4), and
- five node spacings from $L/50$ to $L/200$.

The dependency of the accuracy of the method on the shape parameter as well as the effects of the stencil size and the node spacing were evaluated. Some methods to prevent the matrix from becoming ill-conditioned for high values of C and to reduce the errors on the boundary were also tested.

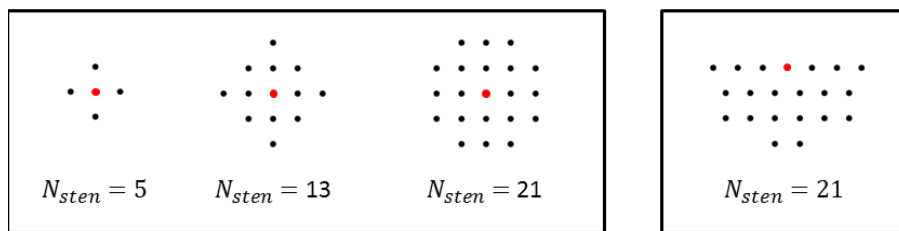


Figure 5.4: Node sets for the size of stencil considered in the tests for infinitely smooth RBF $N_{sten} = 5, 13$ and 21 for interior nodes with centered stencils (left), and node set for a one-sided stencil for a node at the upper boundary of the domain with $N_{sten} = 21$ (right).

For RBF not depending on a shape parameter, the following tests were completed:

- three piecewise smooth RBFs: one TPS function $\phi(r) = r^4 \log r$ to have at least the continuity of the second-order derivatives, and two PHS functions $\phi(r) = r^5$ and $\phi(r) = r^7$,

- added polynomials up to degree 5, and
- stencil sizes in the range $N_{sten} \in [9, 56]$.

To evaluate the accuracy of the estimations, a normalized averaged error is computed for the N nodes in the entire domain:

$$Averaged\ Error = \sqrt{\frac{\sum_{i=1}^N (Lf(\underline{x}_i) - Lf_{theo}(\underline{x}_i))^2}{\sum_{i=1}^N (Lf_{theo}(\underline{x}_i))^2}} \quad (5.15)$$

The domain is discretized with a regular set of nodes with a node spacing $\Delta x = \Delta y = 0.005$ m ($= L/100$). Although a regular grid can be problematic for global RBF methods, it has less of an impact in local RBF-FD method (Fornberg and Flyer, 2015). Moreover, it is easier to conduct convergence studies and to define a regular centered stencil.

Many combinations of the method parameters have been tested and the averaged error for the four derivatives (first and second order in x and y) have been computed. Only the most relevant results and comparisons will be shown and discussed in the following, to illustrate the main characteristics of the method emerging from these tests, and how to relate these observations to the literature.

5.3.3 General results

First, some general observations are made looking at the local error for the estimates of first and second-order derivatives with the MQ RBF (recommended by Franke (1982)), $N_{sten} = 21$ and $C = 0.1$ (Figure 5.5). The local error at \underline{x} is defined as : $|Lf(\underline{x}) - Lf_{theo}(\underline{x})|$. Globally, errors are larger for the second-order derivatives than for the first-order derivatives. As expected, the largest errors occur at the boundary, and more particularly, at the boundary where the stencil is one sided in the direction of the derivative (i.e. for $x = 0$ m and $x = +1$ m in the case of derivatives in x and $y = 0$ m and $y = +1$ m in the case of derivatives in y) whereas they are globally smaller on the other boundaries where the stencil is more elongated in the direction of the derivative.

The averaged error for all the nodes in the domain (global error) is then compared to the averaged error on subsets of nodes. The node subsets are based on the asymmetry of the stencil. Three sets are defined: interior nodes with a centered stencil (Figure 5.4, left), the first row of interior nodes with an asymmetric stencil (denoted as boundary nodes 2 in the figures 5.6, 5.10 and 5.15), and the boundary nodes with a one-sided stencil (Figure 5.4, right). The four averaged errors are plotted as a function of the shape parameter C for the MQ RBF and a stencil $N_{sten} = 21$ in Figure 5.6. The error increases when close to the boundary due to the growing asymmetry of the stencil. Moreover, despite the smaller number of boundary nodes in comparison with interior nodes, the global error is dominated by boundary errors, therefore presenting the same evolution trend with C .

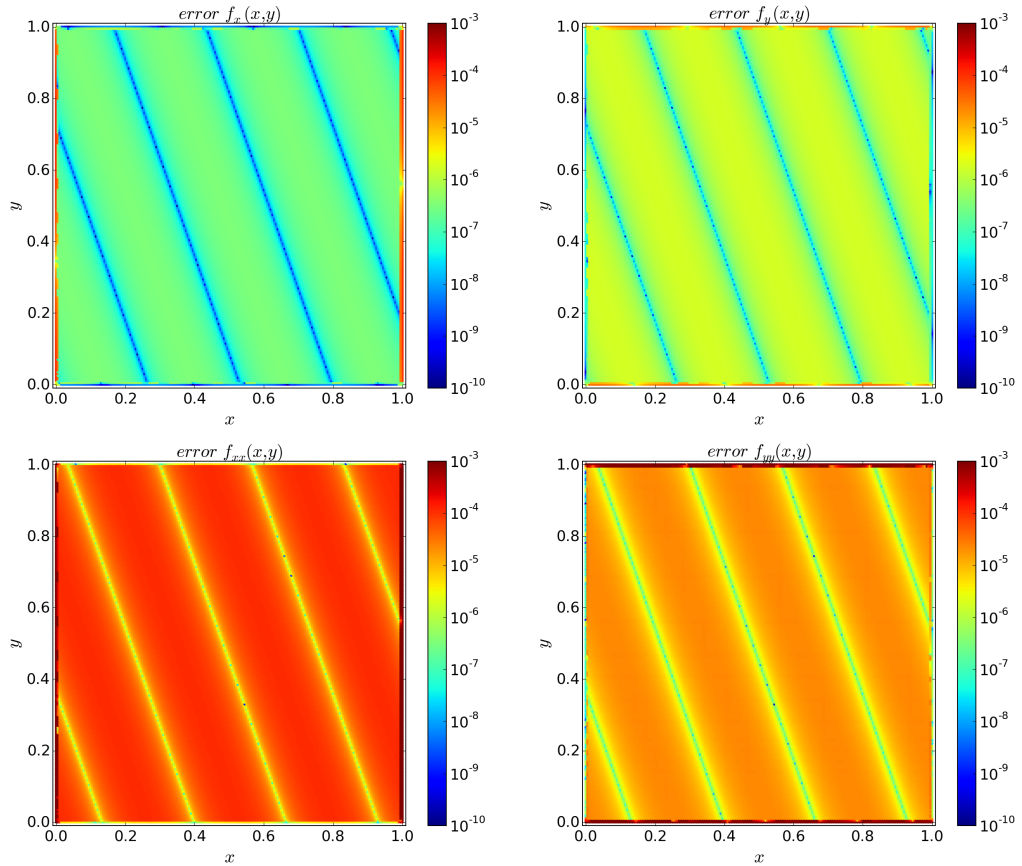


Figure 5.5: Examples of the local errors for the first and second-order derivatives (Figure 5.3) estimated with the MQ RBF, a stencil of 21 nodes, a shape parameter $C = 0.1$ and an added polynomial of degree 0.

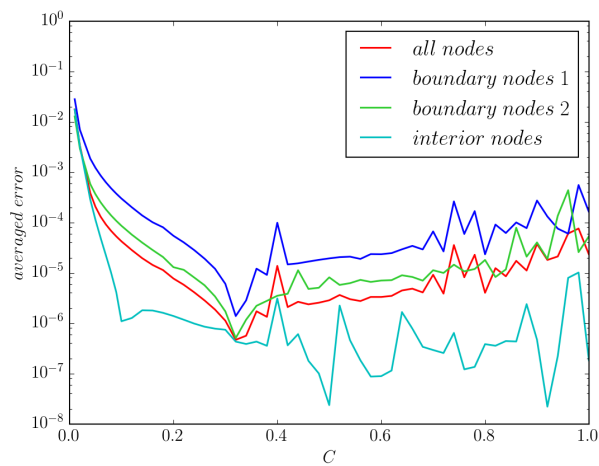


Figure 5.6: Averaged error for f_x as a function of the shape parameter C with the MQ RBF (added polynomial of degree 0 and $N_{sten} = 21$), for the four node sets defined in the text.

In the following presentation of the results, the global averaged error will be shown except when the error behavior in response to the parameter or the method tested is different for the three node sets and deserves to be analyzed specifically.

5.3.4 RBFs depending on a shape parameter C

5.3.4.1 Accuracy as a function of the shape parameter C

The infinitely smooth RBFs all depend on a shape parameter C controlling the flatness of the function: the functions flatten when C is increased (Figure 5.7).

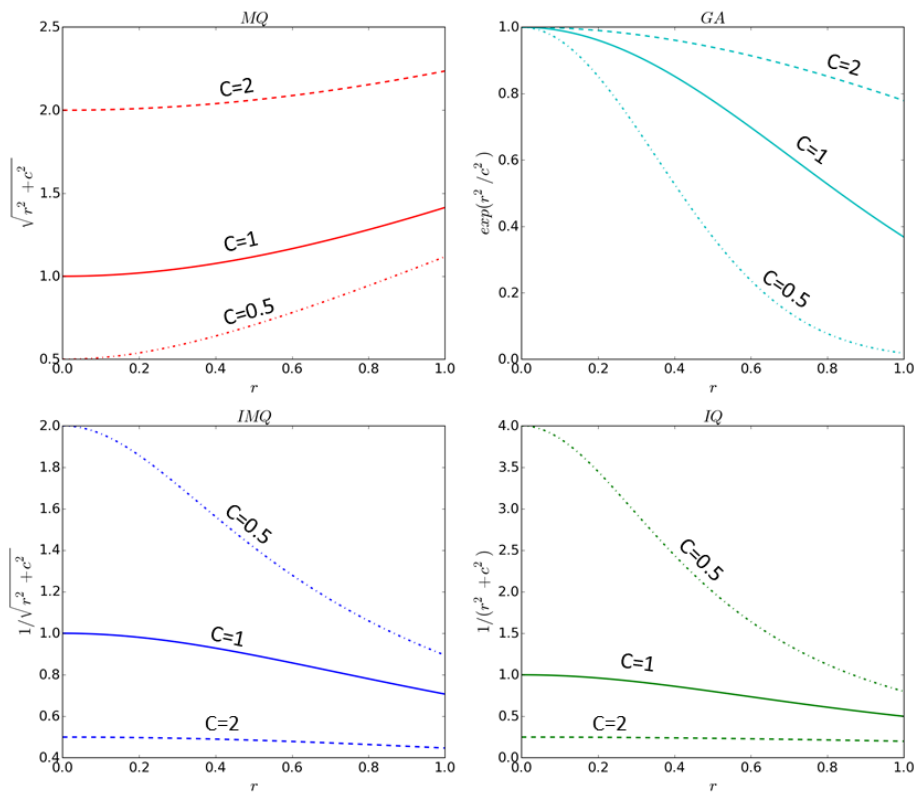


Figure 5.7: The four infinitely smooth RBFs that are studied MQ , GA , IMQ and IQ as a function of the radius $r = \|\underline{x} - \underline{x}_i\|$ with \underline{x}_i the center of the RBF, for three values of the shape parameter ($C = 0.5, 1$ and 2).

With this kind of RBF, the choice of the value of C is a main concern. As can be noted from Figure 5.8, the accuracy of the estimation of the derivatives depends strongly on C . The error is quite high for small C and decreases with increases in C . Nevertheless, if C continues to increase, the derivative estimation eventually becomes unstable and large oscillations of the error appear because the matrix becomes ill-conditioned. Without an ill-conditioned matrix, the error might reach a minimum an optimal C , but sometimes (as it is the case here), the matrix becomes ill-conditioned before this minimum is reached. The four RBFs display the same general behavior

as a function of C , with ill-conditioning appearing for slightly smaller values of C for GA and MQ than for IMQ and IQ . Therefore, examples of the results using one RBF will be shown in the following section for clarity.

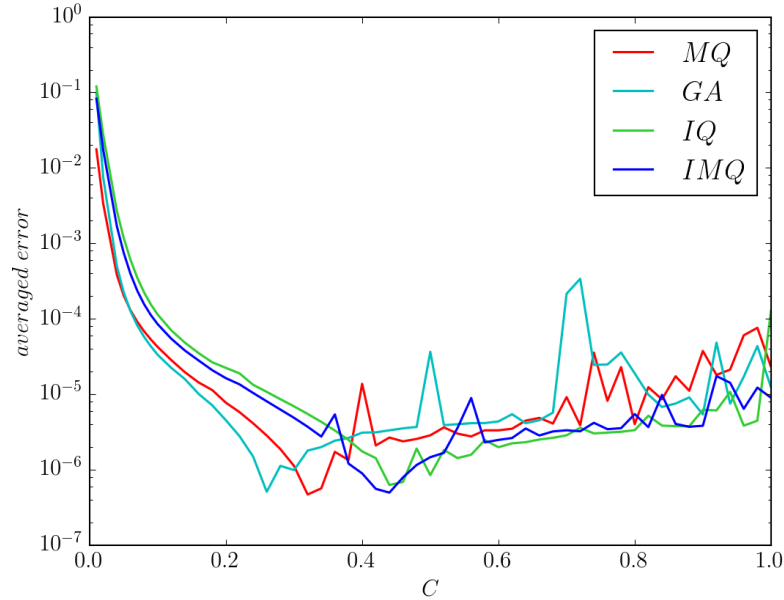


Figure 5.8: Global error for the estimate of f_x , for the four RBFs (see legend) as a function of the shape parameter C (with $N_{sten} = 21$ and added polynomial of degree 0).

From the literature, it is known that the optimal value of C depends on the function considered. Here, it also depends on the derivative estimated (Figure 5.9). First and second-order derivatives in x seem to reach a minimum for the error for $C \approx 0.42$, whereas the matrix becomes ill-conditioned for the first and second-order derivatives in y , before a minimum is reached. It can then be inferred that the optimal C for derivatives in y are larger than for derivatives in x for this particular case (due to the chosen wave direction).

It has already been shown that the errors are larger for nodes at the boundaries than for interior nodes (section 5.3.3, Figure 5.5 and 5.6). Here, the optimal value of C is not the same for interior nodes and boundary nodes (e.g. Figure 5.10 for MQ). The optimal value of C decreases closer to the boundary.

When studying the sensitivity of the error to the stencil size (Figure 5.11), the matrix becomes ill-conditioned for smaller values of C when N_{sten} increases ($C \approx 0.8$ for $N_{sten} = 13$ whereas $C \approx 0.5$ for $N_{sten} = 21$). The accuracy of the derivative estimates is greatly improved by increasing the stencil size from 5 to 13 nodes, and even more with 21 nodes, but more attention has to be paid to the choice of C , since the range of value of C producing a well-conditioned matrix is

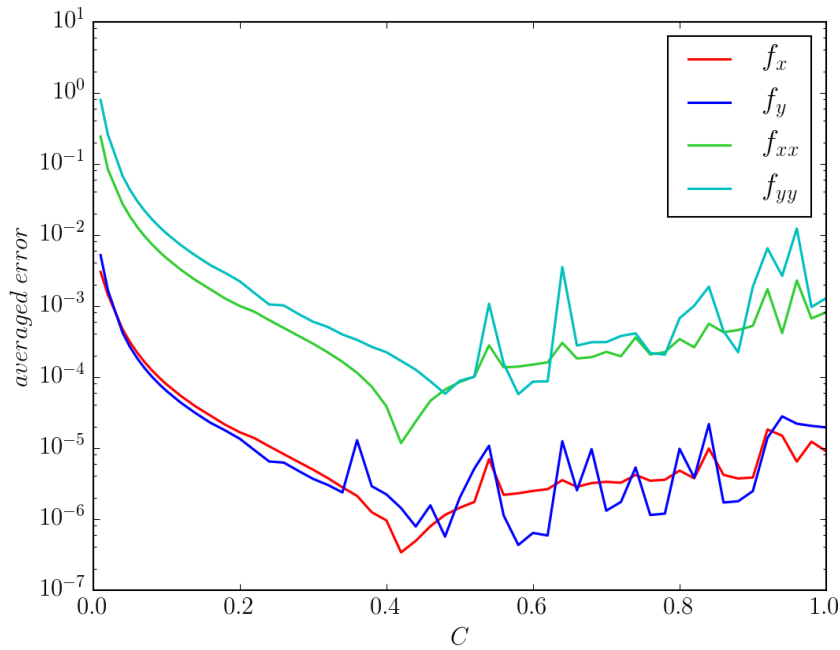


Figure 5.9: Global error for the estimate of the first and second-order derivatives in x and y , for the IMQ RBF as a function of the shape parameter C (with $N_{sten} = 21$ and an added polynomial of degree 1).

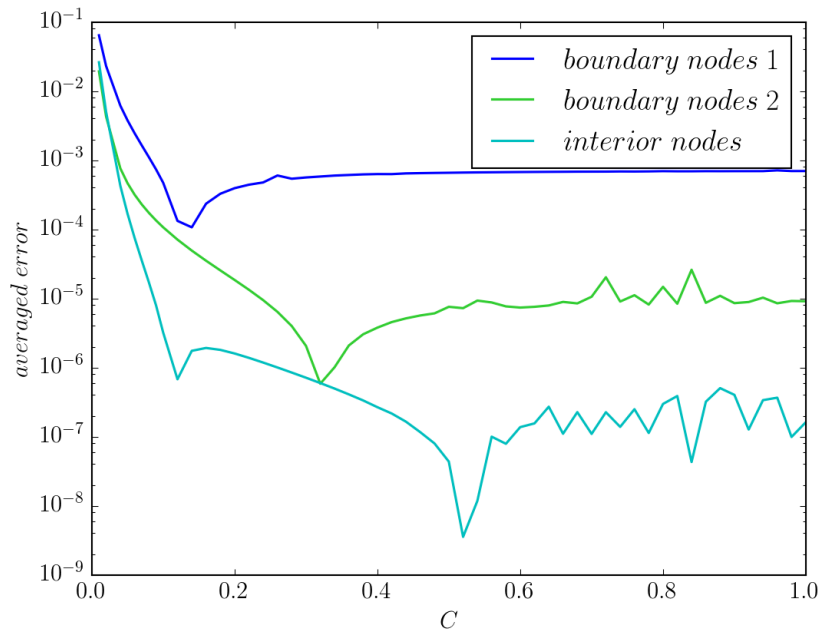


Figure 5.10: Error for the estimate of f_x with the MQ as a function of the shape parameter C (with $N_{sten} = 13$ and added polynomial of degree 0) for the three different sets of nodes defined in Section 5.3.3.

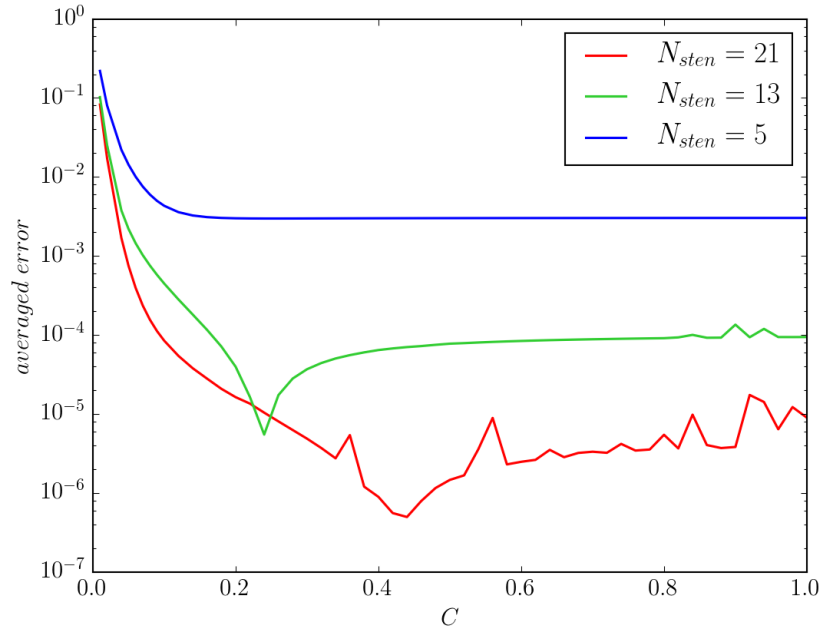


Figure 5.11: Error for the estimate of f_x , for the *IMQ* RBF as a function of the shape parameter C (with added polynomial of degree 0) for different stencil sizes: $N_{sten} = 5, 13$ and 21 .

reduced. In addition, increasing N_{sten} increases the computational time, so a compromise has to be found between accuracy, the difficulties finding an optimal value of C , and the computational time.

With infinitely smooth RBFs, the matrix also becomes ill-conditioned with a decrease in the node spacing. The optimal C is generally insensitive to the node spacing, but if it is decreased too significantly, the matrix may become ill-conditioned before an optimal value of C is reached (Figure 5.12). In general, when the node spacing is decreased, C is also decreased to keep the condition number of the collocation matrix roughly constant. According to [Fornberg and Flyer \(2015\)](#), a mean condition number on the order of $10^{10} - 10^{12}$ was found to give RBF-FD a competitive edge with regard to the accuracy reported by other high-order methods.

Considering all the parameters that need to be taken into account in the determination of a suitable value of C , the choice of the value of the shape parameter C is not straightforward. In the literature, trial and error is the method most often used. Recently, [Bayona et al. \(2010\)](#) derived an analytical expression for the estimation of the error that was then used to develop an algorithm to find the optimal value of C ([Bayona et al., 2011](#)). Nevertheless, it requires a first estimate of the derivatives and C_{opt} depends on the function considered and thus would vary for derivatives of each variable considered. For the application of the RBF-FD method in the model, this is not a suitable option. Although the estimation accuracy can be improved by several orders

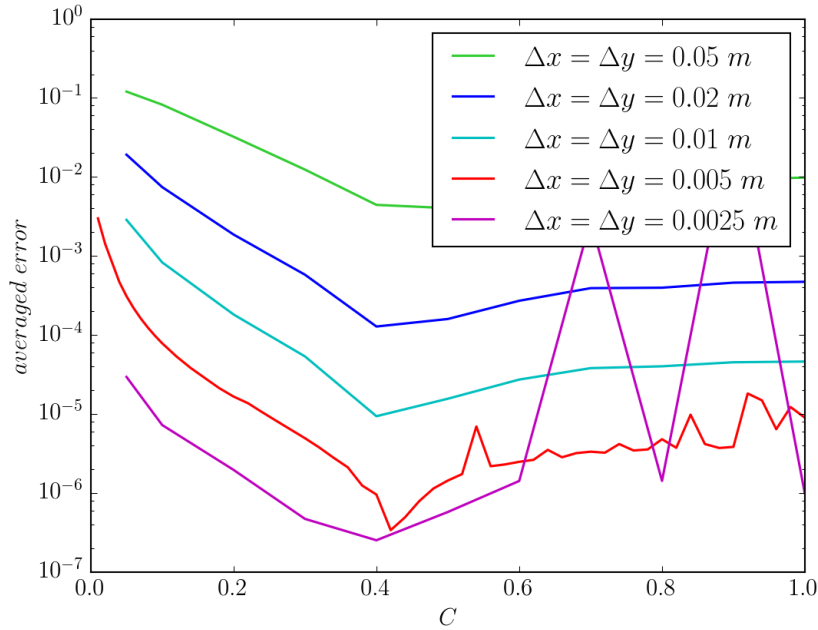


Figure 5.12: Error for the estimate of f_x , for the *IMQ* as a function of the shape parameter C (with added polynomial of order 1 and $N_{sten} = 21$) for several different node-spacings.

of magnitude when C_{opt} is determined, the range of C for which this accuracy is reached is very small and the dependency of C_{opt} on the function makes it unlikely that the optimal range of C is the same for all the function considered in the code (and their derivatives). For implementation reasons, the choice of C is currently limited to a single value to estimate all the derivatives of all the functions, just as for finite difference where the derivative weights depend only on the node placement. This objective leads to focus on the determination of the values of C giving small errors even if it not the smallest that can be obtained and, above all, to avoid an ill-conditioned matrix.

5.3.4.2 Tests to reduce the dependency on the shape parameter C

In the following section, some options to reduce the dependency of the error on C and to postpone the matrix becoming ill-conditioned for higher values of C are tested in order to widen the range of acceptable values for C to decrease the error on the boundaries. Among the possible options that are easily implementable, three options were selected:

- resolution of the linear system with a SVD method instead of a LU decomposition,
- addition of polynomial terms to the RBF interpolants,
- normalization of the stencil.

The SVD method

The resolution of the linear system giving the weights for the derivative estimation is completed with a LU decomposition algorithm. However, it is not the most adapted algorithm when the matrix is ill-conditioned, as is the case with RBF-FD, since large numerical errors can arise. The SVD method is used here as a filtering method by setting to zero all the eigenvalues smaller than a threshold defined as $thresh = \mu s_{max}$, where s_{max} is the largest eigenvalue and μ is a free parameter controlling the filtering (to be set by the user). Three values of the parameter μ were tested $\mu = 10^{-6}$, 10^{-12} and 10^{-15} (Figure 5.13). Small values of μ tend to avoid the problems associated with an ill-conditioned matrix by reaching a plateau for larger values of C , particularly for $\mu = 10^{-15}$. However, if the threshold is too large (i.e. $\mu = 10^{-6}$), the filtering is too strong and information about the system is lost, leading to large errors. Using a SVD method to resolve the system has a stabilizing effect, but the choice of μ must be made with caution: it should be small enough so as not to degrade the basis of the space by a lack of information, but not too small to eliminate the filtering effect.

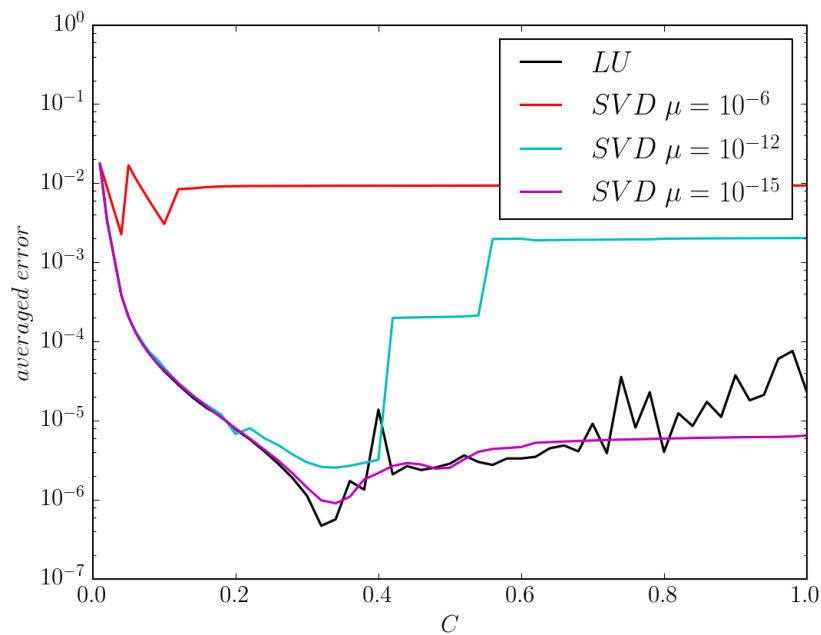


Figure 5.13: Error for the estimate of f_x , for the MQ as a function of the shape parameter C (with added polynomial of degree 0 and $N_{sten} = 21$). Comparison between solving the system with a LU decomposition and using a SVD filtering method for three values of the threshold μ .

The added polynomial

The addition of polynomial terms in the RBF interpolant has often been described as a method to improve the accuracy of the estimation, particularly at the boundaries of the domain (Forn-

berg et al., 2002). The sensitivity of the error to the degree of the added polynomial is studied by increasing its degree from 0 to 2 and comparing it to the results without polynomial terms. In Figure 5.14, the boundary and interior nodes present different behaviors with the increase of the added polynomial degree. For interior nodes (Figure 5.14, right), higher degree polynomials are beneficial for $C < 0.18$, but this improvement is lost for higher values of C . For the nodes on the boundary (Figure 5.14, center), the error (average of the error for boundary node 1 and boundary node 2) is greatly reduced with the addition of a polynomial and increase in degree of the polynomial for $C < 0.05$. From a certain degree of polynomial (depending on N_{sten}), the dependency of the error on C is reduced, and the error minimum as a function of C disappears. The global error (Figure 5.14, left) follows the same trend as the boundary node error. Moreover, since RBFs are not exact for polynomials, it is essential to add at least a constant to the RBF interpolant to be able to estimate the derivative of a constant function accurately.

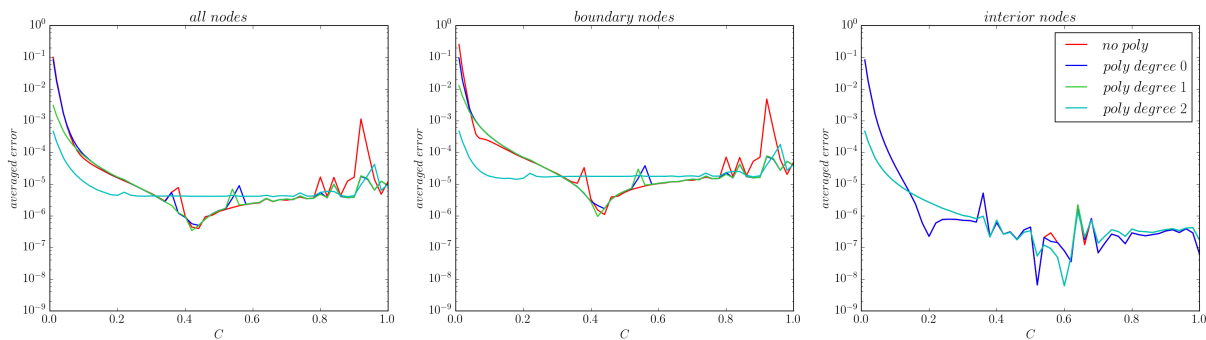


Figure 5.14: Error for the estimate of f_x , for the IMQ as a function of the shape parameter C (with $N_{sten} = 21$) for added polynomials of degree 0 to 2: (left panel) all nodes, (central panel) boundary nodes (boundary nodes 1 and boundary nodes 2), (right panel) interior nodes.

The normalization of the stencil

The last option tested to improve the RBF-FD method is the normalization of the stencil (see Section 5.2.2 for more implementation details). With the normalization, a single value of C is imposed, but the corresponding C in the physical space is modified based on the diameter of the stencil, leading to larger C for boundary nodes in comparison to interior nodes. The main consequence of this normalization (Figure 5.15) is the compression of the boundary node error curve towards the left side of the graph, while the interior node error curve remains the same (only the range of values of the shape parameter giving minimal errors is shifted). The expectation when applying this method is that, for small values of C , the differences between boundary errors and interior errors decrease. For the case considered here, the impact of the normalization of the stencil is not significant (Figure 5.15), and the normalization does not allow increasing the range of optimal values of C . A side effect of the method is that increasing C for the estimation

at the boundary may increase the risk of ill-conditioned matrix for boundary nodes, which is the opposite of the main objective of improving the estimation at the boundaries. Another side-effect is that C_{opt} varies with the refining or coarsening of the node set.

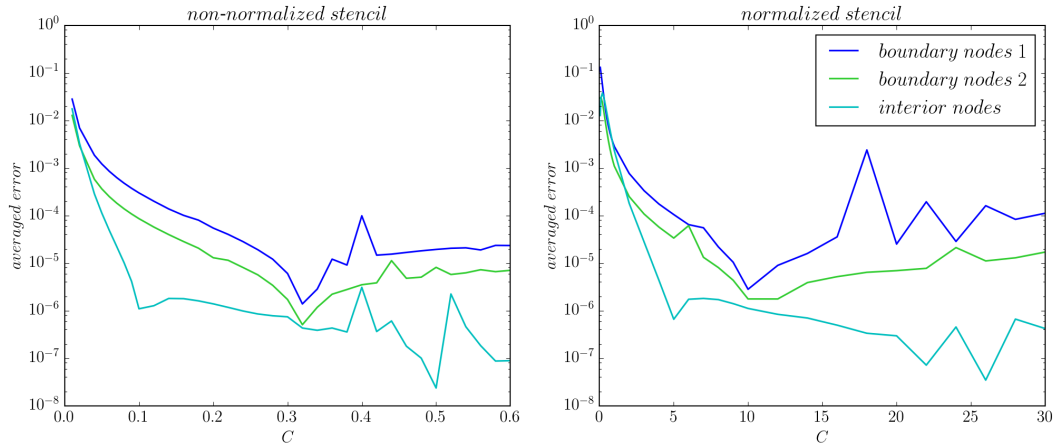


Figure 5.15: Effect of the normalization of the stencil on the error for the estimate of f_x , for the MQ as a function of the shape parameter C (with added polynomial of degree 0 and $N_{sten} = 21$): for the three sets of nodes defined in Section 5.3.3.

5.3.4.3 Conclusions

The choice of an infinitely smooth RBF in the RBF-FD method may be very interesting when it is possible to use it in combination with an algorithm to find the optimal value for C . Otherwise the choice of C may require a calibration based on trial and error, that is only possible when data are available for comparison. With the objective to use the model for operational wave propagation studies it may not be the best option unless the validation with experimental test cases reveals that the results are not so dependent on the choice of the shape parameter.

5.3.5 RBF not depending on a shape parameter

Contrary to infinitely smooth RBFs (Figure 5.7), piecewise smooth RBFs such as TPS and PHS are less regular but present the advantage of being independent of a shape parameter. In this section, three functions are tested: a TPS $r^4 \log r$ and two PHS r^5 and r^7 (Figure 5.16).

5.3.5.1 Comparison with infinitely smooth RBFs

The estimation errors for the four derivatives (f_x , f_y , f_{xx} and f_{yy}) obtained with each piecewise smooth RBF are compared with the results obtained with the IMQ RBF (Figure 5.17). The error decreases when the degree of r increases in the RBF, $\phi(r) = r^7$, producing the best results for

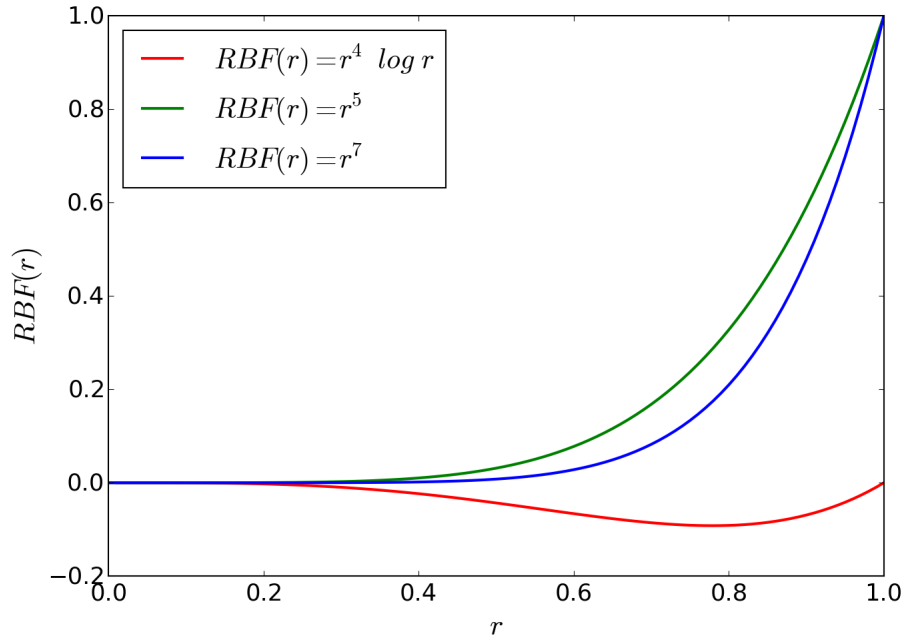


Figure 5.16: The three piecewise smooth RBFs studied, as a function of the radius $r = \|\underline{x} - \underline{x}_i\|$ with \underline{x}_i the center of the RBF.

the four derivatives considered. Piecewise smooth RBFs display smaller errors than the *IMQ* RBF for small values of C . The RBF $\phi(r) = r^7$ produces an error comparable to the minimum error obtained with *IMQ* RBF for f_y and f_{yy} , whereas for the derivatives in x , *IMQ* RBF can reach a smaller minimum error for C around C_{opt} . Although the RBF $\phi(r) = r^7$ may not be the optimal choice since the *IMQ* RBF and an appropriate C can attain a smaller error, the errors are nearly comparable, and the $\phi(r) = r^7$ has the advantage of not relying on the choice of a shape parameter.

Moreover, RBFs of this type are not subjected to saturation errors when the inter-node spacing is decreased (Figure 5.18): the convergence rate is constant. The RBFs $\phi(r) = r^4 \log r$ and $\phi(r) = r^5$ have almost the same convergence rate, which is slower than the convergence rate of $\phi(r) = r^7$. Here the *IMQ* interpolant is augmented with polynomial terms up to degree 1, which allows the convergence rate to decrease without reaching a plateau (as would be the case without an added polynomial). For large Δx , the *IMQ* method converges at the same rate as $\phi(r) = r^7$.

Errors obtained with *TPS* $r^4 \log r$ are larger than errors obtained with *PHS* r^5 and r^7 . Therefore only the *PHS* RBFs will be considered in the remaining tests.

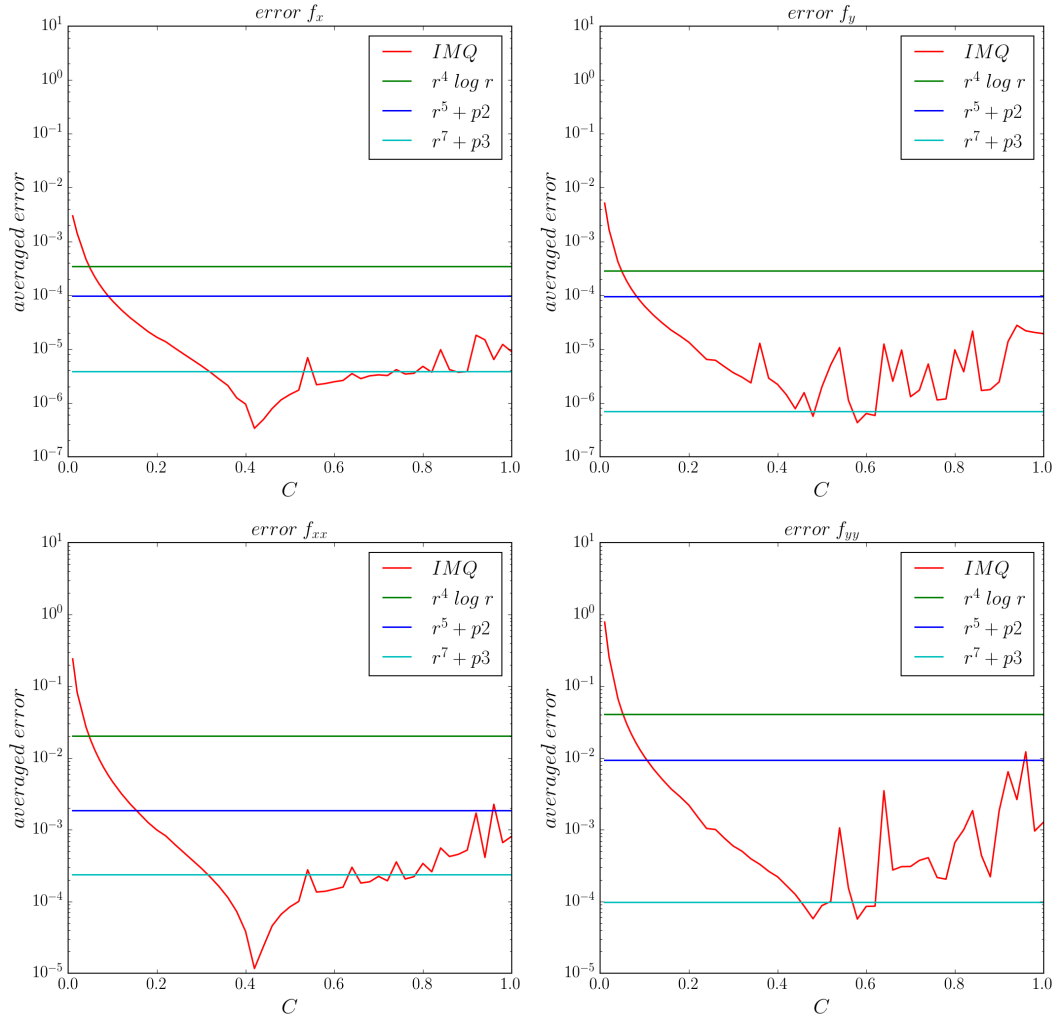


Figure 5.17: Error for the estimate of f_x , f_y , f_{xx} and f_{yy} , for the three piecewise smooth RBFs considered in comparison with the error estimate of the *IMQ* as a function of the shape parameter C (with an added polynomial of degree 0).

5.3.5.2 Comparison between *PHS* r^5 and r^7

For *PHS* RBFs, the addition of polynomial terms is essential to guarantee the invertibility of the collocation matrix, and a minimum polynomial degree is required that depends on the degree of the *PHS*. In parallel, the degree of the added polynomial is limited by the size of the stencil. To ensure that the problem is well-posed, the number of nodes in the stencil has to be larger than the number of independent monomials constituting the basis of polynomials of the same degree as the added polynomial. With these considerations, a series of tests were conducted to study the sensitivity of the error estimation of the *PHS* r^5 and r^7 to the stencil size ($N_{sten} \in [9, 56]$) and to the degree of the added polynomial (varied between 2 and 5).

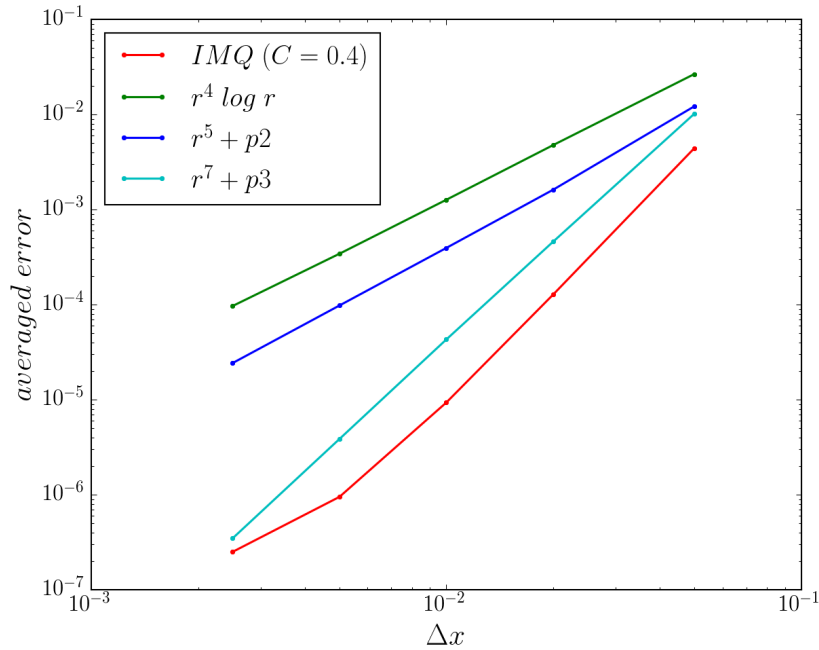


Figure 5.18: Convergence of the error for the estimate of f_x as a function of the spatial resolution Δx . Comparison of the IMQ with $C = 0.4$ and the three piecewise smooth functions (for $N_{sten} = 21$).

With regular node sets, the condition on the minimum stencil size for a given degree of added polynomial is not sufficient to ensure the non-singularity of the matrix. The regularity of the node set does not allow the matrix to be unisolvent for the polynomial basis. The stencil size thus has to be increased to recover the invertibility of the matrix. With an irregular node set this should not occur.

The results obtained with both PHS are compared in Figure 5.19. Similar behavior is observed for first and second-order derivatives in a given dimension. For a given degree of added polynomial, $PHS r^7$ shows smaller errors than $PHS r^5$. Some exceptions occur, for derivatives in x for $N_{sten} \leq 25$ and added polynomial of degree 3, and for the second-order derivative in x with the added polynomial of degree 4. For derivatives in y , there is no much gain in accuracy when the degree of the added polynomial increases from 3 to 4. In all cases, the error is weakly dependent on N_{sten} . Nevertheless, $PHS r^5$ has the advantage to be used with only a second degree polynomial, hence requiring a smaller N_{sten} , and less computational time.

5.3.6 Conclusions and recommendations

The series of tests conducted to study the estimation of the derivatives of a sinusoidal function with the RBF-FD method demonstrate that very accurate results can be obtained with an infinitely smooth function (without significant differences between MQ , GA , IMQ and IQ).

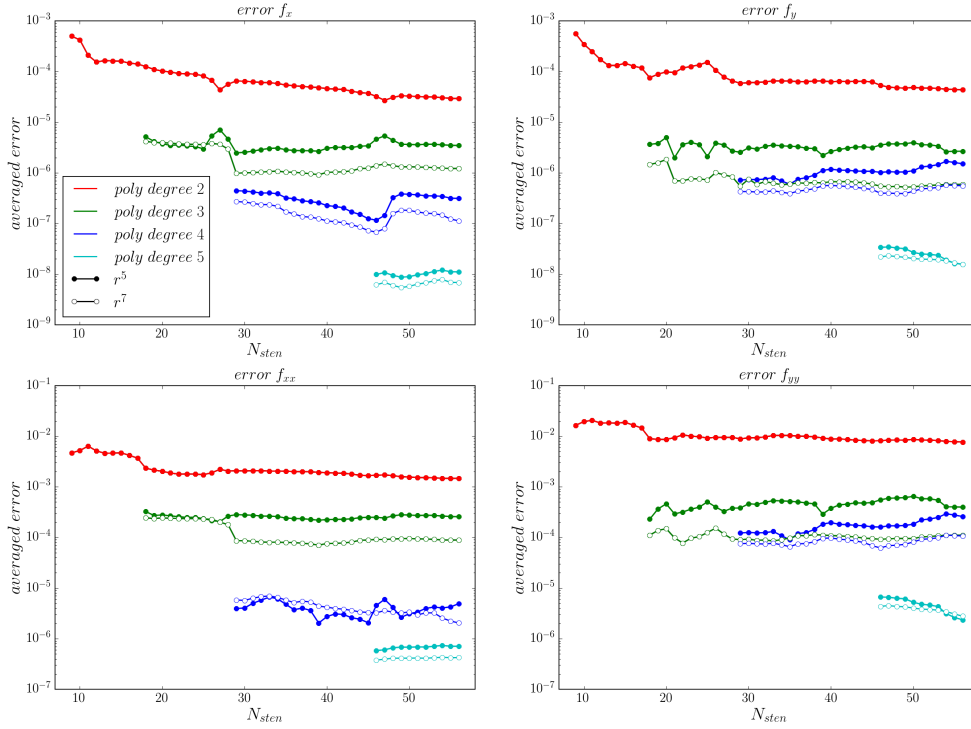


Figure 5.19: Error for the estimate of f_x , f_y , f_{xx} and f_{yy} , for r^5 and r^7 PHS as a function of the stencil size N_{sten} and the degree of the added polynomial (shown in the legend).

However, the fact that these RBFs depend on a shape parameter controlling the accuracy of the approximation, and that the optimal value of this shape parameter depends on the value of the function and its derivatives, make this method quite questionable for the targeted application. The success of the application (for example the performance of the Misthyc code) will depend on the accuracy required for the derivative estimates and how sensitive the model is to that parameter.

To avoid the problem associated with the choice of the shape parameter, PHS RBFs appear to be a good alternative. In particular the PHS r^7 produced nearly the same order of accuracy as the IMQ RBF (for the considered case). Nevertheless, the PHS r^5 is also of interest because even if the accuracy is reduced, smaller values of N_{sten} can be used, meaning a gain in computational time. For a targeted stencil size between 20 and 30 nodes, PHS $r^7 + p3$ are recommended, and if larger stencils can be considered (in the range 30-40) the PHS $r^5 + p4$ or $r^7 + p4$ are an appropriate choice.

Chapter 6

Validation of the 2DH version of the model using RBFs in the horizontal plane

Ce chapitre est consacré à la validation de la version 2DH du modèle, utilisant la méthode RBF-FD pour estimer les dérivées horizontales, à travers l'application à trois cas tests. Le premier cas est un cas invariant en y , d'une vague régulière se propageant dans la direction x . Les résultats sont comparés aux résultats obtenus avec la version 1DH du modèle. Un grand nombre de tests est réalisé sur le type de RBF, la valeur du paramètre de forme et la taille du stencil, confirmant les bonnes performances de la PHS $r^7 + p3$. Le modèle est ensuite utilisé pour simuler deux expériences de propagation de vagues régulières au-dessus de bathymétries différentes : une marche semi-circulaire d'après les expériences de [Whalin \(1971\)](#) et une bosse elliptique submergée d'après les expériences de [Vincent and Briggs \(1989\)](#). Ces deux cas tests montrent que le modèle est capable de reproduire précisément des champs de vague 2D avec des structures complexes ainsi que les effets non-linéaires associés. Ce chapitre se termine sur quelques considérations concernant l'optimisation du code, dont le temps de calcul a largement augmenté avec l'extension en 2DH. Les tests de parallélisation du solveur linéaire MUMPS permettent, dans le cas considéré, une diminution du temps de calcul d'un facteur 3.5 quand le calcul est lancé avec 15 processus MPI. Ce facteur d'accélération, possiblement dépendant du problème testé, reste assez faible. D'autres méthodes comme le recours à des solveurs itératifs ou la décomposition de domaine seront à considérer pour augmenter l'efficacité du code.

This chapter is devoted to the validation of the 2DH version of the model using RBFs with a series of three test cases, followed a discussion of the optimization of the code to reduce computational time that has been considerably increased with the extension of the model to two horizontal dimensions.

The 2DH version of the model is first validated by a comparison to the simulation results obtained with the 1DH version of the model for the case of a regular wave propagating in constant depth in the x direction (invariant in y). The simulation results are then compared to measurements from two laboratory experiments studying the convergence of regular waves propagating over two different bathymetric profiles: a semi-circular step based on the flume experiments of [Whalin \(1971\)](#), and a submerged shoal based on the basin experiments of [Vincent and Briggs \(1989\)](#). The second test case was presented at the conference Journées Nationales Génie Côtier Génie Civil 2016 in Toulon.

6.1 Regular waves propagating over a flat bottom

In Section 5.3, the derivative estimates with the RBF-FD method were studied for a sinusoidal function. Accurate results were achieved for interior nodes, but larger errors appeared at the boundaries. Now, the RBF-FD scheme is introduced in the wave propagation model to extend the 1DH version of Misthyc to 2DH, solving the time-dependent equations without physical diffusion terms. The objective is to determine if the RBF-FD approach is suitable for simulating wave propagation with a fully nonlinear and dispersive wave model. One of the most important obstacles is to evaluate whether larger errors at the boundaries are going to spread inside the domain, degrade the solution and disrupt the stability of the simulation. Boundary errors depend strongly on the type of RBF considered, and the accuracy and stability of the simulation are studied for two infinitely smooth RBF (MQ and GA) with a wide range of shape parameters ($C \in [0.1, 20]$). The stencil size is also varied to study its impact on the solution accuracy. A total of 128 combinations of (C, N_{sten}) are considered with an augmented polynomial of degree 0 (i.e. only a constant coefficient). Two PHS RBF are also tested $r^5 + p2$ with $N_{sten} = 13$ and $r^7 + p3$ with $N_{sten} = 21$. In all of the simulations, the stencil is normalized.

The case of regular waves of amplitude $A = 0.005$ m, period $T = 2.26$ s and wavelength $L = 6.14$ m propagating in constant depth ($h = 1$ m) is considered. The test case is designed to be invariant in the y direction so that the simulation results can be compared with those obtained with the 1DH version of the model. The domain is seven wavelengths long in the wave propagation direction, with a one-wavelength long relaxation zone at the left boundary for wave generation and a two-wavelength long relaxation zone at the right boundary for wave absorption. In the transversal direction, the domain extends over one-tenth of a wavelength. The domain is discretized with irregularly spaced scattered nodes with an average node spacing $r \approx 0.0614$ m ($L/100$) for a total of 9090 nodes, with $N_T = 7$. Impermeable conditions are applied at the lateral boundaries. Waves are propagated during $12T$ with a time step of $\Delta t = 0.0226$ s ($T/100$).

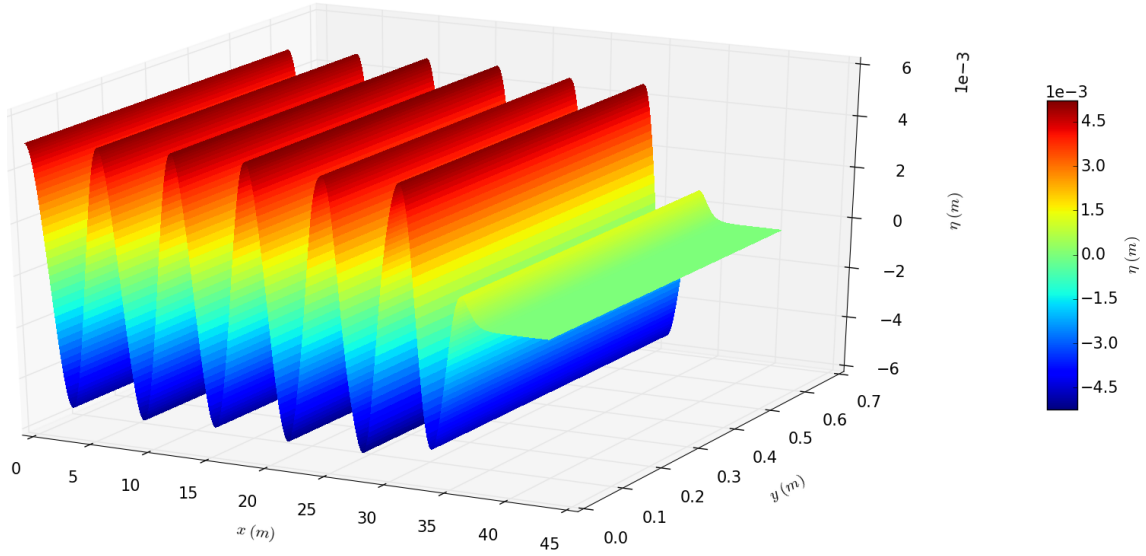


Figure 6.1: Three dimensional view of the free surface elevation at the end of the simulation obtained with PHS $r^7 + p3$ and $N_{sten} = 21$.

At the end of each simulation, the free surface elevation (Figure 6.1) is evaluated by comparison to the 1DH results that are used as the reference solution (η_{ref}), and a normalized averaged error is computed for the N nodes of the domain outside the relaxation zones:

$$averaged\ error = \sqrt{\frac{\sum_{i=1}^N |\eta(\underline{x}_i) - \eta_{ref}(\underline{x}_i)|^2}{\sum_{i=1}^N |\eta_{ref}(\underline{x}_i)|^2}} \quad (6.1)$$

The averaged error is computed for all of the simulations that were stable during the entire $12T$ simulation. The averaged error for each tested simulation is presented in Figure 6.2. Although more simulations remain stable with MQ (47.6%) than with GA (32.8%) RBFs, the same evolution of the error as a function of C is observed for the different values of N_{sten} . For both functions, the error decreases when C increases. Nevertheless, contrary to the results for larger N_{sten} , the error is almost independent of C , for $N_{sten} = 5$ but is large (of the order of 1). Simulations with larger N_{sten} are stable only for small C . When C is increased, the simulations become unstable likely due to an ill-conditioned matrix, as discussed in the previous chapter. For smaller N_{sten} (5 and 13) the simulations are unstable for small C not because of an ill-conditioned matrix but due to large errors in the derivative estimates. The minimum averaged error obtained with infinitely smooth RBFs is about $2 \cdot 10^{-3}$. It is reached for different values of C depending on N_{sten} : $C = 1$ for $N_{sten} = 29$ (MQ), $C = 5$ for $N_{sten} = 13$ (MQ), and $C = 15 - 20$ for $N_{sten} = 9$ (MQ and GA). For a given N_{sten} , the averaged errors obtained with GA are larger than with MQ mainly because they become unstable for smaller C . The $r^5 + p2$ PHS produces an error of approximately $3 \cdot 10^{-3}$, which is slightly larger than the minimum error obtained with MQ for

an optimal C , but better than most of the results with both infinitely smooth RBFs GA and MQ . Finally, for this test case, the PHS $r^7 + p3$ produces far more accurate results than any other RBF with an averaged error of 3.10^{-4} .

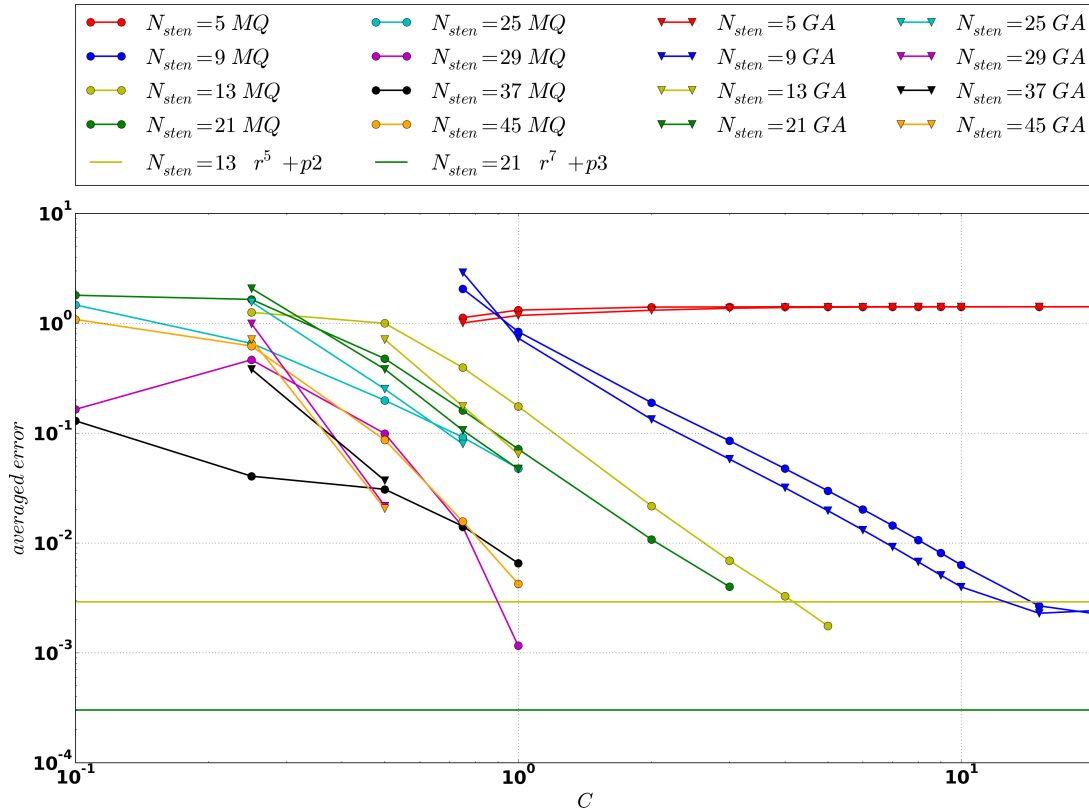


Figure 6.2: Averaged error computed for the free surface elevation at the end of the simulation ($t = 12T$) for all simulations with MQ and GA RBFs (as a function of the shape parameter C for several values of N_{sten}), and for PHS $r^5 + p2$ and $r^7 + p3$ (independent of C) RBFs.

Another way to visualize the results is to plot the error in the (N_{sten}, C) -space (Figures 6.3(a) and 6.4(a) for MQ and GA , respectively). The value of the error is indicated by the colorscale, with large errors in red and small errors in blue. Smaller errors are obtained for larger values of C until a limit is reached and the simulations become unstable. Comparing Figures 6.3(a) and 6.4(a), many fewer simulations are stable with the GA RBF than with the MQ RBF, and the errors obtained using GA RBFs are not as small as those obtained using MQ RBFs.

By looking at the averaged condition number of the collocation matrix (Figures 6.3(b) and 6.4(b)) the simulations generally become unstable when the condition number is larger than 10^{14} . For a given value of (C, N_{sten}) , the condition number is usually larger for GA than for MQ . This likely explains why more simulations are unstable with GA than with MQ for large values of

C and N_{sten} . For small values of C some simulations were unstable even though their corresponding condition numbers were small ($10^2 - 10^3$). In these cases, the instabilities are likely caused by poor derivative estimates because of very narrow basis functions owing to the small C .

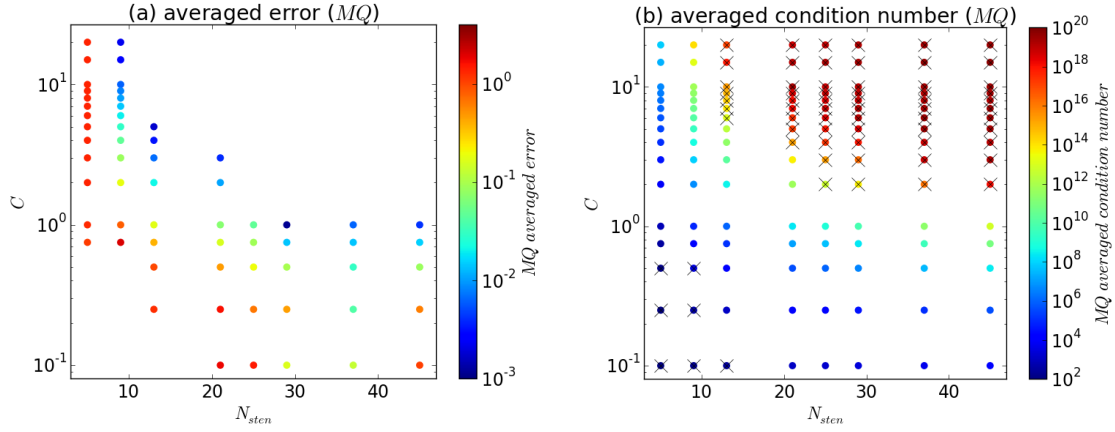


Figure 6.3: (a) Averaged error of the free surface position (Eq.(6.1)) at the end of each simulation, and (b) averaged condition number of the collocation matrix for the MQ RBF in (N_{sten}, C) -space. The crosses indicate simulations that were not stable for the entire $12T$.

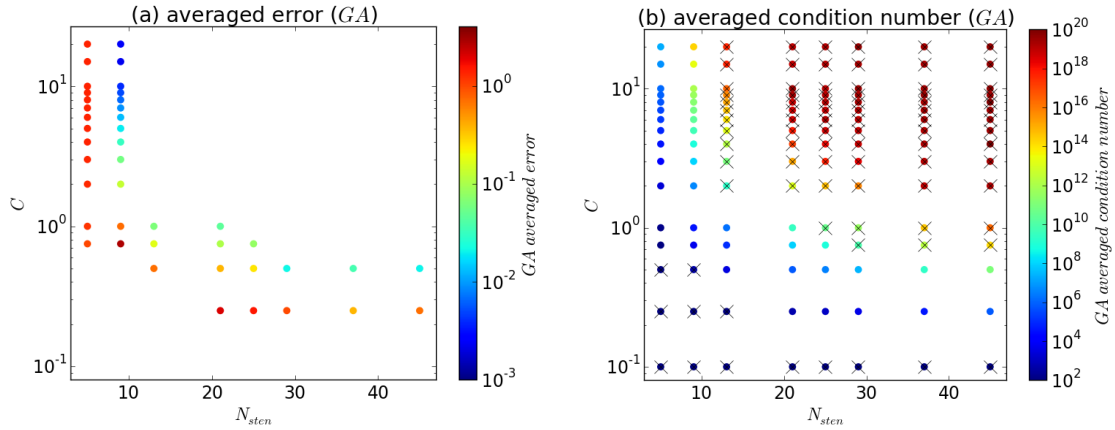


Figure 6.4: (a) Averaged error of the free surface position (Eq.(6.1)) at the end of each simulation, and (b) averaged condition number of the collocation matrix for the GA RBF in (N_{sten}, C) -space. The crosses indicate simulations that were not stable for the entire $12T$.

The dependency of the efficiency of the model on the temporal resolution Δt , the spatial resolution in the horizontal Δx , Δy and the spatial resolution in the vertical N_T , was already studied for the 1DH version of the model (Section 3.2.4.4). It is expected to be similar in the 2DH version for Δt and N_T . The dependency on the spatial resolution however is likely modified due to the fact that in two dimensions, when dividing by two the grid spacing, the number of discretization nodes is not just doubled but roughly multiplied by four. The model's efficiency as a function of

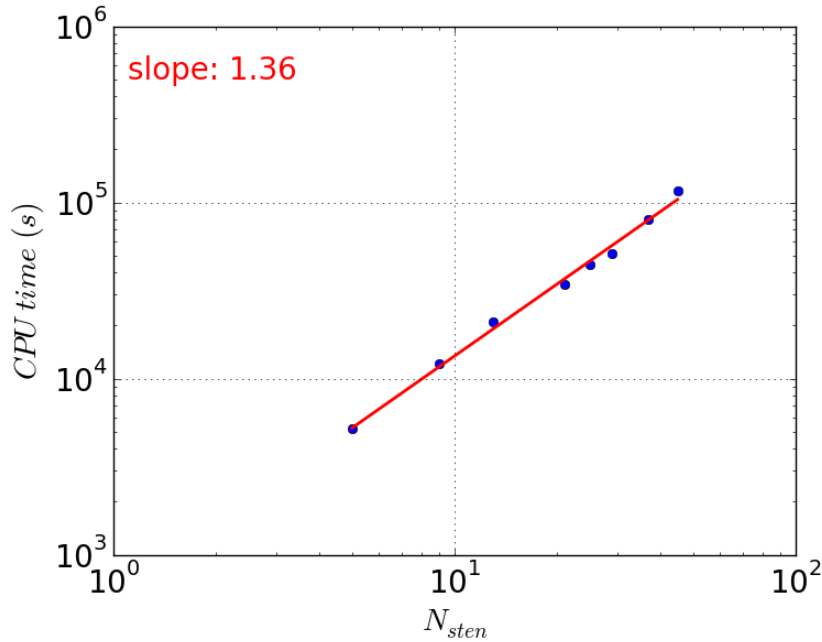


Figure 6.5: CPU time as a function of the stencil size N_{sten} , for simulations using the MQ RBF with $C = 1$ (duration of the simulation $12T$ with $\Delta t = T/100$, using 9090 nodes in the (x, y) -plane and $N_T = 7$).

the horizontal resolution has not been verified here. Nevertheless, the dependency on the size of the stencil N_{sten} is studied here for the MQ RBF with $C = 1$ (Figure 6.5). N_{sten} impacts the efficiency of the model since it modifies the fill-in ratio of the matrix used to solve the Laplace BVP. In the log-log plot (Figure 6.5), the CPU time increases linearly with N_{sten} with a slope of approximately 1.36, showing the importance of minimizing N_{sten} to reduce the model's computational time.

This first test case shows that accurate results can be obtained with the RBF-FD method when resolving a time-dependent PDE without any physical dissipation terms as long as N_{sten} and C are chosen in the appropriate range. The size of the stencil N_{sten} should not be too large since it both limits the range of “admissible” C for infinitely smooth RBFs (for which the simulations remain stable) and increases the computational time for all RBFs. Thus, values of N_{sten} in the range [9,21] appear to be a reasonable compromise between accuracy and efficiency. A larger range of “admissible” C values is possible using MQ instead of GA . The most accurate results are obtained with the PHS $r^7 + p3$. These last two observations may be specific to this test case, but for the following applications, the GA will not be tested further.

6.2 Regular waves propagating over a semi-circular step

Whalin (1971) performed a series of experiments with regular waves propagating over a semi-circular bottom topography that acts as a focusing lens. These experiments were first conducted to test the limit of linear and nondiffractive theory in a convergence zone, considering non-breaking waves with periods of 1, 2 and 3 s for three wave heights. The bottom topography was designed to produce strong wave converge and minimize sidewall effects and dissipation by bottom friction. The wave tank was 6.096 m wide and 25.603 m long. In the experiments, regular waves were generated by a piston wave maker and propagated from a water depth of 0.4572 m to a shallower region of 0.1524 m. The bathymetric profile used for the simulations here is the same as the one presented by Shao and Faltinsen (2014):

$$h(x, y) = \begin{cases} 0.4572, & -20.0 \leq x \leq 10.67 - G(y) \\ 0.4572 + \frac{1}{25}(10.67 - G(y) - x), & 10.67 - G(y) < x < 18.29 - G(y) \\ 0.1524, & 18.29 - G(y) \leq x \leq 35 \end{cases} \quad (6.2)$$

with $G(y) = \sqrt{y(6.096 - y)}$. A 2D view of the bathymetry is shown in Figure 6.6.

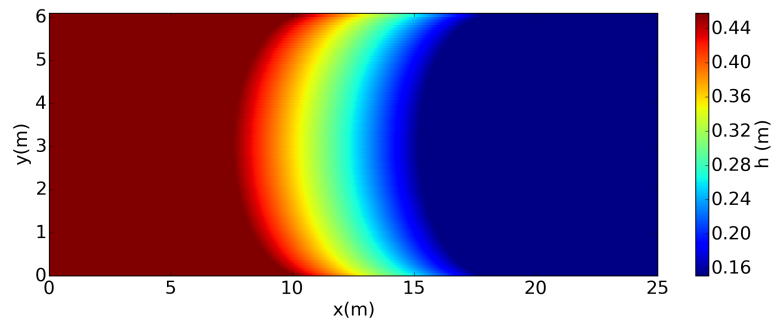


Figure 6.6: Analytical bathymetry (Eq.(6.2)) of the experiments of Whalin (1971).

The wave conditions simulated here correspond to a regular wave with a period $T = 2$ s and wavelength $L = 3.91$ m in the deeper part of the domain, with an amplitude of $A = 0.0075$ m. The computational domain extends from -3.91 m to 32.5 m in the x direction and from 0 to 6.096 m in the y direction. The computational domain is longer than the physical domain in the x -direction to include a one-wavelength long relaxation zone at the left boundary for wave generation and absorption of reflected waves from the underwater topography, and a three-wavelength long relaxation zone at the right boundary for wave absorption. Impermeable conditions are applied at the lateral boundaries.

The domain is discretized with 137,712 scattered nodes with regular node spacings ($\Delta x \approx \Delta y \approx 0.04$ m, or approximately $L/98$). Waves are propagated during 36 seconds (18 periods), with a

constant time step $\Delta t = 0.0178\text{s}$ ($\approx T/112$) and $N_T = 7$. To compute horizontal derivatives, the *PHS* RBF $r^7 + p3$ was used with a stencil size $N_{sten} = 21$. Several additional tests were conducted to evaluate the sensitivity of the results to the node spacing, type of RBF, and stencil size.

The free surface profile at the end of the simulation is shown in Figure 6.7. In the deeper part of the domain ($x < 7.5$ m), waves display 2D behavior with almost no variations in the y direction. The 3D wave patterns develop in the shallower zone where nonlinear effects are important. The convergence of wave energy is caused by the combination of shoaling, diffraction, and refraction over the convergent bathymetric profile.

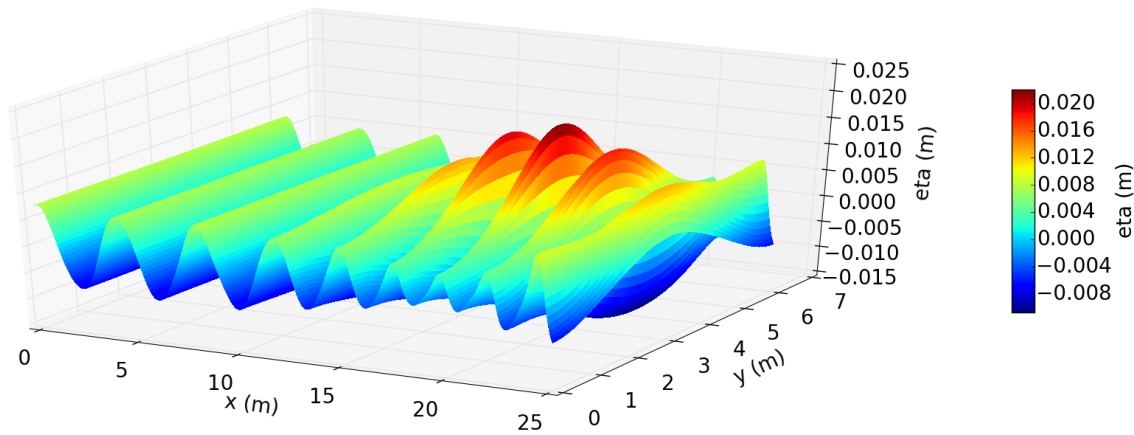


Figure 6.7: Three-dimensional view of the free surface elevation at the end of the simulation ($t = 18T$), obtained with *PHS* $r^7 + p3$ and $N_{sten} = 21$.

The simulated crest and trough elevation envelope along the centerline of the tank ($y = 3.048$ m) shows that before the foot of the slope, the crest and trough are nearly symmetric with respect to the water depth at rest (Figure 6.8). In the shallower zone ($x > 15$ m), there is an increase in the difference between the crest and trough with a decrease in the trough elevation, and an even larger increase in the crest height, breaking the horizontal symmetry observed in the deeper part of the domain. Looking at the free surface profile at the end of the simulation, the vertical asymmetry of the wave increases from $x = 10$ m, displaying a sharper wave front. At the maximum of the crest envelope ($x \approx 20$ m), the wave presents two small lobes on each side, a consequence of the increase of the second harmonic amplitude due to nonlinear effects on the slope.

To examine more closely the nonlinear effects and the energy transfers between harmonics, a Fourier analysis of the simulated wave signal along the centerline of the wave tank was completed to compare to the amplitudes of the first three harmonics from the measurement time series (Figure 6.9). The model accurately reproduces the spatial evolution of the amplitudes of the first three harmonics, corresponding to frequencies f , $2f$ and $3f$. The amplitude of the second

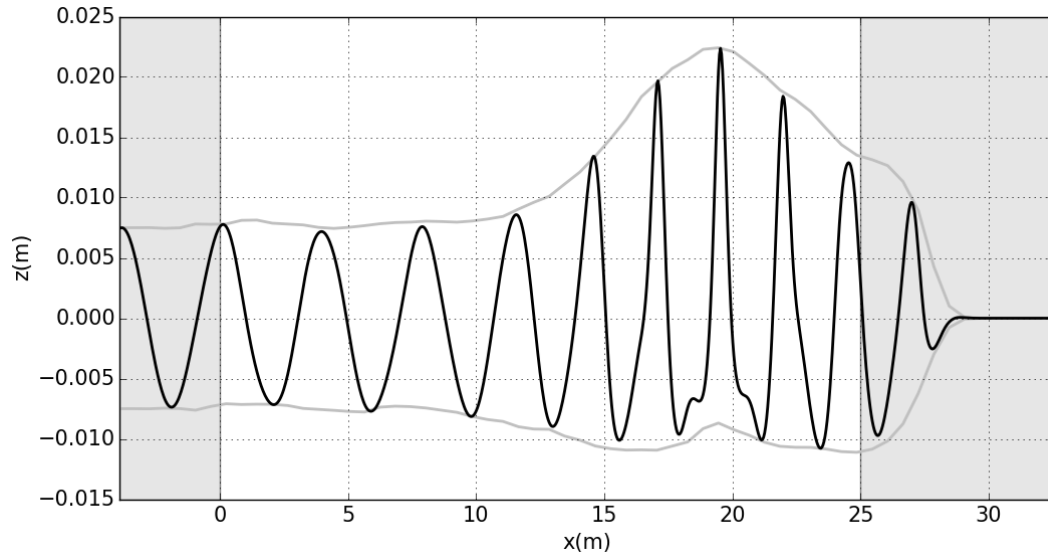


Figure 6.8: Free surface elevation profile along the centerline of the tank at the end of the simulation (black line) and maximum and minimum free surface elevation (wave envelope) during the simulation (gray lines). The light gray shaded areas ($x < 0$ m and $x > 25$ m) indicate relaxation zones for wave generation and absorption.

harmonic is slightly underestimated in the deeper part of the domain, possibly related to the linear wave generation method. In the shallower zone, the second harmonic amplitude is slightly overestimated. As mentioned previously, in the convergence region (around $x = 20$ m), the second and third harmonic amplitudes increase due to energy transfers from the first harmonic. The second harmonic amplitude is about one half of the first harmonic amplitude. In comparison with 1DH cases (Section 3.5 and Section 3.6) the amplitude of the first harmonic does not decrease. According to Whalin (1971), this can be explained by the fact that the rate of decrease due to nonlinear transfers to higher harmonics is compensated by the rate of increase in amplitude along the centerline of the tank due to refraction and shoaling.

A series of tests were conducted to look at the sensitivity of the results as a function of:

- the node distribution: a domain discretized with regularly-spaced or irregularly spaced nodes, with approximatively the same total number of nodes.
- the choice of RBF: the results presented above used the *PHS* RBF $r^7 + p3$ with $N_{sten} = 21$. Here, simulations with the *PHS* RBF $r^5 + p2$ are presented as well as results with the *MQ* RBF for different values of the shape parameter C .
- the node spacing: two coarser regularly distributed node sets are compared.

Details of the simulations are summarized in Table 6.1.

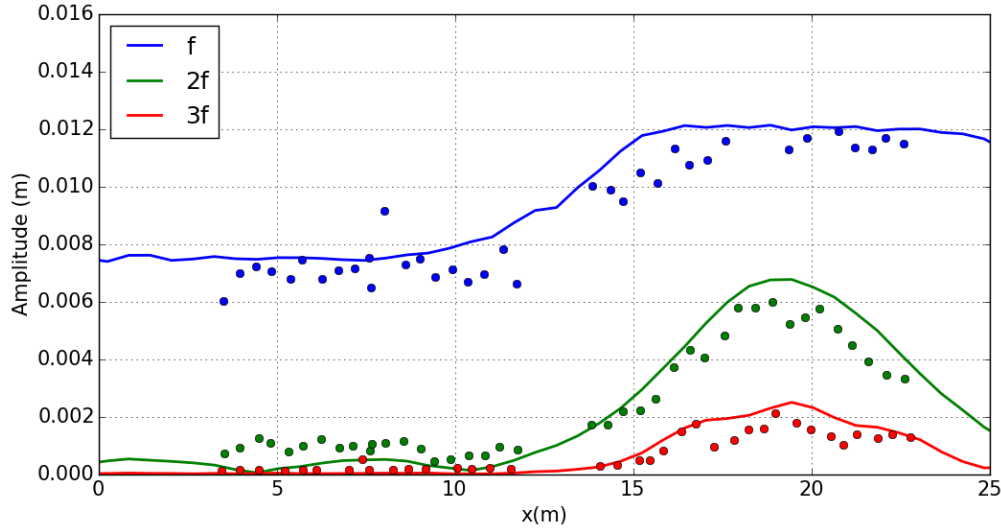


Figure 6.9: Observed (circles) and simulated (solid lines) spatial evolution of the amplitude of first three harmonics (at frequencies f , $2f$ and $3f$) of the free surface elevation for $T = 2$ s, $A = 0.0075$ m of the experiments of Whalin (1971) obtained with *PHS* RBF $r^7 + p3$ with $N_{sten} = 21$.

First, the spatial evolution of the first three harmonics are compared for the simulations with regularly and irregularly spaced nodes, with $\Delta x \approx \Delta y \approx 0.06$ m (Figure 6.10). The results are not very sensitive to the numerical parameters of the simulations. The amplitudes of the three harmonics are very similar along the centerline of the domain. For the regular node set, the use of the *MQ* with $C = 2$ produced results in agreement with the observations. However, for an irregular node set, a series of tests were required to find a suitable value of C to keep the simulation stable. The range of C for which the simulations remain stable with irregular nodes is small. This may be due to the fact that the normalization of the stencil takes into account differences in the maximum distance between nodes, while here the problem may be related to the differences between the minimum distance between nodes. Errors eventually increase locally because of stagnation errors, and these errors continue to grow, making the simulation unstable. Additional tests are needed to verify this hypothesis.

Simulations with the *PHS* $r^5 + p2$ also required also several tests to find a suitable value of N_{sten} . With $N_{sten} = 15$, the simulation was unstable. The stability of the simulation was recovered with $N_{sten} = 18$. Simulations with the *PHS* $r^7 + p3$ were stable with $N_{sten} = 21$.

Finally, once the appropriate combination of numerical parameters is determined to enable stable simulations, the results obtained using the different RBFs are similar. Regular or irregular node spacings do cause significant differences in the results, except for the choice of the shape parameter with for *MQ* RBF.

Simulations	node set	$\Delta x(m)$	RBF type	C	N_{sten}	Δt (s)
reg <i>MQ</i> 1	regular	0.060	<i>MQ</i>	2	13	0.0267
reg <i>MQ</i> 2	regular	0.060	<i>MQ</i>	1	13	0.0267
reg <i>PHS</i> 1	regular	0.060	$r^7 + p3$	-	21	0.0267
reg <i>PHS</i> 2	regular	0.040	$r^7 + p3$	-	21	0.0178
reg <i>PHS</i> 3	regular	0.075	$r^7 + p3$	-	21	0.0333
irreg <i>MQ</i> 1	irregular	≈ 0.060	<i>MQ</i>	1	13	0.0267
irreg <i>MQ</i> 2	irregular	≈ 0.060	<i>MQ</i>	0.75	13	0.0267
irreg <i>PHS</i> 1	irregular	≈ 0.060	$r^7 + p3$	-	21	0.0267
irreg <i>PHS</i> 2	irregular	≈ 0.060	$r^5 + p2$	-	18	0.0267

Table 6.1: Numerical parameters for the nine simulations compared for the case with $T = 2$ s, $A = 0.0075$ m of Whalin (1971). The parameters of the simulations presented in the first part of this section are in bold.

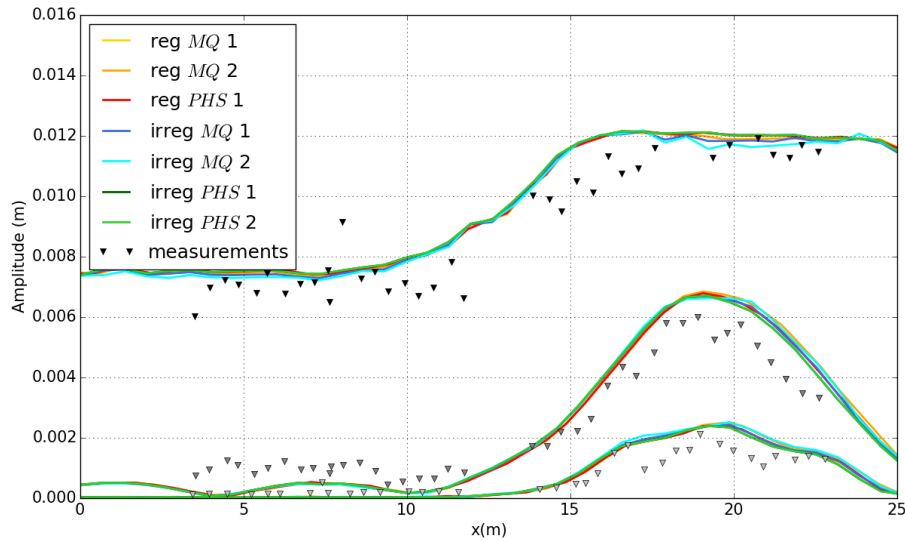


Figure 6.10: Observed (triangles) and simulated (solid lines) spatial evolution of the amplitudes of first three harmonics (at frequencies f , $2f$ and $3f$, as shown in Figure 6.9) of the free surface elevation for the case $T = 2$ s, $A = 0.0075$ m of Whalin (1971): sensitivity of the results to the type of node sets and the choice of RBF.

A second comparison of the spatial evolution of the first three harmonics is made for simulations using a regular grid ($\Delta x = \Delta y$) with three different spatial resolutions: $\Delta x = 0.040$ m, $\Delta x = 0.060$ m, and $\Delta x = 0.075$ m (Figure 6.11). Small differences between the three resolutions are observed for the harmonic amplitudes. The wave envelope obtained with the medium resolution (not shown), shows only small differences in the representation of the peaky crests and

the secondary crest in the convergence zone. An additional simulation was run with a coarser resolution of $\Delta x = 0.090$ m, but the simulation was unstable. Increasing the stencil size was not enough to recover the stability, and the solution found to recover stability was to refine the mesh near the boundaries.

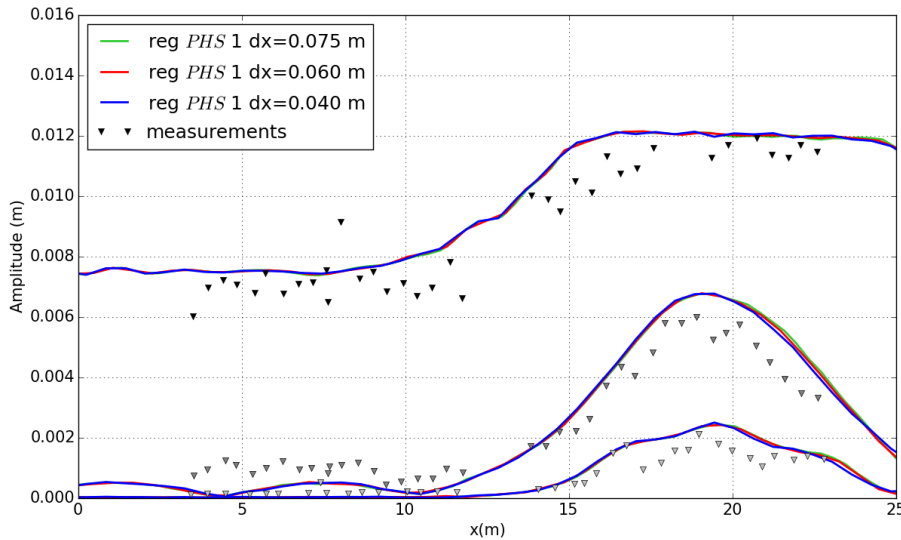


Figure 6.11: Observed (triangles) and simulated (solid lines) spatial evolution of the amplitudes of first three harmonics (at frequencies f , $2f$ and $3f$, as shown in Figure 6.9) of the free surface elevation for the case $T = 2$ s, $A = 0.0075$ m of Whalin (1971): sensitivity of the results to the node spacing, for three resolutions.

A second wave condition with the same period ($T = 2$ s) and an increased amplitude $A = 0.0106$ m was also simulated. The same characteristics of domain extent, time step and vertical resolution are used, but the spatial discretization corresponds to the irregular node set with $\Delta x \approx 0.06$ m used in the test of the former case (Table 6.1). The RBF-FD method is used with the MQ RBF, a shape parameter $C = 1$, and $N_{sten} = 13$. The simulated spatial evolution of the first three harmonics along the centerline of the tank are compared to the experimental data (Figure 6.12). The model reproduces well the spatial evolution of the amplitudes, again underestimating the second harmonic amplitude before the slope. Nevertheless, in the convergent region, the simulated harmonic amplitudes agree well with the experimental measurements. With the increase in the incident wave height, nonlinear effects become more important, and the second amplitude becomes almost two-thirds the amplitude of the first harmonic amplitude at its maximum. The amplitude of the first harmonic also decreases slightly around $x = 20$ m, which did not occur for the case with the smaller wave amplitude. According to Whalin (1971), this decrease can be explained by the fact that in this case, the nonlinear energy transfers to higher frequency components occurs at a faster rate than the energy convergence from refraction, so losses are not compensated exactly.

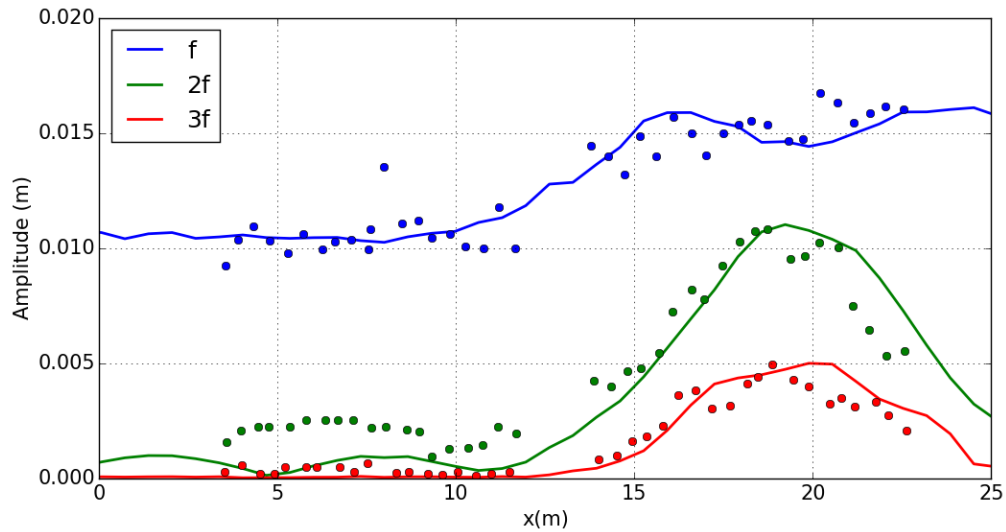


Figure 6.12: Observed (triangles) and simulated (solid lines) spatial evolution of the amplitudes of first three harmonics (at frequencies f , $2f$ and $3f$, as shown in Figure 6.9) of the free surface elevation for the case $T = 2$ s, $A = 0.0106$ m of Whalin (1971).

This second test case shows that 3D wave patterns induced by a specific bottom topography and the associated nonlinear effects can be well reproduced by the model. Moreover, in comparison to the simpler test case of a regular wave propagating over a flat bottom (Section 6.1):

- The choice of the parameters for the RBF-FD method to obtain a stable simulation is more complicated.
- For the MQ RBFs, the stability of the simulations depends strongly on the shape parameter C and the use of an irregular node set can make the choice of C even more difficult. In this case, the implementation of a variable shape parameter based on the distance to the nearest neighbor might improve the stability of the simulations.
- With PHS functions, instability problems may be resolved by increasing the size of the stencil, at least to a certain extent. For very coarse resolution grids, this solution is not sufficient, but the stability can be recovered by increasing the resolution close to the boundary).
- For this test case, MQ is optimal in terms of computational time since it can be used with $N_{sten}=13$, whereas PHS functions require at least $N_{sten} = 18$ to achieve the same accuracy.

6.3 Regular waves propagating over an elliptical shoal

The last test case simulates the propagation of regular waves over a submerged elliptical mound, reproducing the experiments of Vincent and Briggs (1989). The aim of the experiments was to look at the limits of the monochromatic wave approximation for irregular wave conditions, producing a large experimental data set for both monochromatic wave conditions and irregular waves with narrow or broad frequency and directional spreading. In this section, the regular wave condition test case *M1* is considered, with $T = 1.3$ s, $L = 2.3$ m, and $A = 0.0275$ m.

The experiments were conducted in a directional wave basin that is 35 m wide and 29 m long. The measurement area is restricted to a 6.10 m wide by 15.24 m long zone. The elliptical shoal has a major radius of 3.96 m and a minor radius of 3.05 m. Its center is located at $(x_0, y_0) = (6.10$ m, 13.72 m). The shoal boundary is defined by:

$$S(x, y) = \left(\frac{x - x_0}{3.05} \right)^2 + \left(\frac{y - y_0}{3.96} \right)^2 = 1 \quad (6.3)$$

The water depth around the shoal is constant $h(x, y) = 0.4572$ m (i.e. for $S(x, y) > 1$), and the water depth over the shoal is given by the expression:

$$h(x, y) = 0.9144 - 0.7620 \sqrt{1 - \left(\frac{x - x_0}{3.81} \right)^2 - \left(\frac{y - y_0}{4.95} \right)^2} \quad (6.4)$$

The minimum water depth over the center of the shoal is $h_{min} = 0.1524$ m. In the experiments, waves are generated by a directional wave generator. The free surface elevation was measured using an array of nine parallel resistive probes placed along nine different transects (5 parallel and 4 perpendicular to the wave maker). In the following, two transects will be studied (Figure 6.13): the transversal transect 4 ($x = 12.2$ m) and the longitudinal transect at the centerline of the tank, consisting of transects 7 and 9 ($y = 13.72$ m).

To limit the computational time, the simulated domain is smaller than the experimental wave basin. The numerical domain extends from -2.3 m $\leq x \leq 20.5$ m and 3.7 m $\leq y \leq 23.7$ m. Two relaxation zones are added (hatched zones in Figure 6.13): the first is one wavelength long at the left side of the domain for wave generation, and the second is two wavelengths long at the right side of the domain for wave absorption. Impermeable conditions are applied at the lateral boundaries. The domain is discretized by regularly spaced nodes with a resolution of $\Delta x = \Delta y = 0.075$ m, for a total of 81,435 nodes. Waves were generated with an amplitude of $A = 0.02325$ m, using linear wave theory. This value is smaller than the one prescribed to the wavemaker in the experiments, but an adjustment of the incident wave amplitude was necessary to obtain comparable average wave height ($H = 0.0445$ m) at a reference probe located in an unperturbed zone of the domain, upstream of the shoal ($x = 3.05$ m, $y = 21.34$ m).

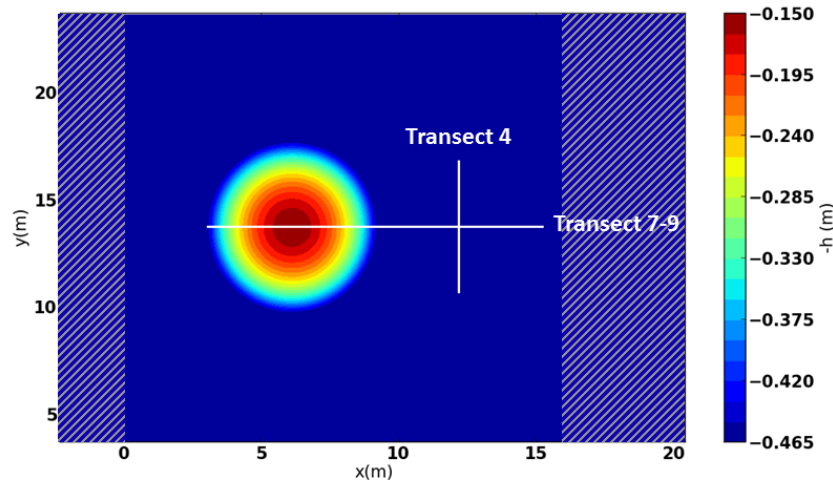


Figure 6.13: Numerical domain and bathymetry of the experiments of Vincent and Briggs (1989). Horizontal and vertical white lines indicate the transects where the comparisons between the simulation results and the experimental measurements are completed. Hatched zones indicate the wave generation (left side) and absorption (right side) zones.

Waves are propagated during approximately 100 s ($\approx 78T$), with a constant time step $\Delta t = 0.036$ s ($\approx T/36$), using $N_T = 5$. To compute the horizontal derivatives, the *PHS* RBF $r^7 + p3$ is used with a normalized stencil of size $N_{sten} = 21$. The sensitivity of the results to the type of *PHS* and to the spatial resolution is briefly studied with a few additional simulations.

The contour plot of the free surface elevation at the end of the simulation, when the periodic steady state is reached, is shown in Figure 6.14. The wave height increases in the zone behind the shoal ($x > 6$ m), and complex 2D patterns of the free surface elevation develop with strong variations in both horizontal directions. The convergence zone along the centerline of the tank is surrounded by rectilinear zones of almost zero amplitude looking like a wake. In addition, the crests and troughs in the y direction are modulated with a characteristic length scale of approximately 3 m due to reflections from the lateral walls. The fact that the computational domain is smaller than the experimental one may increase the importance of lateral reflections and possibly overestimate this effect.

To compare the simulation results with the experimental data, a zero up-crossing analysis of the free surface elevation time series is applied to compute the average wave height along each transect. To conduct the analysis in the same way as for the experiments, a 28-period window of the free surface elevation time series is considered (from $t = 60$ s to 96.4 s). Wave height profiles for the two transects plotted in Figure 6.13 are presented in Figures 6.15 (transect 4) and 6.16 (transects 7 and 9). Because of the reflection effects in the simulation, the variations of the free surface position at a given point in the domain is not perfectly periodic in time. Depending on the location of the node, in addition to the oscillatory evolution of the free surface, spatial

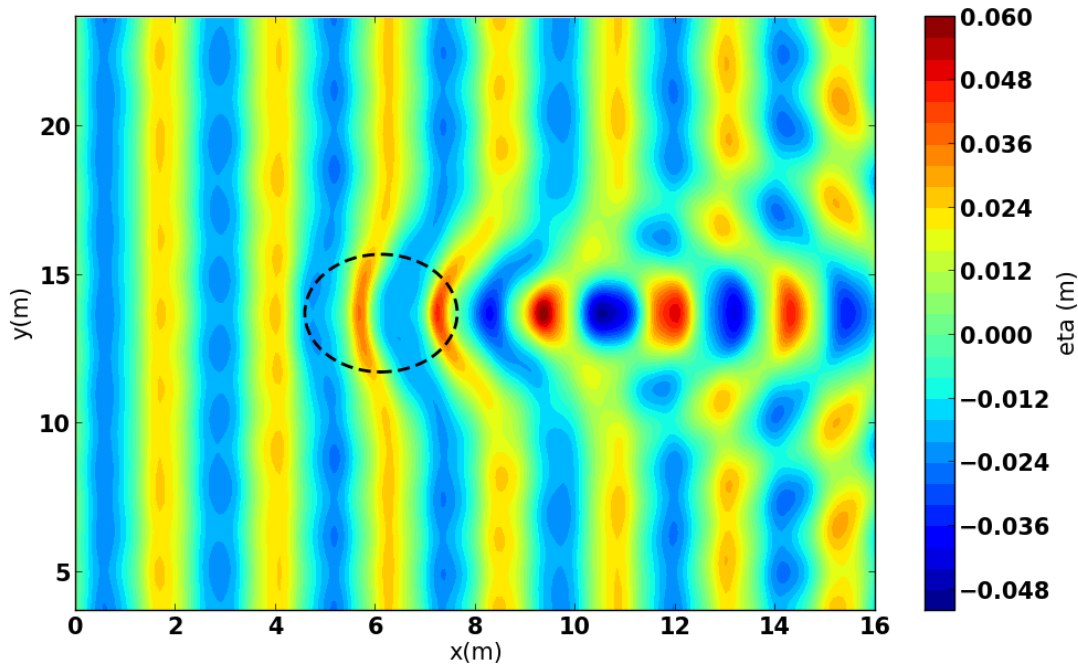


Figure 6.14: Contour plot of the free surface elevation at the end of the simulation ($t \approx 78T$) for case *M1* of Vincent and Briggs (1989). The dotted line indicates the limit of the elliptical shoal.

modulations may also exist. Consequently, the extracted time series of the wave height is not constant. Therefore, here the average simulated wave height profiles are presented with a shaded zone indicating the standard deviation.

Good agreement with the experimental data is observed for the wave height along the perpendicular transect (transect 4, Figure 6.15). The wave height profile presents a maximum at the center, corresponding to the center of the shoal ($y = 13.72$ m), which is more than twice the incident wave height (ratio ≈ 2.03). The amplitude of this maximum is slightly underestimated in the simulations. Moving symmetrically away from the center, two minima are reached, with wave heights less than half the incident wave height (ratios ≈ 0.21 and 0.43 , respectively). Farther from the shoal, the wave height is nearly equal to the incident wave height.

The wave height profile was also studied in the wave propagation direction, along transects 7 and 9 (Figure 6.16). The simulation results agree well with the experimental measurements. The differences are slightly larger than those observed along transect 4. In particular, the increase in the wave height between $x = 4$ m and $x = 6$ m and the peak around $x = 7.5$ m are not reproduced by the model. From $x = 9$ m the simulated wave height profile shows small oscillations that may be due to reflections from the relaxation zone that is not perfectly absorbing.

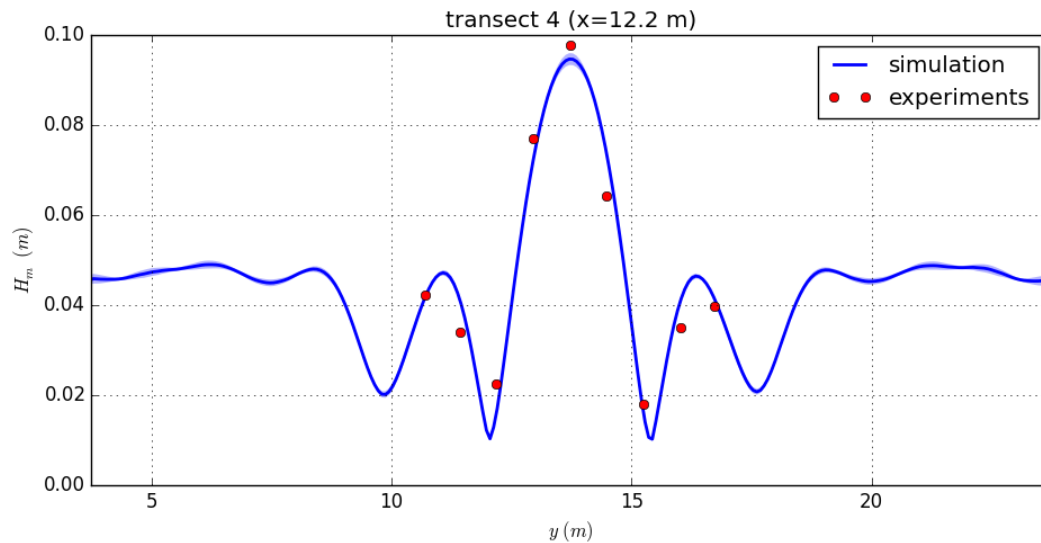


Figure 6.15: Average wave height along transect 4, for case M1 of Vincent and Briggs (1989). The blue shaded zone around the simulation results shows the standard deviation due to reflections.

The experimental measurements show variability between different runs, and by investigating a data point appearing in both profiles ($x = 12.2$, $y = 13.72$ m), the observed wave height is 0.0975 m along transect 4, while it is 0.104 m along transects 7 and 9, which is a difference of approximately 6.25%. Although this variability in the measurements cannot be directly extended to other measurements, it can be used to estimate the order of magnitude of the experimental errors and variability.

The harmonic analysis was performed on the simulated free surface time series along transects 7 and 9, and the evolution of the first three harmonic amplitudes are shown in Figure 6.17. Unfortunately, the experimental time series were not available to perform the same analysis to use as a comparison for the simulation results. Before the shoal, the waves are only weakly nonlinear, and the amplitudes of the second and third harmonic increase over the shoal. The second harmonic amplitude is more than half the amplitude of the first harmonic. This effect is likely caused by the narrowing of the wave crest over the shoal, as seen in Figure 6.14. After the shoal, the amplitude of the first harmonic is more than twice the amplitude before the shoal due to the convergence of wave energy induced by refraction. Nonlinearities are not significant after the shoal, although a modulation of the amplitude of the second harmonic is clearly observed.

The sensitivity of the results to the degree of the *PHS* RBF and to the spatial resolution of the discretization was evaluated. In Figure 6.18, the wave height profiles along transect 4 and transects 7 and 9 are plotted for three different combinations of *PHS* and augmented polynomials: $PHS r^5 + p2$ with $N_{sten} = 15$, $PHS r^5 + p2$ with $N_{sten} = 21$, and $PHS r^7 + p3$ with $N_{sten} = 21$.

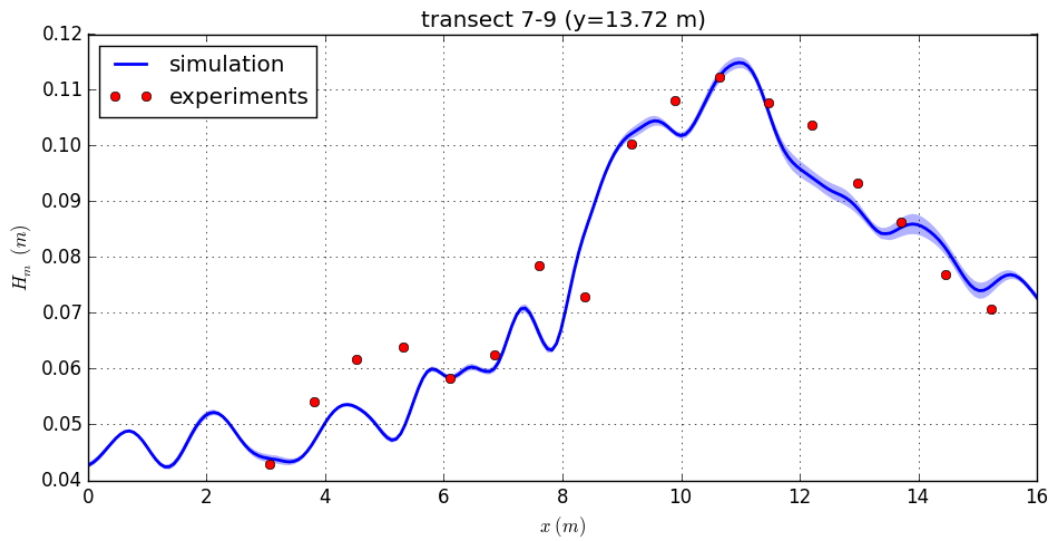


Figure 6.16: Average wave height along transects 7 and 9, for case M1 of Vincent and Briggs (1989). The blue shaded zone around the simulation results accounts for the standard deviation due to reflections.

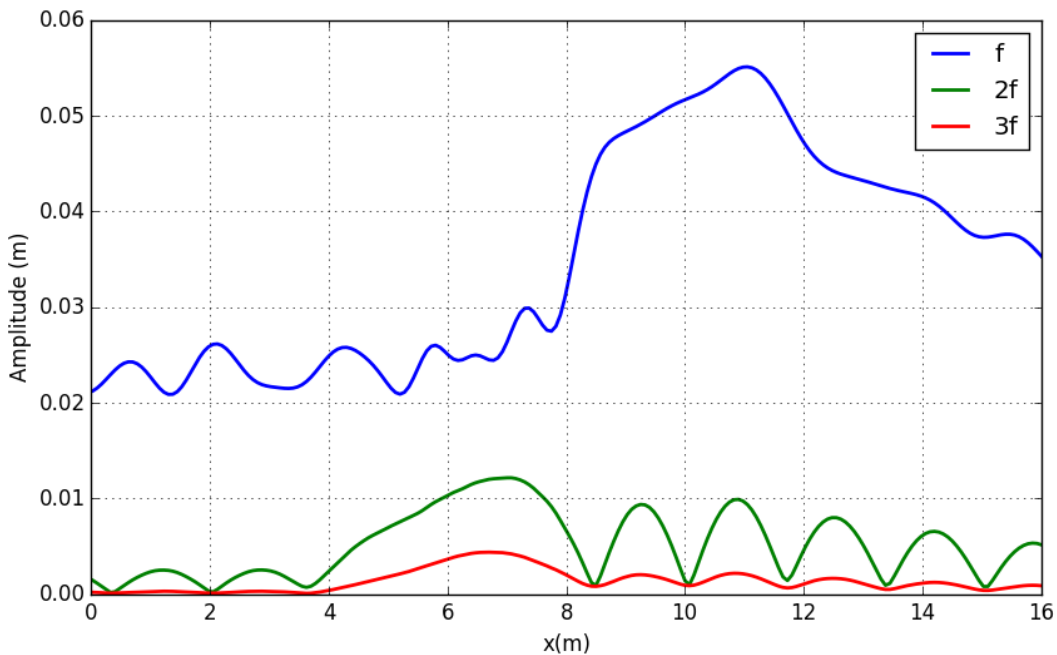


Figure 6.17: Spatial evolution of the first three harmonic amplitudes for the M1 Vincent and Briggs (1989) experiments along transects 7 and 9 ($y = 13.72$ m).

Very similar results are obtained with $PHS r^5 + p2$ for the two different stencil sizes (Figure 6.18). For this case, the accuracy obtained with $N_{sten} = 15$ is sufficient, and this choice of stencil size is optimal to minimize the computational cost. Wave height profiles obtained with $PHS r^7 + p3$ show only small differences along transects 7 and 9 (with a small phase shift), and the evolution trend is globally the same for the three simulations.

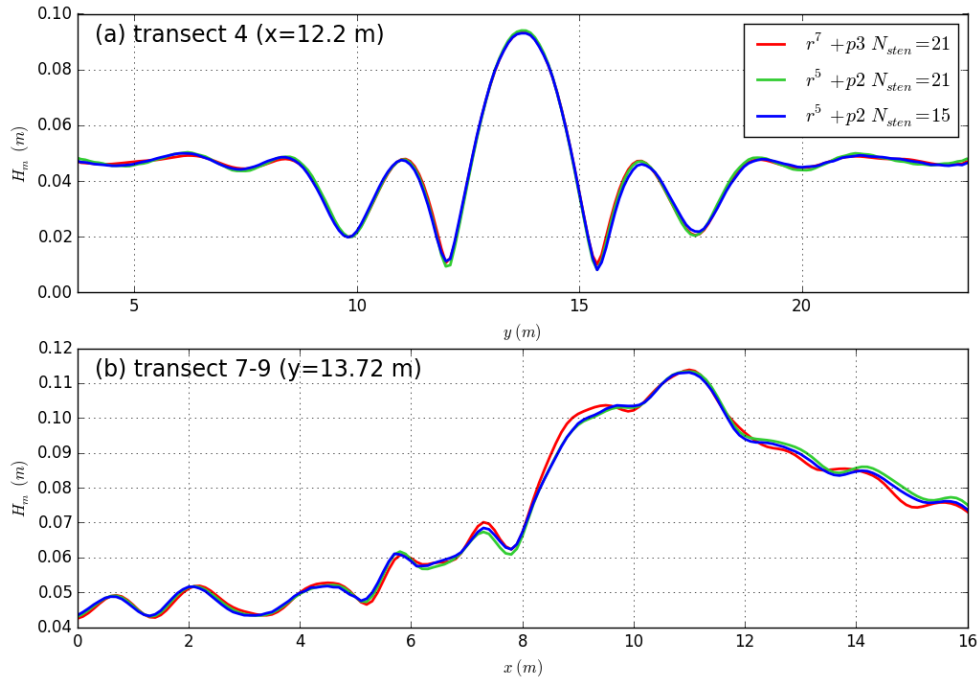


Figure 6.18: Average wave height along transect 4 (top) and transects 7 and 9 (bottom), for case M1 of Vincent and Briggs (1989). Comparison of 3 combinations of PHS RBFs and N_{sten} (see legend).

Additional tests were completed with a coarser discretization of the domain, using $PHS r^7 + p3$ and $N_{sten} = 21$. The node spacing was increased from $\Delta x = 0.075$ m to 0.10 m. Comparisons of the wave height profiles for the two resolutions are shown in Figure 6.19. The wave height profiles along transect 4 are nearly superimposed. Again, the differences are more visible along transects 7 and 9, with only very small errors. The same evolution trend is obtained with both simulations.

This last 3D test case shows that the model is able to reproduce accurately complex 3D wave patterns with smaller characteristic length scales but weaker nonlinear effects than the experiments of Whalin (1971). This test case also demonstrated that a lower degree polynomial function ($PHS r^5 + p2$) with a smaller stencil size can lead to the same accuracy of the final simulation results, with the advantage of a shorter computational time.

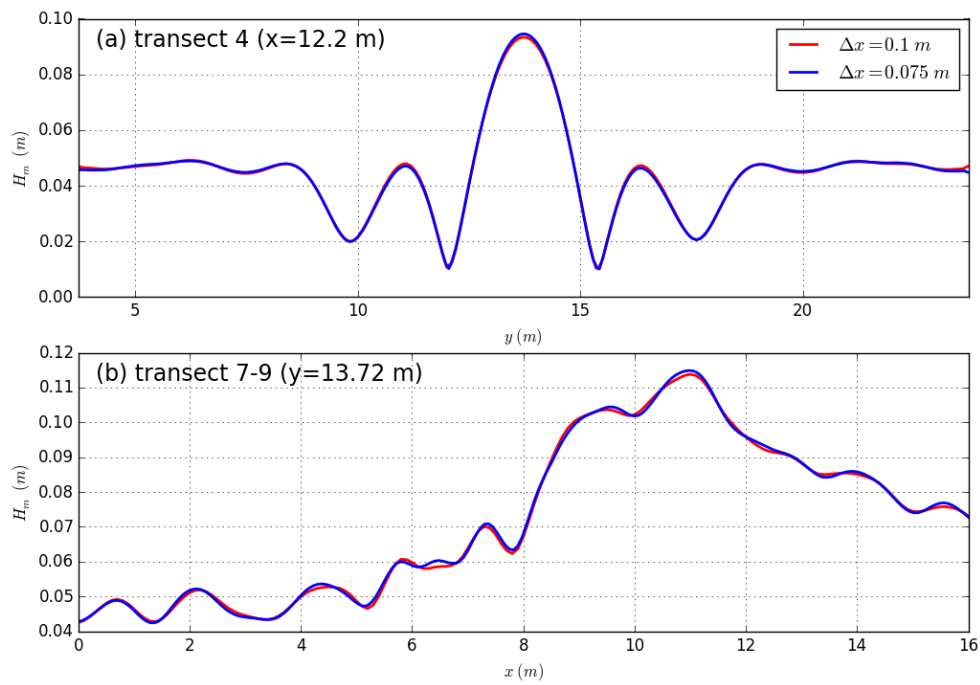


Figure 6.19: Average wave height along transect 4 (top) and along transect 7-9 (bottom), case M1 Vincent and Briggs (1989). Comparison of 2 spatial resolutions.

6.4 Computational cost and optimization

The transition to a 2DH version of the code was accompanied by a significant increase of the computational time. This led to an evaluation of the code to identify the most time consuming parts. Two possible techniques were identified to improve the numerical efficiency: the reordering of the matrix and the parallelization of the direct solver.

6.4.1 Computational requirements of the code

The code was analyzed with the objective of identifying the parts of the code with the highest computational cost. The analysis was conducted for the test case presented in Section 6.2, for which the domain was discretized with 60,716 irregularly-spaced nodes, and $N_T = 7$. The linear system of the Laplace BVP to be solved thus contains 485,728 unknowns.

In this case, the computational time in sequential mode for one time step is 600 s whereas the pre-processing phase (for the entire code) requires only 3.33% of this amount of time (≈ 20 s). The pre-processing time increases with the stencil size, but here it remains negligible in comparison with the processing time for each time step. At each time step, the right-hand sides of the Zakharov equations are calculated four times because of the RK4 scheme used to advance the model in time. Each independent resolution of the Laplace BVP requires approximately 150 s, of which the vast majority of the time is the linear system resolution since less than 1 s is dedicated to constructing the matrix. The most time consuming part of the code is thus the resolution of the linear system.

Therefore, the focus is then made on the direct resolution of the linear system for the Laplace BVP with MUMPS (Amestoy et al., 2006). The resolution with MUMPS is divided into three main phases: analysis, factorization and resolution. Permutation, scaling, and pivot ordering options are available (see the MUMPS Users' guide for more details). The default options are used after verification that they were the optimal choices. No permutation is completed but simultaneous row and column iterative scaling is computed, and the METIS package is used for the pivot ordering. Finally, it is found that the factorization phase is the most time-consuming phase requiring approximately 95% of resolution time.

6.4.2 Matrix reordering

The cost of direct sparse solvers is increased with the scattering of non-zero entries in the matrix. The structure of the matrix is directly related to node ordering. If no attention is paid to node ordering, nearby nodes in physical space may be far in index space. Here, the nodes are indexed arbitrarily beginning anti-clockwise with the boundary nodes and then with increasing x and y for the interior nodes. The matrix associated with the Laplace BVP is sparse but has a large bandwidth (Figure 6.20, left).

During the factorization phase of the resolution with MUMPS, some transformations are applied to make the matrix simpler to solve. Here, the idea is to reorder the nodes with the objective of reducing the analysis and factorization phases with the advantage that node reordering can be done once at the beginning of the simulation as a pre-processing task instead of during the analysis and factorization phases at each time step. With this in mind, a reordering algorithm based on the reverse Cuthill-McKee algorithm was implemented. The original version of the algorithm was slightly modified and simplified to take into account the specificities of case considered:

- all nodes in the domain have the same number of neighbors,
- when a node belongs to the stencil of another node, the inverse is not necessarily true.

The reordering algorithm was first tested for a regular node set of (5×5) nodes using a stencil of $N_{sten} = 5$. Figure 6.20 shows an effective reduction of the bandwidth of the matrix associated to the Laplace BVP. The nonzero entries are more concentrated around the diagonal. Nevertheless, when applied to “real” cases such as the test case presented in Section 6.2 the gain in efficiency was not noticeable. It is likely that the implemented reordering scheme was not beneficial in comparison with the MUMPS internal reordering process.

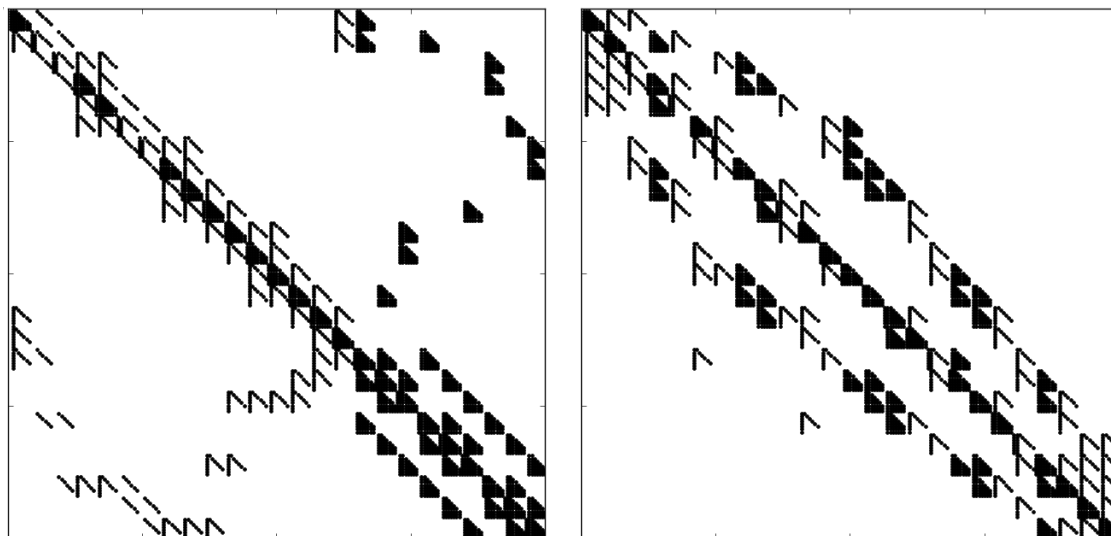


Figure 6.20: Left, sparsity of the matrix associated with the Laplace BVP using a stencil of $N_{sten} = 5$ for a regular node set of (5×5) nodes. Right sparsity of the matrix associated with the Laplace BVP after using an adapted reverse Cuthill-McKee algorithm. The black dots are the nonzero elements.

6.4.3 Parallelization of the linear solver

The numerical model Misthyc was originally implemented in a sequential version, with a potentially parallel version of the MUMPS solver. A first step to parallelizing the code is thus to use

a parallel version of the MUMPS to reduce the computational time required to solve the linear system as each time step.

One of the advantages of MUMPS is the possibility to define the matrix in distributed form, with as many submatrices as the number of MPI processes. The host process then builds the global matrix and solves the system in parallel. Thus, pre-processing tasks such as derivative computations and building of the submatrices can also be handled in parallel after the decomposition of the computational domain into smaller subdomains. Nevertheless, this is not necessarily straightforward and requires sharing data from one subdomain to another (i.e. to compute derivatives). It was tested for the parallelization of the 1DH version of the model without any significant improvement of the in the computational time, likely because the matrix was too small to achieve a real gain with the parallel resolution of the system. The implementation of the 2DH version is more complex and requires more communication between subdomains.

Taking into account that the pre-processing phase and the building of the matrix are not the most computationally expensive tasks in the 2DH version, the choice was made to parallelize only the resolution of the linear system, maintaining the rest of the code in sequential mode. The parallel resolution is managed automatically. Fewer changes of the code are required with this option. This parallelization was tested for the same case considered in Section 6.4.1 using the Athos cluster. The cluster consists of 776 nodes, each with 64 Go RAM, with two processors (2.7 GHz) made up of 6 cores. This capacity is doubled with hyperthreading, enabling 24 processes to be available on each node. The computational time per time-step is recorded when the number of MPI processes is increased from 1 to 24 for one node of the cluster. The speed-up ratio (Figure 6.21) is defined as the ratio between the “real” time necessary to compute one time step with the sequential version of the model and the time required with the parallel version of the model run with N_{proc} MPI processes:

$$speed-up\ ratio(N_{proc}) = \frac{time_{sequential}}{time_{parallel}(N_{proc})} \quad (6.5)$$

where $time_{sequential} = 333$ s for this case. The speed-up ratio increases with N_{proc} , but at a decreasing rate for larger numbers of processors, eventually reaching a plateau. For this case, the maximum speed-up is obtained for $N_{proc} = 15$, leading to a reduction of the computational cost by a factor of 3.5. For large values of N_{proc} the speed-up ratio decreases a little (3.2). It can be noticed that the speed-up ratio for $N_{proc} = 1$ is smaller than one, meaning that is it not appropriate to use the parallel version of the model with only one MPI process. Moreover, the analysis of the speed-up ratio by the parallelization of the solver is made for a rather small 2DH case (485,728 unknowns). The conclusion concerning the optimal number of MPI processes may not be directly applicable to cases with more unknowns. The parallel resolution requires more memory than sequential computation, and larger cases may cause the memory limit for one node

to be surpassed. In this case, the number of nodes needs to be increased, together with the number of MPI processes, to ensure sufficient memory.

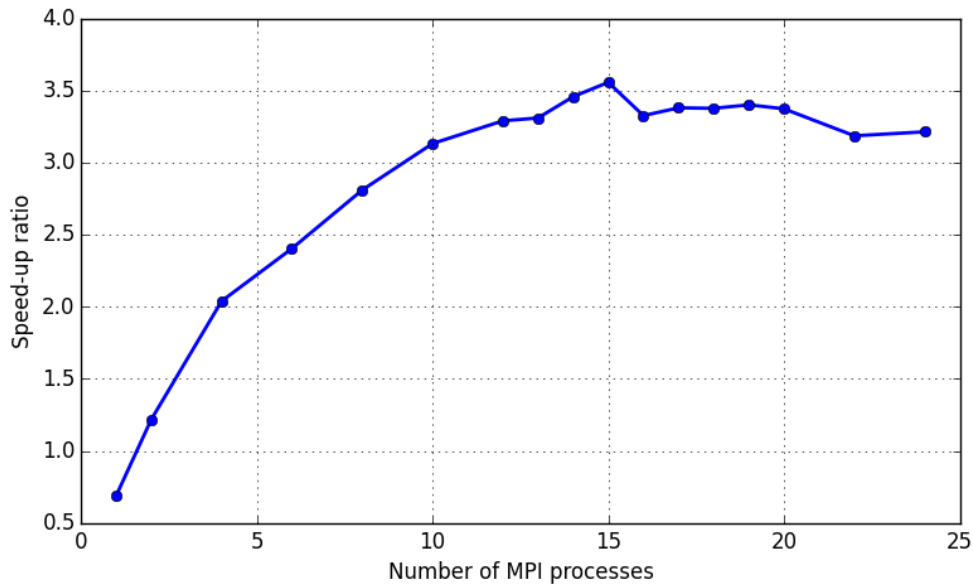


Figure 6.21: Speed-up ratio (Eq.(6.5)) as a function of the number of MPI processes (N_{proc}), for the test case presented in Section 6.2 with 485,728 unknowns.

6.4.4 Summary

These first attempts to optimize the 2DH version of the code are not entirely successful. Although the algorithm for node reordering was efficient in reducing the matrix bandwidth, it did not lead to a reduction in the analysis and factorization steps in MUMPS. Nevertheless, the parallelization of the solver enables improving the efficiency of the model in comparison to the sequential version, and for the case considered here, a maximum speed-up ratio of 3.5 is reached when using 15 MPI processes. These results may be problem-dependent and further tests should be conducted to see how these results can be generalized for larger domains. However, the speed-up ratios are quite small, and the next step towards a more efficient code could be the parallelization by domain decomposition. Other options could be considered including: the use of an iterative linear solver (i.e. GMRES, BiCGSTAB,...), and the use of other time marching schemes, such as Adams-Moulton (AM) and Adams-Bashworth (AB) predictor-corrector schemes, which require fewer resolutions of the Laplace BVP.

Conclusions and perspectives

Au cours de cette thèse, un modèle de vague simulant de manière précise les effets non-linéaires et dispersifs intervenant lors de la propagation des vagues au-dessus de bathymétries variables a été développé et amélioré. La version 1DH du modèle a été validée à travers l'application à de nombreux cas tests, démontrant ses capacités dispersives pour une large gamme de profondeurs relatives. Afin d'élargir le champ d'application du modèle, n'incluant pas de terme de diffusion par hypothèse, une formulation visco-potentielle a été étudiée, permettant de prendre en compte les effets dissipatifs dus à la friction interne et à la friction sur le fond, dans la limite de faible viscosité et faible pente du fond. L'extension du modèle en 2DH avec une approche sans maillage, basée sur la méthode RBF-FD, a été choisie. Les tests de sensibilité aux différents paramètres de la méthode ont abouti à la recommandation de l'utilisation de la RBF PHS $r^7 + p^3$ avec une taille de stencil entre 20 et 30 nœuds pour des applications générales. La comparaison à des résultats expérimentaux pour des cas à bathymétrie variable a montré que cette méthode était applicable pour la propagation de vagues en 2DH. Cependant, plusieurs aspects du modèle peuvent encore être améliorés, notamment l'ajout de conditions aux limites pour permettre la modélisation de cas plus réalistes avec la génération de vagues non-linéaires et la modélisation du run-up. Quant aux processus physiques représentés, la stabilité du terme du frottement sur le fond pourrait être étudiée plus en profondeur et l'inclusion de la dissipation d'énergie induit par le déferlement bathymétrique serait un plus. Concernant les aspects numériques, la robustesse de la méthode RBF-FD reste à améliorer, notamment pour limiter le développement d'instabilités au niveau des bords du domaine du fait des stencils décentrés. Enfin, le passage à la version 2DH du modèle a entraîné une large augmentation du temps de calcul du fait de la dépendance du temps de résolution du problème de Laplace au nombre de nœuds de discrétisation. Des techniques d'optimisation telles que la décomposition de domaines ou l'utilisation de solveurs itératifs pourraient être testées afin de rendre le code plus performant.

The main objective of the PhD thesis was to pursue the development and validation of a deterministic wave model capable of simulating the propagation of irregular and multidirectional sea-states from the offshore (deep water) to the coast over variable bathymetry, with a highly accurate representation of the nonlinear and dispersive effects, for bidimensional (2DH) domains on the order of kilometers. The goal was to simulate practical, 2DH applications with complex coastal domains and bottom bathymetry, thus the model was discretized with scattered nodes (unstructured-type grids) to be able to refine the distribution of nodes at locations of interest, such as zones of significant bottom or coastline variability.

The development of a potential flow model based on the Euler-Zakharov equations began prior to this PhD thesis (Benoit et al., 2013; Yates and Benoit, 2012). An important component of the numerical model is the resolution of the Laplace boundary value problem (BVP). Following previous work, (Yates and Benoit, 2015) concluded that a spectral approach in the vertical (Tian and Sato, 2008) combined with finite difference schemes in the horizontal direction was the optimal approach for the 1DH version of the model that was then developed further in this thesis.

Summary of the main achievements of the PhD thesis

During this PhD thesis, several aspects of numerical wave modeling were addressed, from numerical aspects to physical processes important in wave propagation, leading to a number of improvements and extensions of the computational model.

One of the critical issues in numerical wave modeling is wave generation and absorption. A comprehensive study was conducted on the implementation of specific boundary conditions for wave generation, including a comparison between Dirichlet and Neumann boundary conditions. The selected solution resulted in a combination of classical Dirichlet boundary conditions and the use of relaxation zones. This technique proved to be efficient for both generation and absorption as long as the relaxation zones are properly designed (i.e. length of the zone and shape of the function used to progressively impose the desired solution).

Then, an extensive study of the accuracy of the nonlinear and dispersive capabilities of the model was completed. First, the linear dispersion relation of the model was derived, showing an increase in accuracy with N_T . For instance, the relative error in the calculated wave celerity for flat bottom conditions (in comparison with Stokes' analytical solution) remains smaller than 2.5% for kh up to 100 using $N_T \geq 9$. The linear version of the model was validated with comparisons to analytical solutions of the reflection of regular waves over a Roseau-type bathymetric profile and the generation of waves generated by bottom motions.

The convergence properties of the nonlinear version of the model were studied in detail for moderate to highly nonlinear solitary waves. The order of temporal and spatial (algebraic) con-

vergence were approximately 4-5 for the two less nonlinear cases and 3-4 for the most nonlinear case, in agreement with the properties of the fourth-order Runge-Kutta (RK4) temporal discretization scheme and the fourth-order finite difference schemes used to approximate the horizontal derivatives. The exponential convergence in the vertical dimension obtained with the spectral approach was confirmed, showing an accurate representation of the vertical structure of the potential with a small maximum degree of Chebyshev polynomial.

Finally, the 1DH version of the model was validated with a series of challenging test cases: a moving bottom generating free surface deformations (tsunami-like wave generation), propagation over steep bottom bathymetry (submerged bar, barred beach profile), etc. The comparisons with experimental data showed the accurate simulation of energy transfers between the harmonic components over variable bathymetry and demonstrated the dispersive capabilities of the model. The numerous test cases showed the influence of several numerical parameters, in particular confirming the optimal value of N_T : from 5 to 10, depending on the dispersive characteristics of the test case.

To broaden the range of applications of the model that is by definition non-diffusive, a visco-potential formulation was studied to take into account the effects of bulk viscosity and bottom friction in the Zakharov equations. To our knowledge, this had not yet been done. Boussinesq-type (i.e. long wave) models mainly have been derived from this set of equations. The only study we are aware of involving the Zakharov equations was limited to bulk viscosity terms with an additional assumption of weak nonlinearity (Kakleas and Nicholls, 2010). This new implementation of the visco-potential formulation was validated with comparisons to a linear analytical solution for the decay rate of a standing wave over a flat bottom, and with experimental measurements of the decay and the shoaling of a solitary wave propagating over a flat bottom and then up a mild slope. The application to small-scale experiments studying the propagation of regular waves over a submerged step showed the limits of the derivation and implementation of the bottom friction term. However, satisfactory results in comparison to the experiments were obtained considering only the bulk viscosity terms. In addition, this test case validated the inclusion of surface tensions effects in the model.

The extension of the model to two horizontal dimensions was also an important component of this PhD thesis. A meshless approach, based on the RBF-FD (Radial Basis Function - Finite Difference) method was chosen to allow significant flexibility for the application to real domains, enabling using non-rectangular grids and refining the nodes easily. This method presents the advantage of being similar to finite difference methods and rather simple to implement, not requiring major adaptations of the code. A series of sensitivity tests to the parameters involved in the RBF-FD method were conducted to examine the robustness of this approach for the estimation of derivatives. The application of the 2DH version for the simulation of two different

wave basin experiments showed that it is possible to use this method for 2D wave propagation. However, the method is sensitive to the choice of parameters, in particular the shape parameter for infinitely smooth RBFs. This difficulty can be avoided by using piecewise smooth RBFs that do not depend on a shape parameter. Based on the tests performed here, the present recommendation is to use such piecewise smooth RBFs, in particular the Poly-Harmonic Splines (PHS) of degree 5 or 7, supplemented with an augmented polynomial.

Finally, the numerical efficiency of the 2DH version of the model appeared to be an important obstacle for simulations in large domains. The resolution of the Laplace BVP linear system is the most computationally expensive part of the model. Therefore, an initial attempt to improve the numerical efficiency was to use the parallelized version of the direct linear solver MUMPS. The test conducted for a 60,716 node set with $N_{sten} = 13$ showed a maximum speed-up of 3.5 when the simulation was run with 15 MPI processes. Further tests are needed to generalize these results.

To summarize, at the end of this thesis, an accurate model for simulating nonlinear and dispersive effects occurring during water wave propagation over variable bottom profiles has been developed and improved. The 1DH version has been validated extensively and is applicable for a wide range of relative water depths, and its applicability for 2DH cases has been demonstrated. Considering the work on physical processes, bulk viscous effects and bottom friction are taken into account in the limit of small viscosity and small bottom slope, as well as surface tension effects for short waves.

Perspectives

With the long term objective of applying the model to real and complex nearshore domains, including wave propagation near coastal and harbor structures, work can be done to validate and improve several aspects of the model, in particular: boundary conditions, representation of physical processes, coupling with other models, robustness of the method, and computational efficiency. These topics are discussed hereafter, and some insight is given on possible future developments.

Boundary conditions: Additional realistic boundary conditions must be developed and/or validated. The generation of irregular and directional waves from a prescribed directional spectrum has been implemented using linear wave theory (at the end of the PhD thesis) but requires being validated (e.g. with test cases from [Vincent and Briggs \(1989\)](#) experiments). This will enable forcing the model with spectra obtained from larger scale applications of phase-averaged models (such as Tomawac, Swan, or WaveWatch-III).

The possibility to generate nonlinear (at least at second order) irregular wave fields may improve the stability of the model when generating highly nonlinear wave fields (e.g. [Schäffer, 1996](#); [Yang](#)

[et al., 2014](#)).

Moreover, modeling run-up and run-down on slopes is also of interest to widen the range of applications of the model to “real” coastal problems.

Representation of physical processes: In this work, the representation of bulk viscosity has been carefully validated. However, the implementation of the bottom boundary condition of the visco-potential formulation, to take into account bottom friction effects, still requires improvements in the case where it is used in combination with relaxation zones for wave generation. Moreover, it will be important to derive the expression of the bottom boundary condition without the limitation of a mild bottom slope.

In addition, the calculation of this term is not computationally efficient since it is non-local in time, and thus requires storage of a large amount of data. To optimize the efficiency and memory requirements of the computation of this non-local term, the approximation proposed by [Torsvik and Liu \(2007\)](#) could be tested to evaluate the impact on the accuracy of the results.

The inclusion of energy dissipation through depth-induced wave breaking is necessary for practical applications, though it cannot be simulated directly with a potential flow model. The goal is to extend the model to estimate properly the wave height attenuation due to breaking. This requires the modification of the evolution equations (Zakharov equations), and two methods may be considered: the addition of pressure terms at the free surface to simulate the effects of wave rollers, following [Guignard and Grilli \(2001\)](#), or the addition of an eddy viscosity-like term to the KFSBC and DFSBC ([Tian et al., 2010](#)), following previous works (i.e. [Heitner and Housner, 1970](#); [Kennedy et al., 2000](#); [Zelt, 1991](#)).

The effects of ambient currents could also be considered for applications where tidal or river outflow effects are important.

Coupling with other models: Although some viscous effects are taken into account to model bulk and bottom friction induced viscous dissipation, some applications (i.e. wave-structure interactions, for marine renewable energy devices, offshore platforms, etc.) require a more accurate representation of viscous effects. In particular, it may be necessary to account for vorticity effects, wakes in the lee of structures, the viscous drag part of forces, etc. To achieve this, the Misthyc potential flow model could be coupled with a Navier-Stokes code that takes into account fluid-structure interactions at local scales, for example, following the SWENSE method proposed by [Ferrant et al. \(2003\)](#).

Robustness of the RBF-FD method: The RBF-FD method used to estimate derivatives in the 2DH version of the model when solving the Boundary Value Problem or in the Zakharov equations, is sensitive to the choice of the RBF, the value of the shape parameter C , and the size of the stencil N_{sten} . Finding an appropriate set of parameters for a given application can be a challenge. The main source of instabilities is the lack of accuracy in the estimation of derivatives at and close to the boundaries because of non-centered stencils at these locations. Some techniques

may be tested to reduce the development of instabilities and thus increase the robustness of the model, for example: decreasing the stencil size of boundary nodes (leading to a more diffusive approximation at the boundaries), increasing the degree of the augmented polynomial at the boundary, or refining the mesh when approaching the boundaries.

Another option would be the addition of ghost nodes outside of the domain to reduce the one-sidedness of the stencils of boundary nodes. Nevertheless, the implementation of such a method is not trivial. A common method to stabilize the resolution of PDEs without a physical dissipative term (as is the case for the Zakharov equations) is to add a hyper-viscosity operator to the right hand-side of the evolution equation to introduce artificially a small amount of dissipation that will damp spurious high frequency oscillations. In parallel, alternative options for the resolution of the 2DH problem could also be considered.

Computational efficiency: With a direct solver, the efficiency of the resolution of the Laplace BVP system depend strongly on the number of nodes in the domain, and parallelizing the code with a domain decomposition approach could increase its efficiency (over using simply the parallel version of the linear solver). Other possibilities to reduce the computational cost could be to consider time integration schemes requiring fewer resolutions of the Laplace BVP (i.e. multi-step predictor-corrector schemes) and/or to test iterative solvers, such as GMRES or BiCGSTAB, with suitable preconditioners. Work on these two subjects is currently in progress.

Further validation and applications: Finally, further validation of the 2DH version of the model is required, including cases with complex coastlines and variable bathymetries, islands, coastal structures and a variety of different wave conditions. In the near future, the model will be applied to real coastal cases where field measurements are available or will be collected, in particular within projects related to marine renewable energies (e.g. the ongoing EMACOP French project “Energies MARines COTieres et Portuaires”, and the proposed ANR DiMe project “Dimensionnement et Meteocean: modélisation et observations des états de mer extrêmes déferlants pour les EMR”).

The model may also be used for modeling the generation of waves due to seismic bottom motion or submarine landslide, in particular for the study of tsunamis. It is currently used for that purpose within the PIA-ANR TANDEM (Tsunamis in the Atlantic and the English chaNnel: Definition of the Effects through numerical Modeling, see <http://www-tandem cea.fr/>), where it has proven very accurate to simulate such waves. The test cases “Solitary wave over a flat bottom” of Section 3.2 and “Waves generated by impulsive bottom motion” of Section 3.4 have been considered in this project. Within the same project, the linear and nonlinear versions of the model have been used during the PhD of Marine Le Gal to study the generation phase of tsunami (Le Gal et al., 2017). These applications have demonstrated the applicability of the model to tsunami generation and propagation, and this opens another field of future developments/applications.

Appendix A : Dispersion relation for Misthyc

The dispersion relation of the model depends on the vertical resolution N_T . It can be expressed as a rational function of μ according to Eq.(1.74) repeated here for convenience:

$$\frac{\hat{\omega}_{N_T}^2}{\mu^2} = \left(\frac{C}{\sqrt{gh}} \right)_{N_T}^2 = \frac{1 + \sum_{p=1}^{N_T-2} \alpha_p \mu^{2p}}{1 + \sum_{p=1}^{N_T-1} \beta_p \mu^{2p}}.$$

The values of the coefficients α_p and β_p for N_T from 2 to 9 are presented in Table 2, for N_T from 10 to 12 in Table 3 and, for N_T from 13 to 15 in Table 4.

N_T	α_p for $p = 1$ to $N_T - 2$	β_p for $p = 1$ to $N_T - 1$
2		$\beta_1 = \frac{5}{16}$
3	$\alpha_1 = \frac{3}{32}$	$\beta_1 = \frac{13}{32}$ $\beta_2 = \frac{13}{1536}$
4	$\alpha_1 = \frac{11}{96}$ $\alpha_2 = \frac{1}{512}$	$\beta_1 = \frac{43}{96}$ $\beta_2 = \frac{55}{3072}$ $\beta_3 = \frac{25}{294912}$
5	$\alpha_1 = \frac{25}{192}$ $\alpha_2 = \frac{19}{6144}$ $\alpha_3 = \frac{5}{294912}$	$\beta_1 = \frac{89}{192}$ $\beta_2 = \frac{149}{6144}$ $\beta_3 = \frac{779}{2949120}$ $\beta_4 = \frac{41}{94371840}$
6	$\alpha_1 = \frac{133}{960}$ $\alpha_2 = \frac{21}{5120}$ $\alpha_3 = \frac{203}{5898240}$ $\alpha_4 = \frac{1}{12582912}$	$\beta_1 = \frac{151}{320}$ $\beta_2 = \frac{431}{15360}$ $\beta_3 = \frac{2591}{5898240}$ $\beta_4 = \frac{1769}{943718400}$ $\beta_5 = \frac{61}{45298483200}$
7	$\alpha_1 = \frac{23}{160}$ $\alpha_2 = \frac{443}{92160}$ $\alpha_3 = \frac{197}{3686400}$ $\alpha_4 = \frac{287}{1415577600}$ $\alpha_5 = \frac{7}{30198988800}$	$\beta_1 = \frac{229}{480}$ $\beta_2 = \frac{937}{30720}$ $\beta_3 = \frac{4259}{7372800}$ $\beta_4 = \frac{37507}{9909043200}$ $\beta_5 = \frac{697}{90596966400}$ $\beta_6 = \frac{17}{6088116142080}$
8	$\alpha_1 = \frac{33}{224}$ $\alpha_2 = \frac{857}{161280}$ $\alpha_3 = \frac{1439}{20643840}$ $\alpha_4 = \frac{101}{275251200}$ $\alpha_5 = \frac{11}{15099494400}$ $\alpha_6 = \frac{1}{2174327193600}$	$\beta_1 = \frac{323}{672}$ $\beta_2 = \frac{577}{17920}$ $\beta_3 = \frac{14111}{20643840}$ $\beta_4 = \frac{4495}{792723456}$ $\beta_5 = \frac{27553}{1479750451200}$ $\beta_6 = \frac{1243}{60881161420800}$ $\beta_7 = \frac{113}{27274760316518400}$
9	$\alpha_1 = \frac{403}{2688}$ $\alpha_2 = \frac{2449}{430080}$ $\alpha_3 = \frac{4003}{48168960}$ $\alpha_4 = \frac{1411}{2642411520}$ $\alpha_5 = \frac{121}{79272345600}$ $\alpha_6 = \frac{71}{40587440947200}$ $\alpha_7 = \frac{1}{1515264462028800}$	$\beta_1 = \frac{433}{896}$ $\beta_2 = \frac{137}{4096}$ $\beta_3 = \frac{110681}{144506880}$ $\beta_4 = \frac{136099}{18496880640}$ $\beta_5 = \frac{1688597}{53271016243200}$ $\beta_6 = \frac{299093}{5114017559347200}$ $\beta_7 = \frac{2059}{54549520633036800}$ $\beta_8 = \frac{29}{6284104776925839360}$

Table 2: Dispersion relation coefficients for N_T ranging from 2 to 9

N_T	α_p for $p = 1$ to $N_T - 2$	β_p for $p = 1$ to $N_T - 1$
10	$\alpha_1 = \frac{175}{1152}$ $\alpha_2 = \frac{11593}{1935360}$ $\alpha_3 = \frac{46651}{495452160}$ $\alpha_4 = \frac{32831}{47563407360}$ $\alpha_5 = \frac{263759}{106542032486400}$ $\alpha_6 = \frac{10769}{2557008779673600}$ $\alpha_7 = \frac{979}{327297123798220800}$ $\alpha_8 = \frac{1}{1396467728205742080}$	$\beta_1 = \frac{559}{1152}$ $\beta_2 = \frac{4439}{129024}$ $\beta_3 = \frac{137321}{165150720}$ $\beta_4 = \frac{419743}{47563407360}$ $\beta_5 = \frac{963259}{21308406497280}$ $\beta_6 = \frac{1728347}{15342052678041600}$ $\beta_7 = \frac{14905}{117826964567359488}$ $\beta_8 = \frac{16109}{314205238846291968000}$ $\beta_9 = \frac{181}{45245554393866043392000}$
11	$\alpha_1 = \frac{221}{1440}$ $\alpha_2 = \frac{3443}{552960}$ $\alpha_3 = \frac{96031}{928972800}$ $\alpha_4 = \frac{49463}{59454259200}$ $\alpha_5 = \frac{238111}{68491306598400}$ $\alpha_6 = \frac{166427}{21917218111488000}$ $\alpha_7 = \frac{6721}{818242809495552000}$ $\alpha_8 = \frac{1199}{314205238846291968000}$ $\alpha_9 = \frac{11}{18098221757546417356800}$	$\beta_1 = \frac{701}{1440}$ $\beta_2 = \frac{6481}{184320}$ $\beta_3 = \frac{164387}{185794560}$ $\beta_4 = \frac{1800037}{178362777600}$ $\beta_5 = \frac{147817}{2536715059200}$ $\beta_6 = \frac{8511197}{48217879845273600}$ $\beta_7 = \frac{22222159}{81006038140059648000}$ $\beta_8 = \frac{62507}{314205238846291968000}$ $\beta_9 = \frac{24089}{452455543938660433920000}$ $\beta_{10} = \frac{221}{79632175733204236369920000}$
12	$\alpha_1 = \frac{817}{5280}$ $\alpha_2 = \frac{1627}{253440}$ $\alpha_3 = \frac{68833}{619315200}$ $\alpha_4 = \frac{209039}{217998950400}$ $\alpha_5 = \frac{1403711}{313918488576000}$ $\alpha_6 = \frac{21821}{1883510931456000}$ $\alpha_7 = \frac{2658541}{162012076280119296000}$ $\alpha_8 = \frac{55939}{4713078582694379520000}$ $\alpha_9 = \frac{1703}{452455543938660433920000}$ $\alpha_{10} = \frac{1}{2413096234339522314240000}$	$\beta_1 = \frac{859}{1760}$ $\beta_2 = \frac{9067}{253440}$ $\beta_3 = \frac{903997}{973209600}$ $\beta_4 = \frac{116147}{10380902400}$ $\beta_5 = \frac{4427539}{62783697715200}$ $\beta_6 = \frac{14763743}{60272349806592000}$ $\beta_7 = \frac{280102969}{594044279693770752000}$ $\beta_8 = \frac{275571539}{570282508506019921920000}$ $\beta_9 = \frac{393133}{1659003661108421591040000}$ $\beta_{10} = \frac{6943}{159264351466408472739840000}$ $\beta_{11} = \frac{53}{33636631029705469442654208000}$

Table 3: Dispersion relation coefficients for N_T ranging from 10 to 12

N_T	α_p for $p = 1$ to $N_T - 2$	β_p for $p = 1$ to $N_T - 1$
13	$\alpha_1 = \frac{329}{2112}$ $\alpha_2 = \frac{6671}{1013760}$ $\alpha_3 = \frac{441269}{3746856960}$ $\alpha_4 = \frac{15427241}{14387930726400}$ $\alpha_5 = \frac{2500199}{460413783244800}$ $\alpha_6 = \frac{79}{4960687226880}$ $\alpha_7 = \frac{6053639}{222766604885164032000}$ $\alpha_8 = \frac{639839}{24440678935972282368000}$ $\alpha_9 = \frac{1703}{129273012553902981120000}$ $\alpha_{10} = \frac{403}{136512301256921548062720000}$ $\alpha_{11} = \frac{13}{56061051716175782404423680000}$	$\beta_1 = \frac{1033}{2112}$ $\beta_2 = \frac{4087}{112640}$ $\beta_3 = \frac{517043}{535265280}$ $\beta_4 = \frac{34940501}{2877586145280}$ $\beta_5 = \frac{1395397}{17052362342400}$ $\beta_6 = \frac{1985963}{6314246170214400}$ $\beta_7 = \frac{8162206589}{11583863454028529664000}$ $\beta_8 = \frac{5569937}{6127002157502693376000}$ $\beta_9 = \frac{450917}{70292599566964233388800}$ $\beta_{10} = \frac{70307}{318528702932816945479680000}$ $\beta_{11} = \frac{9703}{336366310297054694426542080000}$ $\beta_{12} = \frac{313}{419785155250724258644324515840000}$
14	$\alpha_1 = \frac{391}{2496}$ $\alpha_2 = \frac{44257}{6589440}$ $\alpha_3 = \frac{729049}{5904138240}$ $\alpha_4 = \frac{1995347}{1700391813120}$ $\alpha_5 = \frac{227614151}{35912275093094400}$ $\alpha_6 = \frac{469327}{22983856059580416}$ $\alpha_7 = \frac{25701259}{643547969668251648000}$ $\alpha_8 = \frac{52251107}{1112050891586738847744000}$ $\alpha_9 = \frac{4550101}{142342514123102572511232000}$ $\alpha_{10} = \frac{251}{21717866109055700828160000}$ $\alpha_{11} = \frac{181}{96104660084872769836154880000}$ $\alpha_{12} = \frac{1}{9226047368147785904270868480000}$	$\beta_1 = \frac{1223}{2496}$ $\beta_2 = \frac{16127}{439296}$ $\beta_3 = \frac{168275}{168689664}$ $\beta_4 = \frac{2006009}{154581073920}$ $\beta_5 = \frac{1103658349}{11970758364364800}$ $\beta_6 = \frac{6289229}{16417040042557440}$ $\beta_7 = \frac{12370703}{12870959393365032960}$ $\beta_8 = \frac{48928807}{33464494422749085696000}$ $\beta_9 = \frac{2438062741}{1850452683600333442646016000}$ $\beta_{10} = \frac{294318169}{444108644064080026235043840000}$ $\beta_{11} = \frac{10095641}{61218668474063954385630658560000}$ $\beta_{12} = \frac{13213}{839570310501448517288649031680000}$ $\beta_{13} = \frac{73}{244482874418021808234454598025216000}$
15	$\alpha_1 = \frac{1375}{8736}$ $\alpha_2 = \frac{6367}{931840}$ $\alpha_3 = \frac{2464733}{19188449280}$ $\alpha_4 = \frac{97800317}{77367827496960}$ $\alpha_5 = \frac{59327977}{8252568266342400}$ $\alpha_6 = \frac{237062291}{9506958642826444800}$ $\alpha_7 = \frac{449249}{8299725799292928000}$ $\alpha_8 = \frac{12573581}{170364698879449890816000}$ $\alpha_9 = \frac{100491779}{1619146098150291762315264000}$ $\alpha_{10} = \frac{191135641}{6217521016897120367290613760000}$ $\alpha_{11} = \frac{1207}{147160260754961428811612160000}$ $\alpha_{12} = \frac{19}{19081143420487466302014750720000}$ $\alpha_{13} = \frac{1}{23284083277906838879471866478592000}$	$\beta_1 = \frac{1429}{2912}$ $\beta_2 = \frac{20729}{559104}$ $\beta_3 = \frac{6554543}{6396149760}$ $\beta_4 = \frac{2405669}{175437250560}$ $\beta_5 = \frac{2517106811}{24757704799027200}$ $\beta_6 = \frac{1424190641}{3168986214275481600}$ $\beta_7 = \frac{411942431}{334644944227490856960}$ $\beta_8 = \frac{2979106457}{1405508765755461599232000}$ $\beta_9 = \frac{461115337}{202393262268786470289408000}$ $\beta_{10} = \frac{614317331}{414501401126474691152707584000}$ $\beta_{11} = \frac{52853}{96676711632997012513751040000}$ $\beta_{12} = \frac{345941}{3428245434547581445595316879360000}$ $\beta_{13} = \frac{7999}{1111285792809190037429339081932800000}$ $\beta_{14} = \frac{421}{4107312290222766378338837246823628800000}$

Table 4: Dispersion relation coefficients for $N_T =$ ranging from 13 to 15

Bibliography

- Y. Agnon, P. A. Madsen, and H. A. Schäffer. A new approach to high-order Boussinesq models. *J. Fluid Mech.*, 399:319–333, 1999.
- P. R. Amestoy, I. S. Duff, J. Koster, and J.-Y. L'Excellent. A fully synchronous multifrontal solver using distributed dynamic scheduling. *SIAM J. of Matrix Anal. and Appl.*, 23(1):15–41, 2001.
- P. R. Amestoy, A. Guermouche, J.-Y. L'Excellent, and S. Pralet. Hybrid scheduling for the parallel solution of linear systems. *Parallel Computing*, 32:136–156, 2006.
- M. Antuono and A. Colagrossi. The damping of viscous gravity waves. *Wave Motion*, 50:197–209, 2013.
- F. Ardhuin. Les vagues: un compartiment important du système terre. Cours ENSTA ParisTech, 2012.
- G. A. Athanassoulis and K. A. Belibassakis. A consistent coupled-model theory for the propagation of small-amplitude water waves over variable bathymetry regions. *J. Fluid Mech.*, 389:275–301, 1999.
- G.A. Barnett. *A Robust RBF-FD Formulation based on Polyharmonic Splines and Polynomials*. PhD thesis, University of Colorado, 2015.
- V. Bayona, M. Moscoso, M. Carretero, and M. Kindelan. RBF-FD formulas and convergence properties. *J. Comp. Physics*, 229:8281–8295, 2010.
- V. Bayona, M. Moscoso, and M. Kindelan. Optimal constant shape parameter for multiquadric based RBF-FD method. *J. Comp. Physics*, 230:7384–7399, 2011.
- V. Bayona, M. Moscoso, and M. Kindelan. Optimal variable shape parameter for multiquadric based RBF-FD method. *J. Comp. Physics*, 231:2466–2481, 2012.
- R. K. Beatson, W. A. Light, and S. Billings. Fast Solution of the Radial Basis Function Interpolation Equations: Domain Decomposition Methods. *J. Sci. Comput.*, 22:1717–1740, 2001.
- F. Becq-Girard, P. Forget, and M. Benoit. Non-linear propagation of unidirectional wave fields over varying topography. *Coast. Eng.*, 38:91–113, 1999.

- F. Behroozi. Fluid viscosity and the attenuation of surface waves: a derivation based on conservation of energy. *Eur. J. Phys.*, 25:115–122, 2004.
- S. Beji and J. A. Battjes. Experimental investigation of wave propagation over a bar. *Coast. Eng.*, 19:151–162, 1993.
- K. A. Belibassakis and G. A. Athanassoulis. A coupled-mode system with application to nonlinear water waves propagating in finite water depth and in variable bathymetry regions. *Coast. Eng.*, 58:337–350, 2011.
- M. Benoit, M.L. Yates, and F. Chazel. A comparison of simulation approaches based on the Zakharov equations for nonlinear waves in the coastal zone. In *Proceedings of the 28th International Workshop on Water Waves and Floating Bodies*, L’Isle-sur-la-Sorgue, France, 2013.
- M. Benoit, C. Raoult, and M.L. Yates. Fully nonlinear and dispersive modeling of surf zone waves: non breaking tests. In *Proceedings of the 34th International Conference on Coastal Engineering*, Seoul, Korea, 2014.
- F. Biesel. Calcul de l’amortissement d’une houle dans un liquide visqueux de profondeur finie. *La Houille Blanche*, 4:630–634, 1949.
- H. B. Bingham and Y. Agnon. A Fourier-Boussinesq method for nonlinear water waves. *Eur. J. Mech. B/Fluids*, 24:255–274, 2005.
- H. B. Bingham and H. Zhang. On the accuracy of finite-difference solutions for nonlinear water waves. *J. Eng. Math*, 58:211–228, 2007.
- J. P. Boyd. *Chebyshev and Fourier Spectral Methods: Second Edition, Revised*. Dover Publications, Mineola, NY, USA, 2001.
- J. P. Boyd. Six strategies for defeating the Runge Phenomenon in Gaussian radial basis functions on a finite interval. *Comp. Math. Applic.*, 60:3108–3122, 2010.
- C. Canuto, M.Y. Hussaini, A. Quarteroni, and T.A. Zang. *Spectral Methods in Fluid Dynamics*. Springer-Verlag Berlin Heidelberg, 1988. Springer Series in Computational Physics.
- R. E. Carlson and T. A. Foley. The parameter r^2 in multiquadratic interpolation. *Comp. Math. Applic.*, 21:29–42, 1991.
- G. Chapalain, R. Cointe, and A. Temperville. Observed and modeled resonantly interacting progressive water-waves. *Coast. Eng.*, 16:267–300, 1992.
- F. Chazel, M. Benoit, A. Ern, and S. Piperno. A double-layer Boussinesq-type model for highly nonlinear and dispersive waves. *Proc. R. Soc. A*, 465:2319–2346, 2009.

- X.B. Chen and F. Dias. Visco-potential flow and time-harmonic ship wave. In *25th International Workshop on Water Waves and Floating Bodies*, Harbin, China, 2010.
- T. B. Christiansen, A. P. Engsig-Karup, and H. B. Bingham. Hybrid-spectral model for fully nonlinear numerical wave tank. In *Proceedings of the 28th International Workshop on Water Waves and Floating Bodies*, L'Isle-sur-la-Sorgue, France, 4p., 2013.
- D. Clamond and D. Dutykh. Fast accurate computation of the fully non linear solitary surface gravity waves. *Computers & Fluids*, 84:35–38, 2013.
- D. Clamond and J. Grue. A fast method for fully nonlinear water-wave computations. *J. Fluid Mech.*, 447:337–355, 2001.
- D. Clamond, D. Fructus, J. Grue, and Ø. Kristiansen. An efficient model for three-dimensional surface wave simulations. part II: Generation and absorption. *J. Comp. Phys.*, 205:686–705, 2005.
- D. Clamond, D. Fructus, and J. Grue. A note on time integrators in water-wave simulations. *J. Eng. Math.*, 58:149–156, 2007.
- A. Clément. Coupling of two absorbing boundary conditions for 2D time-domain simulations of free surface gravity waves. *J. Comp. Phys.*, 126:139–151, 1996.
- P.J. Cobelli, A. Maurel, V. Pagneux, and P. Petitjeans. Global measurement of water waves by Fourier Transform Profilometry. *Exp. Fluids*, 46:1037–1047, 2009.
- G. Contento. Numerical wave tank computation of nonlinear motions of two-dimensional arbitrarily shaped free floating bodies. *Ocean Eng.*, 27:531–556, 2000.
- R. A. Dalrymple and B. D. Rogers. Numerical modeling of water waves with the SPH method. *Coast. Eng.*, 53:141–147, 2006.
- R. A. Dalrymple, A. Herault, G. Bilotta, and R. Farahani. GPU-Accelerated SPH model for water waves and free surface flows. *Coastal Engineering Proceedings*, 1(32):9 p., 2011.
- J. F. Dalzell. A note on finite depth second-order wave-wave interactions. *App. Ocean Res.*, 3(21):105–111, 1999.
- R. G. Dean and R.A. Dalrymple. *Water Wave Mechanics for Engineers and Scientists*. World Scientific Publishing, 1991. Advanced Series on Ocean Engineering, Volume 2.
- F. Dias and C. Kharif. Nonlinear gravity and capillary-gravity waves. *Annu. Rev. Fluid Mech.*, 31:301–347, 1999.
- F. Dias, A.I. Dyachenko, and V.E. Zakharov. Theory of weakly damped free-surface flows: A new formulation based on potential flow solutions. *Physics Letters, A* 372:1297–1302, 2008.

- H. Ding, C. Shu, and D.B. Tang. Error estimates of local multiquadric-based differential quadrature (LMQDQ) method through numerical experiments. *Int. J. Num. Meth. Eng.*, 63:1513–1529, 2005.
- M. Dingemans. Comparison of computations with Boussinesq-like models and laboratory measurements. Mast-G8M technical report, Delft Hydraulics, Delft, The Netherlands, 1994.
- M. W. Dingemans. *Water wave propagation over uneven bottom*, volume 13. World Scientific Publishing, 1997a.
- M. W. Dingemans. *Water wave propagation over uneven bottoms. Part 1 - Linear wave propagation*. World Scientific Publishing, 1997b. Advanced Series on Ocean Engineering, Volume 13.
- E. Dombre, M Benoit, D Violeau, and C. Peyrard. Simulation of floating structure dynamics in waves by implicit coupling of a fully non-linear potential flow model and rigid body motion approach. *J. Ocean Eng. Mar. Energy*, 1:55–76, 2015.
- D. G. Dommermuth and D. K. P. Yue. A high-order spectral method for the study of nonlinear gravity waves. *J. Fluid Mech.*, 184:267–288, 1987.
- B. D. Dore. Some effects of the air-water interface on gravity wave. *J. Geo. & Astro. Fluid Dyn.*, 10:215–230, 1978.
- G. Ducrozet, H. B. Bingham, A. P. Engsig-Karup, F. Bonnefoy, and P. Ferrant. A comparative study of two fast nonlinear free-surface water wave models. *Int. J. Numer. Meth. Fluids*, 69(11): 1818–1834, 2012a.
- G. Ducrozet, F. Bonnefoy, D. Le Touzé, and P. Ferrant. A modified High-Order Spectral method for wavemaker modeling in a numerical wave tank. *Euro. J. Mecha. B/ Fluids*, 34:19–34, 2012b.
- D. Dutykh. Visco-potential free-surface flows and long wave modelling. *European J. of Mech. B/Fluids*, 28:430–443, 2009a.
- D. Dutykh. Group and phase velocities in the free-surface visco-potential flow: New kind of boundary layer induced instability. *Physics Letters A*, 373:3212–3216, 2009b.
- D. Dutykh and F. Dias. Viscous potential free-surface flows in a fluid layer of finite depth. *C.R. Acad. Sci. Paris*, 345:113–118, 2007.
- A. P. Engsig-Karup, J. S. Hesthaven, H. B. Bingham, and P. A. Madsen. Nodal DG-FEM solution of high-order Boussinesq-type equations. *J. Eng. Math*, 56(3):351–370, 2006.
- A. P. Engsig-Karup, H. B. Bingham, and O. Lindberg. An efficient flexible-order model for 3D nonlinear water waves. *J. Comp. Phys.*, 228:2100–2118, 2009.

- A.P. Engsig-Karup. *Unstructured Nodal DG-FEM Solution of High-order Boussinesq-type Equations*. PhD thesis, Technical University of Denmark, 2006.
- G. E. Fasshauer. Solving partial differential equations by collocation with Radial Basis Functions. In L.L. Schumaker (Eds.) A.L. Mehaute, C. Rabut, editor, *Surface Fitting and Multiresolution Methods*, pages 131–138, Chamonix, France, 1997.
- G. E. Fasshauer and J. G. Zang. On choosing "optimal" shape parameter for RBF approximation. *Num. Algo.*, 45:345–368, 2007.
- A. I. Fedoseyev, M. J. Friedman, and E. J. Kansa. Improved multiquadric methods for elliptic partial differential equations via PDE collocation on the boundary. *Comp. Math. Applic.*, 43: 439–455, 2002.
- P. Ferrant, L. Gentaz, B. Alessandrini, D Le Touzé, and Ecole Centrale de Nantes. A Potential/RANSE Approach for Regular Water Wave Diffraction about 2-d Structures. *Ship Technology Research*, 50(4):165–171, 2003.
- N. Flyer, B. Fornberg, V. Bayona, and G. A. Barnett. On the role of polynomials in RBF-FD approximations: I. Interpolation and accuracy. *J. Comp. Phys.*, 321:21–38, 2016.
- C. Fochesato, S. T. Grilli, and F. Dias. Numerical modeling of extreme rogue waves generated by directional energy focusing. *Wave Motion*, 44:395–416, 2007.
- B. Fornberg. Generation of finite difference formulas on arbitrarily spaced grids. *Mathematics of Computation*, 51(184):699–706, 1988.
- B. Fornberg and N Flyer. *A Primer on Radial Basis Functions with Applications to the Geosciences*. Siam, Philadelphia, 2015.
- B. Fornberg and E. Lehto. Stabilisation of RBF-generated finite difference method for convective PDEs. *J. Comp. Physics*, 230:2270–2285, 2011.
- B. Fornberg and C. Piret. A stable algorithm for flat radial basis functions on a sphere. *SIAM J. Sci. Comput.*, 30:60–80, 2007.
- B. Fornberg and Wright. Stable computation of multiquadric interpolants for all values the shape parameter. *Comp. Math. Applic.*, 48:853–867, 2004.
- B. Fornberg and J. Zuev. The Runge phenomenon and spatially variable shape parameters in RBF interpolation. *Comp. Math. Applic.*, 54:379–398, 2007.
- B. Fornberg, T. A. Driscoll, G. Wright, and R. Charles. Observation on the behaviour of radial basis function approximation near boundaries. *Comp. Math. Applic.*, 43:473–490, 2002.

- B. Fornberg, G. Wright, and E. Larsson. Some observation regarding interpolants in the limit of flat radial basis functions. *Comp. Math. Applic.*, 47:37–55, 2004.
- B. Fornberg, E. Larsson, and N. Flyer. Stable Computation with Gaussian Radial Basis Functions. *SIAM J. Sci. Comput.*, 33:869–892, 2011.
- B. Fornberg, E. Lehto, and C. Powell. Stable calculation of Gaussian-based RBF-FD stencils. *Comput. Math. App.*, 65:627–637, 2013.
- R. Franke. Scattered Data Interpolation: Tests of Some Methods. *Math. Comp.*, 38:181–200, 1982.
- D. Fructus and J. Grue. An explicit method for the nonlinear interaction between water waves and variable and moving bottom topography. *J. Comp. Phys.*, 222:720–739, 2007.
- D. Fructus, D. Clamond, J. Grue, and Ø. Kristiansen. An efficient model for three-dimensional surface wave simulations: Part I: Free space problems. *J. Comp. Phys.*, 205:665–685, 2005.
- D. R. Fuhrman and H. B. Bingham. Numerical solution of fully non-linear and highly dispersive Boussinesq equations in two horizontal dimensions. *Int. J. Numer. Meth. Fluids*, 44:231–255, 2004.
- D. R. Fuhrman and P. A. Madsen. Tsunami generation, propagation, and run-up with a high-order Boussinesq model. *Coast. Eng.*, 56:747–758, 2009.
- M. Gouin. *Modélisation déterministe d'états de mer à grande échelle en profondeur variable*. PhD thesis, Ecole Centrale Nantes, 2016.
- M. Gouin, G. Ducrozet, and P. Ferrant. Development and validation of a non-linear spectral model for water waves over variable depth. *Euro. J. Mecha. B/ Fluids*, 57:115–128, 2016.
- S. T. Grilli and J. Horrillo. Numerical generation and absorption of fully nonlinear periodic waves. *J. Eng. Mech.*, 123(10):1060–1069, 1997.
- S. T. Grilli, J. Skourup, and I. A. Svendsen. An efficient boundary element method for nonlinear water waves. *Eng. Anal. Bound. Elem.*, 6(2):97–107, 1989.
- S. Guignard and S. Grilli. Modeling of wave shoaling in a 2D-NWT using a spilling breaker model. In *Proceedings of the 11th ISOPE*, pages 116–123, Stavanger, Norway, 2001.
- P. Guyenne and D. P. Nicholls. A high-order spectral method for nonlinear water waves over moving bottom topography. *SIAM J. Sci. Comput.*, 30(1):81–101, 2007.
- J. L. Hammack. A note on tsunamis: their generation and propagation in an ocean of uniform depth. *J. Fluid Mech.*, 60(4):769–799, 1973.
- R. L. Hardy. Multiquadric equation of topography and other irregular surfaces. *J. Geophys. Res.*, 76:1905–1915, 1971.

- K. L. Heitner and G. W. Housner. Numerical model for tsunami run-up. *ASCE J. Waterway Harbors Coastal Eng. Div.*, 96:701–719, 1970.
- D.M. Henderson and H. Segur. The role of dissipation in the evolution of ocean swell. *Journal of Geophysical Research*, 118:5074–5091, 2013.
- P. Higuera, J. L. Lara, and I. J. Losada. Realistic wave generation and active wave absorption for Navier-Stokes Application to OpenFOAM®. *Coast. Eng.*, 71:102–118, 2013a.
- P. Higuera, J. L. Lara, and I. J. Losada. Simulating coastal engineering processes with OpenFOAM®. *Coast. Eng.*, 71:119–134, 2013b.
- Y. C. Hon and R. Schaback. On unsymmetric collocation by radial basis functions. *App. Math. Comput.*, 119:177–186, 2001.
- J.N. Hunt. Viscous damping of waves over an inclined bed in a channel of finite width. *La Houille Blanche*, 7:836–842, 1952.
- D.D. Joseph and J. Wang. The dissipation approximation and viscous potential flow. *J. Fluid Mech.*, 505:365–377, 2004.
- M. Kakleas and D.P. Nicholls. Numerical simulation of a weakly nonlinear model for water waves with viscosity. *J. Sci. Comput.*, 42:274–290, 2010.
- E. J. Kansa. Multiquadrics - A scattered data approximation scheme with application to computational fluid-dynamics - II Solution to parabolic, hyperbolic and elliptic partial differential equations. *Computers Math. Applic.*, 19:147–161, 1990.
- E. J. Kansa and R. E. Carlson. Improved accuracy of multiquadric interpolation using variable shape parameters. *Computers Math. Applic.*, 24:99–120, 1992.
- E. J. Kansa and H. C. Hon. Circumventing the Ill-Conditioning Problem with Multiquadric Radial Basis Functions: Applications to Elliptic Partial Differential Equations. *Computers Math. Applic.*, 39:123–137, 2000.
- A. B. Kennedy and J. D. Fenton. A fully-nonlinear computational method for wave propagation over topography. *Coast. Eng.*, 32:137–161, 1997.
- A. B. Kennedy, Q. Chen, J. T. Kirby, and R. A. Dalrymple. Boussinesq modeling of wave transformation, breaking, and runup. I: 1D. *J. Waterway, Port, Coast. and Ocean Eng.*, 126(1):39–47, 2000.
- A. B. Kennedy, J. T. Kirby, Q. Chen, and R. A. Dalrymple. Boussinesq-type equations with improved nonlinear performance. *Wave Motion*, 33:225–243, 2001.

- Min Woo Kim, Weoncheol Koo, and Sa Young Hong. Numerical analysis of various artificial damping schemes in a three-dimensional numerical wave tank. *Ocean Eng.*, 75:165–173, 2014.
- J. T. Kirby. Boussinesq models and applications to nearshore wave propagation, surfzone processes and wave-induced currents. In Elsevier V. C. Lakhan, editor, *Advances in Coastal Modeling*, pages 1–31, 2003.
- W. Koo and M.-H. Kim. Freely floating-body simulation by a 2D fully nonlinear numerical wave tank. *Ocean Eng.*, 31:2011–2046, 2004.
- H.-O. Kreiss and J. Olinger. Comparison of accurate methods for the integration of hyperbolic equations. *Telus XXIV*, 3:199–215, 1972.
- H. Lamb. *Hydrodynamics*. Cambridge University Press, 1932.
- J. L. Lara, N. Garcia, and I. J. Losada. RANS modelling applied to random wave interaction with submerged permeable structures. *Coast. Eng.*, 53:395–417, 2006.
- E. Larsson and B. Fornberg. A numerical study of some radial basis function based solution methods for elliptic PDEs. *Computers Math. Applic.*, 46:891–902, 2003.
- M. Le Gal, D. Violeau, and M. Benoit. Influence of timescales on the generation of seismic tsunamis. *Euro. J. Mecha. B/ Fluids*, 2017. (under revision).
- H.V.J. Le Meur. Derivation of a viscous Boussinesq system for surface water waves. *Asymptotic Analysis*, 94:309–345, 2015.
- C. Lee and K. D. Suh. Internal generation of waves for time-dependent mild-slope equations. *Coast. Eng.*, 34:35–57, 1998.
- B. Li and C. Fleming. A three dimensional multigrid model for fully nonlinear water waves. *Coast. Eng.*, 30:235–258, 1997.
- L. S. Liam, D. Adytia, and E. Van Groesen. Embedded wave generation for dispersive surface wave models. *Ocean Eng.*, 80:73–83, 2014.
- J. Lighthill. *Waves in Fluids*. Cambridge University Press, 1978.
- P.L.-F. Liu and A. Orfila. Viscous effects on transient long-wave propagation. *J. Fluid Mech.*, 50: 83–92, 2004.
- P.L.-F. Liu, G. Simarro, and A. Orfila. Experimental and numerical investigation of viscous effects on solitary wave propagation in a wave tank. *Coastal Engineering*, 53:181–190, 2006.
- P.L.-F. Liu, Y.S. Park, and E.A. Cowen. Boundary layer flow and bed shear stress under a solitary wave. *J. FLuid Mech.*, 574:449–463, 2007.

- M.S. Longuet-Higgins. Theory of weakly damped Stokes waves: a new formulation and its physical interpretation. *J. Fluid Mech.*, 235:319–324, 1992.
- L. Lu, L. Cheng, B. Teng, and L. Sun. Numerical simulation and comparison of potential flow and viscous fluid models in near trapping of narrow gaps. *Journal of Hydrodynamics*, 22:120–125, 2010.
- P. Lynett and P. L.-F Liu. A two-layer approach to wave modelling. *Proc. R. Soc. A*, 460:2637–2669, 2004.
- Q. W. Ma, G. X. Wu, and R. Eatock Taylor. Finite element simulation of fully non-linear interaction between vertical cylinders and steep waves. Part 1: Methodology and numerical procedure. *Int. J. Numer. Meth. Fluids*, 36:265–285, 2001.
- P. A. Madsen and H. A. Schäffer. Higher order Boussinesq-type equations for surface gravity waves: derivation and analysis. *Phil. Trans. R. Soc. A*, 356:3123–3181, 1998.
- P. A. Madsen, H. B. Bingham, and H. Liu. A new Boussinesq method for fully nonlinear waves from shallow to deep water. *J. Fluid Mech.*, 462:1–30, 2002.
- P. A. Madsen, D. R. Fuhrman, and B. Wang. A Boussinesq-type method for fully nonlinear waves interacting with a rapidly varying bathymetry. *Coast. Eng.*, 53:487–504, 2006.
- S.R. Massel. Harmonic generation by waves propagating over a submerged step. *Coastal Engineering*, 7:357–380, 1983.
- C.A. Micchelli. Interpolation of Scattered Data; Distance Matrices and Conditionally Positive Definite Function. *Constr. Approx.*, 2:11–22, 1986.
- J.W. Miles and D.M. Henderson. A note on interior vs. boundary-layer damping of surface waves in a circular cylinder. *J. Fluid Mech.*, 364:319–323, 1998.
- E. Monsalve, A. Maurel, V. Pagneux, and P. Petitjeans. Propagation of nonlinear waves passing over submerged step. *Physics Procedia*, 70:863–866, 2015.
- M. Narayanaswamy, A. J. Cabrera Crespo, and M. Gómez-Gesteira. SPHysics-FUNWAVE hybrid model for coastal wave propagation. *J. Hydraul. Res.*, 48:85–93, 2010.
- J. N. Newman and C.-H. Lee. Boundary-Element Methods in offshore structure analysis. *J. Offshore Mech. Arctic Eng.*, 124:81–89, 2002.
- J.A. Nicolás and J.M. Vega. A note on the effect of surface contamination in water wave damping. *J. Fluid Mech.*, 410:367–373, 2000.
- D. Z. Ning and B. Teng. Numerical simulation of fully nonlinear irregular wave tank in three dimensions. *Int. J. Num. Meth. Fluids*, 53:1847–1862, 2007.

- A. Przadka, B. Cabane, V. Pagneux, A. Maurel, and P. Petitjeans. Fourier transform profilometry for water waves: how to achieve clean water attenuation with diffusive reflection at the water surface? *Exp. Fluids*, 52:519–527, 2015.
- C. Raoult, M. Benoit, and M.L. Yates. Validation of a fully nonlinear and dispersive wave model with laboratory non-breaking experiments. *Coastal Eng.*, 114:194–207, 2016.
- M. M. Rienecker and J. D. Fenton. A Fourier approximation method for steady water waves. *J. Fluid Mech.*, 104:119–137, 1981.
- S. Rippa. An algorithm for selecting a good value for the parameter c in radial basis function interpolation. *Ad. Comp. Math.*, 11:193–210, 1999.
- M. Roseau. *Asymptotic Wave Theory*. North-Holland, Amsterdam, Holland, 1976.
- H. A. Schäffer. Second-order wavemaker theory for irregular waves. *Ocean Eng.*, 23:47–88, 1996.
- P. Schmitt and B. Elsaesser. A review of wave makers for 3D numerical simulations. In *Proceedings of the 6th International Conference on Computational Methods in Marine Engineering*, Rome, Italy, 2015.
- S. Shao. Incompressible SPH simulation of wave breaking and overtopping with turbulence modelling. *Int. J. Numer. Meth. Fluids*, 50:597–621, 2006.
- Y.-L. Shao and O. M. Faltinsen. A harmonic polynomial cell (HPC) method for 3D Laplace equation with application in marine hydrodynamics. *J. Comp. Phys.*, 274:312–332, 2014.
- C. Shu, H. Ding, and K.S. Yeo. Local radial basis function-based differential quadrature method and its application to solve two-dimensional incompressible Navier-Stokes equations. *Comp. Meth. Appl. Mech. Eng.*, 192:941–954, 2003.
- G. Simarro, A. Orfila, A. Gal'an, and G. Zarruk. Bottom friction effects on linear wave propagation. *Wave Motion*, 46:489–497, 2009.
- R. A. Smith. An operator expansion formalism for nonlinear surface waves over variable depth. *J. Fluid Mech.*, 363:333–347, 1998.
- S. E. Stead. Estimation of gradient from scattered data. *Rocky Mountain J. Math.*, 14:265–280, 1984.
- G. Stelling and M. Zijlema. An accurate and efficient finite-difference algorithm for non-hydrostatic free-surface flow with application to wave propagation. *Int. J. Numer. Meth. Fluids*, 43:1–23, 2003.
- M. Tanaka. The stability of solitary waves. *Phys. Fluids*, 29(3):650–655, 1986.

- Y. Tian and S. Sato. A numerical model on the interaction between nearshore nonlinear waves and strong currents. *Coast. Eng. J.*, 50(4):369–395, 2008.
- Z. Tian, M. Perlin, and W. Choi. Energy dissipation in two-dimensional unsteady plunging breakers and an eddy viscosity model. *J. Fluid Mech.*, 655:217–257, 2010.
- A. I. Tolstykh and D. A. Shirobokov. On using radial basis functions in a 'finite difference mode' with applications to elasticity problems. *Comp. Mech.*, 33:68–79, 2003.
- T. Torsvik and P.L.-F Liu. An efficient method for the numerical calculation of viscous effects on transient long waves. *Coastal Engineering*, 54:263–269, 2007.
- C. L. Vincent and M. J. Briggs. Refraction-Diffraction of Irregular Wave over a Mound. *J. Wat. Port Coast. Ocean Eng*, 115:269–284, 1989.
- C. Viotti and F. Dias. Extreme waves induced by strong depth transitions: Fully nonlinear results. *Phys. Fluids*, 26, 2014.
- P. Wang, Y. Yao, and M. Tulin. An efficient numerical tank for nonlinear water waves, based on the multi-subdomain approach with BEM. *Int. J. Numer. Meth. Fluids*, 20:1315–1336, 1995.
- B. J. West, K. A. Brueckner, R. S. Janda, M. Milder, and R. L. Milton. A new numerical method for surface hydrodynamics. *J. Geophys. Res.*, 92:11803–11824, 1987.
- R. W. Whalin. The limit of applicability of linear wave refraction theory in a convergence zone. Technical report, DTIC Document, 1971.
- J. Wilkening and V. Vasan. Comparison of five methods of computing the Diriclet-Neumann Operator for the water wave problem. *Nonlinear Wave Equations: Analytic and Computational Techniques, Contemporary Mathematics*, 635:175–206, 2015.
- A. S. M. Wong, Y. C. Hon, T. S. Li, S. L. Chung, and E. J. Kansa. Multizone decomposition for simulation of time-dependent problems using the multiquadric scheme. *Comp. Math. Applic.*, 37:23–43, 1999.
- G. B. Wright. *Radial Basis Function Interpolation : Numerical and Analytical Developments*. PhD thesis, University of Colorado, 2003.
- G. B. Wright and B. Fornberg. Scattered node compact finite difference-type formulas generated from radial basis functions. *J. Comp Phys.*, 212:99–123, 2006.
- G. X. Wu, Q. W. Ma, and R Eatock Taylor. Numerical simulation of sloshing waves in a 3D tank based on a finite element method. *Appl. Ocean Res.*, 20:337–355, 1998.
- L.-F. Xiao, J.-M. Yang, T. Peng, and J. Li. A meshless numerical wave tank for simulation of nonlinear irregular waves in shallow water. *Int. J. Num. Meth. Fluids*, 61:165–184, 2008.

- L. Xu and P. Guyenne. Numerical simulation of three-dimensional nonlinear water waves. *J. of Comp. Phys.*, 228:8446 – 8466, 2009.
- Z. Yang, S. Liu, H. B. Bingham, and J. Li. Second-order coupling of numerical and physical wave tanks for 2D irregular waves. Part I: Formulation, implementation and numerical properties. *Coast. Eng.*, 92:48–60, 2014.
- M. L. Yates and M. Benoit. Accuracy and efficiency of two numerical methods of solving the potential flow problem for highly nonlinear and dispersive water waves. *Int. J. Numer. Meth. Fluids*, 77:616–640, 2015.
- M.L. Yates and M. Benoit. Modélisation non-linéaire et dispersive des vagues en zone côtière: étude comparative de deux méthodes de simulation précises. In *Actes des 13èmes Journées de l’Hydrodynamique*, Chatou, France, 2012.
- V. E. Zakharov. Stability of periodic waves of finite amplitude on the surface of a deep fluid. *J. Appl. Mech. Tech. Phys.*, 9(2):190–194, 1968.
- J. A. Zelt. The run-up of nonbreaking and breaking solitary waves. *Coast. Eng.*, 15:205–246, 1991.
- C. Zhang and W. Duan. Numerical study on a hybrid water wave radiation condition by a 3d boundary element method. *Wave Motion*, 49:525–543, 2012.
- X. T. Zhang, B. C. Khoo, and J. Lou. Application of desingularized approach to water wave propagation over three-dimensional topography. *Ocean Eng.*, 34:1449–1458, 2007.
- B. B. Zhao, R. C. Ertekin, W. Y. Duan, and M. Hayatdavoodi. On the steady solitary-wave solution of the Green-Naghdi equations of different levels. *Wave Motion*, 51:1382–1395, 2014.
- X. Zhou, Y. C. Hon, and J. Li. Overlapping domain decomposition method by radial basis functions. *Appl. Num. Math.*, 44:241–255, 2003.
- L. Zhu, Q. Chen, and X. Wan. Optimization of non-hydrostatic Euler model for water waves. *Coast. Eng.*, 91:191–199, 2014.
- M. Zijlema and G. S. Stelling. Further experiences with computing non-hydrostatic free-surface flows involving water waves. *Int. J. Numer. Meth. Fluids*, 48:169–197, 2005.
- M. Zijlema and G. S. Stelling. Efficient computation of surf zone waves using the nonlinear shallow water equations with non-hydrostatic pressure. *Coast. Eng.*, 55:780–790, 2008.
- M. Zijlema, G. S. Stelling, and P. Smit. SWASH: An operational public domain code for simulating wave fields and rapidly varied flows in coastal waters. *Coast. Eng.*, 58:992–1012, 2011.